

**REPUBLIC OF TURKEY
YILDIZ TECHNICAL UNIVERSITY
GRADUATE SCHOOL OF NATURAL AND APPLIED SCIENCES**

**QUANTITATIVE ANALYSIS OF CARBON NANOTUBE
SUSPENSIONS, SYNTHESIS OF INORGANIC
NANOSTRUCTURED MATERIALS AND THEIR
CHARACTERIZATION**

ALİ CAN ZAMAN

**Ph.D THESIS
DEPARTMENT OF METALLURGICAL AND MATERIALS
ENGINEERING
PROGRAM OF MATERIALS**

**ADVISER
PROF. DR. CENGİZ KAYA
CO- ADVISER
PROF. DR. FİGEN KAYA**

İSTANBUL, 2015

REPUBLIC OF TURKEY
YILDIZ TECHNICAL UNIVERSITY
GRADUATE SCHOOL OF NATURAL AND APPLIED SCIENCES

**QUANTITATIVE ANALYSIS OF CARBON NANOTUBE
SUSPENSIONS, SYNTHESIS OF INORGANIC
NANOSTRUCTURED MATERIALS AND THEIR
CHARACTERIZATION**

A thesis submitted by Ali Can ZAMAN in fulfillment of the requirements for the degree of **DOCTOR OF PHILOSOPHY** is approved by the committee on 06.10.2015 in Department of Metallurgical and Materials Engineering, Materials Program.

Thesis Adviser

Prof. Dr. Cengiz KAYA
Yıldız Technical University

Co- Adviser

Prof. Dr. Figen KAYA
Yıldız Technical University

Approved By the Examining Committee

Prof. Dr. Cengiz KAYA
Yıldız Technical University

Prof. Dr. Figen KAYA
Yıldız Technical University

Prof. Dr. Gültekin GÖLLER
İstanbul Technical University

Prof. Dr. Sedat ALKOY
Gebze Technical University

Prof. Dr. Mehmet Ali GÜLGÜN
Sabancı University

Prof. Dr. Mustafa CİGDEM
Yıldız Technical University

Assoc. Prof. Dr. Yüksel PALACI
Yıldız Technical University

This study was supported by the Scientific and Technological Research Council of Turkey (TUBITAK) Grant No: 109R007. There is also fundings from Yildiz Technical University under contract numbers 2012-07-02-DOP02 and 2012-07-02-KAP05, respectively.

ACKNOWLEDGEMENTS

This labour intensive and compelling work can't be accomplished in isolation. My first acknowledgements are to my mother, father and my brother. Secondly, I'd like to thank my supervisors: Prof. Cengiz Kaya and Prof. Figen Kaya for their advices and encouragement.

Assist. Prof. Cem Bülent Üstündağ, Prof. Gültekin Güller, Prof. Mehmet Ali Gülgün, Prof. Sedat Alkoy, Assoc. Prof. Yuksel Palaci, Dr. Ali Çelik, Prof. Alpagut Kara, Prof. H. Yılmaz Kaptan, Cansu Noberi, Togayhan Kutluk, Assist. Prof. Başar Uyar, Assist. Prof. Zerrin Zerenler Çalışkan and Assist. Prof. Hüseyin Üvet are also acknowledged.

October, 2015

Ali Can ZAMAN

TABLE OF CONTENTS

	Page
ACKNOWLEDGEMENTS.....	iv
TABLE OF CONTENTS.....	v
LIST OF SYMBOLS.....	viii
LIST OF ABBREVIATIONS.....	ix
LIST OF FIGURES.....	xi
LIST OF TABLES.....	xvii
ABSTRACT.....	xviii
ÖZET.....	xxi
CHAPTER 1	
INTRODUCTION.....	1
1.1 Literature Review.....	1
1.1.1 Carbon Nanotubes.....	1
1.1.1.1 Colloids of Carbon Nanotubes and Their Characterization.....	2
1.1.2 Iron Oxides.....	9
1.1.2.1 Applications of Iron Oxides.....	10
1.1.2.2 Structure of Fe ₃ O ₄ and Other Iron Oxides.....	10
1.1.2.3 Synthesis of Iron Oxides: Solvothermal Synthesis.....	11
1.1.2.4 Core Shell Iron Oxide Nanoparticles and Iron Oxide Containing Composites.....	15
1.1.3 Inorganic Nanotubes.....	16
1.1.3.1 Inorganic Nanotube Synthesis.....	16
1.1.3.2 Titanate Nanotubes.....	17
1.2 Objective of the Thesis.....	18
1.3 Hypothesis.....	18
CHAPTER 2	
MATERIALS AND METHODS.....	23
2.1 Suspensions Preparation for Synthesis of Nanocomposites and EPD.....	23

2.2	Method of Quantitative Analysis of Suspensions and Coatings	24
2.3	Carbon Nanotube-Iron Oxide Nanocomposite Synthesis.....	29
2.4	Inorganic Nanotube Synthesis Processes	31
2.5	Other Devices Used in Characterization of Synthesized or Processed Materials	33
CHAPTER 3		
QUANTITATIVE ANALYSIS OF CARBON NANOTUBE DISPERSIONS.....		37
3.1	Colloidal Suspensions of MWCNTs	37
3.2	Determination of Quantity of Polymer Based Dispersant and Carbon Nanotubes in Centrifuged Suspensions and in Coatings.....	39
3.2.1	UV-Vis Measurements	39
3.2.1.1	Carboxyl Functionalized MWCNTs	41
3.2.2	Thermogravimetric Analysis	45
3.2.3	Zeta potential analysis of PVP-MWCNTs IPA suspensions.....	49
3.2.4	EPD and determination of PVP and MWCNTs quantities in coatings.....	53
3.3	Determination of Quantity of SDBS and MWCNTs in Centrifuged Suspensions, EPD and Their Characterization	58
3.3.1	UV-Vis Spectroscopy Analysis	58
3.3.2	TGA measurements	63
3.4	Results	70
CHAPTER 4		
NANOPARTICLE AND NANOCOMPOSITE SYNTHESIS		71
4.1	Solvothermal Synthesis Of Iron Oxide Nanocrystals.....	72
4.1.1	Solvothermal Synthesis of Fe ₃ O ₄	72
4.1.2	Ascorbic Acid Assisted Solvothermal Synthesis of Fe ₃ O ₄	76
4.1.2.1	Ascorbic Acid Assisted Synthesis (FeSO ₄ /Ascorbic Acid Mole Ratio =5).....	77
4.1.2.2	Ascorbic Acid Assisted Synthesis (FeSO ₄ /Ascorbic Acid Mole Ratio =1, 25).....	79
4.1.2.3	Ascorbic Acid Assisted Synthesis (FeSO ₄ /Ascorbic Acid Mole Ratio =0.625).....	84
4.1.3	Glucose Assisted Solvothermal Synthesis of Fe ₃ O ₄	86
4.1.3.1	Glucose Assisted Synthesis of Iron Oxide (FeSO ₄ /Glucose mole ratio =5).....	86
4.1.3.2	Glucose Assisted Synthesis of Iron Oxide (FeSO ₄ /Glucose Mole Ratio =1.25).....	87
4.1.3.3	Glucose Assisted Synthesis of Iron Oxide (FeSO ₄ /Glucose Mole Ratio =0.625).....	90
4.2	Solvothermal Synthesis of Carbon Nanotube/Iron Oxide Hybrid Materials.	92
4.2.1	SDBS Modified MWCNTs and Pure Fe ₃ O ₄ Containing Nanocomposite Synthesis.....	93
4.2.2	PVP Modified Carbon Nanotube and Pure Fe ₃ O ₄ Containing Nanoparticle Synthesis	95
4.2.3	Ascorbic Acid and Glucose Aided Synthesis of PVP or SDBS Modified MWCNTs and Pure Fe ₃ O ₄ Containing Nanomaterials	96
4.3	Results	98

CHAPTER 5

SYNTHESIS OF TITANATE NANOTUBES AND THEIR CHARACTERIZATION

.....	100
5.1 Sequence of Synthesis and Characterization of Titanate Nanotubes	100
5.1.1 TiO ₂ Nanoparticles and Their Characterization	100
5.1.2 Titanate Nanotubes and Their Characterization	103
5.1.3 Colloidal Coatings of Titanate Nanotubes	115
5.2 Results	119

CHAPTER 6

GENERAL RESULTS AND DISCUSSION

6.1 Carbon Nanotube Dispersion in Organic Solvents and Quantitative Analysis	121
6.1.1 SDBS Containing Suspensions	121
6.1.2 PVP Containing Suspensions.....	123
6.1.3 UV-Vis Spectroscopy and Thermogravimetric Analysis	124
6.1.4 EPD and Estimation of Coating Thickness.....	125
6.2 Carbon Nanotube/Iron Oxide Hybrid Nanoparticles.....	126
6.3 Synthesis and Characterization of Titanate Nanotubes	129
6.3.1 Suspension Preparation and EPD of TNTs.....	134
6.4 Future Work.....	135
REFERENCES	136
CURRICULUM VITAE.....	146

LIST OF SYMBOLS

π	Pi bond
α	Absorption coefficient
ϵ	Dielectric constant
E	Electrical field
μ	Micron
Θ	Sigma bond
λ	Wavelength
β	Full width half maximum
ν	Frequency
n	Non-bonding orbital
Θ^*	Non-bonding sigma orbital
π^*	Non-bonding pi orbital
d	Interatomic spacing
eV	Electron volt
W	Watt
mV	Mili volt
$^{\circ}\text{C}$	Celcius
δ_d	Hansen solubility parameter: Dispersion component
δ_p	Hansen solubility parameter: Polar component
δ_h	Hansen solubility parameter: Hydrogen bonding component
pH	Potential of hydrogen
K	Kelvin
M	Meter
J	Joule
H	Plank's constant
E_{bg}	Band gap energy of semiconductor

LIST OF ABBREVIATIONS

ATR	Attenuated total reflection
AFM	Atomic Force Microscope
BSE	Backscattered electron
BSD	Backscattered electron dedector
CTAB	Cetyl trimethylammonium bromide
CHP	Cyclohexyl-pyrrolidinone
DTA	Differential Thermal Analysis
DMF	Dimethylformamide
ESR	Electron Spin Resonance Spectroscopy
EG	Ethylene glycol
FTIR	Fourier Transformation Infrared Spectroscopy
Fe ₃ O ₄	Magnetite
Fe ₃ O ₄ @C	Carbon coated magnetite
IPA	Isopropyl alcohol
NMP	N-Methyl-2-pyrrolidone
Mg	Magnesium
MWCNT	Multi Walled Carbon Nanotube
PVP	Polyvnylpyrrolidone
P2VP	Poly(2-vinylpyridine)
P4VP	Poly(4-vinylpyridine)
PSS	Polystyrene sulfonate
PEG	Polyethylene glycol
RCF	Relative centrifugal force
SE	Secondary electron
SETOV	Single electron trapped oxygen vacancy
SDS	Sodium Dodecyl Sulfate
SWCNT	Single Walled Carbon Nanotube
SDBS	Sodium Dodecyl Benzene Sulfonate
SEM	Scanning Electron Microscopy
TGA	Thermogravimetric Analysis
TEA	Triethanolamine
TEM	Transmission Electron Microscopy
TNT	Titanate nanotube
TNTA	Acid washed titanate nanotube
TNTaq	Only deionized water washed titanate nanotubes

TNTA350N ₂	Acid washed titanate nanotubes calcined at 350°C under N ₂ atmosphere
TNTAH ₂ O ₂	Acid and hydrogen peroxide washed titanate nanotubes
TTIP	Titaniumtetrakisopropoxide
UV-Vis	UV-Visible Absorption spectroscopy
UV	Ultraviolet
VdW	Van der Waals forces
α -Fe ₂ O ₃	Hematite
α -FeOOH	Goethite
γ -FeOOH	Lepidocrocite
γ -Fe ₂ O ₃	Maghemite

LIST OF FIGURES

	Page
Figure 1.1	(a) SWCNTs and (b) MWCNT by [2], [3]. 2
Figure 1.2	Drawing of dissociation of carboxyl groups on carbon nanotubes in water (a); A TEM image which shows result of functionalization (b). Functionalization disrupts CNT integrity, by [10]. 4
Figure 1.3	Molecular structure of SDBS. 4
Figure 1.4	Interaction of (SDS)–CNT in a liquid: (a) below CMC, (b) at the CMC, and (c) above the CMC by Sa et al. [11]. 5
Figure 1.5	Different mechanisms of adsorption of surfactants on CNT surface: (a) encapsulation of CNT by cylindrical surfactant micelle, (b) formation of hemimicelles on carbon nanotube surface and (c) random adsorption of surfactant molecules on nanotube surface by [13], [5]. 6
Figure 1.6	Natural and resonance structure of PVP. 7
Figure 1.7	Possible arrangements of PVP wrapping on SWCNTs surface proposed by O’Connell et al. [7]. A double helix (top), a triple helix (middle) and an internal-rotation induced switch-back (bottom). 8
Figure 1.8	Schematic diagram showing the spin magnetic moment configuration for iron ions in Fe ₃ O ₄ by [32]. 11
Figure 1.9	Drawing of a functionalized CNT and Fe ₃ O ₄ nanoparticles attached on CNT during synthesis. 19
Figure 1.10	Depiction of solvothermally synthesized Fe ₃ O ₄ @C nanoparticle (a), (b) is SEM image of glucose assisted synthesis product (Fe ₃ O ₄ @C); (c) and (d) are depiction and SEM image of result of preliminary experiments revealing a pseudo interaction between nanotubes and nanoparticles. 21
Figure 2.1	Sequence of events for preparation of stable CNT suspensions. 24
Figure 2.2	Illustration of electronic level and discrete rotational and vibrational energy levels above electronic states [83]. 24
Figure 2.3	Electronic transitions of σ , π , and n electrons [83]. 25
Figure 2.4	(a), (b), (c) and (d) are UV-Vis analysis sequences of PVP or SDBS in MWCNTs suspensions. 26
Figure 2.5	Method used to assess MWCNTs’ concentration by using UV-Vis spectra. (a) and (b) are depictions of spectra used in the analysis method. 27
Figure 2.6	EPD apparatus before and after deposition. 28
Figure 2.7	Sequence of events used for the determination of concentration of components in coatings. 28
Figure 2.8	Illustration (a), and images (b) and (c) of mixing sequence before solvothermal synthesis of nanocomposites. 30
Figure 2.9	Magnetic separation and decantation of dissolved impurities in liquids after synthesis. 31

Figure 2.10	Method used in the synthesis of TiO ₂ nanoparticles by sol-gel process. ..	31
Figure 2.11	Method of hydrothermal synthesis of titanate nanotubes.....	32
Figure 2.12	H ₂ O ₂ modification step of titanate nanotubes.....	32
Figure 2.13	Electrical double layer.....	33
Figure 3.1	SEM images of agglomerates of carbon nanotubes in low and high magnifications.	37
Figure 3.2	Result of sedimentation for more than a year for different solvent containing MWCNTs and SDBS suspensions prepared by ultrasonication (bath sonication) and centrifugation (2820 RCF). Initial SDBS and MWCNTs concentrations were the same (before centrifugation).....	38
Figure 3.3	Pristine MWCNTs IPA suspension after ultrasonication (left) and SDBS MWCNTs IPA suspension after centrifugation (right). Both suspensions were 10 times diluted.....	38
Figure 3.4	From left to right 10 times diluted Pristine MWCNTs IPA, PVP MWCNTs IPA and COOH MWCNTs IPA suspensions.....	39
Figure 3.5	UV-Vis spectra of IPA and PVP IPA solutions at different concentrations. Baseline correction was done by subtracting contribution of IPA from PVP solutions.....	40
Figure 3.6	Calibration curve of PVP in IPA.	40
Figure 3.7	UV-Vis spectra of diluted PVP MWCNTs IPA suspensions. They were diluted between 40 and 100 times in this figure.....	41
Figure 3.8	(a) and (b) are FTIR spectra of Pristine MWCNTs IPA (dashed) and COOH MWCNTs IPA suspensions at different wavelength ranges.	42
Figure 3.9	UV-Vis spectra of COOH MWCNTs IPA at different concentrations.	43
Figure 3.10	PVP-MWCNTs IPA, COOH-MWCNTs IPA and resultant spectrum after subtraction of latter from the former.	44
Figure 3.11	Overlapping spectra of PVP MWCNTs IPA before centrifuge and after centrifuge. CF indicates the suspension which is not subjected to centrifugation. Therefore, concentration of MWCNTs is known at that spectrum.	45
Figure 3.12	TG curves of pristine MWCNTs (purple dashed horizontal line), PVP (red continuous curve), dried supernatant of PVP MWCNTs IPA (dashed curve) and dried precipitate of PVP MWCNTs IPA (finer dashed curve).	46
Figure 3.13	(a) Dervative TG curves of PVP, dried supernatant of PVP MWCNTs IPA and dried precipitate of PVP MWCNTs IPA CF; (b) shows TG curves which were shifted (except curve of PVP) to eliminate the mass loss below 250 °C.	47
Figure 3.14	(a) is depiction of neutral structure of PVP molecule and its resonance structure. (b) is Zeta potential distribution of PVP or COOH MWCNTs containing suspensions obtained using Huckel's approximation.....	53
Figure 3.15	(a) SEM images of 70° tilted coating obtained by EPD of PVP MWCNTs IPA 2xMgCl ₂ suspension on stainless steel substrate under 50V DC potential for 10 min. (b) is SEM micrograph of a crack on deposit surface.	54
Figure 3.16	(a) is SEM images of 70° tilted coating obtained by EPD of PVP MWCNTs IPA 2xMgCl ₂ suspension on stainless steel substrate under 50V DC potential for 20 min. (b) is SEM micrograph of a crack on surface.....	55
Figure 3.17	(a) UV-Vis spectra of suspensions analyzed before and after EPD processes and overlapping spectra of COOH MWCNTs IPA with electrophoretic suspensions. (b) is the spectra obtained after subtraction of MWCNTs'	

	contribution. (c) is representing the PVP in the coating which is also shown in (b) as the red curve. (d) is overlapping spectra of EPD suspension after EPD with that of uncentrifuged PVP MWCNTs IPA suspension.....	57
Figure 3.18	Cross-section SEM images of PVP MWCNTs IPA coatings deposited for 20 min. under 50 V. (a) is BSE image; (b), (c) and (d) are SE images.	58
Figure 3.19	UV-Vis spectra of SDBS in IPA at different concentrations.	59
Figure 3.20	Calibration curve of SDBS in IPA. Curve is obtained by using absorbance values at 223 nm for each suspension.	59
Figure 3.21	UV-Vis spectra of SDBS in different concentrations in IPA.	60
Figure 3.22	Calibration curve of SDBS in IPA. Absorbance values at 256 nm were used.	60
Figure 3.23	UV-Vis spectra of 75 times diluted SDBS MWCNTs IPA and COOH MWCNTs IPA. Third spectrum is extracted by subtracting the two spectra.	61
Figure 3.24	(a) UV-Vis spectra of 10 times diluted SDBS MWCNTs IPA and COOH MWCNTs IPA. Green curve is result of subtraction of MWCNTs contribution from SDBS MWCNTs IPA's UV-Vis spectrum. (b) Straight lines are UV-Vis spectra of SDBS IPA and dashed line is extracted spectrum.	62
Figure 3.25	Overlapping spectra of SDBS MWCNTs IPA suspensions before and after centrifuge. CF indicates the uncentrifuged suspensions.....	63
Figure 3.26	(a) TG curves of pure SDBS, dried supernatant of SDBS MWCNTs IPA and dried precipitate of centrifuged SDBS MWCNTs IPA CF obtained in inert atmosphere. (b) First derivative of TGA curves of SDBS, supernatant and precipitate.	64
Figure 3.27	Shifted TGA curves of SDBS, supernatant and precipitate. Supernatant and precipitate curves are shifted to overlap with that of SDBS curve at 275 °C and TG value at 275 °C was set as onset of mass loss.	64
Figure 3.28	Illustration of possible distribution of SDBS molecules and nanotubes in suspension.....	67
Figure 3.29	Zeta potential distribution curves of suspensions. (a) contains curves obtained by using Huckel's approximation and (b) contains curves obtained by using Smoluchowski's approximation. ("Smo" is abbreviation for Smoluchowski's approximation).....	69
Figure 3.30	SEM image of coating obtained by means of EPD of SDBS MWCNTs IPA (a). (b) contains examples of MWCNTs coatings from suspensions prepared with different solvents.	69
Figure 4.1	(a) is the image taken just after mixing FeSO ₄ .7H ₂ O and NaOH (both are dispersed in EG prior to mixing) and (b) is image taken 10 minutes after complete mixing of all raw materials. Dark green color transformed into brown in time during nitrogen bubbling and ultrasonication.	73
Figure 4.2	SEM images of Fe ₃ O ₄ nanoparticles synthesized without using an additive at 200 °C for 12h. from FeSO ₄ and NaOH in organic solvents (IPA-EG mixture); (a), (b), (c) and (d) are all micrographs of Fe ₃ O ₄ , arrow in (c) represents a relatively small spherical particle and arrow in (d) is indicating one example of a big octahedron shape particle.....	74
Figure 4.3	XRD graph of Fe ₃ O ₄	75
Figure 4.4	FTIR spectrum of Fe ₃ O ₄	75
Figure 4.5	(a) Volumetric gas absorption, desorption isotherm of Fe ₃ O ₄ , (b) BET plot of Fe ₃ O ₄ (10.7 g/m ²).	76

Figure 4.6	(a), (b) and (d) are SE SEM images of Fe ₃ O ₄ nanocrystals. (c) is BSE image (FeSO ₄ /Ascorbic acid mole ratio =5). Arrows indicate grooves on nanoparticle surfaces.	77
Figure 4.7	(a),(b), (c) and (d) are SEM images of Fe ₃ O ₄ nanocrystals (FeSO ₄ /Ascorbic acid mole ratio =5). Particles have octahedral, spherical or distorted octahedral morphology.	78
Figure 4.8	SEM images of ascorbic acid assisted synthesis result of Fe ₃ O ₄ nanoparticles (FeSO ₄ /Ascorbic acid mole ratio =5). From (a) to (e) images are SE images, (f) is a BSE image.	80
Figure 4.9	XRD graph of synthesized Fe ₃ O ₄ (FeSO ₄ /Ascorbic acid mole ratio =1.25). Note that signal to noise ratio is decreased compared to pure Fe ₃ O ₄ because of amorphous carbon in the structure.	81
Figure 4.10	FTIR spectrum of ascorbic acid assisted synthesis product (FeSO ₄ /Ascorbic acid mole ratio =1.25). Top spectrum belongs to waited powder in air having red-brown color and spectrum at the bottom is that of powder measured immediately after synthesis.	82
Figure 4.11	(a) is Adsorption-desorption isotherm of Fe ₃ O ₄ samples and (b) is BET graph of Fe ₃ O ₄ (FeSO ₄ /Ascorbic acid mole ratio =1.25) (16.735 m ² /g)..	83
Figure 4.12	Suspensions of iron oxide nanoparticles (FeSO ₄ /Ascorbic acid mole ratio =1.25): (a) and (b) are before and after magnetic separation of aqueous suspension, respectively. (c) contains butanolic and aqueous Fe ₃ O ₄ suspensions after ultrasonication, (d) contains same suspensions in (c) after rest for some time, (e) is a suspension containing same Fe ₃ O ₄ nanoparticles revealing their color.	84
Figure 4.13	(a), (b), (c) and (d) are SEM images of ascorbic acid assisted synthesis products at various magnifications (FeSO ₄ /Ascorbic acid mole ratio =0.625).	85
Figure 4.14	FTIR spectrum of Fe ₃ O ₄ nanoparticles synthesized with the aid of ascorbic acid (FeSO ₄ /Ascorbic acid mole ratio =0.625).	86
Figure 4.15	(a), (b), (c) and (d) are SEM images of synthesized Fe ₃ O ₄ nanoparticles at different magnifications (FeSO ₄ /glucose mole ratio =5).	87
Figure 4.16	(a), (b), (c) and (d) are SEM images of synthesized Fe ₃ O ₄ nanoparticles with the aid of glucose at different magnifications (FeSO ₄ /glucose mole ratio =1.25). Yellow circle in (a) indicates an example of irregular shape particle.	88
Figure 4.17	XRD graph of Fe ₃ O ₄ nanocrystals (FeSO ₄ /glucose mole ratio =1.25). There is a decrease in signal to noise ratio compared to pure Fe ₃ O ₄ due to amorphous carbons' presence.	88
Figure 4.18	FTIR spectrum of glucose assisted synthesis products (FeSO ₄ /glucose mole ratio =1.25).	89
Figure 4.19	(a) is Nitrogen adsorption desorption isotherm of Fe ₃ O ₄ powders and (b) is BET isotherm (FeSO ₄ /glucose mole ratio =1.25 (21.3 m ² /g)).	90
Figure 4.20	SEM images of glucose assisted synthesis products. (a) and (b) are relatively lower magnification images and (c) and (d) are higher magnification images. Red arrows indicate particles having irregular morphology (FeSO ₄ /glucose mole ratio =0.625).	91
Figure 4.21	XRD graph of synthesized product (FeSO ₄ /glucose mole ratio =0.625). .	91
Figure 4.22	FTIR spectrum of iron oxide nanoparticles (FeSO ₄ /glucose mole ratio =0.625).	92

Figure 4.23	Consecutive washing with water during magnetic separation after synthesis of Fe ₃ O ₄ SDBS MWCNTs. Ultrasonication prior to magnetic separation causes phase separation (Magnets are below the bottles).....	93
Figure 4.24	(a) and (b) are low magnification SEM images of Fe ₃ O ₄ SDBS MWCNTs, (c) and (d) are high magnification images, clearly showing particles are glued by the presence of excess SDBS. Arrows indicate rectangular prism shape particles.....	94
Figure 4.25	SEM images of Fe ₃ O ₄ PVP MWCNTs. (a) and (b) are relatively low magnification images. (c) and (d) are higher magnification images revealing most of the particles have octahedral geometry, but there are few particles possess irregular geometry.	95
Figure 4.26	(a) is SEM image of water washed ascorbic acid aided synthesis product. Most of MWCNTs are washed away during separation. (b) is synthesis product without <u>PVP and MWCNTs</u> addition, (c) is higher magnification image of Fe ₃ O ₄ -PVP-MWCNTs (FeSO ₄ /Ascorbic acid =1.25), (d) is resultant sediment after washing with acetone.....	96
Figure 4.27	Glucose aided synthesis result of Fe ₃ O ₄ @C-MWCNTs nanomaterials. PVP was used for dispersion of MWCNTs.	97
Figure 4.28	Secondary electron (a) and backscattered electron (b) SEM images of products (Fe ₃ O ₄ @C MWCNTs) prepared by mixing with acetone each time prior to magnetic separation, (c) and (d) are samples subjected to magnetic separation dispersed in acetone and water, respectively. Along with Fe ₃ O ₄ @C nanoparticles, SDBS and MWCNTs migrate towards magnets in acetone.....	98
Figure 5.1	TEM images of TiO ₂ nanoparticles synthesized via Sol-gel.....	101
Figure 5.2	XRD graphs of synthesized and calcined pure (TiO ₂) or S-doped TiO ₂ (1STiO ₂ , 4STiO ₂) nanoparticles.	102
Figure 5.3	XRD patterns of TiO ₂ and doped TiO ₂ s between 2 theta degrees of 23° and 28° (Curves were shifted for clarity on y-axis).	102
Figure 5.4	(a) and (b) are SEM images of acid washed titanate nanotubes (TNTA), (c) and (d) are TEM images of TNTA.	104
Figure 5.5	TEM images of acid washed nanotubes calcined at 450 °C. Tubular structure becomes disrupted at this temperature range. (a) contains rod like particles mostly and (b) contains spherical ones.....	105
Figure 5.6	(a) and (b) are TEM images of TNTA _{350N₂} (Calcined and acid washed nanotubes), (c) and (d) are TEM images of H ₂ O ₂ washed and calcined TNTAs.	106
Figure 5.7	(a) and (b) are relatively low magnification TEM images of sulphur doped TNTAs, (c) and (d) are higher magnification TEM images. Tubularity couldn't be relatively successfully preserved as in the case of undoped samples.	107
Figure 5.8	FTIR spectra of nanotubes: (a) contains spectra of synthesized and modified nanotubes not subjected to calcination and (b) contains FTIR spectra of calcined samples (350 °C).	108
Figure 5.9	XRD patterns of synthesized, washed and calcined nanotube samples. "A" letter denotes anatase TiO ₂ , "T" denotes titanate and "ST" denotes sodium titanate.	110
Figure 5.10	BET plot of TNTA sample degassed at 150 °C. Acid washed titanate nanotubes has 549 m ² /g specific surface area.	110

Figure 5.11	Particle size analysis results for stable optically clear dilute suspensions which were also subjected to UV-Vis absorption spectroscopy analysis for band gap calculation.	111
Figure 5.12	(a) UV-Vis absorption spectra of titanate nanotubes. (b) Tauc plots of selected nanotubes obtained from the above spectra.	112
Figure 5.13	ESR spectra of TNTA350N ₂ , TNTA450N ₂ and TNTAH ₂ O ₂ 350N ₂	114
Figure 5.14	(a) Electron Spin resonance spectra of TNTA350N ₂ and 4STNTA350N ₂ . (b) ESR spectra of 4STNTA350N ₂ and 4STNTAH ₂ O ₂ 350N ₂	115
Figure 5.15	Schematic illustration of proton capture of TEA from butanol molecule.	116
Figure 5.16	Image of 2 months waited TEA containing butanolic suspensions (4 g/L solid content is fixed for all samples.).....	117
Figure 5.17	(a) Illustration of EPD cell, (b) images of as synthesized and acid washed nanotube (TNTA) coatings obtained from different suspensions with varying TEA content.	118
Figure 5.18	Optical microscopy images of uncoated metallic foam (a), TNTA coated metallic foam (b); (c) and (d) are SEM images of coatings on metallic foams.	119

LIST OF TABLES

	Page
Table 3.1	Calculated Concentrations of PVP and MWCNTs in Supernatants by using Uv-Vis and TGA analysis.....49
Table 3.2	Zeta potentials of PVP MWCNTs IPA and COOH MWCNTs IPA suspensions.....50
Table 3.3	Calculated Concentrations of PVP and MWCNTs in Supernatant by using UV-Vis spectroscopy and TGA analysis.....66
Table 3.4	Zeta potentials of SDBS containing suspensions..... 68

ABSTRACT

QUANTITATIVE ANALYSIS OF CARBON NANOTUBE SUSPENSIONS, SYNTHESIS OF INORGANIC NANOSTRUCTURED MATERIALS AND THEIR CHARACTERIZATION

Ali Can ZAMAN

Department of Metallurgical and Materials Science Engineering

Ph.D Thesis

Adviser: Prof. Dr. Cengiz KAYA

Co-adviser: Prof. Dr. Figen KAYA

This thesis consists of two separate studies. Under the scope of the first study dispersion of carbon nanotubes in organic solvents was carried out and carbon nanotube reinforced iron oxide composites were produced. MWCNTs suspensions were prepared in environments where IPA is the solvent. To provide homogeneous dispersion of MWCNTs in IPA, PVP and SDBS were utilized as additives. Ultrasonic mixing and subsequent to this operation implementation of centrifugation facilitated acquiring both PVP and SDBS containing stable suspensions. Zeta potential analysis and sedimentation tests indicate that suspensions are stable. UV-Vis absorption spectroscopy was used to determine concentrations of PVP, SDBS and MWCNTs in suspensions in which information about concentration of components is lost by implementation of centrifugation. TGA was also performed on dried precipitates and suspensions for comparison with UV-Vis analysis results.

MWCNTs were coated on metallic substrates by means of EPD. While performing EPD with PVP containing MWCNTs suspensions, it is found that acquiring of adherence of MWCNTs on substrate surface couldn't be established; this problem was overcome by adding magnesium ions in suspensions at certain concentrations. It is realized that UV-Vis spectroscopy can be used to estimate material quantity in coatings obtained by means of EPD. It is found that evaluation of UV-Vis spectra of suspensions before and after EPD process facilitated estimation of material quantity in coatings and at the same time it enabled calculation of coating thickness, but this technique neglects porosity in coating.

Solvothermal synthesis was used to produce MWCNTs Fe₃O₄ composite materials. In composite making process prepared MWCNTs suspensions were mixed with precursors of Fe₃O₄ nanoparticles before synthesis. To facilitate interaction between MWCNTs and Fe₃O₄ nanoparticles in order to provide homogeneous dispersion of components in the structure, surface of Fe₃O₄ nanoparticles were coated with carbon during synthesis; subsequently this interaction was examined whether it is existing or not. Glucose and ascorbic acid was used in order to prepare Fe₃O₄@C core-shell nanoparticles by means of solvothermal synthesis (200 °C, 12 h.). It is understood from XRD analysis that synthesized nanoparticles are Fe₃O₄. FTIR investigations revealed that glucose or ascorbic acid aided synthesis products contain carbon and OH functional groups in their structure. It is understood from the SEM investigations that nanoparticles which are obtained by the aid of glucose or ascorbic acid possess spherical morphology; however after synthesis facilitated without addition of this two materials resulted in Fe₃O₄ nanoparticles having octahedron shapes.

It is found that Fe₃O₄@C core-shell spherical nanoparticles are composed of smaller sub 100 nm sized particles. As a result of applied magnetic fields on MWCNTs- Fe₃O₄@C suspensions, it is shown that components separate; while Fe₃O₄@C nanoparticles migrate towards magnets, nanotubes remain in suspension. The reason behind phase separation is believed to be the the consequence of functional groups present on carbonized particle surfaces'. It can be also said that both SDBS and PVP do not provide sites for nanoparticles to crystallize on nanotube surfaces.

Second study of this thesis is about production and characterization of inorganic nanotubes.

Sulphur doped or pure TiO₂ nanopartilces were produced by means of sol-gel process. For doping process of TiO₂, starting materials of TiO₂ were mixed with thiourea (CH₄N₂S) during sol-gel process. Titanate nanotubes were produced from TiO₂ nanoparticles by hydrothermal synthesis (130 °C, 24h.) under alkali environments. It is understood from the result of TEM analysis that produced nanotubes are around 10 nm in diameter and 100 nm in length. As a result of washing with dilute acids and water, nanotubes transformed into hydrogen titanates by the removal of sodium in their structure. TEM analysis revealed that hydrogen titanate nanotubes remain intact at 350°C, but they transform into thin nanorods and nanoparticles by decomposing at 450 °C. UV-Vis absorption spectroscopy was used to assess the electron energy band gaps of nanotubes which were subjected to different processes. Apart from doping and calcination some titanate nanotubes were analyzed after H₂O₂ washing. It is revealed that among investigated nanotubes the lowest band gap values (3.27 eV) were obtained from H₂O₂ washed and subsequently calcined (350°C) samples. It is understood that band gap value of sulphur doped and subsequently calcined (350°C) nanotubes (3.31 eV) is almost the same as that of undoped and subsequently calcined nanotubes (3.30 eV). It is understood that upon washing nanotubes with H₂O₂, the ESR signal corresponding to SETOV diminish. Therefore, the decrease in band gap value is attributed the elimination of SETOV by H₂O₂.

In addition, nanotube coatings were obtained on conductive substrates by means of EPD. It is understood that butanol-TEA solvent-dispersant combination enable production of relatively stable nanotube suspensions which can be used in electrophoretic deposition processes.

Key words: Carbon Nanotube, Suspension, Quantitative Analysis, UV-Vis Absorption Spectroscopy, Electrophoretic Deposition, Fe₃O₄, Nanoparticle, Solvothermal Synthesis, Hydrothermal synthesis, MWCNT, TiO₂, Inorganic nanotube

KARBON NANOTÜP SÜSPANSİYONLARININ KANTİTATİF ANALİZİ, İNORGANİK NANOYAPILI MALZEMELERİN ÜRETİMİ VE KARAKTERİZASYONU

Ali Can ZAMAN

Metalurji ve Malzeme Mühendisliği Anabilim Dalı

Doktora Tezi

Tez Danışmanı: Prof. Dr. Cengiz KAYA

Eş Danışman: Prof. Dr. Fiğen KAYA

Bu tez iki farklı çalışmadan meydana gelmektedir. İlk çalışma kapsamında karbon nanotüplerin organik solventler içinde dağılımı sağlanmış ve karbon nanotüp takviyeli demir oksit kompozitler üretilmiştir. Çok duvarlı karbon nanotüp süspansiyonları izopropil alkolün çözücü olarak kullanıldığı ortamlarda hazırlanmıştır. Çok duvarlı karbon nanotüplerin izopropil alkol içinde homojen dağılımının sağlanması için PVP ve SDBS katkı malzemeleri olarak kullanılmıştır. Yüksek frekanslı ses dalgaları ile karıştırma ve bu işlem sonrasında merkezkaç uygulanması hem PVP hem de SDBS içeren kararlı süspansiyonların elde edilmesini mümkün kılmıştır. Zeta potansiyeli ölçümleri ve çökeltme/tortulaşma testleri süspansiyonların kararlı olduğuna işaret etmektedir. UV-Vis absorpsiyon spektroskopisi, uygulanan merkezkaç ile bileşenlerinin derişim bilgisi yitirilen süspansiyonların içindeki PVP, SDBS ve çok duvarlı karbon nanotüp derişiminin saptanmasında kullanılmıştır. Kurutulmuş çökelti ve süspansiyonlar üzerine TG analizleri de gerçekleştirilerek UV-Vis analizleri sonuçları ile karşılaştırma yapılmıştır.

Metalik plakalar üzerine çok duvarlı karbon nanotüpler elektroforetik biriktirme yöntemi ile kaplanmıştır. PVP içeren karbon nanotüp süspansiyonları ile elektroforetik biriktirme gerçekleştirilirken karbon nanotüplerin plaka yüzeyine tutunmasının sağlanamadığı görülmüştür; bu sorunun üstesinden süspansiyonlara belirli konsantrasyonlarda magnezyum iyonlarının eklenmesi ile gelinmiştir. UV-Vis spektroskopisinin elektroforetik biriktirme yöntemi ile elde edilen kaplamalar içindeki malzeme miktarının tahmin edilmesinde kullanılabiliceği görülmüştür. Elektroforetik kaplama süreci öncesinde ve sonrasında süspansiyonların UV-Vis spektrumlarının incelenmesi kaplama içindeki malzeme mikratının tahminini ve aynı zamanda kaplama kalınlığının

hesaplanmasını mümkün kılabilceği görülmüştür; ancak bu yöntem kaplama içindeki gözenekliliği hesaba katmamaktadır.

Solvotermal sentezleme yöntemi çok duvarlı karbon nanotüp Fe_3O_4 karma malzemelerinin elde edilmesinde kullanılmıştır. Karma malzeme üretim sürecinde, hazırlanan çok duvarlı karbon nanotüp süspansiyonları Fe_3O_4 'ün başlangıç malzemeleri ile sentez öncesinde karıştırılmıştır. Çok duvarlı karbon nanotüplerle Fe_3O_4 nanoparçacıkların arasında homojen dağılımın sağlanması için gerekli olan etkileşimin elde edilmesi için Fe_3O_4 nanoparçacıkların yüzeyleri sentez esnasında karbon kaplanmıştır; daha sonrasında etkileşimin gerçekleşip gerçekleşmediği incelenmiştir. Glükoz ve askorbik asit $Fe_3O_4@C$ çekirdek-kabuk nanopartiküllerin üretiminde kullanılmıştır. XRD analizleri sonucunda anlaşılmıştır ki sentezlenen nanopartiküller Fe_3O_4 'tür. FTIR analizleri sonucunda glükoz ve askorbik asit katkısı ile elde edilen ürünlerin karbon ve hidroksil fonksiyonel gruplarını içerdiği anlaşılmıştır. Taramalı elektron mikroskobu görüntülemeleri sonucunda glükoz ya da askorbik asit katkısı ile elde edilen nanopartiküllerin küresel şekillere sahip oldukları; ancak bu iki katkı malzemesini içermeyen gerçekleştirilen sentezler sonucunda octahedron biçiminde Fe_3O_4 nanoparçacık oluştuğu görülmüştür.

$Fe_3O_4@C$ küresel nanoparçacıkların, boyutları 100 nm'den daha küçük olan küresel parçacıklardan oluştuğu görülmüştür. Çok duvarlı karbon nanotüp- $Fe_3O_4@C$ kompozitlerinin süspansiyonları üzerine uygulanan manyetik alanlar neticesinde bileşenlerin ayrışma gösterdiği görülmüştür. $Fe_3O_4@C$ nanoparçacıklar manyetik alanlara yönelirken nanotüpler askıda kalmaktadır. Faz ayrışmasının nedeninin karbonize olmuş nanoparçacıkların yüzeyinde oluşan işlevsel gruplar sonucunda oluştuğu düşünülmektedir. Ayrıca söylenebilir ki hem SDBS'nin hem de PVP'nin nanotüp yüzeylerinde nanopartiküllerin çekirdekleneceği bölgeler oluşturmamaktadır.

Tezin ikinci çalışması inorganik nanotüplerin üretimi ve karakterizasyonu ile ilgilidir.

Sol-gel yöntemi ile kükürt ile katkılandırılmış ya da saf TiO_2 nanoparçacıklar üretilmiştir. TiO_2 nanoparçacıkları katkılandırma işlemi için sol-gel esnasında TiO_2 'nin başlangıç malzemeleri ile tiyöüre (CH_4N_2S) karıştırılmıştır. Hidrotermal sentezleme yöntemi ile (130 °C, 24h.) alkali ortamlarda TiO_2 nanoparçacıklardan titanat nanotüpler üretilmiştir. TEM analizleri sonucunda elde edilen nanotüplerin yaklaşık olarak 10 nm çapında ve 100 nm boyunda oldukları anlaşılmıştır. Seyreltik asit ve su ile yıkama neticesinde yapılarındaki sodyumun giderilmesi ile sentezlenen nanotüpler hidrojen titanatlara dönüştürülmüştür. TEM analizleri sonucunda hidrojen titanat nanotüplerin 350 °C'de kalsinasyon sonrasında bütünlüklerini korudukları; ancak 450 °C'de parçalanarak kısa nanoçubuklara ve küresel nanopartiküllere dönüştükleri görülmüştür. UV-Vis absorpsiyon spektroskopisi farklı şekilde işlemlerden geçirilmiş nanotüplerin elektron enerji bant aralıklarının tayininde kullanılmıştır. Kalsinasyon ve katkılandırma dışında bazı hidrojen titanat nanotüpler ayrıca H_2O_2 ile yıkanmalarının ardından analiz edilmiştir. İncelenen nanotüpler içinde en düşük bant aralığına sahip olan nanotüplerin (3.27 eV) H_2O_2 ile yıkanmış ve sonrasında 350 °C'de kalsine edilmiş olanlar oldukları saptanmıştır. Kükürt ile katkılandırılmış ve sonrasında kalsine edilmiş olan nanotüplerin bant aralığı değerinin (3.30 eV) katkılandırılmamış ama kalsine edilmiş olanlarla neredeyse aynı değerde (3.31 eV) olduğu anlaşılmıştır. Nanotüplerin H_2O_2 ile yıkandıklarında yapılarında bulunan tek elektron hapsolmuş oksijen boşuklarına ait elektron spin rezonans sinyalinin azalma gösterdiği anlaşılmıştır. Böylelikle, bant aralığındaki azalmanın tek

elektron hapsolmuş oksijen boşluklarının H_2O_2 ile ortadan kaldırılması neticesinde gerçekleştirdiđi düşünölmektedir.

Ayrıca elektroforetik biriktirme yöntemi ile iletken plakalar üzerine nanotüp kaplamaları elde edilmiştir. Butanol-triethanolamine çözücü-dađıtıcı bileşiminin elektroforetik kaplama süreçlerinde kullanılabilen görelî kararlı nanotüp süspansiyonları üretimini mümkün kıldıđı görölmüştür.

Anahtar Kelimeler: Karbon Nanotüp, Süspansiyon, Kantitatif Analiz, UV-Vis absorpsiyon spektroskopisi, Elektroforetik Biriktirme, Fe_3O_4 , Nanoparçacık, Solvotermal sentezleme, Hidrotermal sentezleme, Çok Duvarlı Karbon Nanotüp, TiO_2 , İnorganik nanotüp

INTRODUCTION

1.1 Literature Review

1.1.1 Carbon Nanotubes

Carbon is the most versatile element in periodic table. Since carbon can form infinite number of compounds. This ability is related to types of bonds that carbon can form. Carbon can make single, double and triple bonds. A carbon atom contains six electrons. The electron configuration of carbon is $(1s^2)(2s^2)(2p^2)$. In ground state carbon contains two unpaired electrons in its outer shell. At first glance, it is expected that carbon can make two bonds, but owing to small energy difference between 2s and 2p state, an electron in 2s state can excite to 2p state and carbon atoms may form 4 bonds. Carbon has several allotropes by virtue of its bonding ability. Diamond and graphite are the two well-known forms of crystalline carbon. If Carbon atoms undergo sp^3 hybridization, it forms diamond by making four bonds each. In graphite, sp^2 hybridization occurs, where each atom is connected evenly to three carbons (120°) in the xy plane. There is a weak π bond in z direction. pz orbital is responsible for the van der Waals attractions. The electrons in pz orbital are no longer occupied by atoms. They are free to move (delocalized). This ability of delocalization of electrons in graphite gives graphite its electrical conductivity. The other allotrope of carbon is carbon nanotubes. Carbon nanotubes have attracted great deal of attention since their discovery by Iijima [1]. They can be considered wrapped up sheets of single or multi layer of graphite sheets. There are two types of carbon nanotubes: SWCNTs (Figure 1.1a) and MWCNTs (Figure 1.1b). They can be produced by several techniques: arc discharge, laser ablation, chemical vapour deposition, hydrothermal synthesis are most well-known examples.

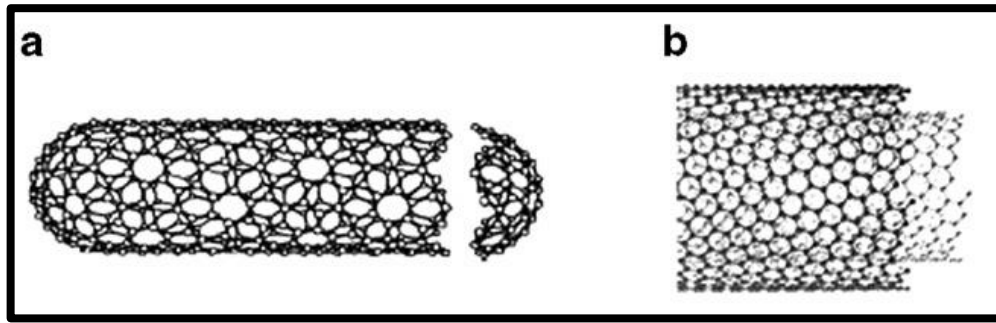


Figure 1.1 (a) SWCNTs and (b) MWCNT by [2], [3].

Carbon nanotubes have attracted great deal of attention. Because the hidden properties of graphite emerges in carbon nanotubes. Delocalized electron in graphitic structure gives nanotubes extremely high electrical conductivity along the tube axis. Unfortunately, conductivity is very sensitive to crystallinity and presence of defects in nanotubes. High conductivity and high aspect ratio of carbon nanotubes makes them one of the ideal candidates in composite making since percolation threshold for conductivity can be very low in carbon nanotube composites. The second interesting property of carbon nanotubes is the mechanical strength. Therefore there is an extensive research on carbon nanotube composites possessing high mechanical strength.

Carbon nanotube composites are generally made by mixing of starting materials in wet environments. This mixing processes is difficult since nanotubes tend to cluster. The clustering of nanotubes in matrices limits their utilization. For example, Thermal conductivity of graphite along its planar direction is 1000 W/m K, while the Thermal conductivity of SWNT and MWNT is 2400 and 1980 W/m K, respectively [4]. However, the reported values for bundles of CNT resemble those of in-plane and cross-plane graphite [5].

1.1.1.1 Colloids of Carbon Nanotubes and Their Characterization

Carbon nanotubes show strong intertubular forces causing big agglomerate, rope and bundle formation, migitating their solubility in solvents [6]. These strong Van der Waals interactions between nanotubes estimated to be around 500eV per micrometer of tube-tube contact [7]. To get over this problem several approaches were used by researchers. One approach is to use suitable solvents without addition of dispersants. Bergin et al. investigated dispersability of SWCNTs in range of solvents [8]. Some of the examples of these solvents are DMF (dimethylformamide), NMP (*N*-methyl-pyrrolidinone) and DMA

(dimethylacetamide). They obtained nanotube dispersions containing only individual nanotubes and small bundles in some solvents. Their best result was obtained with CHP (cyclohexyl-pyrrolidinone), it reached a dispersability of 3.5 ± 0.4 mg/mL. They have measured the dispersibility of SWNTs in a range of good solvents by measuring the concentration of nanotubes remaining after centrifugation. They also found out that successful solvents tend to have surface energies very close to surface energy of graphite and this translates to surface tension (40mJ/m^2). They also studied nanotube dispersability using Hansen solubility parameters (δ_D , δ_H , δ_P) and found that dispersive component of Hansen solubility parameter is in correlation with dispersability of SWCNTs. Besides, DMF is one of the solvents found to be successful in dispersing nanotubes. It is also found that DMF damage the structure of SWCNTs and it is very toxic [9]. Dispersion of nanotubes in solvents without modification is promising but using exotic, toxic solvents may limit their use. Especially, when dispersions are used in synthesis processes such as solvothermal synthesis. Because all the components (starting materials) prior to synthesis process should be dissolved or at least suspend in solvents.

Second approach to disperse carbon nanotubes is called “Covalent functionalization”. Acid treatment is the most known technique used to change surface structure of carbon nanotubes by attachment of carboxyl groups on nanotube surfaces. One example of this treatment was done by Shieh et. al [10]. They found that acid treated CNTs were insoluble in an aqueous solution at pH 0. They are soluble in those at pH 4 and higher with their solubility monotonically increasing with pH up to pH 10. The solubility of carbon nanotubes is reached by dissociation of carboxyl groups on nanotube surfaces (Figure 1.2a). Unfortunately, covalent functionalization deteriorates conjugated π system of carbon nanotubes. Figure 1.2b shows an example of resultant nanotube structure after acid treatment at 60°C for 3 h.

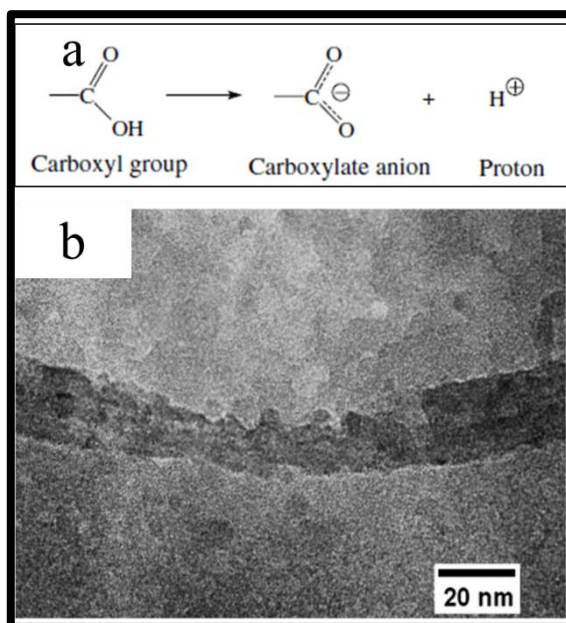


Figure 1.2 Drawing of dissociation of carboxyl groups on carbon nanotubes in water (a); A TEM image which shows result of functionalization (b). Functionalization disrupts CNT integrity, by [10].

The third approach used in dispersion of nanotubes is non-covalent functionalization. In non covalent functionalization processes molecules attach to surface of nanotubes and provide stability. Since there is only van der Waals attractions, π system of nanotubes remain intact. Surfactants are one of the examples extensively used in dispersion of carbon nanotubes. Surfactants have both polar and apolar head groups and thereby they adsorb interfaces between immiscible bulk phases such as oil and water [5]. Surfactants are classified according to charge of their head group: cationic, anionic, nonionic or zwitterionic surfactants are present. One of the most investigated examples of surfactants is SDBS in carbon nanotube system. Figure 1.3 shows the molecular structure of SDBS.

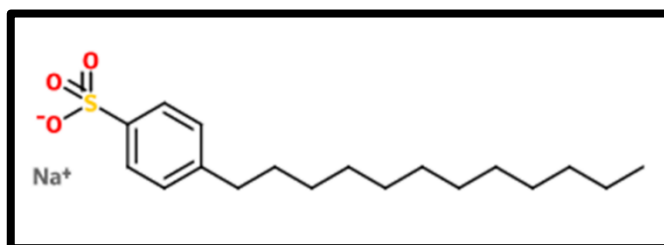


Figure 1.3 Molecular structure of SDBS.

One of the important aspects of surfactants in solvents is critical micelle concentration. Below a certain concentration called “critical micelle concentration” surfactant molecules present as individual entities in solvent. Above critical micelle concentration surfactant

molecules form micelles in solvents. Arrangement of surfactants in solvents under the presence of carbon nanotubes can be different. Figure 1.4 shows different interactions. Below CMC, some of surfactant molecules are adsorbed on nanotubes (Figure 1.4a). Increasing surfactant concentration causes saturation of surface coverage on nanotube surface. Additional increase in surfactant concentration lead to formation of micelles in the bulk solution. Since there is no room for adsorption on nanotube surface and air water interface.

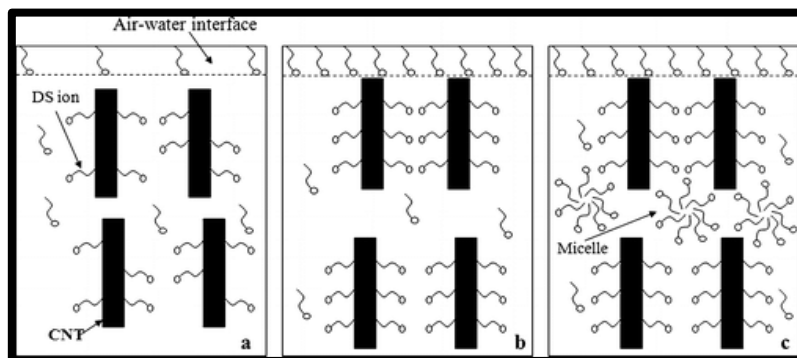


Figure 1.4 Interaction of (SDS)–CNT in a liquid: (a) below CMC, (b) at the CMC, and (c) above the CMC by Sa et al. [11].

The adsorption of surfactants onto inorganic and organic surfaces usually depends on the chemical characteristics of particles, surfactant molecules and solvent [5]. Therefore, different surfactants show different dispersing abilities and even different arrangements on carbon nanotube surfaces. For example, Fleming et al. showed that SDS forms ordered hemicylindrical aggregates on nanotube surfaces [12]. Presence of aromatic rings on surfactants provide good surfactant tube affinity. Therefore, surfactants like SDBS show high dispersability. By virtue of its benzene ring SDBS adsorbs on carbon nanotube surface by π - π stacking interaction. SDBS is known to be better in dispersing carbon nanotubes than SDS. Since SDS does not have an aromatic ring. There may be different arrangements of surfactants on nanotube surfaces. Figure (1.5a, b and c) shows different probable arrangements of SDBS on nanotube surface. Figure 1.5a shows encapsulation of a carbon nanotube by a cylindrical micelle. And Figure 1.5b illustrates formation of hemimicelles on on nanotube surface and finally Figure 1.5c shows the random adsorption of surfactant molecules.

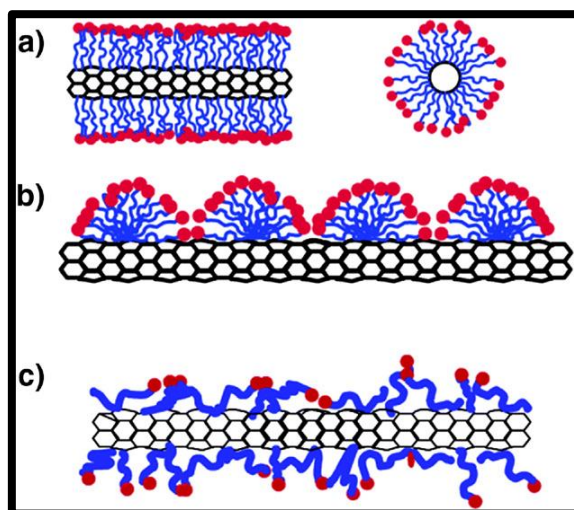


Figure 1.5 Different mechanisms of adsorption of surfactants on CNT surface: (a) encapsulation of CNT by cylindrical surfactant micelle, (b) formation of hemimicelles on carbon nanotube surface and (c) random adsorption of surfactant molecules on nanotube surface by [13], [5].

Several surfactants were investigated by researchers. For example, Rastogi et al. compared dispersion capability of SDS, Tween 80, Tween 20 and Triton X-100 [14]. They found that among four surfactants stated above Triton X-100 was found most successful by virtue of its benzene ring.

Polymers or biomolecules such as DNA can also be used in dispersion of carbon nanotubes. Polymers are large molecules and comprised of small units called monomers. The property of monomers are important since they determines the nature of interaction between molecules. Hence, solubility of polymers in solvents is determined by the nature of monomers. In addition, adsorption behavior of polymers onto nanotube surfaces is determined by the nature of the monomer as well. There are currently two main theories on the mechanism of nanotube dispersion by polymers: wrapping and non-wrapping [15]. One of the early examples of using polymer dispersants for carbon nanotubes is done by O'Connell et al [7]. They successfully dispersed SWCNTs in water by using PVP and PSS. They proposed that polymers wrap on nanotube surface. Yu et al. used PVP along with surfactant CTAB and found that there is a synergy between PVP and CTAB [15]. Therefore, PVP and CTAB dispersion is better compared to dispersions of CTAB and PVP alone. They stated that PVP stays as a separate entity in the solution rather than wrapping nanotube surface. They also found that different molecular weights of PVP have different dispersion capability. The most potent dispersing agent was PVP having

molecular weight of 10.000. They stated that minimum required distance needed for nanotubes to not to be attracted is very close to hydrodynamic diameter of PVP having molecular weight of 10.000. Therefore, it is better in dispersing. Hasan et al. used PVP to disperse SWCNTs in N-methyl-2-pyrrolidone (NMP) [16]. According to their study, addition of PVP even without implementing ultrasonication debundling of SWCNTs can occur. In addition, their results indicate that the debundling process is diameter sensitive and is more efficient for larger diameters. In another study, Manivannan et al. prepared stable suspensions in water and in organic solvents by using PVP and attributed the dispersion quality to the formation of hydrogen bonds between polymer and water molecules where SWNTs are wrapped by PVP through van der Waals forces [17]. Figure 1.6 shows natural and resonance structure of PVP.

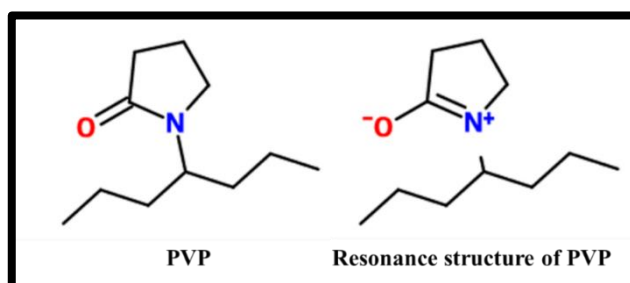


Figure 1.6 Natural and resonance structure of PVP.

Choice of solvent is also crucial in obtaining high quality dispersions. Rouse et al. [18] used P4VP for dispersion of SWCNTs. They found that increasing P4VP/SWCNT ratio from 2 to 15 increased concentration of dispersed SWCNTs. They stated that P4VP is tightly bound to the nanotube bundles, and therefore once absorbed the bundles cannot further exfoliate. The stability of the polymer/nanotube (P4VP/SWCNT ratio = 2) dispersions was found to decrease monotonically from ethanol to while ethanol dispersions had stabilities of greater than 6 weeks, weeks, dispersions in octanol were only stable for 1-2 days. They also tried to disperse carbon nanotube using P2VP. However their attempts failed. They proposed that the failure is because of the pyridyl nitrogen being sterically hindered from interacting with the nanotube by the polymer backbone. Figure 1.7 shows some possible mechanisms of arrangement of PVP molecules on SWCNT surface.

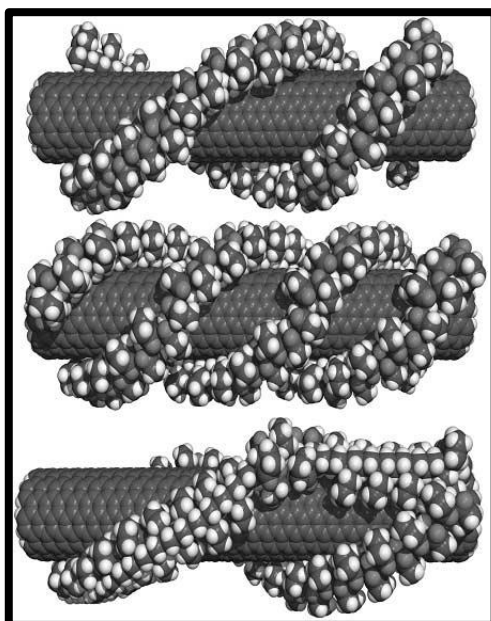


Figure 1.7 Possible arrangements of PVP wrapping on SWCNTs surface proposed by O’Connell et al. [7]. A double helix (top), a triple helix (middle) and an internal-rotation induced switch-back (bottom).

Carbon nanotubes can be in the form of large aggregates, small bundles or individual entities in solvents. Individualization of nanotubes is crucial step in utilization of carbon nanotubes. Moore et al. [19] studied the variation of the fraction of nanotubes remaining after centrifugation with a surfactant, Sun et al. [20] stated that this information can give information about amount of nanotubes dispersed, but not about dispersion quality. Level of nanotube bundling can be evaluated by using AFM. This was achieved by analyzing the bundle diameter and length distributions by AFM for samples deposited on SiO₂ surfaces for a range of concentrations [20]. UV-Vis absorption spectroscopy is widely used to assess the dispersion quality. Simply, UV-Vis analysis of suspensions before centrifugation and after centrifugation gives a clue about concentration and quality of dispersions. Because bundled CNTs have lower extinction coefficient than dispersed CNTs. So if two solutions contain same amount of CNTs, but one contains individual CNTs and the other has agglomerated CNTs, the absorbance of suspensions in UV-Vis region would be different. Namely, dispersed CNTs containing suspension would have higher absorbance value. Sun et al. [20] used 4 metrics to assess the dispersion of CNTs. It was found that each of these dispersion-quality metrics scaled very well with the measured zeta potential of the surfactant-nanotube dispersion. Therefore measuring zeta potential can give a clue about dispersion state of nanotubes in suspensions.

Ultrasonication provides debundling of carbon nanotubes. Unfortunately, some nanotubes remain agglomerated or in bundled form in suspensions even after high power ultrasonication. To remove excess amount of additives and bundled nanotubes centrifugation is implemented. After centrifugation supernatants show better stability. However, material concentration becomes unknown after centrifugation which is crucial for example, in composite making since net influence of CNTs and additives can be evaluated only by knowing the quantities of these materials. Salzman et al. carried out Raman Spectroscopic route to assess quantity of carbon nanotubes in suspensions [21]. UV-vis spectroscopy is a well-known and implemented technique in determination of CNTs' quantities in suspensions. If nanotubes are present as only one dispersing component of suspension quantitative analysis is easy [22]. If UV-Vis spectra of known quantities of carbon nanotube suspensions are used to plot calibration curves then CNT content can be calculated by using UV-Vis spectrum of unknown suspension [23], But if carbon nanotubes are dispersed in solvents with the aid of surfactants determination of quantity of carbon nanotubes and additives becomes more difficult. Because CNTs and additives can show overlapping absorbances. Attal et al. [24] used thermogravimetric analysis and UV-Vis absorption spectroscopy to assess amount of surfactants and carbon nanotubes in suspensions. They used dried supernatant for concentration determination by TGA. They stated that sample inhomogeneity, sample compaction during drying, and oxide formation of the catalysts are critical factors that could cause substantial errors in the obtained TGA data analysis. In UV-Vis analysis they used varying SDBS solution as background while keeping SWCNTs-SDBS suspension concentration constant. Thereby, they could determine surfactant concentration. They also used CTAB-SWCNTs suspension spectrum and subtracted SWCNTs contribution from SDBS-SWCNTs spectrum. CTAB is useful because it does not absorb in UV-Vis region. Finally they determined concentration of SDBS by using a calibration curve. Shtein et al. [25] improved this study and combined UV-Vis and TGA. They determined concentration of components by TGA analysis of dried supernatant and dried precipitate.

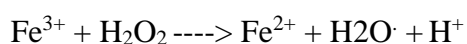
1.1.2 Iron Oxides

Iron oxides are compounds of iron and oxygen. There are sixteen iron oxyhydrides and oxides, α -Fe₂O₃, α -FeOOH, γ -FeOOH, β -FeOOH, γ -Fe₂O₃, Fe₃O₄ are the most known examples.

1.1.2.1 Applications of Iron Oxides

Fe₃O₄ is a versatile materials can be used in various applications such as in energy storage devices, catalytic applications, magnetic storage, and biomedical applications: targeted drug delivery and hyperthermia treatments a contrast agent for magnetic resonance imaging.

To sustain our current living standards or to have a prospect about our future contaminant removal is an important aspect of our civilization. Since pollutants in water will eventually effect human health. Fenton reactions can be one of the good solutions. Iron and iron compounds is used in fenton reactions in which organic contaminants in water can be oxidized. Fenton reaction is the reaction taking place under the presence of ferrous iron ions and H₂O₂. As they combine they generate radicals which is shown in flollowing equations:



The conditions such as H₂O₂ concentration, Fe²⁺/H₂O₂ ratio, pH and reaction time affect efficiency of the reaction [26]. The optimal pH value of 3 is accepted for Fenton process in which the quantum yield of ·OH radical generation at this value is the most [27] Iron oxides are used heterogenous catalysts because of their fenton oxydation system, abundance, lower cost and easy separation [28].

For wastewater treatment Fe₃O₄, α-FeOOH, γ-Fe₂O₃, α-Fe₂O₃ are widely used. However Fe₃O₄ is gaining interest for use in heterogeneous catalysis reactions like fenton reactions compared to other iron oxides. The reason behind is, spinels' catalytic activity occures mainly due to the octahedral cations and Fe₃O₄ (as having a spinel structure) has octahedral Fe²⁺ cations exposed in crystallites [29]. Surface area, pore size and crystallinity affect the acitivity of Fe₃O₄ and other iron oxides [28].

1.1.2.2 Structure of Fe₃O₄ and Other Iron Oxides

Hematite (α-Fe₂O₃) and goethite (α-FeOOH) are the most favorable phases since the arrangement of atoms in these compounds provide the lowest thermodynamic conditions. The structure is similar to that of corundum, and consists essentially of a dense

arrangement of Fe^{3+} ions in octahedral coordination with oxygens in hexagonal closest-packing. The structure can also be described as the stacking of sheets of octahedrally (six-fold) coordinated Fe^{3+} ions between two closed-packed layers of oxygens. Since Fe is in a trivalent state (ferric Fe), each of the oxygens is bonded to only two Fe ions, and therefore, only two out of three available oxygen octahedrons are occupied. This arrangement makes the structure neutral with no charge excess or deficit [30]. In Fe_3O_4 oxygen atoms arranged in a hexagonal patterns and the Fe^{3+} cations occupy both octahedral and tetrahedral sites but Fe^{2+} cations only occupy tetrahedral sites. $(\text{Fe}^{3+})_{\text{tet}}[\text{Fe}^{2+}\text{Fe}^{3+}]_{\text{oct}}\text{O}_4$. Fe ions exist in both +2 and +3 valence states in the ratio of 1:2. Fe_3O_4 show ferrimagnetic behavior. Figure 1.8 shows the arrangements of spin magnetic moments of Fe ions. Spin magnetic moments of Fe^{3+} ions in tetrahedral and octahedral sites are parallel to each other; however their direction are opposite. Spin magnetic moments of Fe^{3+} ions cancel out each other and they don't contribute to magnetization of the solid. But, magnetic moments of Fe^{2+} ions aligned in the same direction. This is responsible for magnetization of Fe_3O_4 [31].

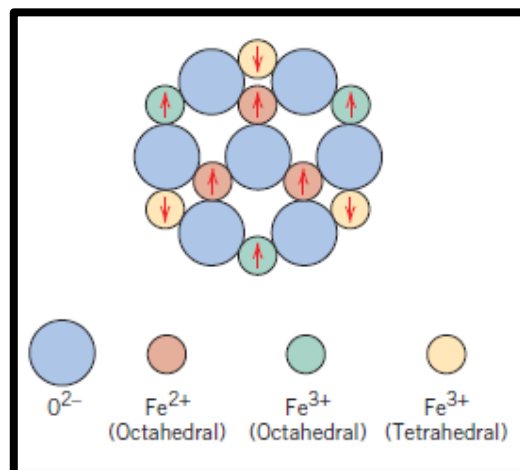


Figure 1.8 Schematic diagram showing the spin magnetic moment configuration for iron ions in Fe_3O_4 by [32].

1.1.2.3 Synthesis of Iron Oxides: Solvothermal Synthesis

The properties of nanoparticles is dependent on particle size, morphology, degree of crystallization, chemical composition and they are regulated by different synthesis methods. There are various ways to synthesize Fe_3O_4 : Co-precipitation, Thermal decomposition, Sol-gel, Microemulsion, Sonochemical, Spray pyrolysis, Laser pyrolysis or deposition [33]. Commonly liquid media (mostly aqueous) is readily used to produce

iron oxide nanoparticles via co-precipitation of ferrous (Fe^{2+}) and Ferric (Fe^{3+}) ions containing salt solutions, but the drawback of this route is difficulty in controlling particle size and distribution [34], especially if one wants to make monodisperse particles. Since careful adjustment of the pH value is crucial [35]. Solution based synthesis such as solvothermal synthesis is attractive since it promises easy adjustment of particle size, shape and size/shape distribution, simply by varying the synthesis conditions. Solvothermal synthesis is a heterogeneous or homogeneous chemical process taking place in solvent with the aid of surfactants, chelating agents or mineralizers. The synthesis conditions are regulated by the choice of the solvent, chemical composition and concentration of the precursor, complexing agents, ionic strength, reducing, oxidizing agents.

Wulff's facet argument is the most referred model in terms of defining crystal shape at equilibrium conditions. Crystallographic shapes are determined by the growth rate of different facets. Different facets have different surface energies. Particles are enclosed by the facets that have the lowest surface energy. Octahedra is favored for face centered cubic crystal structure (Fe_3O_4 and $\gamma\text{-Fe}_2\text{O}_3$) with a (111) planes surrounding the surface [36]. However, the theorem is not enough to understand the shape evolution at any time, since it considers the equilibrium state where thermodynamics of the system takes over [37]. Morphology is also dependent on the driving force or chemical potential difference in the crystallization process [38]. This phenomenon is related to the supersaturation of the system [38] Having low chemical potentials favor polyhedral crystals formation whereas high chemical potential or driving force favor formation of dendritic crystals [38]. Concentration of the iron source increases the the driving force, and hence have a vital effect on morphologies of the products [39]. Different morphologies is the result of different rate of growing facets under nonequilibrium conditions; for example sphere may be the result of slow growing facets grow in a similar rate, which have the lowest possible surface to volume ratio [36].

The iron source has a high influence on the properties of the final product such as crystal morphology since it acts differently in different solvents. Ferrocene [40], Iron sulfate [36], $\text{Fe}(\text{NO}_3)_3 \cdot 9\text{H}_2\text{O}$ [41], $\text{FeCl}_3 \cdot 6\text{H}_2\text{O}$ [42], $\text{FeCl}_2 \cdot 4\text{H}_2\text{O}$ [43] or mixture of different iron chlorides (to provide $\text{Fe}^{3+}/\text{Fe}^{2+}$ molar proportion to be 2) [44], potassium ferricyanide [45], iron(III) acetylacetonate [35], [46] are the examples of iron sources utilized in hydrothermal or solvothermal synthesis. The important thing to consider is precursors has

their own disposition under the same or different conditions; for example Wang et al. argues about partly controversial findings in the literature in some applications in which ferrocene is used at relatively low temperatures, because the required temperature for the ferrocene decomposition is higher than 250 °C [40]. Besides, iron sources have different solubility in different solvents which may restrict their use in a particular solvent, and different ions of the precursor and their concentration may have an effect on the particle size and morphology.

Solvents has a great influence on particle size and morphology. Since solubility, and solvent-solute interaction are important. They acts not only as a solvent but also as a stabilizer and reducing agent. Solvents act differently under different temperature and pressure (PT) regimes. For example, in one study, effects of IPA and water is compared. When the pure water is used instead of IPA, the final structure end up with a few octahedrons, with size varying in a large range and lots of irregular polyhedra [40]. Zhao et al. have found similar results; they obtained octahedra and irregular particles as they use water in solvent mixture [36].

In addition to other factors influencing synthesized products' properties, pH of the suspension is also an important aspect. It influences chemical potential environment of the system. Hence it affects thermodynamics and kinetics of the system.

Some of the findings in literature are reviewed here to provide a deeper understanding of wet chemical synthesis of iron oxide nanoparticles. Sun et al. [35] obtained monodispersed particles through the reaction of metal acetylacetonate and 1,2-hexadecanediol in phenyl ether and benzyl ether. They firstly keep the reaction mixture at 200°C, and subsequently They increased the reflux temperature to higher temperature regimes depending on the solvents used. As the reaction temperature increased the particle size also increased. They found out that directly increasing from room temperature to reflux temperature yielded nanoparticles with varying size distribution. Therefore, they proposed that the nucleation of Fe₃O₄ nanoparticles under that experimental conditions is not a fast process. X. Wu et al. [47] used hydrazine for the reduction of iron salt and used hydrothermal synthesis. According to their findings If Hydrazine is sufficient, FeOOH is formed by the reaction of iron salt at low temperatures (10°C) under the presence of water. Increasing the temperature even to 40°C yield partially Fe₃O₄ crystallization. If Hydrazine is insufficient no pure face could be obtained, the product would be a mixture of Fe₂O₃ and Fe₃O₄. Increasing the hydrothermal

temperature to 160°C yield better crystallized Fe₃O₄ particles. Increasing temperature increases the particle size. The particles synthesized at 160°C had wide size distribution due to the Oswald ripening. They argue that the process involves dissolution and recrystallization. This seems to be right since the FeOOH crystallites rod shaped or irregular in shape. After the transformation they become nanoparticles having low aspect ratio. J. Zhang et al. [48] used hydrazine to reduce iron ions in the precursor, K₃[Fe(CN)₆]. Water was used as solvent. The synthesis conditions were 200 °C for 12 h. The shape of the crystal was regulated by the absence or presence of NaOH at different quantities. Dendritic and irregular shape particles were obtained in the absence of NaOH. They postulated that between 0.5-2 mol/l NaOH concentration is suitable for the growth of Fe₃O₄ microoctahedrons. Otherwise mixed morphologies: particles, octahedrons, and sheets could be obtained. Changing the reaction temperature while keeping the other properties constant end up with mixture of dendrites and particles at 160°C and 180°C. Fe₃O₄ couldn't be obtained at 160°C. Probably because iron forms tightly or loosely bound complexes with anions or counter ions. The type of the counter ion may affect the kinetics of the reactions. Also crystal growth can be regulated by the choice of proper counter ion. At 200 °C well developed octahedrons could be obtained. Further increase in temperature distorts the octahedron shape of the crystal (220°C). At constant temperature (200 °C) the reaction yields sheets (1 h.), then they began to convert into small octahedrons and octahedrons grow until 12 h. of synthesis. Zou et al. produced 2D fractals [39]. They investigated the effect of temperature, presence of additives and amount of precursor on the evolution of fractals [39]. They used PEG. Without the presence of PEG-20000 irregular large particles were obtained. Hydrazine is also important to obtain Fe₃O₄ crystals. Since oxidation of Fe²⁺ to Fe³⁺ is needed. They also found out that below 200 °C they couldn't obtain pure Fe₃O₄. The decomposition temperature of ferrocene is considerably high (>240°C), therefore high reaction temperatures are needed for that reaction to totally proceed. If the precursor concentration is low only Fe₃O₄ nanowires and some nanoparticles can be produced.

Magnetic properties can be tuned by changing the particle size, morphology [49] type and crystallinity of the products. Besides, cationic distribution, vacancies, nonstoichiometry, spin canting prevail the properties [44], [50], [51], [52]. The crystal shape has an influence on the magnetic properties such as magnetic dipole moment may take the long axis of the material as the easy axis [53]. Magnetic properties including surface exchange and

magnetic anisotropy differs from bulk or between nanoparticles (having different sizes) of the same material. The difference is due to the fraction of surface atoms in nanoparticles that are not fully coordinated [54]. Reduction in particle size lead to novel properties such as paramagnetism. Presence of different facets on the surface of nanoparticles should also influence the magnetic properties since the coordination number of atoms on the surface varies. Y. Zheng et al. [55] obtained nanoparticles having diameter of about 27 nm. The saturation magnetization of the particles is 3.69 emu/g at 300 K. They attribute this small value of saturation magnetization to the particle size and the presence of surfactants on the crystal surfaces. X. Wu et al. used hydrazine hydride aqueous solution without the aid of surfactants and obtained a saturation magnetization 14.5 emu/g for the samples prepared at 160 °C for 12h. [47].

1.1.2.4 Core Shell Iron Oxide Nanoparticles and Iron Oxide Containing Composites

Many materials are considered potential drug carriers Fe_3O_4 is a promising candidate because drugs can be targeted by means of magnetic fields [56]. A major advantage of magnetic drug targeting over conventional methods is the possibility to turn off drug delivery immediately which reduces the drug built up over time [56]. Surface structure of iron oxides is not sufficient to allow for effective utilization of this materials. To overcome this problem coating of iron oxides can be conducted which provide functional groups on iron oxide surface such as COOH. Besides, core-shell particles are more stable than pure Fe_3O_4 nanoparticles, and hence agglomeration and environmental degradation of nanoparticles can be prevented [57], [58]. Charge density of lithium ion batteries are the most chosen batteries for portable electronic devices since they exhibit high energy density. The performance significantly relies on anode materials used. Transition metal oxides show promising properties when used as anode materials. They exhibit high theoretical capacity [59], [60]. Cyclic performance of anode materials can be enhanced by using anode materials having porous and hollow structures [61]. Carbon coating on iron oxide has been proved to improve the electrochemical performance of nanostructured anode materials due to its high conductivity, good lithium permeability, and flexibility to hold the structure integrity. [62].

Encapsulation of nanomaterials by carbon is an easy process by solvothermal synthesis. by heating the aqueous glucose solution at 160–180°C which is higher than the normal

aromatization and carbonization of glucose [63]. Several attempts can be applied to synthesize core-shell iron oxide materials. Chen et al. [64] used $\text{FeCl}_3 \cdot 6\text{H}_2\text{O}$, NaOH and dodecylamine to solvothermally synthesize Fe_3O_4 nanoparticles. Then another hydrothermal approach is implemented under the presence of glucose to coat iron oxide nanoparticles. One step solvothermal or hydrothermal approach can be conducted to synthesize $\text{Fe}_3\text{O}_4@\text{C}$ core-shell nanoparticles [65].

Electrochemical capacitors or supercapacitors have been attracting interest due to their high power density compared to conventional capacitors [66]. Electrochemical capacitors can be divided into two kinds. Electrical double layer capacitors (EDLC) are one of the two which achieve energy storage by double layer capacitance. Capacitance is proportional to the surface area of the electrical double layer. Therefore, activated carbons are readily used as electrode materials. The second electrochemical capacitors are called pseudocapacitors which use conductive polymers or metal oxides such as iron oxide on the electrode surface. Ruthenium oxide (RuO_2) is the most promising oxide for pseudocapacitance but it is expensive. On the other hand Fe_3O_4 is promising because it is cheap and abundant. Hybrid capacitors may also be obtained for improved capacitance by incorporation of metal oxides in carbonaceous material [67].

1.1.3 Inorganic Nanotubes

Carbon nanotubes are the best known nanotubes first demonstrated by [1], but there are also different possibilities to make nanotubes. For example, layered inorganic compounds possess structures comparable with the structure of graphite [68]. Transition metal dichalcogenides (sulphides, selenides and tellurides) are among those examples. Halides (chlorides, bromides and iodides), oxides, hydroxides are important examples [68]. Materials such as perovskite titanates and spinels have also been reported [69]. Nanotubes of elemental materials such as Tellurium nanotubes have also been reported [70], [71].

1.1.3.1 Inorganic Nanotube Synthesis

The underlying mechanisms of nanotube formation can be classified into two mechanisms [72]: first, self-organization such as self-rolling, Ostwald ripening, oriented attachment, and Kirkendall effect. Second mechanism is done by using sacrificial templates, nanowires and nanoparticles. Synthesis methods are diverse: mostly for

synthesis of oxide nanotubes solvothermal and hydrothermal synthesis is used[69]. CVD, electric arc discharge, laser ablation and sol gel are methods of synthesis [69].

Hydrothermal processing can be defined as any homogeneous (nanoparticles) or heterogeneous (bulk materials) reaction in the presence of aqueous solvents or mineralizers under high pressure and temperature conditions to dissolve and recrystallize (recover) materials that are relatively insoluble under ordinary conditions [73]. If reaction medium is different than water, the synthesis process is called solvothermal synthesis.

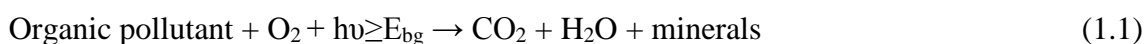
Water, ammonia, alcohols, glycols, ketones, ionic liquids, aromatic hydrocarbons are among the materials used as solvents in solvothermal synthesis of nanomaterials. Reaction medium have a big influence on resultant materials. Solvents with different physicochemical properties have a pronounced effect on the crystallinity and morphology of the final nanocrystals by influencing the solubility, reactivity, diffusion behavior, and crystallization kinetics (crystal nucleation and growth rate) [74] [75]. Solubility of raw materials is an important physicochemical and technological parameter which strongly influences the rate of dissolution and degree of supersaturation, and therefore the rate of nuclei formation [76]. Crystallization of nanoparticles is dependant on the dielectric constant of the solvent to a large extent, but not exclusively [77].

Hydrothermal/Solvothermal route was widely used for synthesising nanotubes. There are several examples of inorganic nanotubes. For example, Silver telluride nanotubes were synthesized by hydrothermal process without a template or surfactant. The starting materials are simple: sodium tellurate and silver nitrate [78]. In one study, tellurium nanotubes were prepared by mixing tellurium powder, PEG, PVA and PVP. Mixture is placed in teflon lined stainless-steel autoclave and heated in an oven at 160°C for 48 h. [71]. Titanate nanotubes are among the examples. They are readily synthesized by means of hydrothermal synthesis since it is easy to prepare conditions for the formation of nanotubes.

1.1.3.2 Titanate Nanotubes

Semiconductor photocatalysis is a possible route to clean water, air and surfaces [79], [80], [81].

The mechanism roughly explained as follows [82]:



TiO₂ is the most well known photocatalytic material. It attracted great deal of attention because of its effectivity for organic pollutant removal. TiO₂ has a band gap of 3.2 eV. The treshold for activation to trigger photodegradation can be achieved by treatment with UV light. Unfortunately, only 6-8 % of sun light is in the UV spectrum. Therefore, researchers trying to find a way to shift the band gap of TiO₂. In addition, surface properties of TiO₂ is also important in improving kinetics of photocatalytic activity. Since photocatalysis involves reactions happening on catalyst surface. Titanate nanotubes are attractive because they can exhibit exceptionally high surface area.

1.2 Objective of the Thesis

There is two separate objective of this thesis. They can be outlined as follows:

1. Production of carbon nanotube reinforced Fe₃O₄ nanocomposites in which carbon nanotubes are homogeneously dispersed.
2. Production of Titanate or TiO₂ nanotubes exhibiting enhanced visible light activity during photocatalysis.

1.3 Hypothesis

In electrochemical double-layer capacitors activated carbon is used because of its low cost and high surface area. But low electrical conductivity limits the use of activated carbon. Carbon nanotubes are better candidates because they have better charge transfer ability and electrical conductivity. In pseudocapacitors metal oxides could be used as electrode materials. Fe₃O₄ has been investigated extensively because of its low cost and abundance. Incorporation of carbon nanotubes in metal oxide matrix may increase the power density of hybrid capacitors owing to a synergistic effect. The benefit of presence of carbon nanotubes in metal oxide matrix stems from generation of interaction between nanotubes and metal oxide, thereby components can be homogeneously distributed in the structure. This interaction can be accomplished by presence of functional groups on nanotube surface. Oxygen containing groups creates sites for metal oxide particles to interact and crystallize during synthesis processes as shown in Figure 1.9.

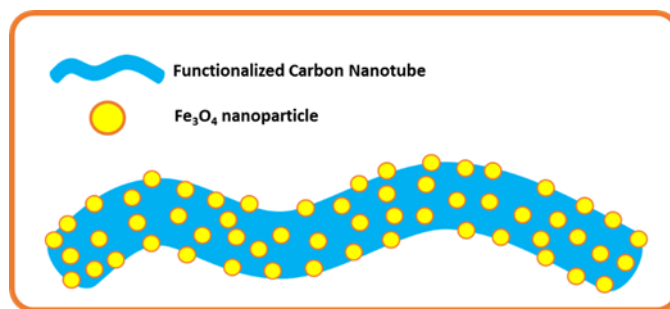


Figure 1.9 Drawing of a functionalized CNT and Fe_3O_4 nanoparticles attached on CNT during synthesis.

There is an unavoidable problem resulting from the presence of oxygen containing functional groups on nanotubes: nanotubes lose their integrity at the expense of decoration with functional groups. Because during generation of surface functional groups (covalent functionalization) carbon-carbon bonds break resulting in disruption in π conjugated system of carbon nanotubes. Since most of the atoms lie on the surface of multi wall carbon nanotubes, effect of surface functionalization is pronounced. Eventually unique properties of nanotubes diminish such as electrical conductivity.

Some challenges need to be overcome to make homogeneously dispersed pristine (covalent attachment of moieties is prevented) carbon nanotube containing iron oxide nanocomposites and coatings for electrode materials in energy storage applications. Firstly, before synthesis of nanocomposites, MWCNTs should be homogeneously dispersed in solvents with the aid of proper dispersants. SDBS was found to be suitable in some range of solvents. Some of these solvents were investigated for the first time in our study as far as we know with this surfactant combination in terms of carbon nanotube dispersion. Butanol, IPA and Amyl alcohol was found to be suitable for maintaining highly stable solvents. IPA was chosen and used in further processes.

Since our aim was to compare composite and MWCNTs coatings. We have produced MWCNTs coatings. We have found that both SDBS-IPA and PVP-IPA systems could be useful to obtain electrophoretic deposition of pristine MWCNTs.

Aggregated nanotubes can be separated by application of ultrasonication and with careful choice of solvent and dispersant. But ultrasonication does not provide total exfoliation of carbon nanotubes. A consecutive centrifugation is employed to sediment hard agglomerates of nanotubes. However this arises a problem. Centrifugation eliminates the information about the concentration of dispersant and MWCNTs. This information is

important because careful examination of composite properties requires the knowledge of concentration or ratio of materials inside.

UV-Visible absorption spectroscopy and TG analysis were utilized methods in literature to estimate quantity of materials in centrifuged carbon nanotube aqueous suspensions. We have taken this knowledge and tailored for our organic solvent containing dispersions. In addition, we have found that by UV-Vis examination of suspensions before EPD and after EPD process, it is possible to estimate coating thickness while surface area of the coating and densities of deposited materials are known.

Solvothermal synthesis was chosen for nanocomposite production. The challenge of providing interaction between nanotube and nanoparticles (to provide homogeneous dispersion of components) during synthesis was tried to overcome in a novel way. Namely, rather than covalent attachment of functional groups on carbon nanotubes, we have chosen to carbonize the surface of Fe₃O₄ nanoparticles. Thereby we have produced core-shell Fe₃O₄@ nanoparticles.

We have chosen 2 dispersant (SDBS: surfactant, PVP: polymer) for nanotube dispersion as explained above. These dispersants were also aimed to be used as potential coupling agents for providing sites for attachment of nanoparticles during crystallization process on nanotube surfaces.

Our first aim is to get a morphology like in Figure 1.9 after synthesis. But it turns out that carbonized nanoparticles are super-particles having several hundred nanometers in diameter which are combination of smaller nanoparticles as shown in Figure 1.10a and b. We went on working on this nanoparticle system since it may also work on providing homogenous dispersion. It should be noted that for carbonization of the oxide surface glucose is generally used during solvothermal synthesis. We also introduced ascorbic acid (alongside glucose) which is investigated but as far as we know haven't been used in literature at such high temperature regimes (200°C). We have found that ascorbic acid also creates particles resembling those of done with glucose assisted synthesis.

In composite production preliminary experiments were provoking because as shown in Figure 1.10c and d. we thought that there is an interaction between nanotubes and nanoparticles. This pseudo interaction is believed to be the result of insufficient removal of dispersants which are causing aggregation of both nanotubes and nanoparticles during filtration by magnetic separation. Subsequent experiments revealed that if magnetic

separation and removal-addition of water were consecutively applied on synthesized products, nanotubes and nanoparticles eventually separate. This phase separation was pronounced if the synthesized suspension is subjected to ultraconication.

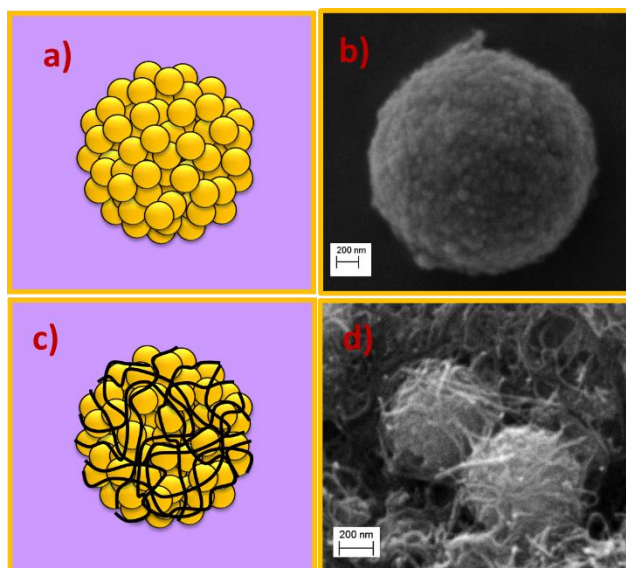


Figure 1.10 Depiction of solvothermally synthesized $\text{Fe}_3\text{O}_4@\text{C}$ nanoparticle (a), (b) is SEM image of glucose assisted synthesis product ($\text{Fe}_3\text{O}_4@\text{C}$); (c) and (d) are depiction and SEM image of result of preliminary experiments revealing a pseudo interaction between nanotubes and nanoparticles.

This thesis also contains a second study conducted on synthesis and processing of titanate nanotubes. Titanate nanotubes are subject of an intense research since they resemble titanium dioxide and adopt its properties such as photocatalytic activity. The choice of this material over titanium dioxide was its high surface area which may increase the rate of reaction during photocatalysis. Titanate nanotubes may be used in self-cleaning coatings. The most important concept in self-cleaning surfaces or coatings is the breakdown of organic pollutants should be done in sunlight. Unfortunately, titanate nanotubes activate by UV light irradiation. At sea level only 6 % of solar spectrum contains UV light. Therefore, shifting the activation (redshift of electron energy band gap) of titanate nanotubes under visible spectrum is needed.

In our study, we have synthesized titanate nanotubes in a simple and known way by means of hydrothermal synthesis and tried different approaches and compared them in terms of their effect on band gap values. Effect of calcination on integrity of nanotubes were investigated before. There was also an approach about hydrogen peroxide treatment on nanotubes to examine the change in crystal structure. Doping was also applied on titanate

nanotubes. During the preparation of this thesis as far as authors knew there was limited or small amount of research conducted on sulphur doping of titanate nanotubes. So we examined the effect of presence of sulphur in titanate nanotubes. Sulphur doping was investigated on TiO₂ nanoparticles before in literature. One of the novelties of our study is trials of converting sulphur doped TiO₂ nanoparticles into doped nanotubes during hydrothermal conditions. Besides, comparison of different treatments (calcination, hydrogen peroxide washing and sulphur doping) on band gap values needs to be investigated area of research. In addition, we looked for whether there is a synergistic effect present by sulphur doping, hydrogen peroxide washing and calcination on band gap values of titanate nanotubes. We have also examined the effect of different treatments on band gap values by using techniques such as ESR.

We also investigated to production potentially functional photocatalytic coatings. Butanol-triethanolamine mixture was found to successful on EPD of titanate nanotubes on conductive substrates.

MATERIALS and METHODS

2.1 Suspensions Preparation for Synthesis of Nanocomposites and EPD

Figure 2.1 shows a drawing of sequence of events for preparation of carbon nanotube suspensions. Firstly, MWCNTs (Thomas Swann Co. 30 nm in diameter and 30 μm in length) were mixed with excess amount of additives (2 g/L PVP or 2 g/L SDBS) in IPA. Dispersant to MWCNTs ratio is more than enough. This information was obtained by detailed analysis of suspensions having different ratios but the finds are not represented in this thesis. Ultrasonication was conducted by using an ultrasonicator (Bandelin Sonorex HD 3100) with a Ti6Al4V tip (KE76). Tip was immersed around 1 cm below the liquid surface. Ultrasonication was conducted in an ice bath. The power output of device was set to 20%. After ultrasonication, centrifugation was conducted (12000 RCF (relative centrifugal force) for 30 min.) and supernatant was decanted. Sigma Sartorius 3-18K centrifuge was used in the process of preparation of suspensions. Centrifuged suspensions were then used in synthesis and deposition processes.

Functionalized MWCNTs were also prepared to obtain only MWCNTs containing isopropanolic suspensions. Functionalization was obtained by treatment of MWCNTs (0.1 g/L) with 3/1 volume percent mixture of H_2SO_4 (95 wt. %) and HNO_3 (65 wt. %) solutions. After 3 hours of treatment under ultrasonic bath at 45°C , MWCNTs were filtered with water (Ph 7) and dried. Dried MWCNTs were mixed with IPA and ultrasonicated with ultrasonic probe for 30 min. After centrifugation at 12000 RCF for 30 min. COOH MWCNTs IPA was obtained.

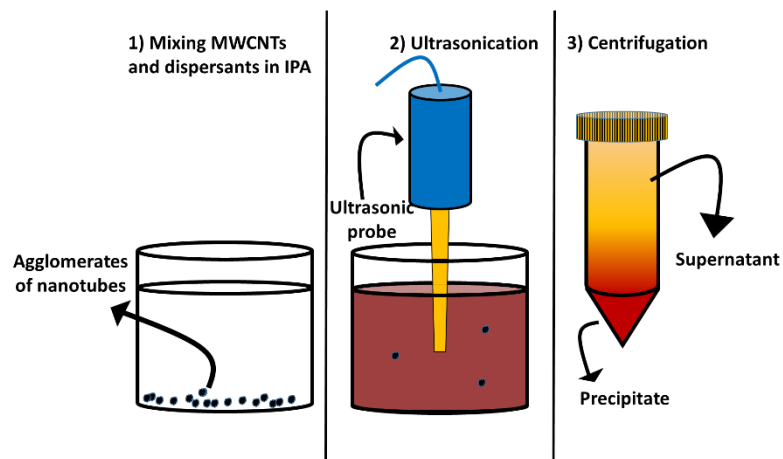


Figure 2.1 Sequence of events for preparation of stable CNT suspensions.

2.2 Method of Quantitative Analysis of Suspensions and Coatings

UV-Vis spectroscopy was mainly used for the determination of concentration of additives and carbon nanotubes in centrifuged suspensions (supernatants). PGeneral T80+ UV-Vis spectrophotometer was used in experiments.

Many molecules absorb ultraviolet or visible radiation. Different molecules absorb radiation in different wavelengths. Photon absorbing moieties are called chromophores. When a molecule absorbs a photon its energy content increases and it is the sum of electronic, vibrational and rotational energies (Figure 2.2). If energy of photons is enough to cause transitions of electrons from ground state to high energy state, it is absorbed. Since many transitions with different energies occur, peaks become broadened in UV-Vis spectrum.

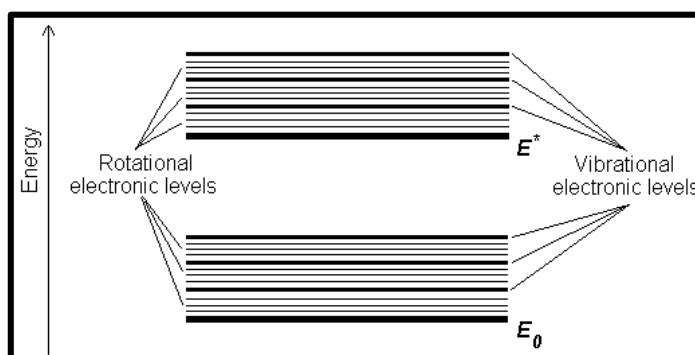


Figure 2.2 Illustration of electronic level and discrete rotational and vibrational energy levels above electronic states [83].

The absorption in radiation can induce different electronic transitions of electrons in the valance shell of chromophores. Electrons can be in σ bonding orbitals, π bonding orbitals

and n non-bonding orbitals. Electronic transitions from ground state to excited state absorb photons. It is shown in Figure 2.3 shows electronic transitions. $\sigma\text{-}\sigma^*$ transitions do not fall to UV-Vis range since they are very energetic. For example, $\sigma\text{-}\sigma^*(\text{C-H})$ transition takes place at 122 nm for CH_4 . In UV-Vis spectroscopy $\pi\text{-}\pi^*$ (These transitions need an unsaturated group in the molecule to provide the π electrons) and $n\text{-}\pi^*$ transitions generally occur.

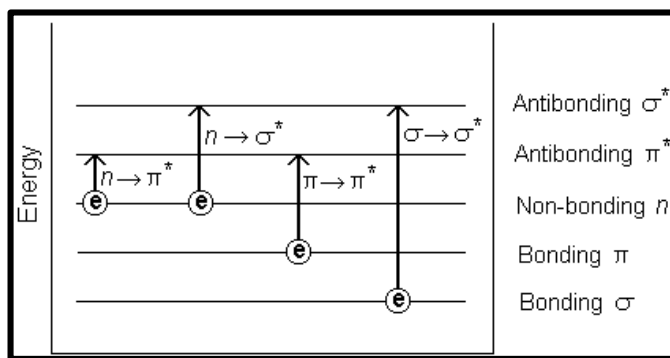


Figure 2.3 Electronic transitions of σ , π , and n electrons [83].

Quantitative analysis of materials could be conducted using UV-Vis spectroscopy since absorption at a specific wavelength may obey Beer-Lambert Law.

Figure 2.4 shows the technique used for quantitative analysis of suspensions. Firstly, suspensions were properly diluted and their absorbance spectra were obtained (Figure 2.4a). Secondly, UV-Vis spectra of carboxyl group functionalized centrifuged stable MWCNTs suspensions (COOH-MWCNTs) were used. COOH-MWCNTs dilution was precisely adjusted to provide overlapping of former and latter UV-Vis spectra in visible and infrared region (Figure 2.4b). Thirdly, spectra of dispersant containing MWCNTs suspensions and only nanotube containing MWCNTs suspensions were subtracted from each other (Figure 2.4c). Resultant spectrum was used to assess additive concentration in suspensions. A calibration curve was obtained from UV-Vis spectra of only additive containing IPA solutions or suspensions at different concentrations at specific wavelengths (223 nm for SDBS, 207 nm for PVP). Subsequently absorbance value of the peak was used to assess the additive concentration (Figure 2.4d).

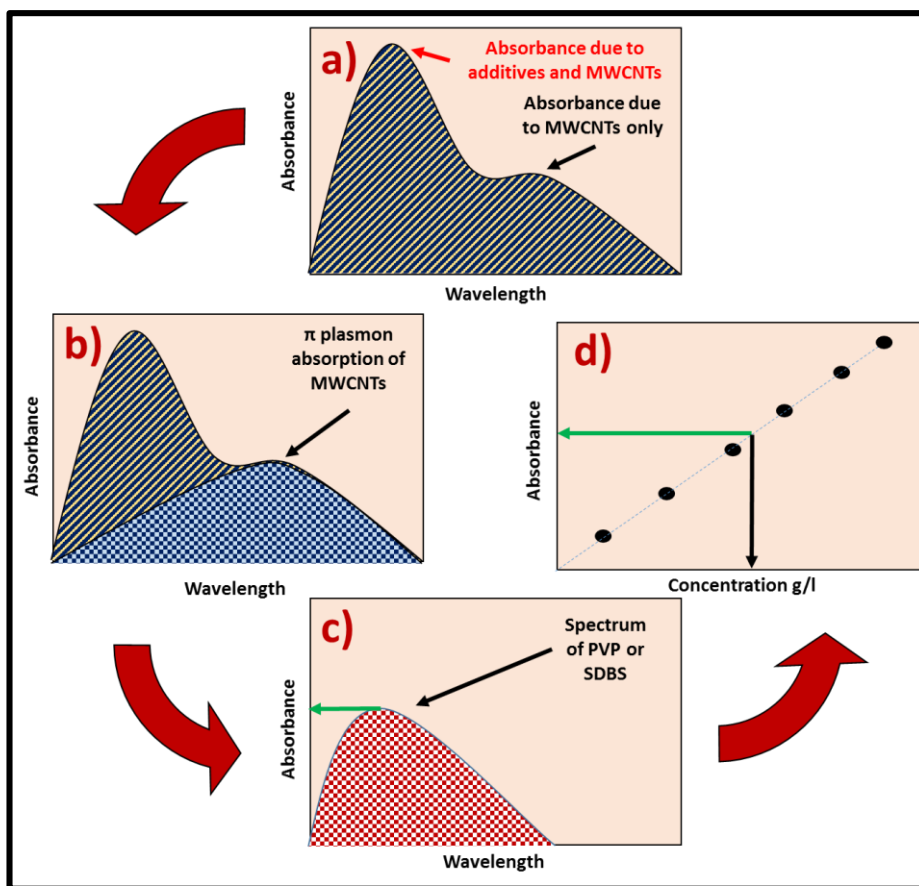


Figure 2.4 (a), (b), (c) and (d) are UV-Vis analysis sequences of PVP or SDBS in MWCNTs suspensions.

MWCNT concentration in suspensions was determined by overlapping spectra. Unknown concentration of WMCNTs can be calculated by overlapping spectrum of this suspension (having unknown concentration of MWCNTs) with that of a suspension having known information about concentration. In our experiments we calculated MWCNTs concentrations by using suspensions which are not subjected to centrifugations. Thereby initial concentration of MWCNTs (0.1 g/L) was known. Figure 2.5 shows depiction of overlapping of suspensions.

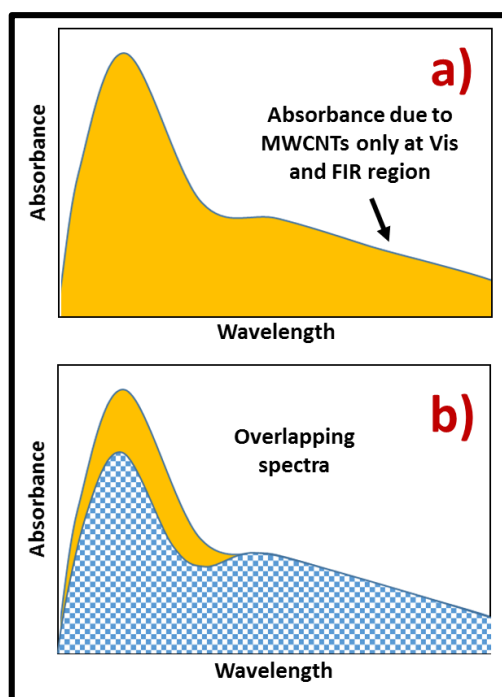


Figure 2.5 Method used to assess MWCNTs' concentration by using UV-Vis spectra.

(a) and (b) are depictions of spectra used in the analysis method.

Suspensions prepared by using PVP is denoted as PVP MWCNTs IPA, and the other one is denoted as SDBS MWCNTs IPA. Uncentrifuged suspensions can be identified by the CF sign. Both PVP MWCNTs IPA and SDBS MWCNTs IPA suspensions were subjected to EPD processes, but only coatings obtained by PVP MWCNTs IPA suspensions were subjected to quantitative analysis by UV-Vis spectroscopy. The reason behind only evaluating depositions obtained by means of PVP MWCNTs IPA suspensions is not deliberate. We randomly pick one suspension and assessed the properties to show this technique is applicable.

EPD process of MWCNTs from PVP MWCNTs IPA suspensions were obtained on stainless steel substrates (Figure 2.6). The electrode distance was kept 1.5 cm. A direct current of 50 V was applied on suspensions for 10 min. and 20 min., respectively. Magnesium chloride IPA solutions (100 g/L) were prepared prior to deposition processes and added to the suspensions in order to enable deposition and adhesion of MWCNTs on substrate surface during deposition owing to presence of magnesium ions.

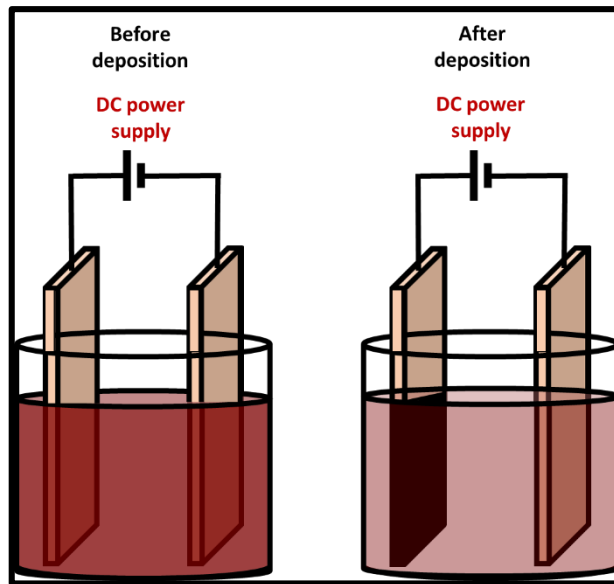


Figure 2.6 EPD apparatus before and after deposition.

Before EPD, concentrate magnesium chloride containing suspension was properly diluted and subjected to UV-Vis analysis. Subsequently, EPD was implemented to the analyzed suspension. Same amount of dilution was subjected to the used suspension before UV-Vis measurement. To determine additive concentration from the UV-Vis spectra of suspensions, contribution of MWCNTs to the absorption was subtracted as explained in Figure 2.7. Finally resultant spectra subtracted from each other. The obtained spectrum is representing the additive in coating.

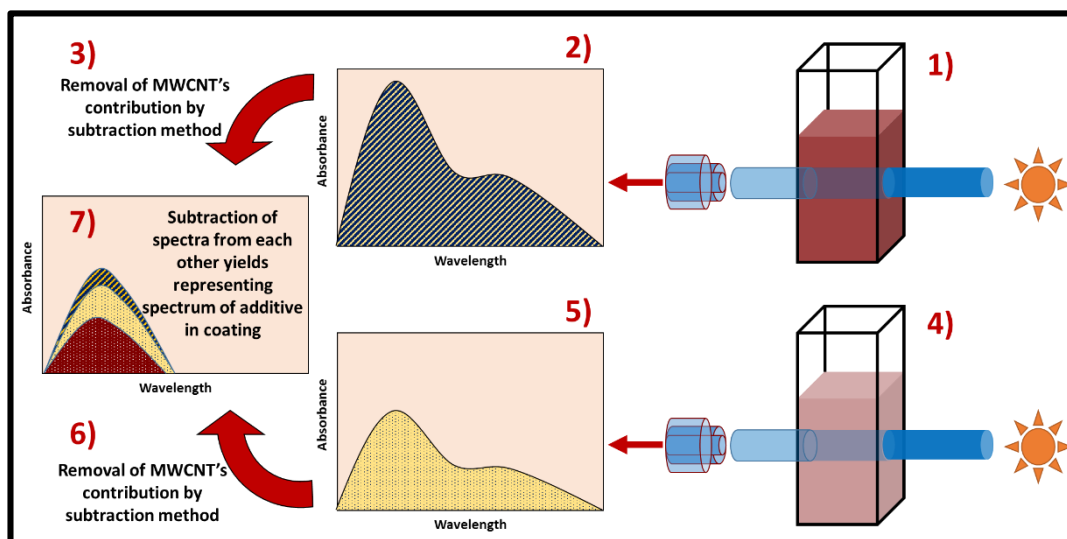


Figure 2.7 Sequence of events used for the determination of concentration of components in coatings.

A quartz cuvette was used in all experiments. Different quartz cuvettes of different brands shows different absorbance values at especially low absorbance values. In addition two identical quartz cuvette of same brand can show different absorbances at particular wavelengths. To minimize the error. Only one cuvette was used. Before measurements background subtraction was done by filling the quartz cuvette with pure solvents.

2.3 Carbon Nanotube-Iron Oxide Nanocomposite Synthesis

Iron oxide synthesis processes carried out under solvothermal conditions. Firstly, raw materials were mixed during ultrasonication in a flask under nitrogen bubbling as shown in Figure 2.8a, b and part c. While pure IPA (45 mL) is being kept and ultrasonicated in flask, raw materials dropwisely added to the solution within first 5 min. of 20 min. mixing process. The order of addition of starting materials is as follows: NaOH/Ethylene glycol solution, Ascorbic acid or Glucose/EG solution and FeSO₄/EG solution. 60 ml of total synthesis mixture contains 0,001 mole FeSO₄ in 5 mL EG. NaOH concentration in Ethylene glycol is 0.4 g/5 mL. Ascorbic acid and glucose concentration were regulated according to Fe²⁺ ion molar concentration. Ascorbic acid and glucose were always dissolved in 5 mL of EG. Fe/Ascorbic acid or glucose mole ratios are 8, 1.25 and 0.625 in different experiments (They were conducted to understand the suitable amount of hydrocarbon to convert nanoparticles into carbon-iron oxide core shell nanoparticles.). Preperation of MWCNTs-iron oxide nanocomposites was carried out by using PVP MWCNTs IPA or SDBS MWCNTs IPA instead of using pure IPA in synthesis mixture. It should be noted that MWCNTs concentration in the mixture could be calculated by UV-Vis analysis results. Thereby MWCNTs/Fe₃O₄ ratio in the final product could be calculated as well. Solvothermal synthesis was performed at 200°C for 12 h. Liquid loading in synthesis autoclave is 70 V. %.

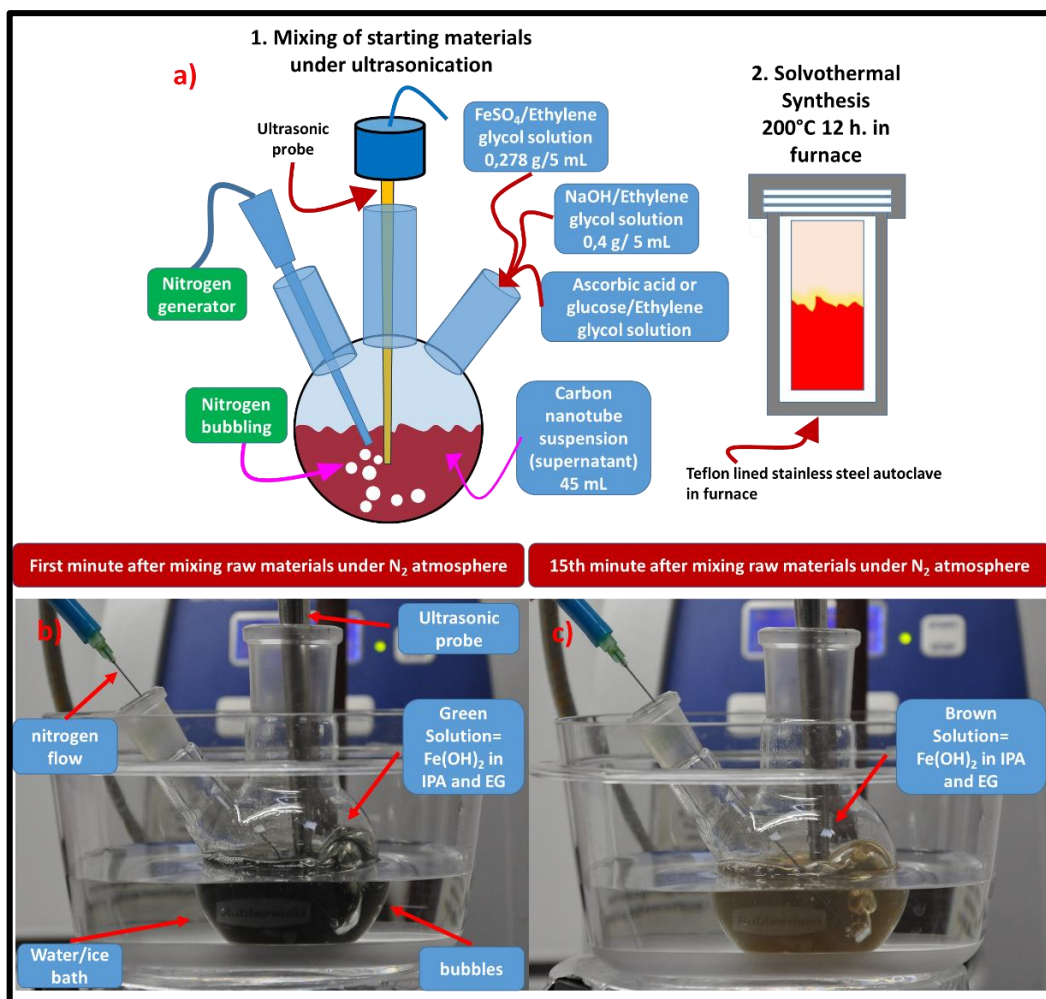


Figure 2.8 Illustration (a), and images (b) and (c) of mixing sequence before solvothermal synthesis of nanocomposites.

Synthesis mixture contains excess amount of NaOH and NaSO₄ and other impurities in its structures. Removal of these impurities was obtained by magnetic separation as shown in Figure 2.9. In each magnetic separation step dissolved impurities in IPA or water were removed.

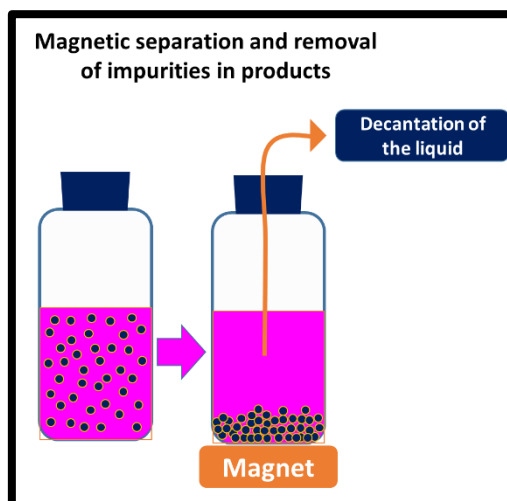


Figure 2.9 Magnetic separation and decantation of dissolved impurities in liquids after synthesis.

2.4 Inorganic Nanotube Synthesis Processes

Titanate nanotubes were prepared from TiO_2 nanoparticles. Therefore, firstly TiO_2 nanoparticles were produced by sol-gel process. The synthesis sequence is shown in Figure 2.10. Sulphur doped TiO_2 nanoparticles were prepared by dissolving thiourea in water before TTIP addition. Mole ratios of thiourea to Ti is 1 or 4. Doped TiO_2 nanoparticles were denoted as 1S- TiO_2 and 4S- TiO_2 according to thiourea/Ti ratio. Both doped particles were used for nanotube preparation but only 4S- TiO_2 derived nanotubes were characterized.

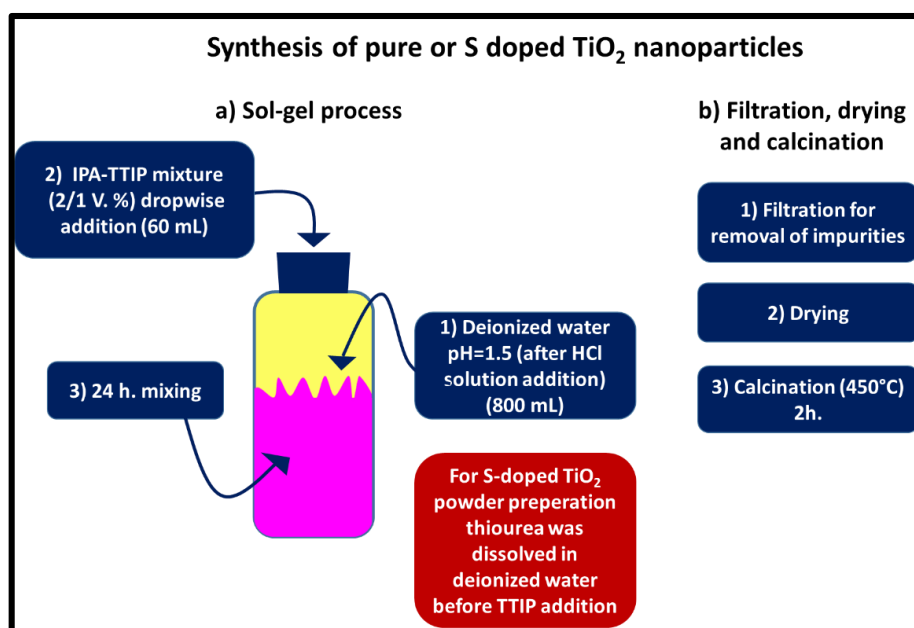


Figure 2.10 Method used in the synthesis of TiO_2 nanoparticles by sol-gel process.

Titanate nanotube preparation was carried out as shown in Figure 2.11. Sulphur doped titanate nanotubes were prepared by using 4S-TiO₂ nanoparticles in synthesis.

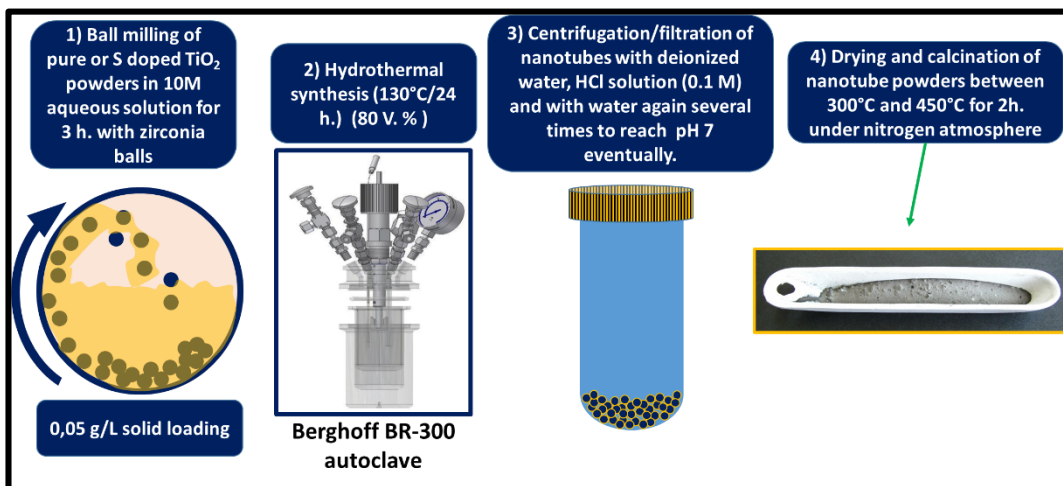


Figure 2.11 Method of hydrothermal synthesis of titanate nanotubes.

H₂O₂ modification was conducted by washing synthesized and dried hydrogen titanate nanotubes (they are acid washed they don't contain sodium) with 3 wt. % H₂O₂ solution as shown in Figure 2.12. It is believed that peroxy groups present on nanotubes provide a vivid yellow-orange color to the mixture. After washing with water (centrifugation) this color disappears.

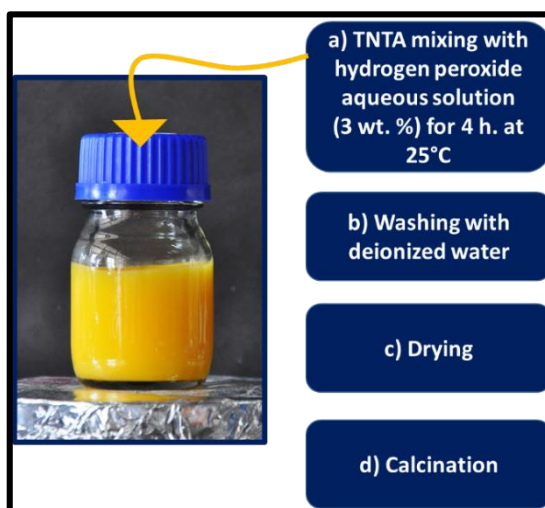


Figure 2.12 H₂O₂ modification step of titanate nanotubes.

UV-Vis spectra of titanate nanotube suspensions were prepared by addition of 1 g/L TNT and 0.5 g/L TEA to 5 ml butanol and subsequently suspensions were sonicated in Bandelin Sonorex HD3100 ultrasonicator with a MS72 tip for 10 min. under 10% amplitude. Suspensions were then filtered with a syringe filter having 0.45 µm pores. UV-

Vis spectrum of each TNT was obtained by removing contribution of TEA from spectra. For this purpose a spectrum of TEA in butanol was obtained and used in subtraction.

2.5 Other Devices Used in Characterization of Synthesized or Processed

Materials

Zeta potential analysis was conducted to assess the degree of stability of obtained suspensions.

Particles tend to sink when a suspension is left to rest. If particles are small enough and if they acquire enough charges on their surfaces, then suspension may stay stable for long period of time. Electrical state of charged surface is determined by spacial distribution of ions around it [84]. It has traditionally been called electrical double layer, although it is often more complex than just two layers. Quantitative analysis of stability of suspensions can be done by determination of zeta potential values. Zeta potential is the magnitude of repulsion between particles in suspension by means of electrical double layers around particles. Figure 2.13 shows an illustration of electrical double layer.

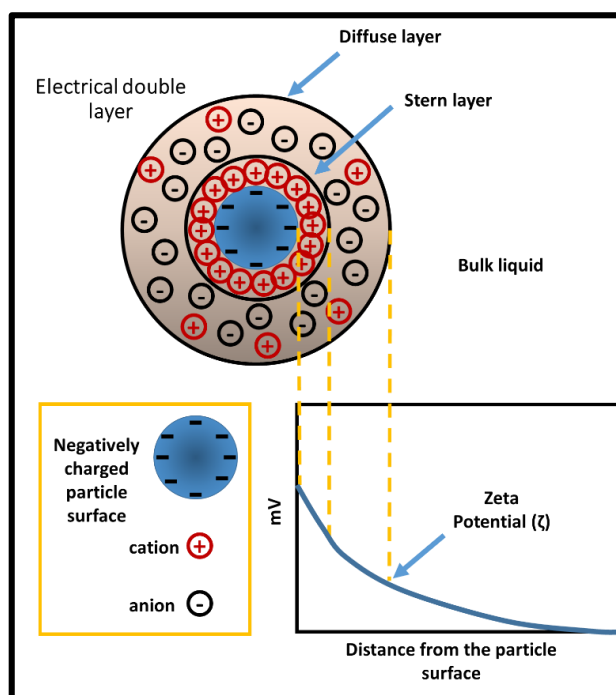


Figure 2.13 Electrical double layer.

Generally, zeta potential measurements were carried out by measurement of mobility of nanoparticles and subsequently conversion of mobility to zeta potential by using Henry equation. Electrophoretic mobility, μ ($\text{m}^2\text{V}^{-1}\text{s}^{-1}$) is the magnitude of velocity divided by the magnitude of the electric field strength:

$$\mu = \frac{V}{E} \quad (2.1)$$

μ is electrophoretic mobility measured by instrument, V is velocity of particles and E is electric field strength.

Zeta potential is related to electrophoretic mobility through equation below:

$$\mu = \frac{2\varepsilon\zeta f(\kappa\alpha)}{3\pi\eta} \quad (1.2)$$

ε is dielectric constant of the solvent, ζ is zeta potential, $f(\kappa\alpha)$ is Henry function and η is viscosity.

$f(\kappa\alpha)$ is referred to as Henry's function where α is the radius of the particle. κ is referred to as the Debye parameter and can be calculated from the electronic charge, Boltzmann's and Avagadro's constants, the absolute temperature and the ionic strength. Double layer thickness can be determined by using following equation:

$$\frac{1}{\kappa} = \left[\frac{\varepsilon\varepsilon_0KT}{2000e^2IN_A} \right]^{1/2} \quad (1.3)$$

ε is the dielectric constant of the solvent, ε_0 is the vacuum permittivity ($8.854 \times 10^{-12} \text{ A}^2 \text{ s}^4 \text{ kg}^{-1} \text{ m}^{-3}$), K is the Boltzmann constant ($1.38 \times 10^{-23} \text{ J K}^{-1}$), T is the temperature in Kelvin (298 K), e is the elementary charge ($1.602 \times 10^{-19} \text{ C}$), I is the ionic strength in molarity, and N_A is Avogadro's number ($6.022 \times 10^{23} \text{ mol}^{-1}$).

The ionic strength, I , can be calculated from the pH value of suspension:

$$I = [\text{H}^+] = 10^{-\text{pH}} \quad (1.4)$$

$1/\kappa$ is approved as electrical double layer thickness (Debye length). The charged region around a particle drops to about 2% of the surface charge at a distance approximately $3/\kappa$ from the particle. For ionic strength around 0.01 mol/L then $3/\kappa$ is around 10nm and for ionic strength around 10^{-5} mol/L then $3/\kappa$ is around 280nm [85]. $f(\kappa\alpha)$ value is dimensionless. Huckel and Smoluchowski approximations modify Henry's equation by changing Henry's function. For polar media Smoluchowski approximation is used and $f(\kappa\alpha)$ is taken 1.5 and in non-polar media Huckel approximation is used where $f(\kappa\alpha)$ is taken 1. Zeta potential is function of several factors. pH, concentration of particles, ionic strength of the medium affect magnitude and sign of zeta potential. For example, In particular small quantities (parts per million) of polyvalent ions (for example calcium

(Ca²⁺) ions), (iron (III) ions (Fe³⁺) or other impurities can significantly affect the magnitude of zeta potential [86]. In this study zeta potential measurements were conducted using Malvern Zetasizer Nano ZS. Folded capillary cells (DTS1070) are used as measurement cuvettes. Measurements were conducted at 25 °C. Suspensions were placed in folded capillary cells and waited for 120 seconds. It should be noted that during the zeta potential measurements to prevent electroosmosis stoppers are generally placed on folded capillary cells. But it aroused a problem in our experiments. Prior to each analysis standard samples were measured. If the stoppers are placed on cells magnitude of zeta potentials was found to yield wrong values. Therefore our measurements were conducted without using stoppers. Even if magnitude of zeta potentials may be slightly different from reality or may be repeatability is low due to contribution of electroosmosis, we believe that they allow for comparison between zeta potentials of different suspensions in our experiments. Because In each experiment several measurements were conducted for each of suspensions and we found out that the results of magnitudes of zeta potentials are close.

FTIR analysis was conducted using Perkin Elmer Spectrum 100. Prior to each analysis a background subtraction was implemented. Perkin Elmer Spectrum 100 was used in all experiments. Spectrum range was spanned from 4000cm⁻¹ to 650cm⁻¹.

A transmission electron microscope (TEM: JEOL 2100 JEM HRTEM) and 2 scanning electron microscopes (Zeiss Evo LS 10 and JEOL 7000F) were used. Zeiss Evo Ls 10 has a LaB₆ electron source. Fe₃O₄ and carbon nanotube samples were analysed using 20kV and 15kV accelerating voltages by Zeiss, respectively. Titanate nanotubes were imaged at low accelerating voltages. During the preparation of these thesis, the scanning electron microscope had a problem which is limiting the resolution of the device. The ground contact has very high resistance. This manifests itself as jagged edges in SEM images. To get over the problem scanning speeds were considerably lowered and amount of integration implemented on scanned lines increased (noise reduction level is increased). As a result edges and images had possessed smooth appearances (Figure 3.15b) and resolution decreased as well. This jagged edges become pronounced at low accelerating voltages.

Quantachrome Quadrasorp SI was used Surface area and pore size analysis of materials. For plotting adsorption desorption isotherms 72 adsorption points and 22 desorption points were selected. Iron oxide nanoparticles were degassed at 60 °C for at least 16 h.

Hitachi SII6000 was used for TG analysis. During TG analysis 2cc/min. nitrogen flow was maintained in each experiment. SDBS containing MWCNTs dried products were analyzed in alumina cuvettes. PVP MWCNTs containing cuvettes were analyzed in aluminium cuvettes.

XRD analysis was performed in two devices. Titanate nanotubes characterization was carried out in Pananalytical 'xpert Pro. Iron oxide nanomaterials synthesis was conducted in Rigaku Miniflex. Iron oxide XRD graphs contain low signal to noise ratio, probably because of the limit of resolution of the device. In addition, XRD graphs of carbon containing iron oxide nanoparticles exhibit worse signal to noise ratio. This is believed to be result of carbon which is in amorphous state.

Along with SEM, TEM and XRD, synthesized nanotubes are characterized by using Electron spin resonance spectroscopy (Bruker EMX-131) to detect defects in the structure which may shed light on the photocatalytic behavior of nanotubes.

Some materials can exhibit paramagnetic behavior because of unpaired electron spins. When an electron is placed in a magnetic field, there is two possible spin states of the electron having different energies. In ESR magnetic field is varied, and a constant or pulsed electromagnetic wave is also applied in the microwave range. An absorption spectrum is obtained when the energy difference between to spin states of the electron is equal to the radiation. This is called field of resonance. Absorption is not unique to magnetic field of frequency of radiation. But, the term g factor (proportionality factor) may yield important information.

$$g = h.v/\mu_b.B_0 \quad (5.3)$$

g is proportionality factor, h is Plank's constant, v is the frequency of the applied magnetic field, μ_b is Bohr magneton and B_0 is applied magnetic field.

QUANTITATIVE ANALYSIS OF CARBON NANOTUBE DISPERSIONS

Nanotubes are known to entangle and form agglomerates due to VdW forces and because of their high surface area. Figure 3.1 shows a pristine carbon nanotube bundle in low and high magnifications.

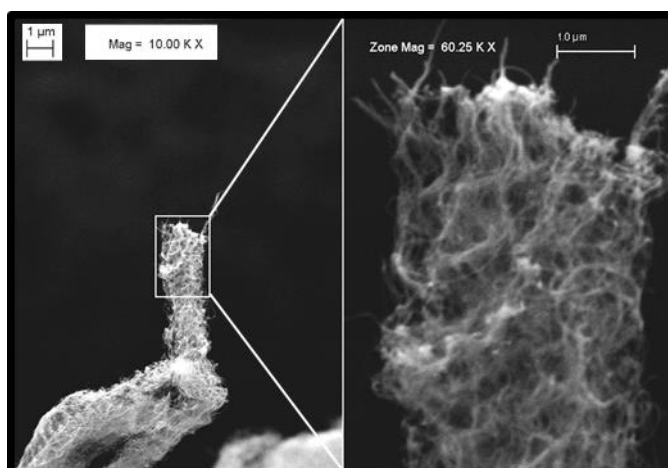


Figure 3.1 SEM images of agglomerates of carbon nanotubes in low and high magnifications.

3.1 Colloidal Suspensions of MWCNTs

Prior to determination of dispersion quality and quantitative analysis of contents in supernatants, sedimentation tests were conducted on supernatants. SDBS was successfully used as a dispersant. SDBS was added to IPA, butanol, acetyl acetone and amyl alcohol by ultrasonication followed by centrifugation. Subsequently, supernatants were left for resting. Some suspensions show stability even for years. For example, butanolic and amyl alcoholic suspensions are stable for more than a year. On the other hand isopropyl alcoholic suspensions are stable for months. Acetyl acetic suspensions are stable for about one week or two weeks. And finally ethanolic suspensions are not

stable. Figure 3.2 shows from left to right ethanolic, isopropyl alcoholic, butanolic, amyl alcoholic and acetyl acetic SDBS containing MWCNTs suspensions after centrifugation. These suspensions had been left for sedimentation for more than a year.

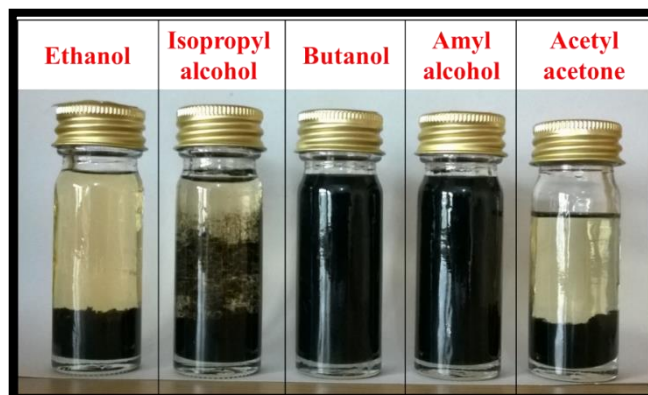


Figure 3.2 Result of sedimentation for more than a year for different solvent containing MWCNTs and SDBS suspensions prepared by ultrasonication (bath sonication) and centrifugation (2820 RCF). Initial SDBS and MWCNTs concentrations were the same (before centrifugation).

Pristine MWCNTs IPA suspensions were also prepared to observe sedimentation behavior. Figure 3.3 shows 10 times diluted (initially 0.1 g/L MWCNTs containing) suspensions and 10 times diluted SDBS-MWCNTs-IPA suspension. Pristine MWCNTs tend to form visible agglomerates when diluted while SDBS aided MWCNTs dispersions in IPA form solution-like homogeneous colloids.

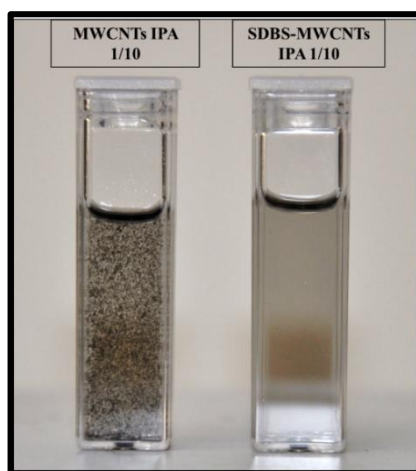


Figure 3.3 Pristine MWCNTs IPA suspension after ultrasonication (left) and SDBS MWCNTs IPA suspension after centrifugation (right). Both suspensions were 10 times diluted.

In further experiments IPA containing suspensions were chosen. Because these suspensions show high stability for months, cheap and less toxic. These suspensions were quantitatively analyzed in order to assess material content in supernatants prior to composite production.

Alongside SDBS several dispersants were also used for generation of homogenous dispersions of MWCNTs. PVP was found to be successful (more successful than SDBS in terms of quantity of MWCNT that it can disperse under same conditions). Same preparation procedures were implemented on PVP modified MWCNTs suspensions in IPA. Carboxyl group containing MWCNTs were dispersed in IPA (COOH-MWCNTs IPA) without using a dispersant. COOH-MWCNTs IPA suspensions were also stable for long periods of time as PVP and SDBS modified suspensions. Figure 3.4 shows dilute Pristine MWCNTs IPA, PVP-MWCNTs IPA and COOH-MWCNTs IPA suspensions. COOH group containing and PVP containing MWCNTs suspensions are stable and do not exhibit turbidity.

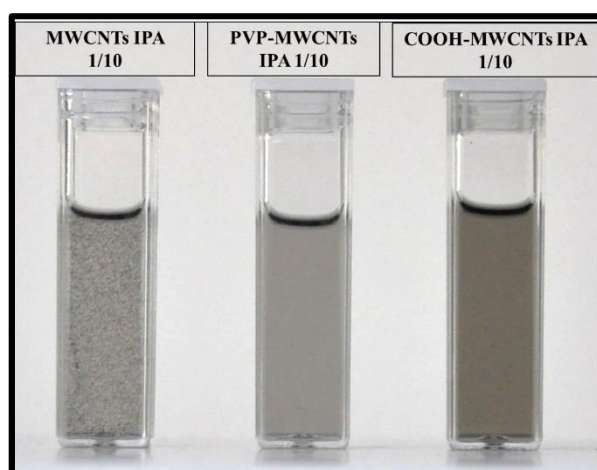


Figure 3.4 From left to right 10 times diluted Pristine MWCNTs IPA, PVP MWCNTs IPA and COOH MWCNTs IPA suspensions.

3.2 Determination of Quantity of Polymer Based Dispersant and Carbon Nanotubes in Centrifuged Suspensions and in Coatings

3.2.1 UV-Vis Measurements

Determination of PVP and MWCNTs content in centrifuged suspensions were conducted using UV-vis spectroscopy and TGA. Figure 3.5 shows UV-vis spectrum of pure IPA and PVP solutions in IPA in different concentrations. Dashed curve corresponds to IPA. UV Cut-off wavelength for IPA is 205 nm - 207 nm. Around (especially below)

this value quantification become very hard or impossible. Because device only accurately measures quantity of materials between absorbance values of 0.1 and 2.

Baseline correction of PVP containing suspensions was done by subtracting UV-Vis spectrum of IPA from UV-Vis spectra of PVP suspensions. PVP has an intense peak just on the UV cut off wavelength of IPA (207nm). The intense peak of PVP is due to the carbonyl functional group in ring structure ($n \rightarrow \pi^*$). $n \rightarrow \pi^*$ transition generally takes place at higher wavelengths, but inductive effect of adjacent nitrogen atom takes up electrons from carbon in carbonyl group and hence lone pair of electrons in oxygen becomes tightly bound to oxygen atom, as a result $n \rightarrow \pi^*$ transition becomes energetic.

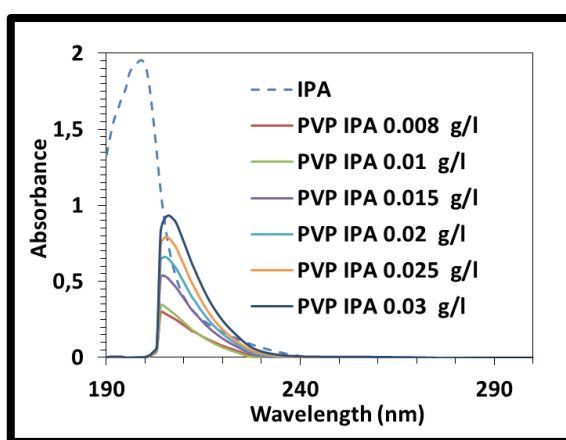


Figure 3.5 UV-Vis spectra of IPA and PVP IPA solutions at different concentrations. Baseline correction was done by subtracting contribution of IPA from PVP solutions.

Figure 3.6 shows calibration curve of PVP in IPA.

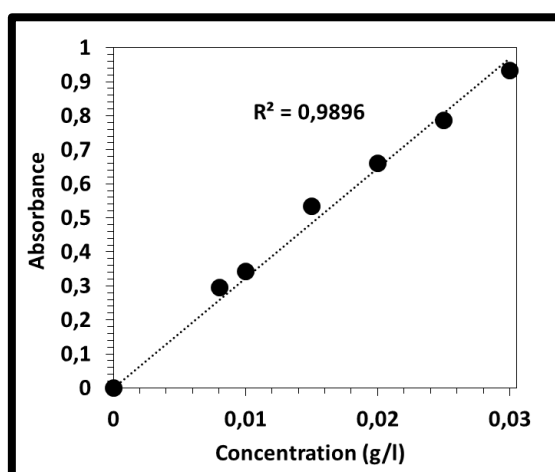


Figure 3.6 Calibration curve of PVP in IPA.

Figure 3.7 shows UV-Vis spectra of centrifuged diluted PVP modified MWCNTs IPA suspensions. Each spectrum contains two different peaks. Intense peaks belongs to PVP

and broader peaks are related to MWCNTs. Quantification experiments cannot be done by only using these spectra because MWCNTs contribute to absorbance of peak of PVP. We simply subtracted spectra only belonging to MWCNTs from these overlapping multi peak containing spectrum to obtain PVP spectrum. Attal et al. [3] made similar experiments to determine surfactant content in aqueous suspensions.

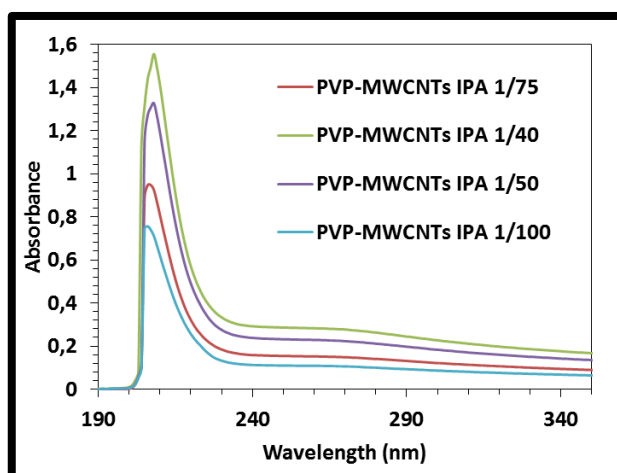


Figure 3.7 UV-Vis spectra of diluted PVP MWCNTs IPA suspensions. They were diluted between 40 and 100 times in this figure.

3.2.1.1 Carboxyl Functionalized MWCNTs

Pristine MWCNTs suspensions are not totally suitable for use in UV-vis measurements since agglomerates of nanotubes does not reflect the true shape of absorbance peak especially at high concentrations and the spectrum curve may become distorted. Carboxyl group functionalized nanotubes can be homogeneously dispersed in IPA. Carboxyl group functionalized MWCNTs containing IPA suspensions were prepared in similar way to PVP modified MWCNTs' suspensions. FTIR analysis were performed in order to detect functional groups on modified nanotubes though it is slightly out of the scope. If pristine MWCNTs were analyzed, we would see no detectable peak in the spectrum. This also applies to pristine MWCNTs IPA suspensions which contain peaks only corresponding to IPA.

Figure 3.8a, part b are the overlapping FTIR spectra of pristine MWCNTs IPA suspensions and COOH MWCNTs IPA suspensions, respectively. Unlike Pristine MWCNTs IPA, COOH MWCNTs IPA suspension spectrum has two characteristic peaks present only in that spectrum. 1650 cm^{-1} peak corresponds to C=C stretching vibration

(Figure 3.8a) and 1250cm^{-1} peak belongs to C-C stretching vibration (Figure 3.8B). Nitric acid treatment causes nanotubes to have carboxyl groups. Functionalization couldn't be deduced directly because because of the ATR used, C=O peaks are obscured. However, dispersion efficiency of carbon nanotubes by means of functionalization enabled dedection of carbon-carbon double and single bonds.

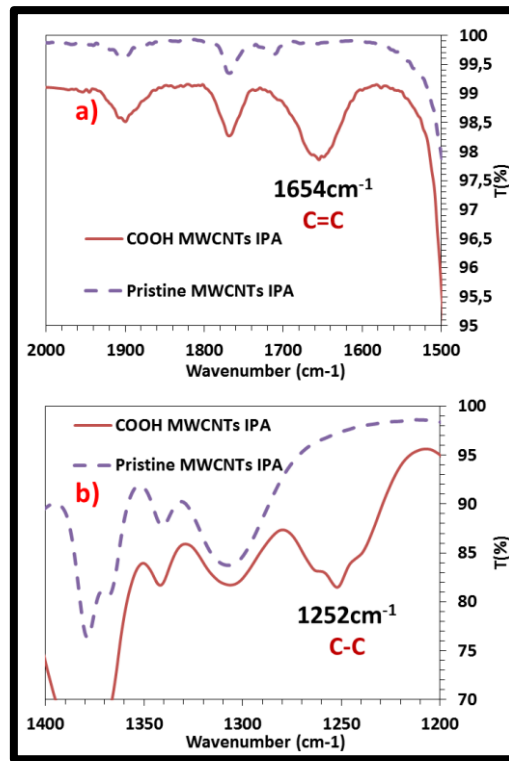


Figure 3.8 (a) and (b) are FTIR spectra of Pristine MWCNTs IPA (dashed) and COOH MWCNTs IPA suspensions at different wavelength ranges.

Figure 3.9 shows UV-vis spectra of COOH MWCNTs IPA in different concentrations. The broad peak at 256nm is due to π plasmon absorption. Since all absorbance is due to MWNCTs, it could be used in subtracting the contribution of MWCNTs from UV-vis spectra of PVP MWCNTs IPA.

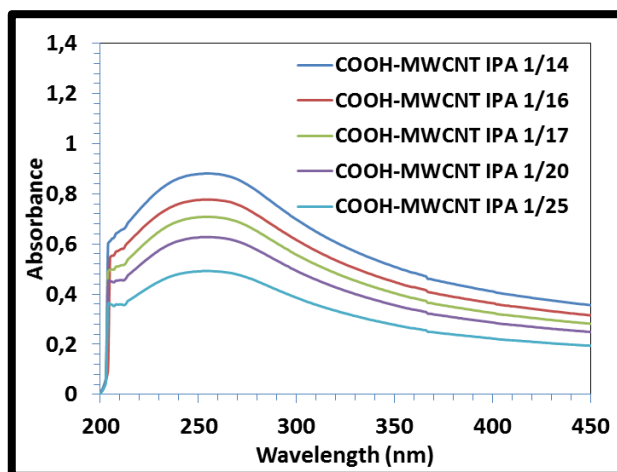


Figure 3.9 UV-Vis spectra of COOH MWCNTs IPA at different concentrations.

To obtain reliable results in estimation of PVP concentration (quantitatively), the values of absorbance were initially kept in range of 0.1 and 2 for spectra. We also considered the absorption due to the background. For example, the absorbance value at wavelength of 205nm for 75 times diluted suspension (PVP-MWCNTs IPA) is actually just below absorbance value of 2. In addition, if the absorbance is too low, device fails to accurately measure the absorbance values, therefore we couldn't dilute PVP-MWCNTs to relatively low levels. Namely, 100 times dilution found to be too low and 50 times dilution is too high (Dilution factors are specific to this PVP MWCNTs suspensions only). We found out that 75 times dilution give reliable estimations for this system since the results are in correlation with TGA results. The dilution is not universal to all suspensions. The reasons behind finding optimum dilution factor of 75 is because of the nature of the materials (their light absorbing capability) and their ratio.

At low concentrations, contribution of MWCNTs in absorbance is not accurately measured giving overestimated results in terms of PVP concentration. On the other hand relatively high concentrations end up with underestimated results. Figure 3.10 shows overlapping spectra of dilute COOH-MWCNTs and 75 times diluted PVP-MWCNTs suspensions. The third spectrum is the extracted spectrum after subtraction of MWCNTs' contribution. The absorbance value corresponds to 1.95 g/L PVP. We have also conducted same experiments on 100 times and 50 times diluted suspensions. Results obtained from 100 times and 50 times diluted suspensions are 2.08 g/L and 1.84 g/L, respectively. Dried supernatant weight is 2.0425 g/L. So 100 times diluted suspension give an overestimated result. 50 times dilution is also wrong because it is an underestimate.

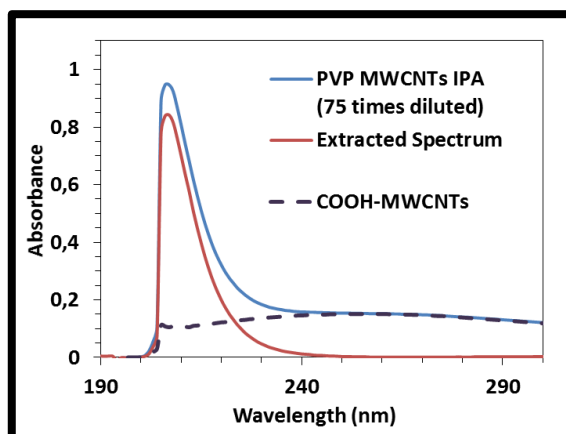


Figure 3.10 PVP-MWCNTs IPA, COOH-MWCNTs IPA and resultant spectrum after subtraction of latter from the former.

Estimation of carbon nanotube content can be done in different ways: Attal et al estimated SWCNTs content by subtracting the concentration of surfactant from the weight of dried supernatant [24] Sun et al. [20] calculated carbon nanotube content by comparison of spectra obtained before centrifuge and after centrifuge. Y. Ye et al. [87] determined MWCNTs content by plotting a calibration curve belonging to MWCNTs in electrophoretic suspensions. Figure 3.10 shows overlapping spectra before centrifuge and after centrifuge. When comparing the data, it is also found that at relatively low concentrations device does not give reliable results. Namely, 25 times diluted centrifuged and uncentrifuged suspensions overlap. This data is inaccurate since there exists a sediment after centrifugation. On the other hand 5 times diluted PVP MWCNT IPA suspensions overlap with 6 times diluted uncentrifuged PVP-MWCNTs IPA suspension (Figure 3.11). In addition, 10 times diluted and 12 times diluted corresponding Spectra of suspensions also overlap. Using this data MWCNTs content was found 0,083 g/L. This result is close to TG analysis results which will be explained later. Giordani et al. [88] stated that, concentrate suspensions containing aggregates of nanotubes has lower extinction coefficients compared to low concentration dispersions. So the results obtained by comparing overlapped spectra of centrifuged and uncentrifuged suspensions slightly different from actual values of concentrations. They are slight underestimates. Overlapping suspensions (before centrifuge and after centrifuge) overlap at IR and visible range (because only contribution in this region is due to MWCNTs), but they gradually diverge at UV region. The divergence is arising from the different PVP concentrations present in diluted suspension.

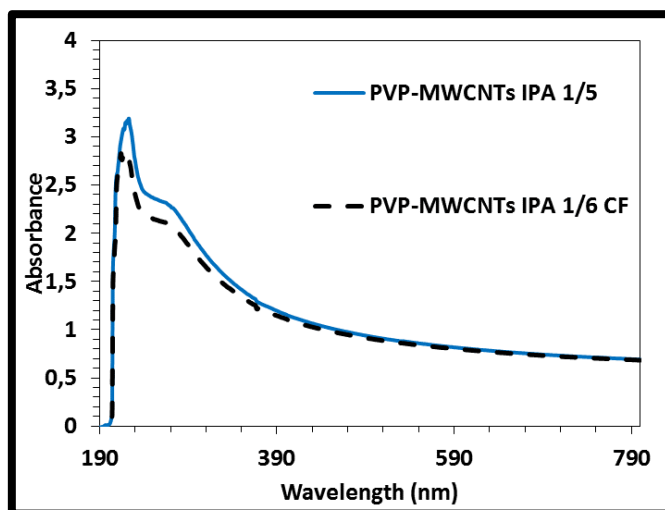


Figure 3.11 Overlapping spectra of PVP MWCNTs IPA before centrifuge and after centrifuge. CF indicates the suspension which is not subjected to centrifugation.

Therefore, concentration of MWCNTs is known at that spectrum.

3.2.2 Thermogravimetric Analysis

Thermogravimetric analysis was performed to interpret the results obtained by UV-Vis spectroscopy. Namely, UV-Vis spectroscopy results may differ according to concentrations of the suspensions. Therefore, UV-Vis results were compared with another method to determine optimum dilution needed before UV-Vis measurements. Shtein et al. implemented TG measurements both on precipitate and supernatant to determine CNT weights [25]. We follow similar route to determine ratios between MWCNTs and PVP in precipitate and in supernatant as well. By knowing concentration of dried precipitate and supernatant, it is possible to determine concentration of PVP and MWCNTs. Figure 3.12a shows TG curves of MWCNTs, pure PVP, dried supernatant of PVP-MWCNTs IPA suspension and dried precipitate obtained after centrifugation. MWCNTs does not show significant mass loss at this region under inert atmosphere. So mass losses of supernatant and precipitate belongs only to PVP. Curves were shifted in order to accurately calculate the concentrations. Because TG curves of PVP, supernatant and precipitate have different mass changes and mass change rates at low temperatures.

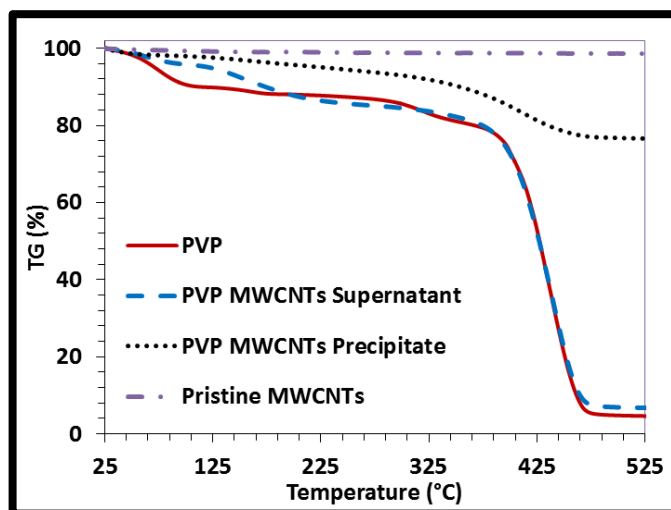


Figure 3.12 TG curves of pristine MWCNTs (purple dashed horizontal line), PVP (red continuous curve), dried supernatant of PVP MWCNTs IPA (dashed curve) and dried precipitate of PVP MWCNTs IPA (finer dashed curve).

DTG curves of PVP, precipitate and supernatant are shown in Figure 3.13a. Curves are shifted and the values made positive to be distinguished easily. Lowest mass loss rate regions at relatively low temperatures may be selected to overlap the curves at a suitable temperature. After overlapping true ratio between PVP and MWCNTs can be found. Since mass loss rate at around 250 °C is almost horizontal to the x axis, this temperature is selected as starting point. Correlated curves are shown in Figure 3.13b. Subsequently, percentage of mass differences were used at 500 °C and concentrations were calculated.

The residual mass between 250 °C (we consider it as room temperature) and 500 °C is 5.4%, 9.8% and 79.7% for PVP, supernatant and precipitate, respectively. Using these data and concentrations of supernatant and precipitate, individual concentrations were calculated. The sequence of calculation is shown between Equation 3.1 and Equation 3.6 using the data of dried supernatant and PVP.

$$2.0425 \text{ g/L} = \text{concentration of supernatant obtained by measuring dry weight} \quad (3.1)$$

Since the TG curve of supernatant is shifted to higher values in order to overlap with that of PVP the amount of shifting should be considered for TG of supernatant.

$$101,727 \text{ wt. \%} = 2.0425 \text{ g/l shifted concentration} \quad (3.2)$$

$$100 \text{ wt. \% supernatant} = 2.0078 \text{ g/L} \quad (3.3)$$

After correlation we assume that 2.0078 g/L is the sum of both concentration of PVP and MWCNTs (Equation (3.4)).

$$100 \% W_{\text{PVP}} + 100 \% W_{\text{MWCNTs}} = 2.0078 \text{ g/L (at } 25 \text{ }^\circ\text{C)} \quad (3.4)$$

100% of nanotubes preserves their integrity at 500 °C. Therefore, there is no mass change for nanotubes. But only 9.8 wt. % of supernatant is present.

$$5.49\% W_{\text{PVP}} + 100\% W_{\text{MWCNTs}} = 0.198 \text{ g/L (at } 500 \text{ }^\circ\text{C)} \quad (3.5)$$

$$1.809 \text{ g/L} = 94.51\% W_{\text{PVP}} \quad (3.6)$$

$$W_{\text{PVP}} = \underline{1.914 \text{ g/L}} \quad (3.7)$$

$$W_{\text{MWCNTs}} = 2.0078 - 1.914 = \underline{0,093 \text{ g/L}} \quad (3.8)$$

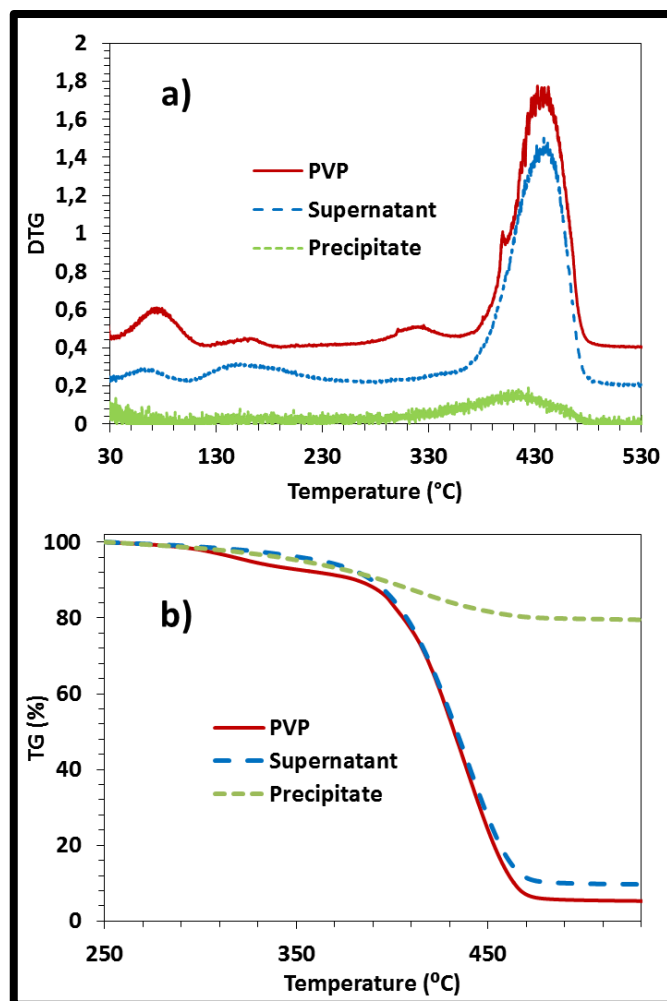


Figure 3.13 (a) Dervative TG curves of PVP, dried supernatant of PVP MWCNTs IPA and dried precipitate of PVP MWCNTs IPA CF; (b) shows TG curves which were shifted (except curve of PVP) to eliminate the mass loss below 250 °C.

Same procedure was applied to precipitate and through mass balance PVP and MWCNTs concentration in supernatant was calculated by using the dried precipitate concentration (0,054 g/L).

Equations (3.9), (3.10), (3.11), (3.12), (3.13), (3.14), (3.15), (3.16), (3.17) and (3.18) shows calculation sequence used in determination of concentrations.

$$0.0452 \text{ g/L} = \text{concentration of dried precipitate obtained by measuring dry weight} \quad (3.9)$$

Since the TG curve of precipitate was shifted to lower values in order to overlap with that of PVP, the amount of shifting should be considered. Result is equation (3.10).

$$92.919 \text{ wt. \%} = 0.0452 \text{ g/L shifted concentration} \quad (3.10)$$

$$\text{Dried supernatant } 100 \text{ wt. \%} = 0.0484 \text{ g/L} \quad (3.11)$$

Unlike calculations conducted on dried supernatant and corresponding TG curves, we tailored the dried precipitate concentration by increasing its amount.

$$100 \% W_{\text{PVP}} + 100 \% W_{\text{MWCNTs}} = 0.0484 \text{ g/L (at } 25 \text{ }^\circ\text{C)} \quad (3.12)$$

100% of nanotubes preserves their integrity at 500 °C, and the residual mass of dried precipitate is 79.77% of total at 500 °C.

$$5.49\% W_{\text{PVP}} + 100\% W_{\text{MWCNTs}} = 0.0386 \text{ g/L (at } 500 \text{ }^\circ\text{C)} \quad (3.13)$$

$$0.0386 \text{ g/L} = 94.51 \% W_{\text{PVP}} \quad (3.14)$$

$$W_{\text{PVP}} = 0.0408 \text{ g/L in precipitate} \quad (3.15)$$

$$W_{\text{MWCNTs}} = 0.0484 - 0.0408 = 0.0075 \text{ g/L} \quad \text{in precipitate} \quad (3.16)$$

$$W_{\text{PVP in supernatant}} = 1,959 \text{ g/L MWCNTs} \quad (3.17)$$

$$W_{\text{MWCNTs in supernatant}} = 0.0925 \text{ g/L MWCNTs} \quad (3.18)$$

Table 3.1 shows calculated concentration values using UV-Vis and TG.

Table 3.1 Calculated Concentrations of PVP and MWCNTs in supernatants by using Uv-Vis spectroscopy and TGA

Technique	Used component of technique	Material in supernatant	Concentration in supernatant (g/L)
UV-Vis	Dilute supernatant	PVP in supernatant	1,95
UV-Vis	Overlapping suspensions before CF and after CF*	MWCNTs in supernatant	0,08
TG	TG of supernatant and PVP	PVP in supernatant	1,91
TG	TG of supernatant and PVP	MWCNTs in supernatant	0,09
TG	TG of precipitate and PVP	PVP in supernatant	1,95
TG	TG of precipitate and PVP	MWCNTs in supernatant	0,09

*CF is indication for uncentrifuged suspension

3.2.3 Zeta potential analysis of PVP-MWCNTs IPA suspensions

Zeta potential measurements conducted to materialize the dispersion state of suspensions. PVP is known to wrap graphite surface and form globular clusters [12]. Wrapping on nanotube surfaces provides colloidal stability via steric stabilization. In addition to this enhanced dispersion could be achieved by centrifugation [19]. Presence of individual or small bundles nanotubes in PVP-MWCNTs IPA suspensions accounts for retention of

stability for months. Besides, stability is key feature of a successful EPD or composite making. Sun et al. [20] found out dispersion quality can be quantified with zeta potential. Zeta potential is the measure of repulsion or attraction between particles (bundles or individual nanotubes in our case) in suspensions and provide quantified information about stability. Table 3.2 shows zeta potentials and FWHM values of suspensions. Prior to EPD, suspensions were mixed with Magnesium chloride solutions, this suspensions are called electrophoretic suspensions. Electrophoretic suspensions (will be used in coating processes) are denoted as PVP MWCNTs IPA xMgCl₂ (4.87mM MgCl₂), PVP MWCNTs IPA 2xMgCl₂ (9.64mM MgCl₂) and MWCNTs IPA 4xMgCl₂ (18.88 mM MgCl₂).

Table 3.2 Zeta potentials of PVP MWCNTs IPA and COOH MWCNTs IPA suspensions

Material	pH	Zeta potential (mV) (Huckel approximation)	FWHM (mV)
PVP MWCNTs IPA	Natural	-35.9	132,69
PVP MWCNTs IPA CF*	Natural	-34,9	165,72
COOH MWCNTs IPA	Natural	-47,5	131,79
PVP MWCNTs IPA xMgCl₂	Natural	28,6	133,25
PVP MWCNTs IPA 2xMgCl₂	Natural	19,7	122,51
PVP MWCNTs IPA 4xMgCl₂	Natural	16,8	131,14

*CF is abbreviation for uncentrifuged suspension

Zeta potentials can be represented by using different approximations. There are generally two choices: Huckel's and Smoluchowski's. Huckel's approximation is known to be valid in non-polar solvents containing particles having diameter lower than 100nm and possessing thick double layers [89]. Length of carbon nanotubes is obviously higher than 100 nm, but IPA is a non-polar or semi-polar solvent, therefore we have chosen to

demonstrate Huckel's approximation's results instead of Smoluchowski's (valid for aqueous suspensions). In addition, one can easily convert that of Huckel's into Smoluchowski's by multiplying it with $2/3$.

If the magnitude of zeta potential is greater than ± 15 , it can be considered stable [90]. It should be noted that steric stabilization may also provide stability at zeta potentials even close to zero [91]. As produced CNTs have small and positive zeta potential in acidic region with an isoelectric point in the pH range 5-8 [92]. PVP successfully provide a high zeta potential value to MWCNTs suspensions in IPA. Sign of the charge is negative for both PVP and COOH functional group containing nanotube suspensions. Though uncentrifuged suspensions contain higher amount of PVP, zeta potential for PVP MWCNTs IPA CF is -34,9mV which is slightly lower than zeta potential value of centrifuged suspension (-35,9mV). Highest zeta potential values is obtained in COOH-MWCNTs IPA suspensions (-47,5mV).

Though small amount of charger salt addition to suspensions is beneficial, excess amounts of salts decreases stability. As $MgCl_2$ content in PVP-MWCNTs IPA suspensions increases magnitude of zeta potential decreases gradually from 28.6mV to 16.8mV. Sarkar et al. [93] stated that ionic concentration in liquid reduces the size of the double layer region and consequently the electrophoretic mobility and hence zeta potential. We also found out that electrophoretic suspensions are not stable for long period of times despite the fact that they can be used in EPD (used immediately after vigorous mixing). This may be due to the suppressed double layers which may allow adjacent particles to get closer till Van der Waals attractions dominate.

Zeta potential measurement of carbon nanotubes are not totally accurate because carbon nanotubes are rod-like particles. It is known that depending on the magnitude of zeta potential Smoluchowski's approximation results are up to 20% overestimate for rod-like particles [94]. Huckel approximation also fails to predict actual values of zeta potential since both Huckel and Smoluchowski approximations designed for spherical particles [95]. So we assume that our results are slight overestimates.

Carboxyl functionalized carbon nanotubes is known to exhibit isoelectric points at very low pH values [92]. The reason behind is the high density of negatively charged functional groups on graphite surface. PVP containing suspensions are similar to COOH-

MWCNTs since they accumulate large amount of negatively charged groups on nanotube surface.

PVP has pyrene rings in its structure as illustrated in Figure 3.14a. This ring structure may attach on nanotube surface by π - π stacking interaction and create a polymer shell on nanotube surface. Wang et al. [96] stated that in polar solvents electron spin density in pyrene rings localized on nitrogen atom creating negatively charged oxygen containing carbonyls exhibiting hydrophilicity. Neutral structure and resonance structure of PVP is shown in Figure 3.14a. Zeta potential is determined by negatively charged oxygen containing carbonyl group probably because nitrogen atom is shielded by polymer backbone. In addition, sign of charge for Mg^{2+} containing suspension is positive. Because Mg^{2+} ions may be attracted and stitched to negatively charged carbonyl groups of PVP molecules and provide varying magnitudes of zeta potentials related to its concentration.

Figure 3.14b shows zeta potential distribution of suspensions. Values are obtained by using Huckel's approximation. Sun et al. [20] and White et al. [91] encountered broadening and attribute this phenomenon to probable variation of surfactant molecules adsorbed on tubes. Though we don't use surfactants this variations of PVP adsorption may also happen in our suspensions. Sun et al. also stated that angular distribution of nanotubes may also contribute peak broadening [20]. Mobility of differently oriented nanotubes is different, highest for nanotubes aligned horizontally to electrical field and lowest for vertically aligned ones. Nanotubes eventually rotate and move horizontally to the electrical field. Time taken for the rotation of molecules from low mobility state and to high mobility state may be influenced by concentration of solids in the structure as well. As a consequence high concentrations may noticeably contribute to peak broadening. White et al. [91] also attributed peak broadening due to the presence of SWCNTs with many diameters and chiralities. In addition one factor may contribute to peak broadening is high signal to noise ratio (process fault) resulting from high concentration samples being measured.

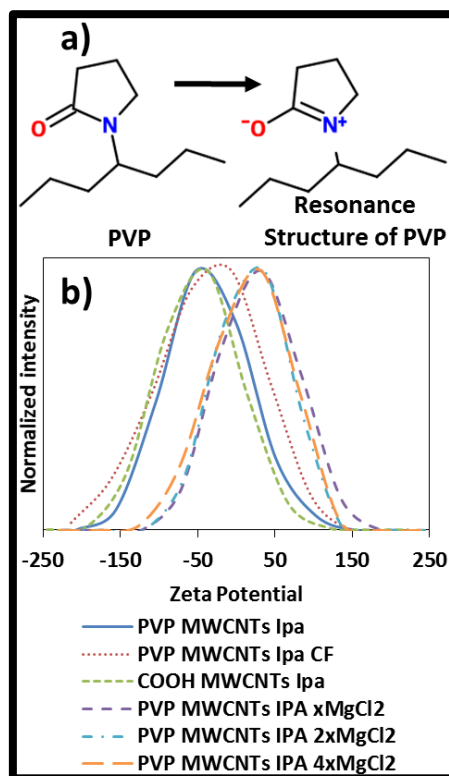


Figure 3.14 (a) is depiction of neutral structure of PVP molecule and its resonance structure. (b) is Zeta potential distribution of PVP or COOH MWCNTs containing suspensions obtained using Huckel's approximation.

3.2.4 EPD and determination of PVP and MWCNTs quantities in coatings

Without addition of charger salt PVP-MWCNTs IPA suspensions are not successful in obtaining coatings on substrates. Materials can accumulate, but they don't adhere to electrode surface (Stainless steel grade: 316). It is known that presence of charger salts in suspensions can improve adhesion of CNTs to substrates [92]. Besides, they are known to improve suspension stability at very low quantities [92]. For example, Oh et al. mixed MgCl₂ and COOH-CNTs in ethyl alcohol and performed EPD [97]. It is proposed that Mg⁺ ions form hydroxides at the surface of the negative electrode which assists the interfacial bonding [98].

Zeta potential is an important factor in obtaining good deposits during EPD. EPD obtained from low zeta potential suspension may end up with porous sponge-like deposits [24]. Though PVP MWCNTs IPA xMgCl₂ suspension has higher zeta potential value than the other MgCl₂ containing suspensions. It was not used since it does not provide enough adhesion to substrate surface. PVP MWCNTs IPA 2xMgCl₂ suspension was used in EPD processes because it has slightly higher zeta potential compared to PVP

MWCNTs IPA 4xMgCl₂ and it is successful in adhesion as well. Presence of charger salt reversed the deposition electrode compared to PVP MWCNTs IPA suspensions and, hence deposits formed on negatively charged electrodes.

2 different depositions were implemented in terms of duration of deposition. Deposition voltage was not precisely determined. We have found that 50V electrical potential is appropriate for deposition. It should be noted that 50 V potential can be considered slightly high. But we need high deposition rate to benefit from the diminishing stability. Figure 3.15a and b show SEM images of coating obtained after 10 min. EPD process. 10 min. coating has a smooth surface, but there is cracks on the coating as well (Figure 3.15b). We knew that deposition under high voltages may yield rough coating surfaces, however as shown in SEM micrographs in Figure 3.15, 50V electrical potential may be acknowledged as appropriate.

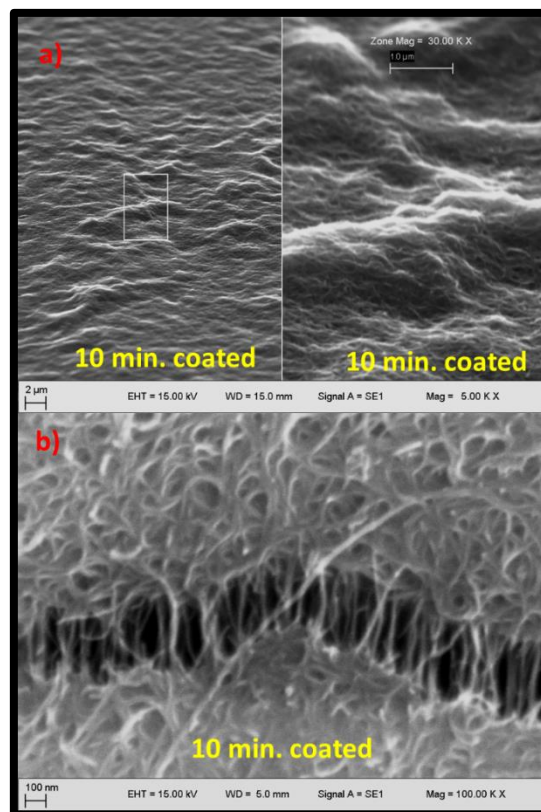


Figure 3.15 (a) SEM images of 70° tilted coating obtained by EPD of PVP MWCNTs IPA 2xMgCl₂ suspension on stainless steel substrate under 50V DC potential for 10 min. (b) is SEM micrograph of a crack on deposit surface.

Figure 3.16a shows tilted SEM micrograph of coating obtained after 20 min. deposition. Unlike 10 min. coated sample 20 min. coating ends up rougher surface; this may be the consequence of higher thickness of the coating which is causing greater mismatch in

contraction in different parts of the coating during evaporation of the solvent. Both of the coatings exhibit cracking. The number and the gap between the cracks is larger in 20 min. coated sample (Figure 3.16b). In every crack nanotubes make bridging, but since the gap between sides is wide, some nanotubes pull out from their sockets in 20 min. coated deposit. It is believed that it is possible to avoid cracking by drying the green density in controlled atmosphere. In addition, by using a solvent having lower evaporation rate compared to IPA at room temperature would lead to crackless coatings even if they were dried in an uncontrolled atmosphere.

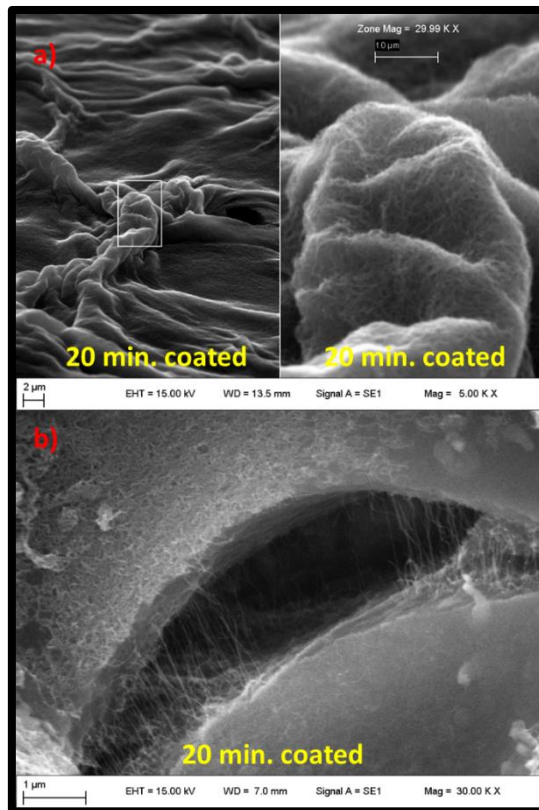


Figure 3.16 (a) is SEM images of 70° tilted coating obtained by EPD of PVP MWCNTs IPA 2xMgCl₂ suspension on stainless steel substrate under 50V DC potential for 20 min. (b) is SEM micrograph of a crack on surface.

It is possible to estimate the ratio and concentration of components in coatings by using UV-Vis spectroscopy. Concentration determination of PVP in coating was performed by subtracting UV-Vis spectra of 75 times diluted suspensions before EPD deposition and after EPD. But, before subtraction contribution of MWCNTs needs to be subtracted from UV-vis spectras. Figure 3.17a shows UV-Vis spectra of suspensions measured before and after EPD and, overlapping spectra of COOH-MWCNTs with each PVP MWCNTs spectrum. Resultant spectra obtained after subtraction of MWCNTs' contributions are

shown in Figure 3.17b; since those extracted spectra represent PVP concentration in suspensions before and after EPD process, subtraction of these two spectra could give a representation of UV-Vis spectrum of PVP in coating. Figure 3.17b shows extracted PVP spectrum in coating and Figure 3.17c is the same spectrum in which y axis is narrowed. The absorbance value is 0.077 at its peak. Considering 75 times dilution resulting concentration of PVP in coating is calculated 0.178 g/L. Since 5.1 ml of suspension is used, amount of PVP in coating is found 0.0009g. MWCNTs concentration was calculated by overlapping different spectra. It should be noted that we neglected absorbance due to the presence of $MgCl_2$.

In visible and infrared region contribution to UV-Vis spectra is due to presence of MWCNTs only. By comparing overlapping spectra, it is possible to determine MWCNTs concentration of the other suspension. Figure 3.17d shows overlapping spectra of PVP-MWCNTs IPA CF suspension (centrifugation is not implemented) and spectrum of suspension measured after 20 min. of EPD. MWCNTs' concentration in processed suspension is found 0.058 g/L. Initial concentration of centrifuged suspension was found 0.083g/L. Therefore, MWCNTs concentration in coating is 0.025 g/L. Thereby, 0.00012g of MWCNTs is present in the coating. The initial ratio of PVP to MWCNTs is ~23. On the other hand, in the coating the ratio turned out to be 7.5. Ratio of MWCNTs considerably higher in coating compared to supernatant.

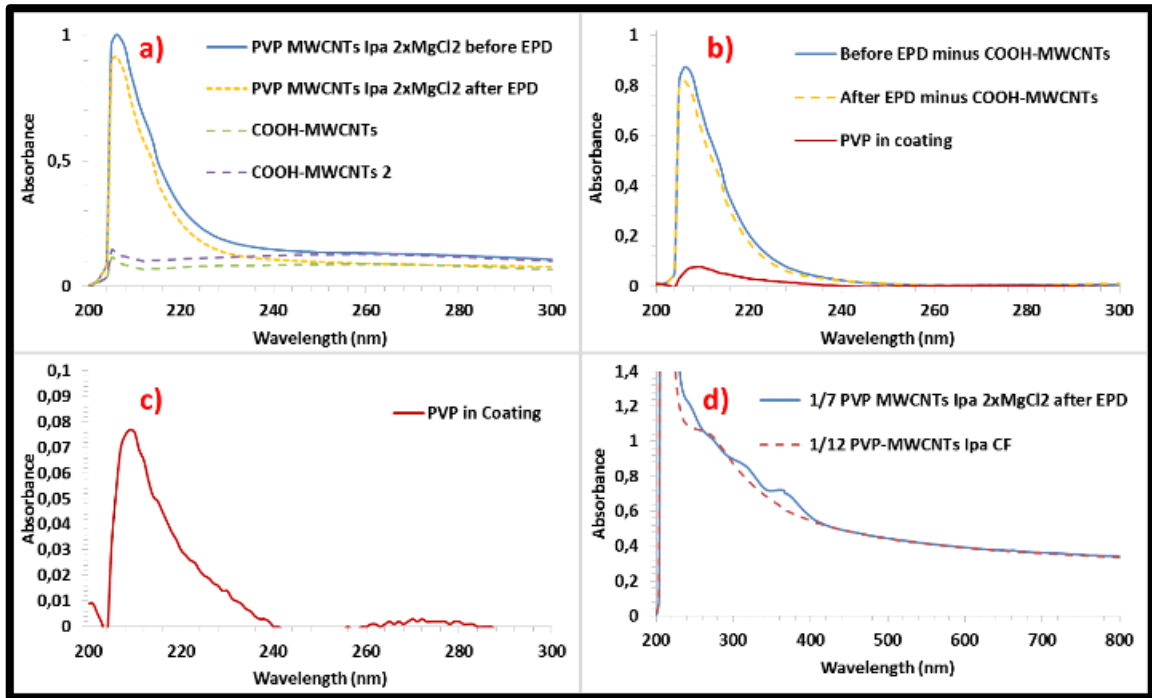


Figure 3.17 (a) UV-Vis spectra of suspensions analyzed before and after EPD processes and overlapping spectra of COOH MWCNTs IPA with electrophoretic suspensions. (b) is the spectra obtained after subtraction of MWCNTs' contribution. (c) is representing the PVP in the coating which is also shown in (b) as the red curve. (d) is overlapping spectra of EPD suspension after EPD with that of uncentrifuged PVP MWCNTs IPA suspension.

By knowing amount of material coated on a substrate, surface area of coating and densities of coated materials, it is possible to determine thickness of the coating. Exact determination requires completely smooth and dense coating. But in our case it would be a very rough estimate since our coating has high roughness. In addition, deposition took place in two sides of the deposition electrode. But, deposition on surface which is not facing counter electrode can be negligible since most of the coating obtained on counter electrode facing side. Surface area of the coating is 0.83 cm^2 . Density of PVP and MWCNTs are accepted as 1.2 g/cm^3 and 2.1 g/cm^3 , respectively. Considering these values, resultant coating volume turn out 0.000807 cm^3 and the thickness of coating is estimated $9.72 \text{ }\mu\text{m}$.

We have also compared the UV-Vis spectroscopy result with SEM images of cross-section of coatings. Figure 3.18 shows cross-section SEM images of coating deposited for 20 min.

Coating thickness of the sample is around 20 μm as evident in SEM images. There is a difference between UV-Vis spectroscopy measurements and SEM measurements. Estimation conducted via UV-Vis spectroscopy assumes that coatings do not contain porosity. In reality, coating should contain certain amount of porosity. Therefore, in reality SEM images should always exhibit thicker coatings compared to UV-Vis results.

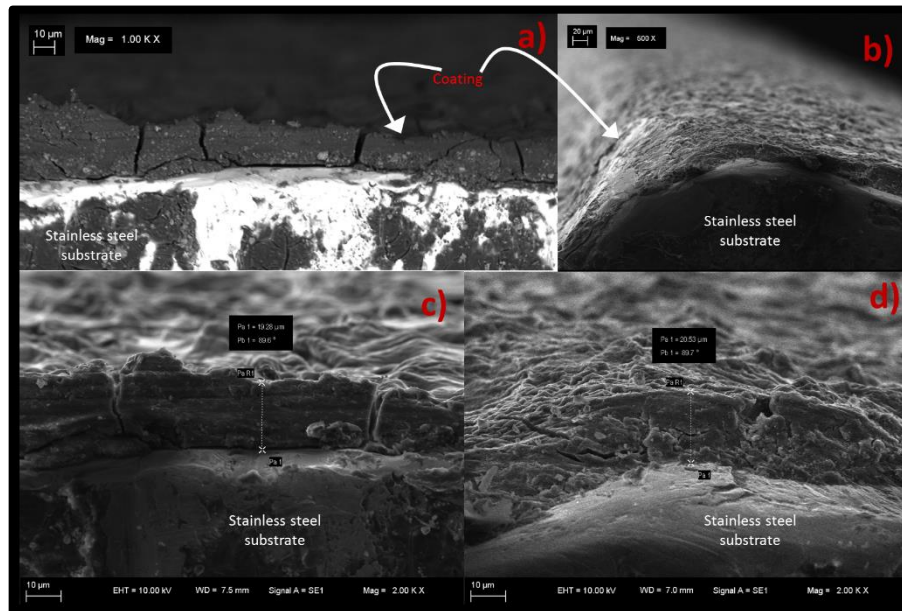


Figure 3.18 Cross-section SEM images of PVP MWCNTs IPA coatings deposited for 20 min. under 50 V. (a) is BSE image; (b), (c) and (d) are SE images.

3.3 Determination of Quantity of SDBS and MWCNTs in Centrifuged Suspensions, EPD and Their Characterization

In this study, SDBS was also used to disperse carbon nanotubes. Since the aim of the research is to make carbon nanotube iron oxide nanocomposites we had to investigate different dispersants for carbon nanotube dispersion and also different coupling agents for the synthesis of iron oxide coated carbon nanotube composites or vice versa.

3.3.1 UV-Vis Spectroscopy Analysis

Figure 3.19 shows UV-Vis spectra of SDBS in IPA. J. Geng et al. [99] observed that SDBS has 3 peaks centered at ~ 194 nm and ~ 225 nm, and a third but weak band at ~ 260 nm. They used aqueous solutions, therefore the resultant peaks becomes slightly shifted in our solutions but we see the 3 peaks as well. First peak is observed at 206nm. The accuracy of this peak is low in terms of quantitative analysis since it is below the UV cut-off wavelength of IPA. Geng et al. [99] used this peaks to observe critical micelle

concentration of SDBS in water. However we didn't observe such threshold in absorbance to observe CMC values for SDBS IPA suspensions. So this peak is discarded in analysis. The second peak is at 223-224 nm. These peaks were used in quantitative analysis since the absorbance is related to concentration for this peak. There is a third broad and weak peak at 256 nm. Attal et al. observed that peak and stated that this peak does not increase its intensity with increasing concentration. On the other hand we have found that quantitative analysis can be done by using that peak but it is not reliable (it will be explained later). We also observed that with increasing concentration these peaks shift. J. Geng et al. [99] stated that such a shift may be understood in terms of the formation of micelles and the consequent changes in the electrons' locations and distributions within SDBS molecules.

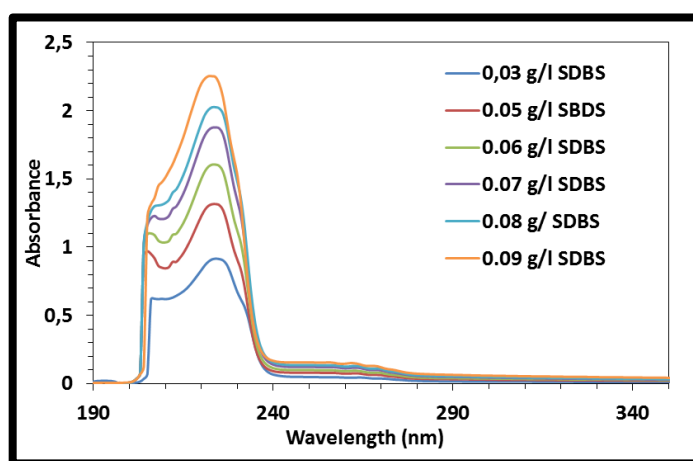


Figure 3.19 UV-Vis spectra of SDBS in IPA at different concentrations.

A calibration curve belonging to SDBS was plotted by using data of absorbance values at 223 nm (Figure 3.20).

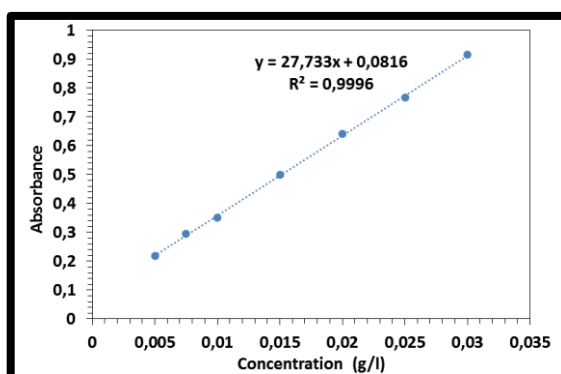


Figure 3.20 Calibration curve of SDBS in IPA. Curve is obtained by using absorbance values at 223 nm for each suspension.

Figure 3.21 shows UV-Vis spectra of same SDBS IPA solutions shown in Figure 3.21. Since 256 nm peak increases its intensity with increasing concentration, it could also be used for quantitative analysis as well. Unlike other peaks vibrational modes of this peak can be clearly seen. In one excited electronic state there is 3 vibrational levels caused by excitation of electrons in benzene rings.

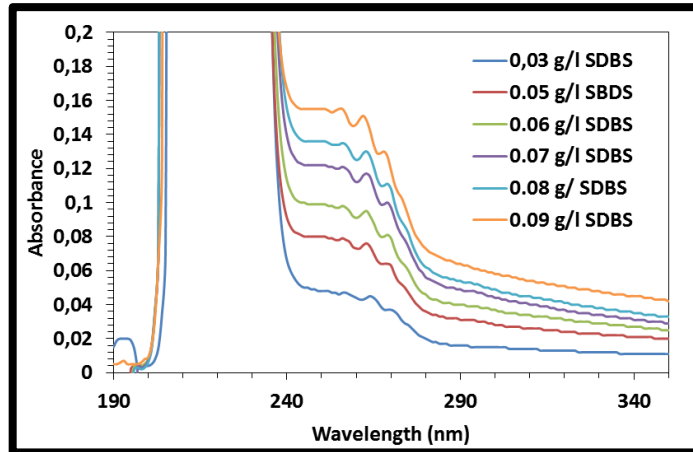


Figure 3.21 UV-Vis spectra of SDBS in different concentrations in IPA.

Calibration curve of 256 nm peak is shown 3.22. Since the R^2 value is indication of the degree of linearity of curves.

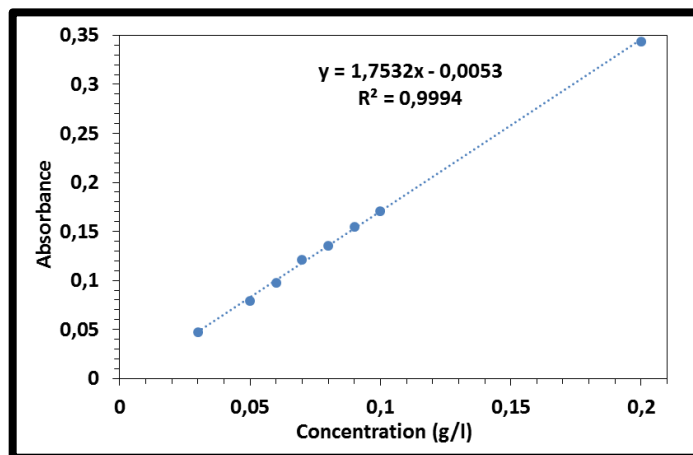


Figure 3.22 Calibration curve of SDBS in IPA. Absorbance values at 256 nm were used. UV-Vis spectra of SDBS and MWCNTs containing suspensions are actually sum of two absorbance spectra, one is belonging to SDBS and the other is belonging to MWCNTs. When trying to find unknown quantities of a particular material, a characteristic peak and a calibration curve for that peak is required. In our case, simple reading the absorbance value of SDBS MWCNTs IPA suspensions' spectrum at 223 nm is not usable, because

MWCNTs contribute to the absorbance of SDBS because of overlap. Figure 3.23 shows UV-Vis spectra of 75 times diluted SDBS MWCNTs IPA suspensions, dilute spectrum of COOH MWCNTs Ipa suspension and the resultant spectrum obtained after subtraction of COOH MWCNTs spectrum from SDBS MWCNTs IPA spectrum. The peak value is used for determination of SDBS concentration. SDBS concentration is found 1.56 g/L. Dilution is important since at relatively low and high concentrations device fails to give reliable results. Trial and error approach was done to assess the best estimate of SDBS concentration by comparing and evaluating results obtained from differently diluted suspensions. 50 times diluted SDBS MWCNTs IPA suspensions end up 1.64 g/L and using 100 times diluted suspensions the resultant SDBS concentration is 1.4 g/L. 50 times diluted and 100 times diluted suspensions give underestimated or overestimated results because concentration obtained from 75 times diluted suspensions match with quantitative analysis results of TG analysis.

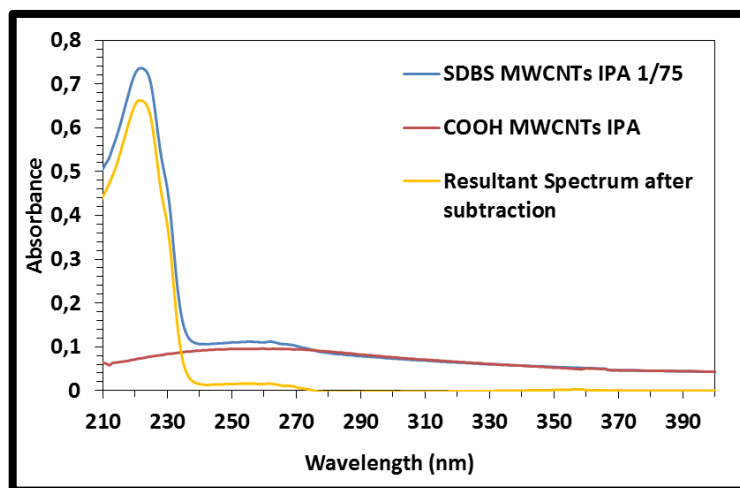


Figure 3.23 UV-Vis spectra of 75 times diluted SDBS MWCNTs IPA and COOH MWCNTs IPA. Third spectrum is extracted by subtracting the two spectra.

We also made quantitative analysis by using 256 nm peak of SDBS. Figure 3.24a shows UV-Vis spectra of 10 times diluted SDBS MWCNTs IPA (blue), COOH MWCNTs Ipa and resultant spectrum after subtraction. Figure 3.24b shows overlapped spectrum of result of subtraction (dashed curve) and SDBS IPA spectra in different concentrations. By using calibration curve SDBS concentration was found 0.76 g/L. Interestingly, 0.76 g/L is a contradictory result but almost half the value (ratio: 0.49) results obtained using peak at 223 nm. The reason for that misleading result is due to an unavoidable experimental fault. SDBS molecules absorbs small amount of UV, visible and infrared light in the spectrum, we normally neglect it but its effect become pronounced in this

application because 256 nm peak is very weak; therefore, neglected absorption due to SDBS is considerably high in this peak region during quantitative analysis. Therefore the result is misleading. This neglected absorbance is reflected in extracted spectrum in Figure 3.24b, namely SDBS molecules normally absorb photons in all wavelengths, but extracted spectrum starts to absorb photons at 280 nm.

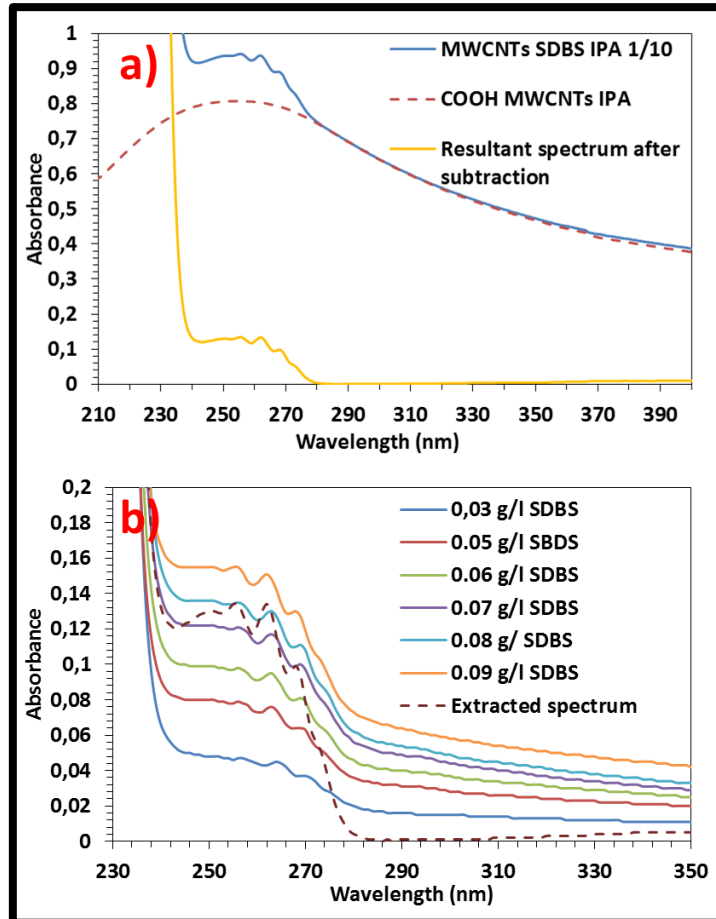


Figure 3.24 (a) UV-Vis spectra of 10 times diluted SDBS MWCNTs IPA and COOH MWCNTs IPA. Green curve is result of subtraction of MWCNTs contribution from SDBS MWCNTs IPA's UV-Vis spectrum. (b) Straight lines are UV-Vis spectra of SDBS IPA and dashed line is extracted spectrum.

MWCNTs concentration is determined by overlapping diluted suspension. Figure 3.25 shows overlapping spectra of suspensions of SDBS MWCNTs IPA. 8 times diluted uncentrifuged suspension spectrum overlaps with 5 times diluted centrifuged suspension. At low concentrations device fails to accurately measure values. This manifest itself as coinciding 25 times diluted centrifuged suspension curve and those of 50 times diluted uncentrifuged suspension. Concentration of MWCNTs is calculated 0.06 g/L.

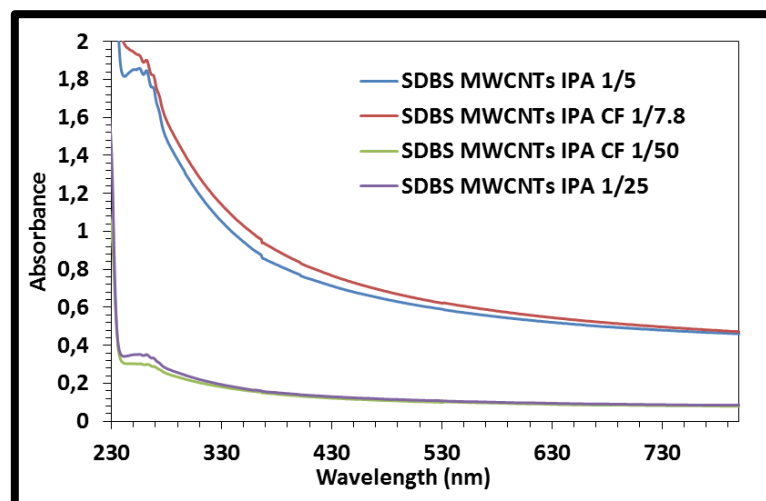


Figure 3.25 Overlapping spectra of SDBS MWCNTs IPA suspensions before and after centrifuge. CF indicates the uncentrifuged suspensions.

3.3.2 TGA measurements

Determination of concentrations of surfactant and MWCNTs was done by calculating the ratio of MWCNTs and SDBS in supernatant and precipitate. Dry weights of supernatant and precipitate were also measured to be used in calculations. Figure 3.26a shows TGA curves of SDBS, supernatant and precipitate. SDBS has a characteristic mass losses at 470 °C and at 750 °C. Since MWCNTs remain almost intact at around 500 °C, one can expect that TGA curve of supernatant should lie at higher TGA values than SDBS. However, in our case supernatant curve is under SDBS curve. The reason for this is different contaminant and moisture contents in SDBS and supernatant. Figure 2.26b shows derivative TGA curves. Different amount of masses leaves the systems and it causes uncomparable curves, we have chosen an almost zero mass loss rate region in curves to set a point to shift TGA curves or to acknowledge this point as onset of mass loss. 275 °C was chosen for shifting curves and 825 °C was chosen to compare remaining mass of the 3 curves.

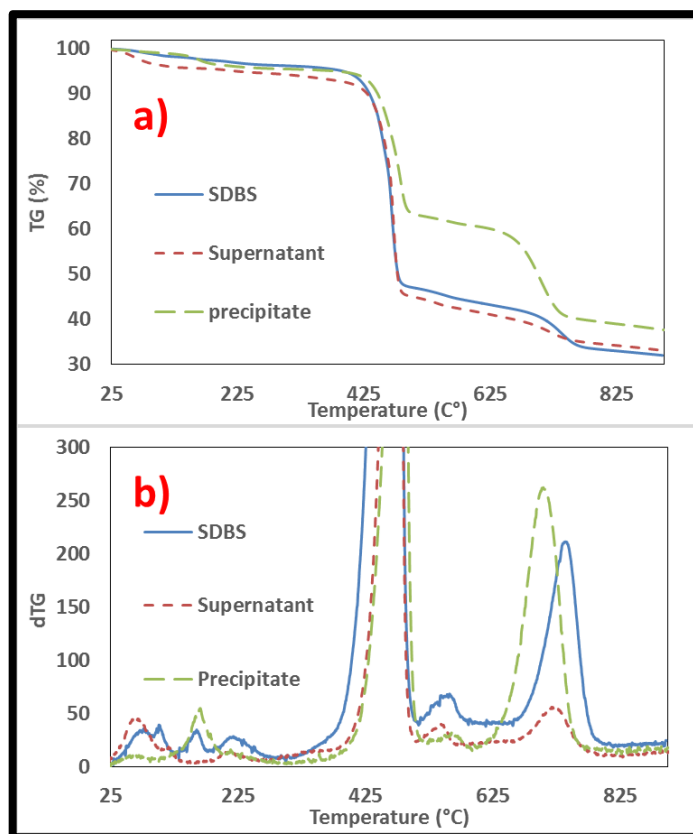


Figure 3.26 (a) TG curves of pure SDBS, dried supernatant of SDBS MWCNTs IPA and dried precipitate of centrifuged SDBS MWCNTs IPA CF obtained in inert atmosphere. (b) First derivative of TGA curves of SDBS, supernatant and precipitate.

Figure 3.27 shows shifted curves of supernatant and precipitate and SDBS (TGA curve of pure SDBS is not shifted). Besides, starting point to mass loss is set to 275 °C.

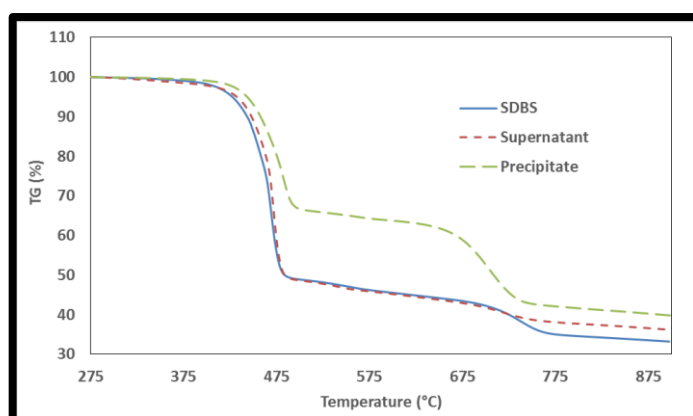


Figure 3.27 Shifted TGA curves of SDBS, supernatant and precipitate. Supernatant and precipitate curves are shifted to overlap with that of SDBS curve at 275 °C and TG value at 275 °C was set as onset of mass loss.

Sequence of calculation of SDBS and MWCNTs concentration using TGA curves is shown in Equations between (3.19) and (3.25)

$$1.71 \text{ g/L is actual dried supernatant concentration} \quad (3.19)$$

$$\text{Dried supernatant} = 1.68007 \text{ g/L} \quad (3.20)$$

This is the obtained value after shifting TGA curve. Because concentration at 275 °C is acknowledged as onset of mass loss. Therefore TGA curve is shifted and it is reflected in the representation of concentration.

$$W_{\text{SDBS}} + W_{\text{MWCNTs}} = 1.68007 \text{ g/L (25 °C)} \quad (3.21)$$

89.5% of nanotubes preserves their integrity at 825 °C (This information is obtained from TGA curves of pristine MWCNTs)

Remaining mass of supernatant at 825 °C:

$$34.21\% W_{\text{SDBS}} + 89.5 W_{\text{MWCNTs}} = 0,627 \text{ g/L (at 825 °C)} \quad (3.22)$$

Subtracting (3.21) from (3.22) eliminates the weight of MWCNTs

$$61.77 \% W_{\text{SDBS}} = 0.979 \text{ g/L} \quad (3.23)$$

$$W_{\text{SDBS}} = \underline{1.585 \text{ g/L}} \quad (3.24)$$

$$W_{\text{MWCNTs}} = 1.68 - 1.585 = \underline{0.094 \text{ g/L}} \quad (3.25)$$

Precipitate was also used to calculate MWCNTs and SDBS content in supernant.

$$0.47 \text{ g/L} = \text{measured concentration of dried precipitate} \quad (3.26)$$

$$W_{\text{SDBS}} + W_{\text{MWCNTs}} = 0.466 \text{ g/L (at 25 °C)} \quad (3.27)$$

Remaining mass of precipitate at 825 °C:

$$34.21\% W_{\text{SDBS}} + 89.5\% W_{\text{MWCNTs}} = 0.191 \text{ g/L} \quad (2.28)$$

Subtracting (3.28) from (3.29) eliminates the weight of MWCNTs:

$$0,274 \text{ g/L} = 65.79 \% W_{\text{SDBS}} \quad (3.29)$$

$$W_{\text{SDBS}} = 0.407 \text{ g/L (in precipitate)} \quad (3.30)$$

$$W_{\text{MWCNTs}} = 0,466 - 0,407 = 0,058 \text{ g/L (in precipitate)} \quad (3.31)$$

Initially suspension contains 2 g/l SDBS and 0.1 g/L MWCNTs.

$$\text{In supernatant } W_{\text{SDBS}} = 1,593 \text{ g/L} \quad (3.32)$$

$$\text{In supernatant } W_{\text{MWCNTs}} = 0,042 \text{ g/L} \quad (3.33)$$

Table 3.3 shows summary of calculated concentrations of MWCNTs and SDBS in supernatant. It is found that calculated SDBS concentrations are close to each other. Results of different measurements are similar: 1.569 g/L for UV-Vis 1.585 g/L and 1.593 g/L for TGA analysis. Average of 3 different results for SDBS concentration is 1.58 g/L. MWCNTs results on the other hand deviates more than SDBS's results. We think that TGA results obtained by using curve of supernatant does not give reliable result because MWCNTs/SDBS ratio in supernatant is very low compared to precipitate leading to a misleading result. There is a big deviation in results in terms of MWCNTs.

Table 3.3 Calculated Concentrations of PVP and MWCNTs in Supernatant by using UV-Vis spectroscopy and TGA analysis

Technique	Used component of technique	Material in supernatant	Concentration in supernatant (g/L)
UV-Vis	Peak at 223 nm	SDBS in supernatant	1.56
UV-Vis	Overlapping suspensions before and after CF*	MWCNTs in supernatant	0.06
TGA	TGA of supernatant and SDBS	SDBS in supernatant	1.58
TGA	TGA of supernatant and SDBS	MWCNTs in supernatant	0.09
TGA	TGA of precipitate and SDBS	SDBS in supernatant	1.59
TGA	TGA of precipitate and SDBS	MWCNTs in supernatant	0.04

*CF denoted suspensions analyzed before centrifugation.

Schematic illustration of interaction between SDBS and MWCNTs in IPA is shown in Figure 3.28. SDBS probably forms hemicylindrical micelles on nanotube surface and provide stabilization. Excess amount of SDBS forms micelles between nanatoubes.

Formation of micelles in semi-polar or non-polar solvents by SDBS molecules is actually controversial. Because intensive DLS particle size measurements does not give reliable results to confirm that micelles are present. Obviously particles can be detected in SDBS-IPA suspensions by DLS, but we actually attribute this particles to contaminants surrounded by SDBS molecules.

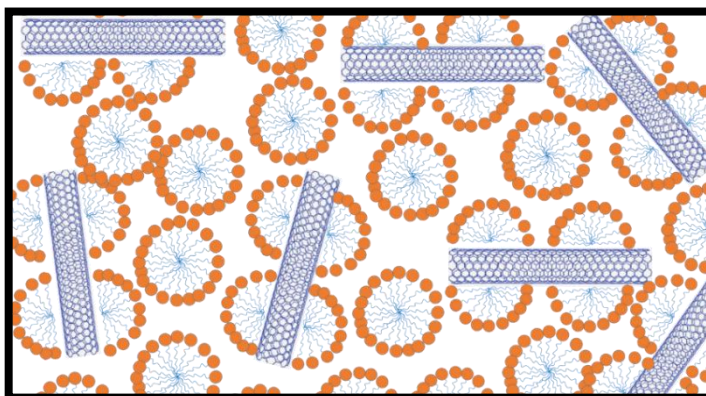


Figure 3.28 Illustration of possible distribution of SDBS molecules and nanotubes in suspension.

Zeta potential values for suspensions are shown in Table 3.4. SDBS MWCNTs IPA suspension has a +44.6 mV zeta potential value. Before centrifugation process suspension stability was also assessed. The zeta potential value of suspensions of SDBS MWCNTs IPA before centrifugation is +54.4 mV. Compared to centrifuged suspensions uncentrifuged suspensions have 10 mV higher zeta potential. The reason behind this difference is because of higher amount of surfactant present in suspensions before centrifuge. We also found that if initial concentration of MWCNTs was increased to 0.2 g/L and after ultrasonication/centrifugation, the resultant supernatant has higher zeta potential value compared to initially 0.1 g/L MWCNTs containing suspension. We also investigated the zeta potential values of SDBS-IPA suspensions. Only 0.5 g/L SDBS containing suspension show a zeta potential of +55.3 mV.

Table 3.4 Zeta potentials of SDBS containing suspensions.

Material	Zeta potential (mV) (Huckel's approximation)	Zeta potential (mV) (Smoluchowski's approximation)
SDBS MWCNTs IPA	+44.6	29.6
SDBS MWCNTs IPA CF*	+54.4	35.5
SDBS 0.2MWCNTs IPA**	+53.3	33.2
0.5 g/L SDBS IPA ***	+55.3	34.6

*CF denotes suspensions which are not centrifuged.

** Initially 0.2 g/L MWCNTs and 2 g/l SDBS containing centrifuged suspension.

*** 0.5 g/L SDBS containing IPA solution.

Figure 3.29 shows zeta potential distribution curves of suspensions. Figure 3.29a shows distribution curves obtained using Huckel's approximation and Figure 3.29b shows distribution curves obtained using Smoluchowski's approximation. Huckel's approximation give rise to wider zeta potential distribution compared to Smoluchowski's. Distribution curves are all broad. The reason for that is because of shape of nanoparticles. MWCNTs are high aspect ratio molecules. Only SDBS containing suspensions also shows broad zeta potential distribution. This may be giving a hint about shape and length of micelles. SDBS micelles are thought have high aspect ratio rather than having spherical shape.

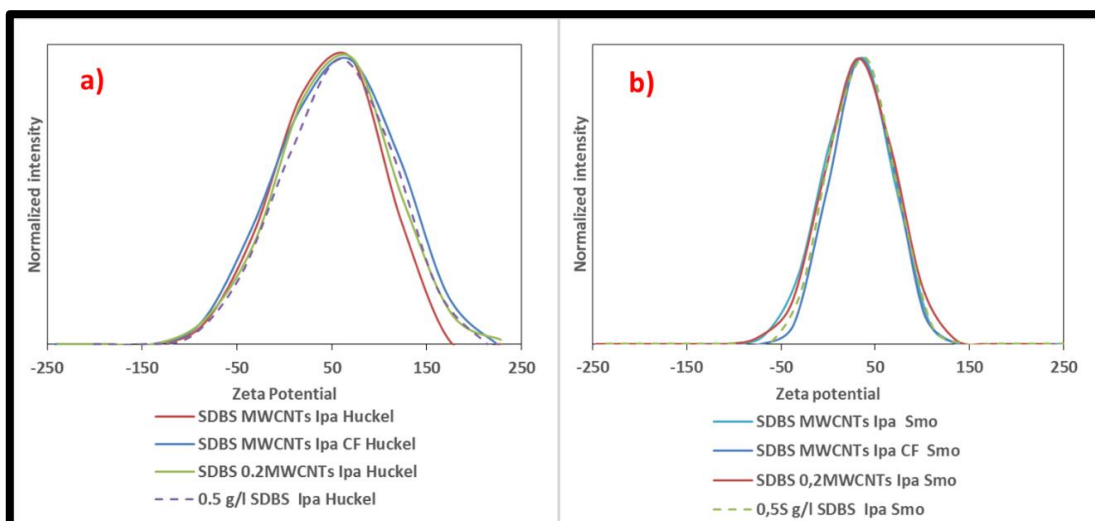


Figure 3.29 Zeta potential distribution curves of suspensions. (a) contains curves obtained by using Huckel's approximation and (b) contains curves obtained by using Smoluchowski's approximation. ("Smo" is abbreviation for Smoluchowski's approximation)

Figure 3.30a shows coating obtained using EPD out of SDBS MWCNTs IPA suspension. Figure 3.30b shows images of coatings obtained by using different suspensions. From left to right the solvents used in electrophoretic suspensions are IPA, butanol, amyl alcohol and acetyl acetone. Process and preparation parameters are the same for all coatings. The thickest coatings obtained from acetyl acetonic suspensions.

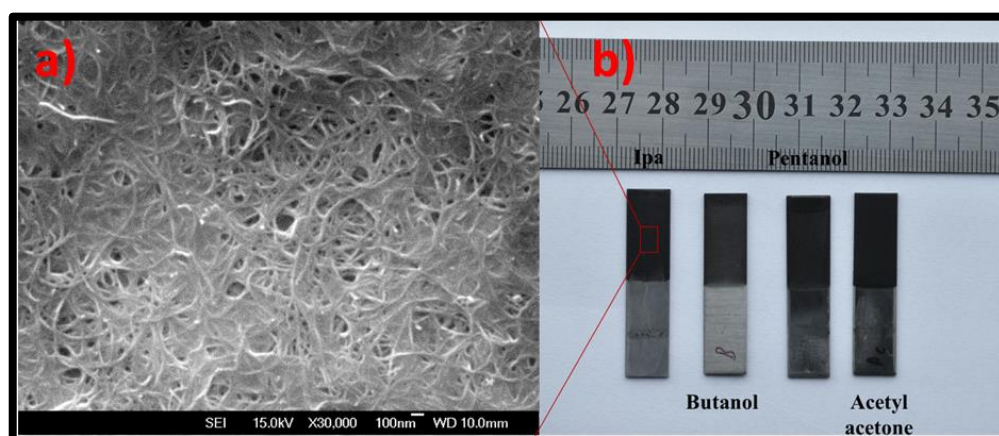


Figure 3.30 SEM image of coating obtained by means of EPD of SDBS MWCNTs IPA (a). (b) contains examples of MWCNTs coatings from suspensions prepared with different solvents.

3.4 Results

1. Stable suspensions of MWCNTs were prepared by using PVP and SDBS in organic solvents. Ethanol does not provide stability when using SDBS as dispersant.
2. UV-Vis absorption spectroscopy was used to determine polymer dispersant and MWCNTs concentration in centrifuged suspensions.
3. UV-Vis analysis give slightly underestimated results in terms of MWCNTs concentration compared to TG analysis results.
4. PVP molecules provide negative surface charge to MWCNTs probably due to localization of electrons on carbonyl oxygen.
5. Zeta potential distribution curves of MWCNTs suspensions are broad due to high aspect ratio of MWCNTs.
6. EPD of PVP MWCNTs IPA suspensions is not possible without a modification. Because MWCNTs does not adhere to substrates. Presence of Mg^{2+} ions was found to provide adhesion of MWCNTs on substrate surfaces.
7. 10 min. coating of $MgCl_2$ added PVP MWCNTs IPA suspensions has smooth surface. On the other hand 20 min. deposition end up with a rough surface (50V DC potential difference, 1.5 mm electrode separation.).
8. UV-Vis spectroscopy was found to be useful in calculating MWCNTs and PVP concentration in coatings.
9. By evaluating density values of MWCNTs and PVP, and concentration values of the components obtained by UV-Vis analysis, it was possible to estimate coating thickness.
10. SEM images of cross-section of 20 min. deposited coating revealed that thickness of the coating is around twice the estimated value. Because estimation neglects porosity in coatings.

NANOPARTICLE AND NANOCOMPOSITE SYNTHESIS

Solvothermal synthesis was used to produce iron oxide nanocrystals. Different approaches were tried. We have both synthesized pure iron oxide nanoparticles and hybrids of iron oxide and carbon nanotubes. In initial experiments hydrazine hydride was used to synthesis iron oxide nano crystals and carbon nanotube iron oxide hybrids, but in latter experiments hydrazine was discarded for several reasons; one is the high toxicity of hydrazine and the second is unsuitability of hydrazine since it causes aggregation of MWCNTs.

Literature information gives a clue about which route to follow to synthesis nanoparticles and at the same time provide interaction between carbon nanotubes and nanoparticles being synthesized in solvothermal environments. If carbon nanotubes are functionalized with functional groups such as carboxylic acid groups, monomers attach and crystallize on the functional groups on nanotubes. However functionalization is a tedious, time consuming process and most importantly pristine nanotubes can't preserve their integrity after functionalization. Thus, in our experiments we searched for ways to produce carbon nanotube-iron oxide hybrid materials by using pristine nanotubes. We investigated the effect of carbon coating on iron oxide nanoparticles on producing iron oxide carbon nanotube hybrid nanomaterials. At the same time we have used two dispersants to try to enable the crystallization process. Especially PVP seemed promising since it has a carbonyl group on its aromatic ring. This aromatic ring is stacked upon the surface of nanotubes therefore we assume that crystallization process may take place on nanotube surface.

EG and IPA mixture was used as a solvent in synthesis process. IPA is chosen because it is successful to disperse MWCNTs with the aid of dispersants. IPA is a low polarity solvent, as a result of this, solubility of chemicals such as ascorbic acid, iron sulfate and other ionic or polar compounds is limited or negligibly low. Therefore, EG is selected to assist the synthesis for its miscibility in IPA and it also can dissolve ascorbic acid and iron sulfate. The second reason for

choosing EG is its high reducing ability. In EG, Fe^{2+} ions stay reduced for long periods of time (oxidation state of iron in FeSO_4 is only 2^+).

During solvothermal synthesis FeSO_4 is dissociated and form $\text{Fe}(\text{OH})_2$. If the liquid environment contain dissolved oxygen then, evolved Fe^{2+} ions oxidize to form Fe^{3+} and consequently, $\text{Fe}(\text{OH})_3$ emerges in time. We have avoided evolution of $\text{Fe}(\text{OH})_3$ since it cannot convert into Fe_3O_4 without addition of extra materials like ammonium acetate. To keep the system as simple as possible to do not disturb the dispersion state of nanotubes we have avoided addition of extra material in synthesis mixtures. Synthesis in our study occurs by reaction of iron salt with NaOH and the evolved iron hydroxides transform into iron oxide during heat treatment.

Fe_3O_4 requires molar ratio of $\text{Fe}^{2+}:\text{Fe}^{3+} = 1:2$. Under inert atmosphere, the reaction taking place is shown in (4.1) and (4.2). The conversion of $\text{Fe}(\text{OH})_2$ to Fe_3O_4 under anaerobic conditions is called Schikorr reaction [100]:



4.1 Solvothermal Synthesis Of Iron Oxide Nanocrystals

4.1.1 Solvothermal Synthesis of Fe_3O_4

Figure 4.1 shows images soon after (5th min. of mixing) (a) and 15 min. after (b) mixing $\text{FeSO}_4 \cdot 7\text{H}_2\text{O}$ (solution in EG), NaOH (solution in EG) in IPA during nitrogen gas bubbling. Just after addition of $\text{FeSO}_4 \cdot 7\text{H}_2\text{O}$, solution becomes dark green, confirming evolution of $\text{Fe}(\text{OH})_2$. As time passes green color transforms into brown during nitrogen bubbling continues. It is believed that the change in color is result of gradual removal of oxygen from the system. Traces of oxygen may impart a greenish color to $\text{Fe}(\text{OH})_2$.

During filtration process after synthesis of iron oxide nanoparticles, magnetic separation was implemented to remove impurities. Synthesized products (particles) precipitate in time clustering at the bottom by moving through the magnet. After magnetic separation of synthesized suspension containing nanoparticles, solution of the suspension is transparent and yellowish in color. Solution probably contains sodium hydroxide, water and sodium sulfate in its structure, this combination give fair yellowish color to the solution. After synthesis with aid

of ascorbic acid and glucose, the color of solution becomes dark red. This may be result of aromatic and polymeric compounds.

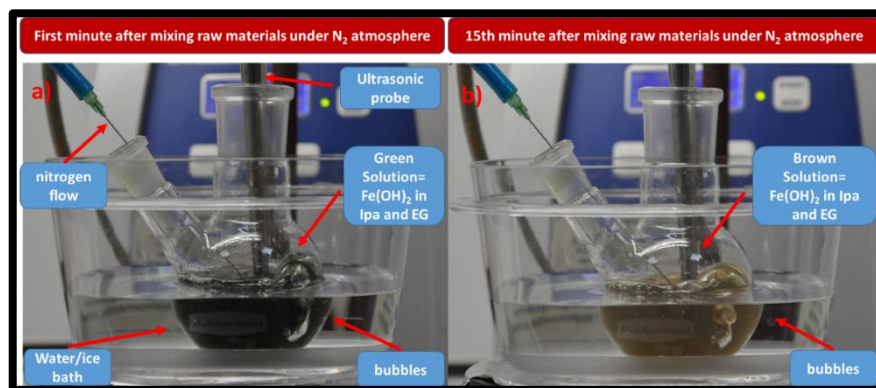


Figure 4.1 (a) is the image taken just after mixing $\text{FeSO}_4 \cdot 7\text{H}_2\text{O}$ and NaOH (both are dispersed in EG prior to mixing) and (b) is image taken 10 minutes after complete mixing of all raw materials. Dark green color transformed into brown in time during nitrogen bubbling and ultrasonication.

Figure 4.2 shows SEM images of synthesized iron oxide nanocrystals. All images are secondary electron SEM micrographs. Figure 4.2a and b were taken at 30kx magnification and Figure 4.2c and d were taken at magnifications of 100kx and 150kx, respectively. The crystals formed have octahedral geometry. Morphology can be clearly seen in Figure 4.2c and d. According to Wulff's argument, during crystal growth crystallographic shapes are determined by growth rate of different facets. Different facets have different surface energies. Particles are covered by facets that have the lowest surface energy. Octahedra is favored for face centered cubic crystal structure (Fe_3O_4 , $\gamma\text{-Fe}_2\text{O}_3$) with a (111) planes surrounding the surface [36]. It should be noted that under equilibrium conditions this theorem works where thermodynamics takes over [37]. Smaller particles seem irregular in shape, a typical example is shown in Figure 4.2c as shown in red circle. Diameter of this particle is 140nm and it is almost spherical. Big particles on the other hand are in the shape of octahedrons, in Figure 4.2d red arrow indicates an example of an octahedral particle having 348nm diagonal length. Length distribution of nanoparticles is not homogenous. There are nanoparticles having diameters as low as ~50 nm and as high as 550 nm. Mean particle diameter is 175 nm.

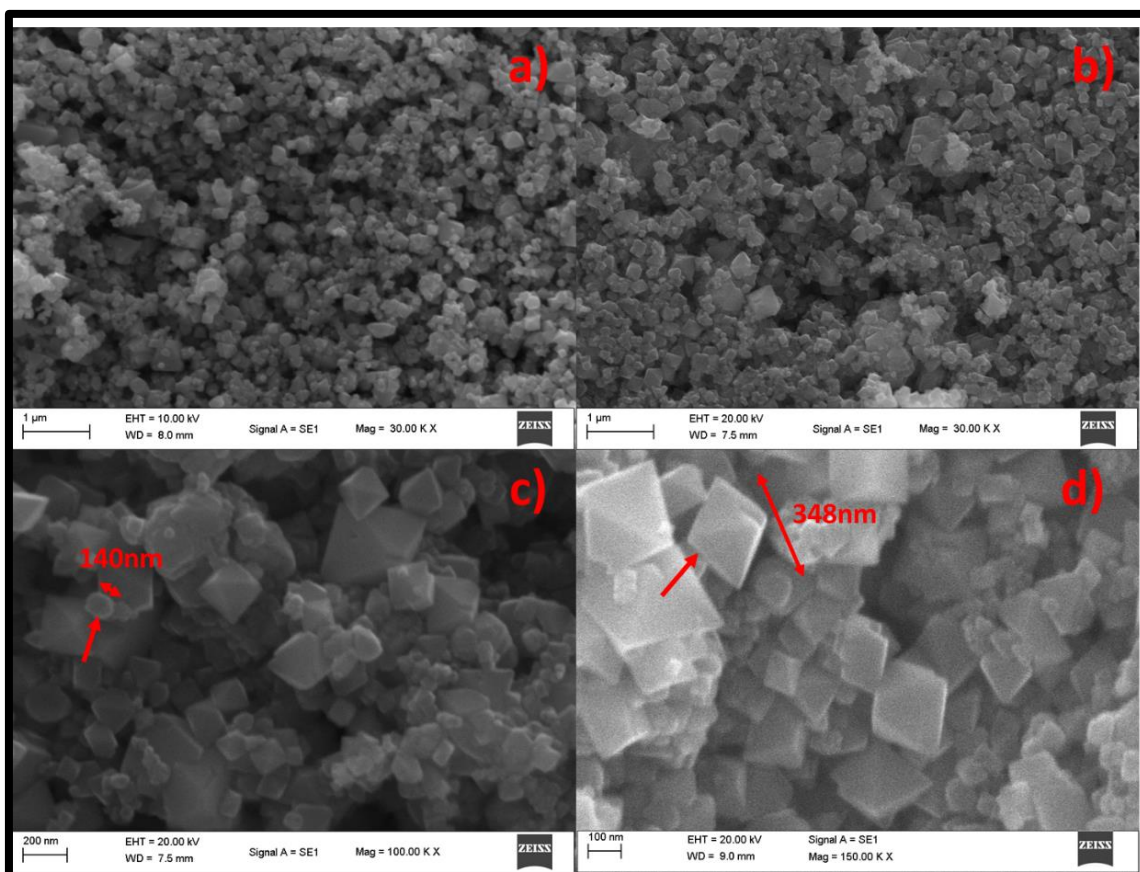


Figure 4.2 SEM images of Fe_3O_4 nanoparticles synthesized without using an additive at 200°C for 12h. from FeSO_4 and NaOH in organic solvents (IPA-EG mixture); (a), (b), (c) and (d) are all micrographs of Fe_3O_4 , arrow in (c) represents a relatively small spherical particle and arrow in (d) is indicating one example of a big octahedron shape particle.

Fe_3O_4 is magnetic, during removal of impurities from the synthesized mixture, decantation with magnets gives a clue about the structure of iron oxide: products respond to magnet. XRD graph of Fe_3O_4 is performed to assess the crystal structure of synthesized iron oxide (Figure 4.3). The peaks at 2 theta degrees of 30° (220), 35° (311), 43° (400), 56° (511) and 62° (440) corresponds to Fe_3O_4 .

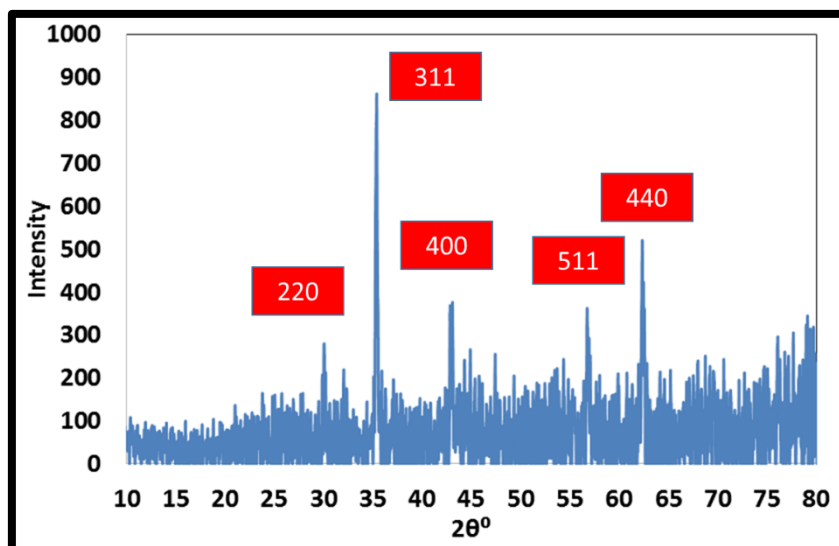


Figure 4.3 XRD graph of Fe_3O_4 .

FTIR analysis was also implemented on Fe_3O_4 nanoparticles. Figure 4.4 shows FTIR analysis of Fe_3O_4 nanocrystals. The nature of ATR (Diamond/Zinc selenide) used limits the detectability of functional group present. Namely, Fe-O bond is expected to present at around 590cm^{-1} . Zinc selenide ATR cannot read frequencies lower than 650cm^{-1} . Besides, Synthesized Fe_3O_4 black, dark grey in color, this coloration absorbs most of the photons and creates difficulty on assessment of functional groups of black samples. Therefore, it is a featureless spectrum. To make a comparison between ascorbic acid and glucose aided synthesis products, This IR spectrum is presented to exhibit the change in IR absorption of pure Fe_3O_4 and $\text{Fe}_3\text{O}_4@\text{C}$ products.

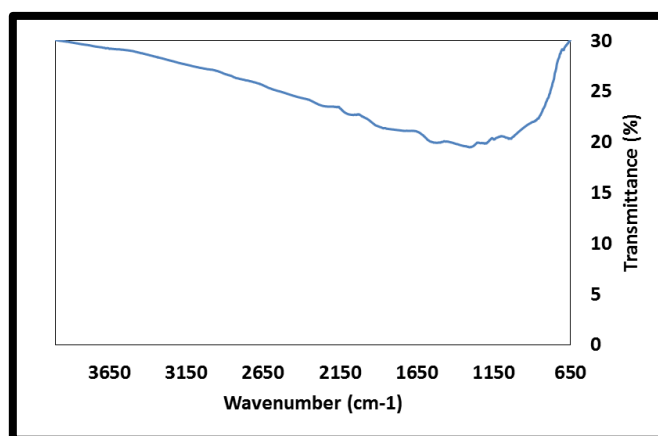


Figure 4.4 FTIR spectrum of Fe_3O_4 .

Surface properties of synthesized products were also investigated whether to determine there is porosity present or not. Volumetric gas absorption desorption isotherm results is shown in Figure 4.5a. The isotherm is a typical type 2 isotherm (a typical isotherm shape of nonporous material).

Desorption isotherm is shown in red. Figure 4.5b is BET plot of Fe_3O_4 , extracted from the isotherm above it. Specific surface area of Fe_3O_4 is 10.7 g/m^2 . Specific surface area of iron oxide is low because it is composed of relatively large particles and does not contain pores on crystal surfaces as shown in SEM images.

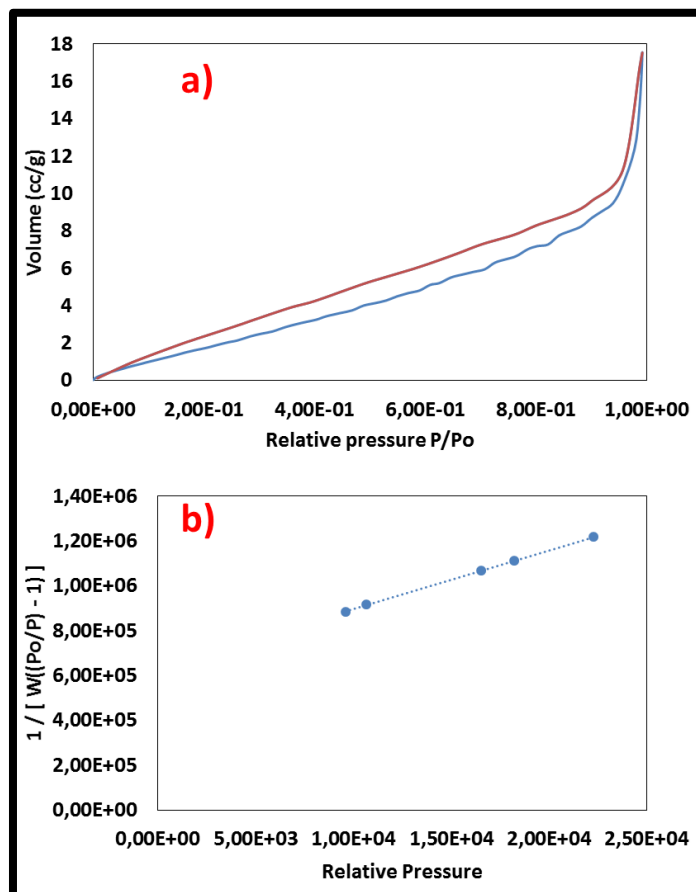


Figure 4.5 (a) Volumetric gas absorption, desorption isotherm of Fe_3O_4 , (b) BET plot of Fe_3O_4 (10.7 g/m^2).

4.1.2 Ascorbic Acid Assisted Solvothermal Synthesis of Fe_3O_4

Ascorbic acid is an excellent one electron reducing agent, it can reduce ferric (Fe^{3+}) ion into ferrous (Fe^{2+}) ion [101] and hence can be used to synthesis Fe_3O_4 . Besides, ascorbic acid used as a coating agent or additive in several wet chemical processes [102], [103]. In our experiments ascorbic acid is first dissolved in EG, then it is injected in NaOH and FeSO_4 containing IPA-EG mixture. 3 distinct experiments were carried out. Each time different amount of ascorbic acid was added to the solution, they were synthesized and characterized. The mole ratios between iron sulfate and ascorbic acid are 0.625, 1.25 and 5 in each three different experiments.

4.1.2.1 Ascorbic Acid Assisted Synthesis ($\text{FeSO}_4/\text{Ascorbic Acid Mole Ratio}=5$)

SEM images of synthesized products are shown in Figure 4.6 at different magnifications. Figure 4.6a, b and c are secondary electron SEM images. Figure 4.6c is backscattered electron image. Octahedron shape is partially preserved in crystals. There are also particles having spherical morphology. Mean particle size is 310 nm. Small particles possessing diameters as low as 90 nm and big ones having more than 600 nm in length are present in synthesized product. It seems that compared to pure Fe_3O_4 , ascorbic acid addition increased the particle size. There is another aspect needs to be mentioned. In Figure 4.6c and d red arrows indicate grooves on nanoparticle surfaces. This is believed to be result of chemical interaction between ascorbic acid or remnants of ascorbic acid with crystallized iron oxide nanoparticles.

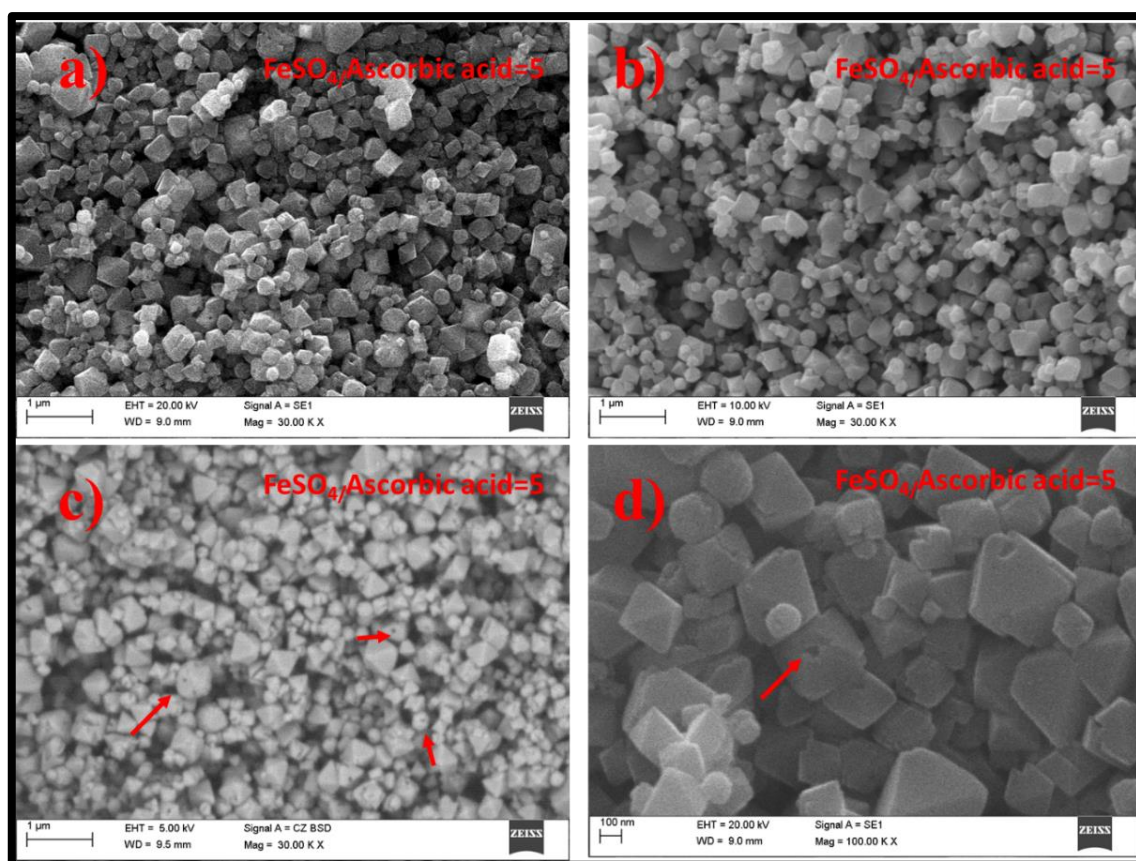


Figure 4.6 (a), (b) and (d) are SE SEM images of Fe_3O_4 nanocrystals. (c) is BSE image ($\text{FeSO}_4/\text{Ascorbic acid}$ mole ratio =5). Arrows indicate grooves on nanoparticle surfaces.

Figure 4.7 shows additional SEM images of synthesis products. Figure 4.7a and b contains typical product particle morphology. As in the case of pure iron oxide, there are particle having undistorted octahedral shape, on the other hand some particles have distorted octahedral shape. Besides, spherical shape particles are also present. Surface of spherical particles are not smooth as in the case of octahedral particles, because they are composed of smaller spherical particles

(This will be discussed later). Figure 4.7c contains a typical distorted octahedron, as mentioned above this is due to the presence of ascorbic acid. Since the amount of ascorbic acid is not enough such distortion or spherical shape evolution aren't reflected in all particles. Figure 4.7d shows an example of irregular shape large particle. Figure 4.7e and f shows mentioned spherical superparticles along with octahedrons.

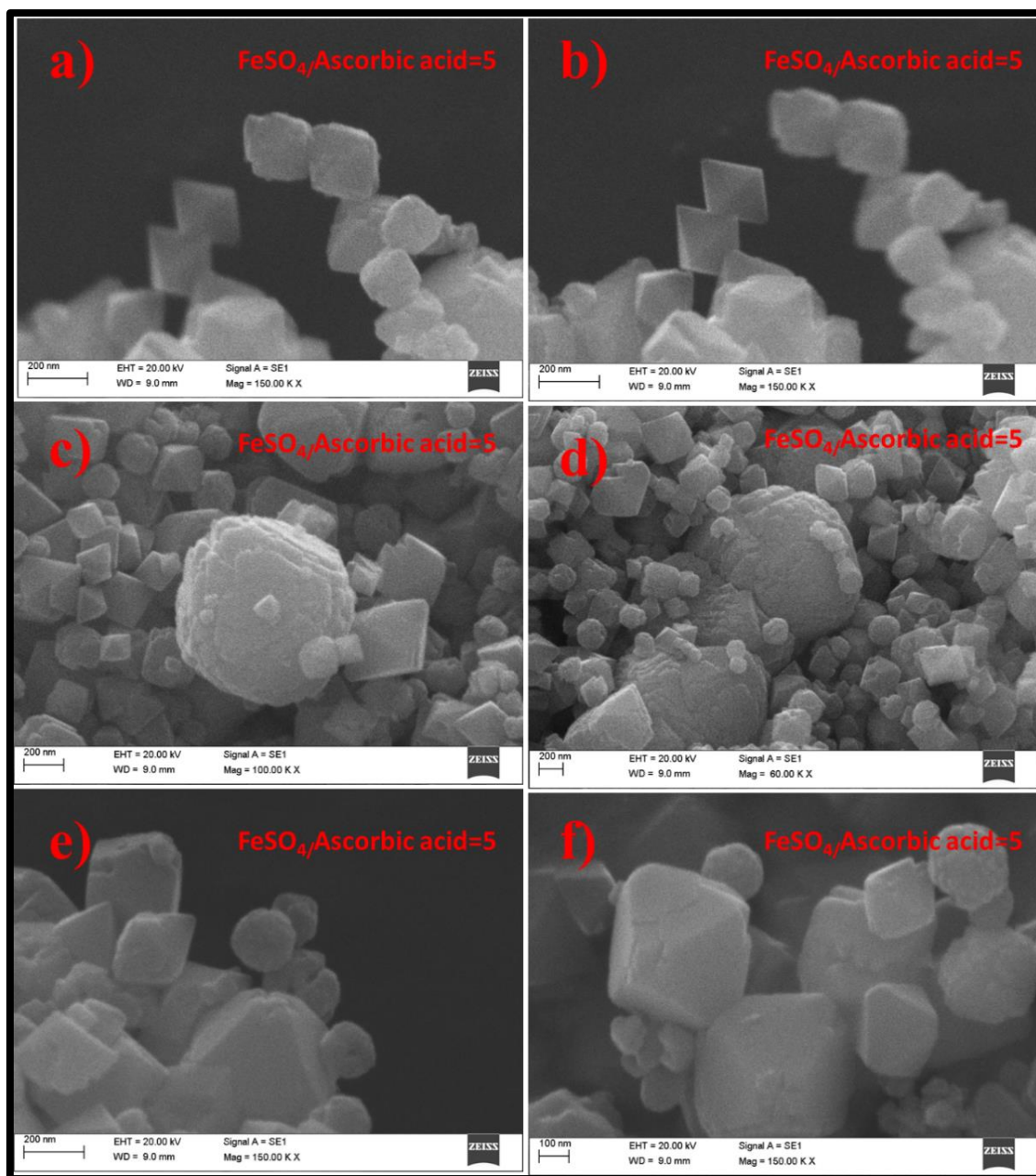


Figure 4.7 (a),(b), (c) and (d) are SEM images of Fe_3O_4 nanocrystals ($\text{FeSO}_4/\text{Ascorbic acid}$ mole ratio =5). Particles have octahedral, spherical or distorted octahedral morphology.

4.1.2.2 Ascorbic Acid Assisted Synthesis (FeSO₄/Ascorbic Acid Mole Ratio =1, 25)

Increasing ascorbic acid content in synthesis mixture profoundly affects product morphology and size. Figure 4.8a to Figure 4.8f are SEM images of synthesized products having 1, 25 FeSO₄ and Ascorbic acid mole ratio. Particles are composed of smaller nanoparticles (Figure 4.6c and e). There are particles having diameter of as low as 120 nm and as high as 2 μm. Mean particle diameter is 480 nm. Literature gives examples of this kind of superparticles obtained by addition of glucose or other organic molecules. Under high temperature conditions ascorbic acid decompose to give molecules of lower molecular weight and sp² hybridized carbon. Carbon can crystallize and form a carbon shell on iron oxide surface. Figure 4.6f is backscattered electron image performed to assess whether there is a coating on the surface, but the images does not give any clue about the presence of carbon on the surface of nanoparticles. The reason behind not seeing an elemental contrast in backscattered electron images is: the carbon shell may be very thin (few nanometers in diameter).

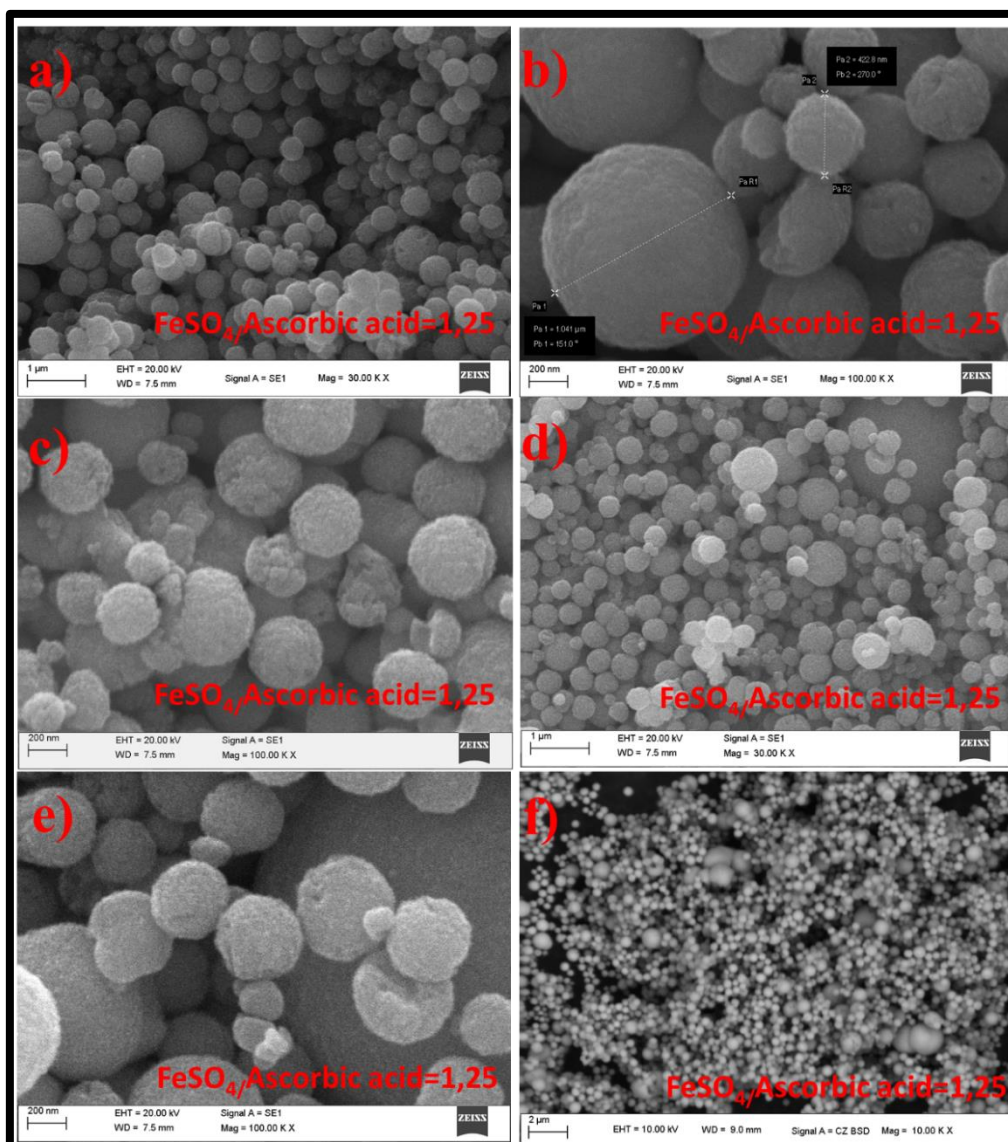


Figure 4.8 SEM images of ascorbic acid assisted synthesis result of Fe_3O_4 nanoparticles ($\text{FeSO}_4/\text{Ascorbic acid}$ mole ratio =5). From (a) to (e) images are SE images, (f) is a BSE image.

XRD analysis of products is shown in Figure 4.9. Though signal to noise ratio is low, it can be deduced that the product corresponding to Fe_3O_4 since indexed (311), (511) and (400) planes are corresponding to Fe_3O_4 . The low signal to noise ratio is probably because of amorphous carbon present in the structure.

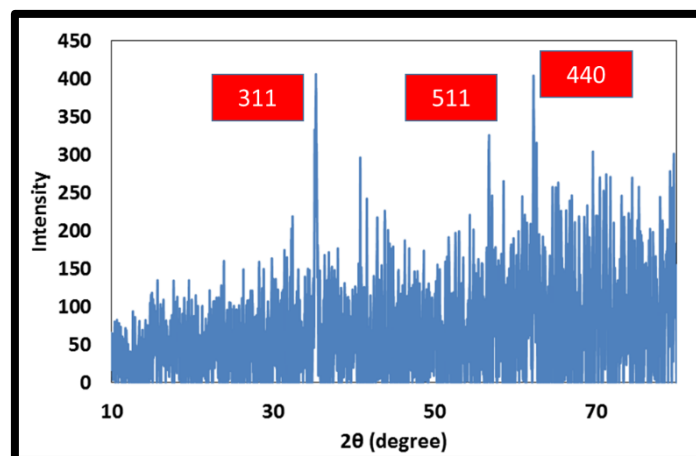


Figure 4.9 XRD graph of synthesized Fe_3O_4 ($\text{FeSO}_4/\text{Ascorbic acid}$ mole ratio = 1.25). Note that signal to noise ratio is decreased compared to pure Fe_3O_4 because of amorphous carbon in the structure.

Since XRD analysis does not give any clue about presence of phases other than Fe_3O_4 . FTIR analysis were performed as well.

Ascorbic acid assisted synthesis products show different coloration and it is a time dependent. Namely, newly synthesized and purified ascorbic acid assisted synthesized Fe_3O_4 nanocrystals has the same color as pure Fe_3O_4 , but in time, they transform into a substance having dark reddish color. Oxidation of Fe_3O_4 may cause Fe_3O_4 to hematite transformation. Red color is distinctive amongst iron oxide since $\alpha\text{-Fe}_2\text{O}_3$ is red. XRD analysis revealed that Fe_3O_4 present in synthesized red powder and in addition, the products show magnetic response. If there had been a partial transformation to hematite, it couldn't have been detected by methods used. But there is an aspect needs to be considered. Ascorbic acid partially decompose at high temperatures and remnants of it cover the surface of nanoparticles. Besides, residues of ascorbic acid on the surface of particles may make an unknown reaction to make the material appear reddish. More analysis needs to be done.

FTIR spectrum of ascorbic acid assisted synthesized product is shown in Figure 4.10. Top spectrum is aged red colored powder and the spectrum at the bottom is the same material analyzed immediately after synthesis. There is no difference in terms of IR absorption since they exhibit same absorption peaks.

Fe-O stretching vibration band emerges around 570 cm^{-1} . Unfortunately, the range of FTIR cannot reach that frequency. Broad and relatively intense band at 1598 cm^{-1} corresponds to C=C stretching vibration in aromatic rings [104]. Presence of this peak is a proof of presence of carbon in the structure. Carbon layers may present on the iron oxide surface composed of

stitched benzene rings (aromatic groups) as carbon nanotubes. The peak at 1371 cm^{-1} may correspond to O-H bending vibration [105] since carbon coating may have large amount of functional groups on its surface. The peak at 1371 cm^{-1} may also correspond to C-OH stretching vibration [105]. The band at around 1050 cm^{-1} can be attributed to C-O groups [106]. Samples degassed at $60\text{ }^{\circ}\text{C}$ for 18 h. (prior to BET analysis) in a degasser, were also investigated in FTIR. Degassed samples also show same peaks of samples characterized before degassing. Therefore, the hydroxyl groups present on materials can be considered not physically absorbed water.

Weak bands at 2900s cm^{-1} and 2800s cm^{-1} is due to the stretching vibration of C-H bond (containing sp^3 hybridized carbon). Presence of this group may mean that ascorbic acid may not totally transformed into carbon. Remnants of it probably contain sp^3 hybridized carbon. Sreeja et al. [102] also used ascorbic acid during synthesis of iron oxide. Synthesis technique of Sreeja et al. is slightly different from that of us since they coat iron oxide with ascorbic acid and derivatives at mild temperatures ($90\text{ }^{\circ}\text{C}$). Therefore, ascorbic acid preserved its integrity. The importing thing in their finds is: after synthesis C=C and C=O bands of ascorbic acid shifted to lower values in synthesized products. They attribute this to chemical binding of functional groups on iron oxide surface [102]. We have also encountered that shift. IR peak of C=C bond in ascorbic acid is around 1655 cm^{-1} (Spectrum of ascorbic acid is not shown), on the other hand synthesised products have C=C vibration mode at lower frequencies (1598 cm^{-1}). We can conclude that carboneaceous species may have binded to the surface of iron oxide nanoparticles after synthesis thus they have formed shell like structures on iron oxide nanocrystals.

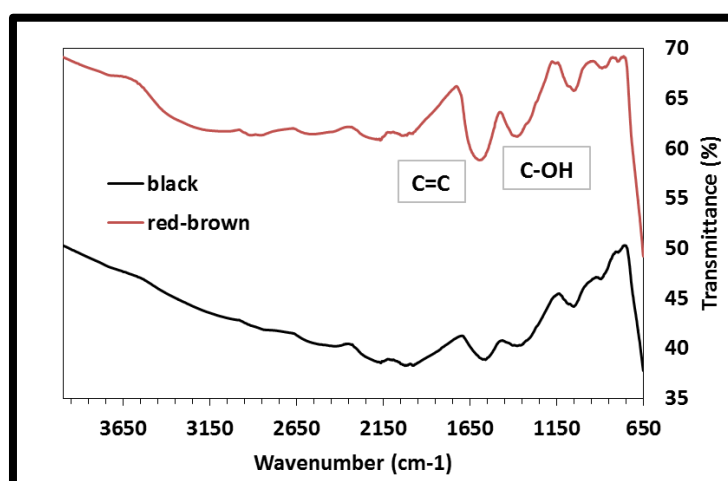


Figure 4.10 FTIR spectrum of ascorbic acid assisted synthesis product ($\text{FeSO}_4/\text{Ascorbic acid}$ mole ratio =1.25). Top spectrum belongs to waited powder in air having red-brown color and spectrum at the bottom is that of powder measured immediately after synthesis.

Adsorption desorption isotherm and corresponding BET analysis of coated samples is shown in Figure 4.11. Adsorption isotherm is typical type II non-porous material. BET analysis revealed that there is no significant change in surface area over Fe₃O₄. Specific surface area of sample is 16.735 m²/g.

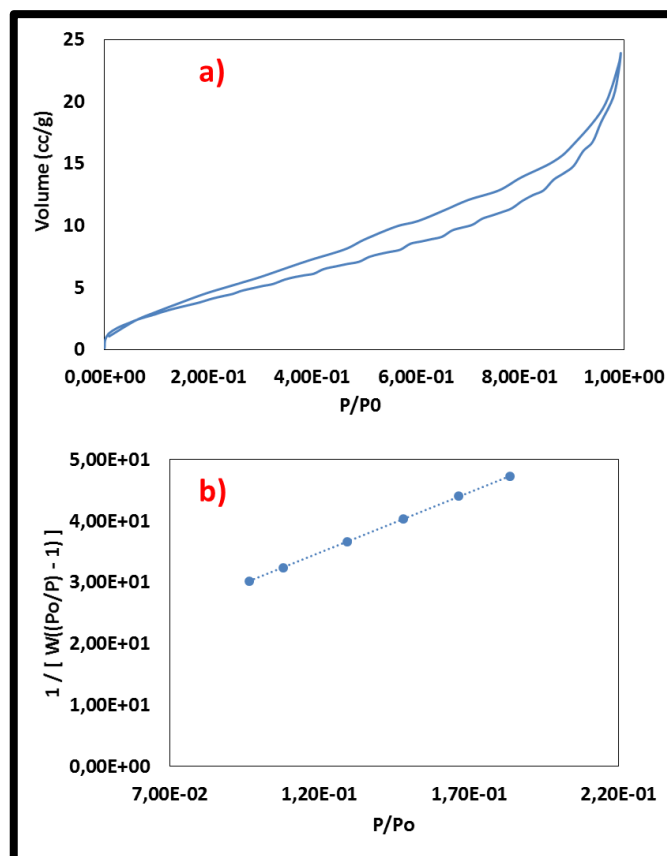


Figure 4.11 (a) is Adsorption-desorption isotherm of Fe₃O₄ samples and (b) is BET graph of Fe₃O₄ (FeSO₄/Ascorbic acid mole ratio =1.25) (16.735 m²/g).

An example of magnetic response of synthesized materials in distilled water is shown in Figure 4.10a and b. Suspension is prepared and shaken, immediately after placing on magnet, all nanoparticles settled down. Figure 4.12c and d shows butanolic suspension on the left and on the right side there is aqueous suspension of particles synthesized with aid of ascorbic acid. After resting for a considerably small period of time, it is revealed that suspensions are not stable (4.10d). We conducted this experiments to understand whether the suspensions of this synthesized particles are suitable for EPD or not without an addition of a dispersant. Figure 4.12e clearly shows red-brown color of synthesized iron oxide nanoparticles (with the aid of ascorbic acid) in suspension.

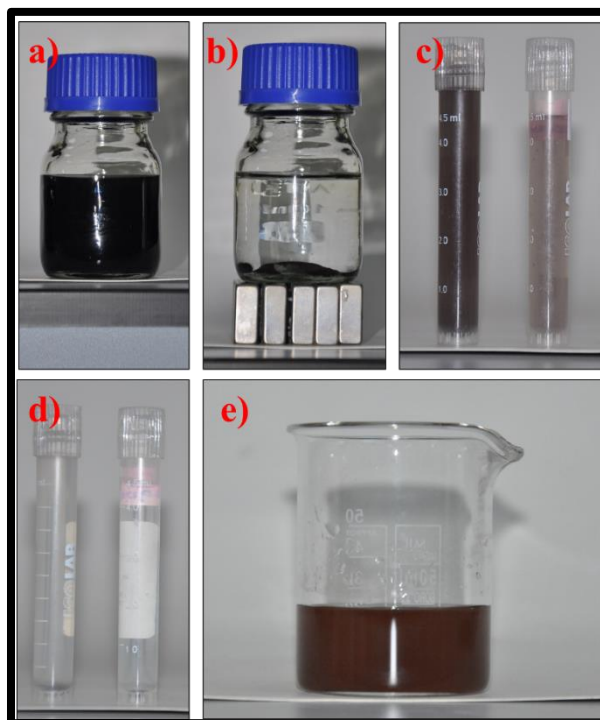


Figure 4.12 Suspensions of iron oxide nanoparticles ($\text{FeSO}_4/\text{Ascorbic acid}$ mole ratio =1.25): (a) and (b) are before and after magnetic separation of aqueous suspension, respectively. (c) contains butanolic and aqueous Fe_3O_4 suspensions after ultrasonication, (d) contains same suspensions in (c) after rest for some time, (e) is a suspension containing same Fe_3O_4 nanoparticles revealing their color.

4.1.2.3 Ascorbic Acid Assisted Synthesis ($\text{FeSO}_4/\text{Ascorbic Acid}$ Mole Ratio =0.625)

SEM images of synthesized samples are present in Figure 4.13a, b, c and d. Particle size of samples is ranging from around 130 nm to 850 nm. Mean particle diameter is 590 nm. Particle size gradually increase with increasing ascorbic acid content. Particles have spherical morphology. Surface of particles is not smooth. This is arising because they are composed of smaller nanoparticles. As in the case previously explained sample synthesized containing half amount of ascorbic acid, synthesized products are black initially.

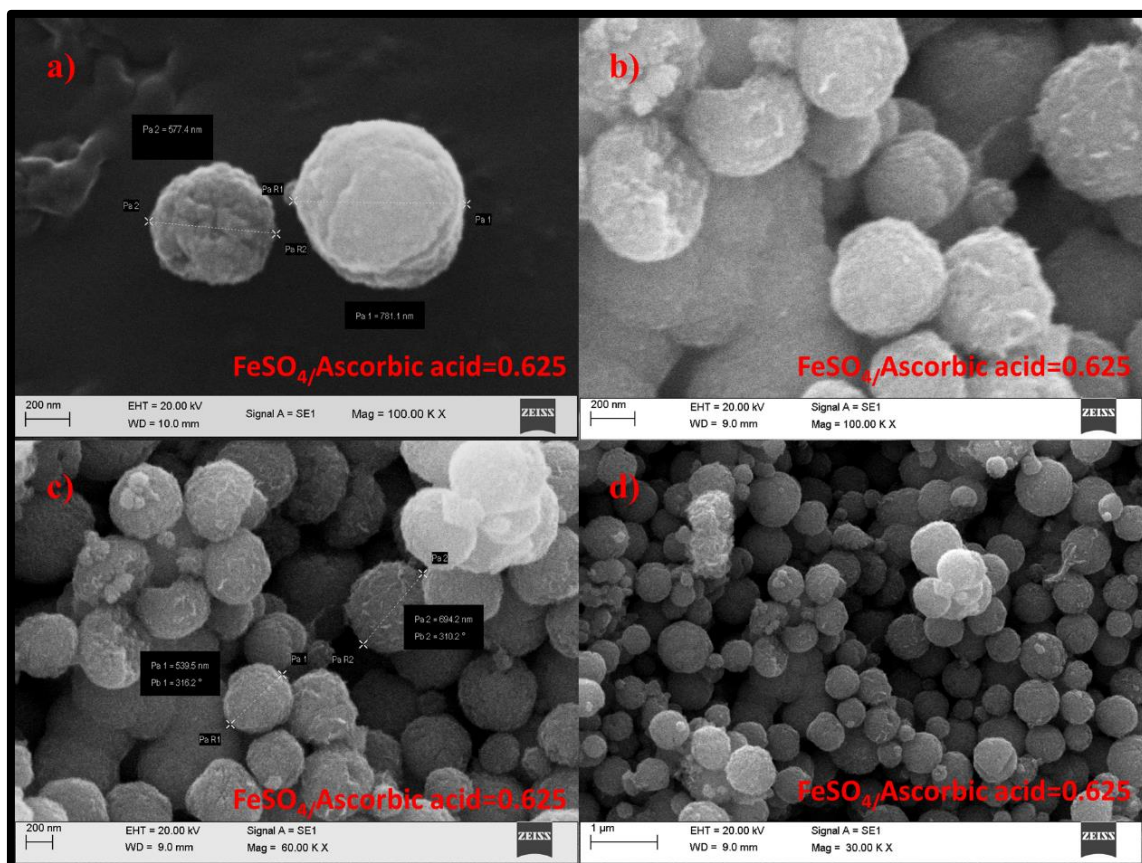


Figure 4.13 (a), (b), (c) and (d) are SEM images of ascorbic acid assisted synthesis products at various magnifications ($\text{FeSO}_4/\text{Ascorbic acid}$ mole ratio = 0.625).

FTIR measurements of synthesized products reveal presence of carbon in the structure (Figure 4.14). Compared to synthesized products obtained with $\text{FeSO}_4/\text{Ascorbic acid}$ mole ratio = 1.25, peaks intensified revealing that carbon containing shell on nanoparticles thickens. The bands at 1088 cm^{-1} and 1381 cm^{-1} corresponds to C-OH stretching and O-H bending vibrations [107]. Qi et al. attribute this bands to incomplete carbonization of glucose along with presence of numerous hydrophilic groups[107]. Band at 1624 cm^{-1} is assigned to C=C vibration. Zheng et al. [65] used glucose instead of ascorbic acid and obtained same absorption peaks and they attribute 1624 cm^{-1} peak to carbonization of glucose. Similarly, it can be said that ascorbic acid carbonizes during synthesis at $200\text{ }^\circ\text{C}$ for 2h. The results indicate that there is a carbon in the structure and contain hydroxyl functional groups on the surface. Zheng et al. [65] stated that it may provide excellent dispersibility in aqueous solution because of presence of functional groups, but our samples are not stable in water.

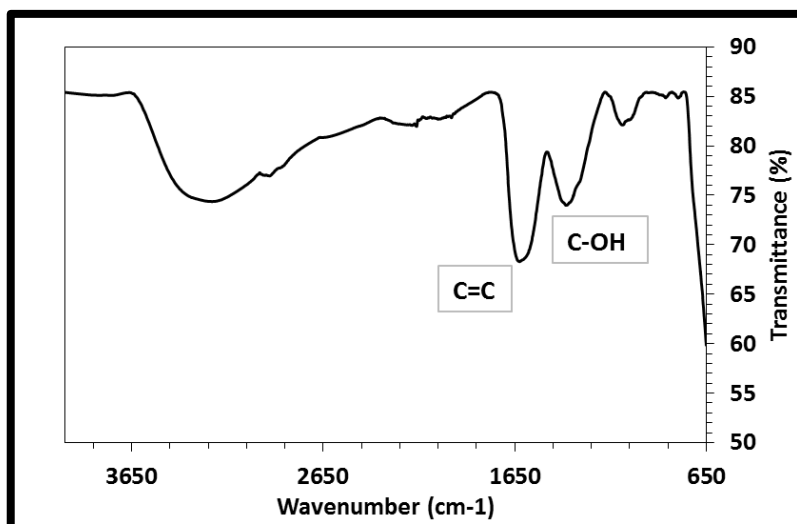


Figure 4.14 FTIR spectrum of Fe_3O_4 nanoparticles synthesized with the aid of ascorbic acid ($\text{FeSO}_4/\text{Ascorbic acid mole ratio} = 0.625$).

4.1.3 Glucose Assisted Solvothermal Synthesis of Fe_3O_4

Glucose assisted synthesis was performed similar to the studies of Zheng et al. [65]. As implemented in the case of ascorbic acid assisted synthesis different amount of glucose was added to synthesis mixtures. $\text{FeSO}_4/\text{glucose mole ratios}$ are 5, 1.25, and 0.625.

4.1.3.1 Glucose Assisted Synthesis of Iron Oxide ($\text{FeSO}_4/\text{Glucose mole ratio} = 5$)

SEM images of products are shown in Figure 4.12. As shown in Figure 4.15a distribution of morphology of the products varies from octahedrons to spheres. Average particle size of octahedrons is around 300 nm. Spheres are bigger. Mean particle size of spheres is 850nm. Figure 4.15b shows a hemispherical particle. Figure 4.15c shows a typical superparticle composed of smaller particles having diameters of around 50nm, size of this particular particle is 630 nm. Figure 4.15d is an example of one of the particles having grooves in one side. Some particles contain spherical pores and some contain slit like pores as this particle. Results clearly reveal that FeSO_4 glucose ratio of 5 is not enough to fully transform nanoparticles into nanometer sized spherical superparticles. In comparison with ascorbic acid assisted synthesis products, glucose causes formation of big, even micron sized spherical particles on the other hand ascorbic acid creates distorted octahedral particles and small spherical particles having same size as octahedral particles.

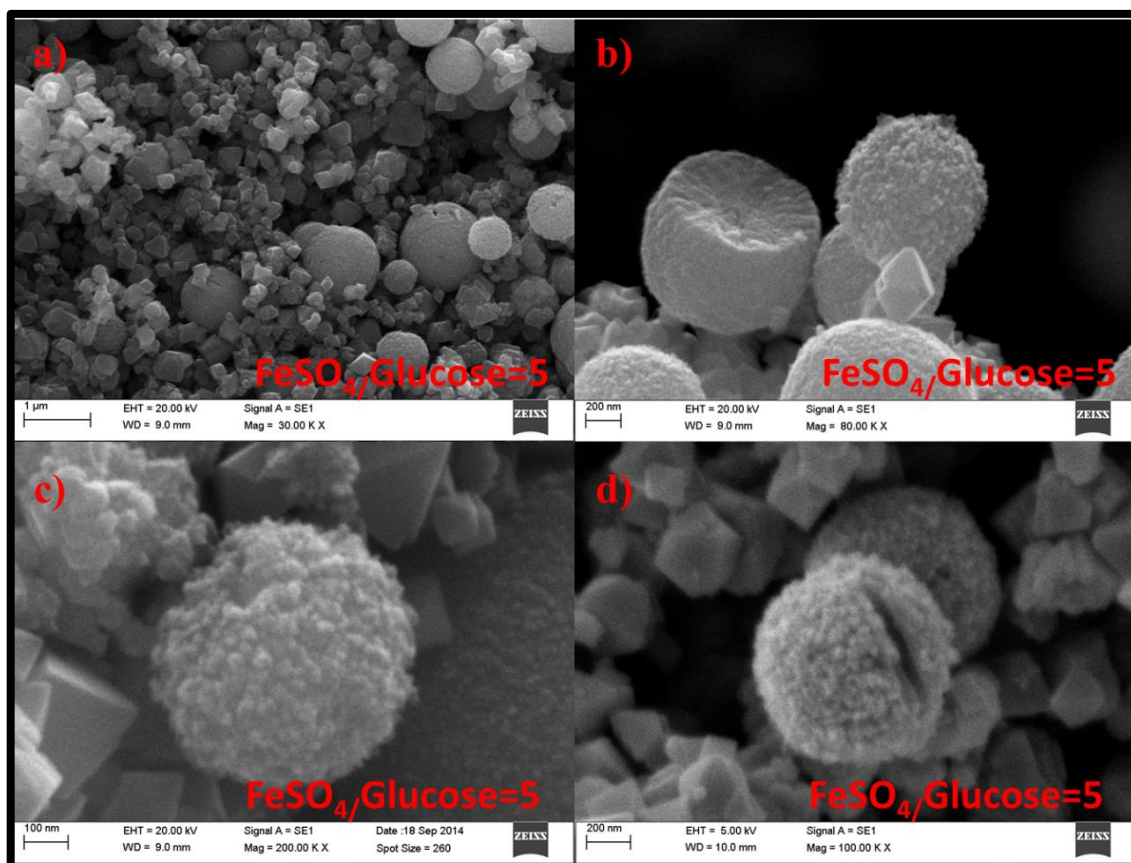


Figure 4.15 (a), (b), (c) and (d) are SEM images of synthesized Fe_3O_4 nanoparticles at different magnifications ($\text{FeSO}_4/\text{glucose}$ mole ratio = 5).

4.1.3.2 Glucose Assisted Synthesis of Iron Oxide ($\text{FeSO}_4/\text{Glucose}$ Mole Ratio = 1.25)

Increasing $\text{FeSO}_4/\text{glucose}$ mole ratio dramatically changes morphology compared to 4 times lower amount glucose added synthesis products. Figure 4.16 shows SEM images of products. Most of the particles are in spherical shape (Figure 4.16a), but there are few particles possessing irregular shapes (indicated in yellow circle). It can be said that to transform the whole structure into spherical particles mole ratio of FeSO_4 to glucose should be almost 1.25. Actually, the value should be slightly higher than this amount. Average particle size is 1060 nm.

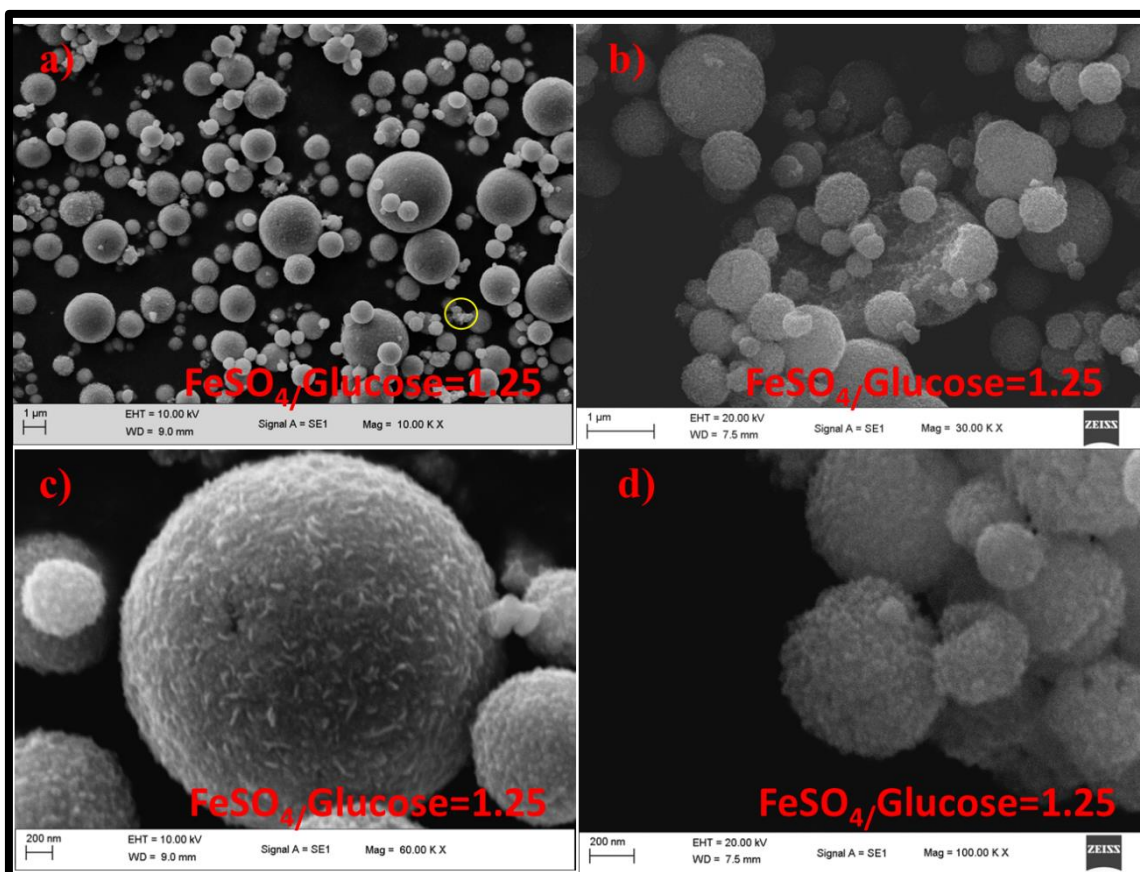


Figure 4.16 (a), (b), (c) and (d) are SEM images of synthesized Fe_3O_4 nanoparticles with the aid of glucose at different magnifications ($\text{FeSO}_4/\text{glucose}$ mole ratio = 1.25). Yellow circle in (a) indicates an example of irregular shape particle.

Figure 4.17 shows XRD graph of synthesized iron oxide nanocrystals. (311), (511) and (440) peaks correspond to Fe_3O_4 .

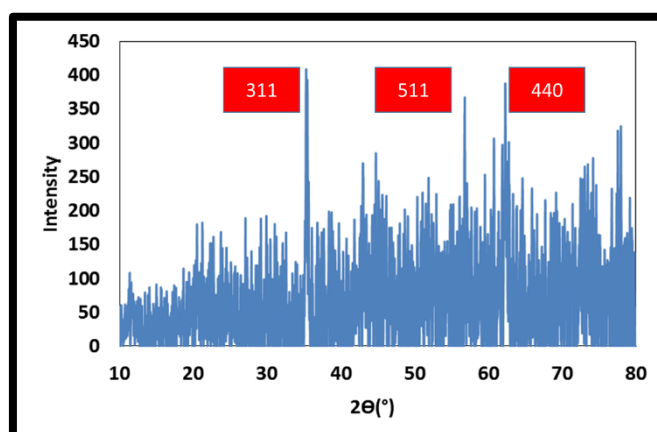


Figure 4.17 XRD graph of Fe_3O_4 nanocrystals ($\text{FeSO}_4/\text{glucose}$ mole ratio = 1.25). There is a decrease in signal to noise ratio compared to pure Fe_3O_4 due to amorphous carbons' presence.

FTIR spectroscopy was implemented to assess the present functional groups. Figure 4.18 shows IR spectrum of synthesized samples. Peaks at 1570 cm^{-1} , 1369 cm^{-1} , 1058 cm^{-1} , 894 cm^{-1} and 796 cm^{-1} are also present in samples synthesized with the aid of ascorbic acid. 1570 cm^{-1} peak correspond to C=C vibration, this peak is evidence of presence of carbon in the structure.

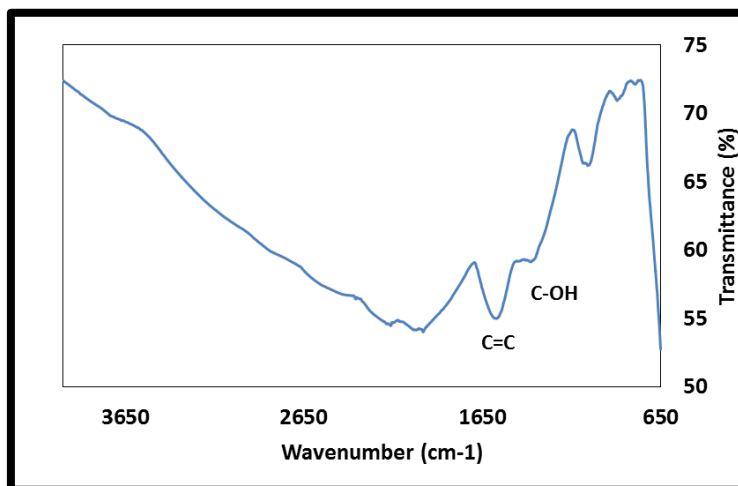


Figure 4.18 FTIR spectrum of glucose assisted synthesis products ($\text{FeSO}_4/\text{glucose}$ mole ratio =1.25).

Nitrogen adsorption desorption isotherm of iron oxide nanoparticles is shown in Figure 4.19a. Synthesized materials possessing type II isotherm, revealing the products are non-porous. BET isotherm is shown in Figure 4.19b. Specific surface area is $21.3\text{ m}^2/\text{g}$. Since nanoparticles are not hollow they don't show a significant specific surface area. Besides, particle size is high which eventually is manifested as low specific surface area.

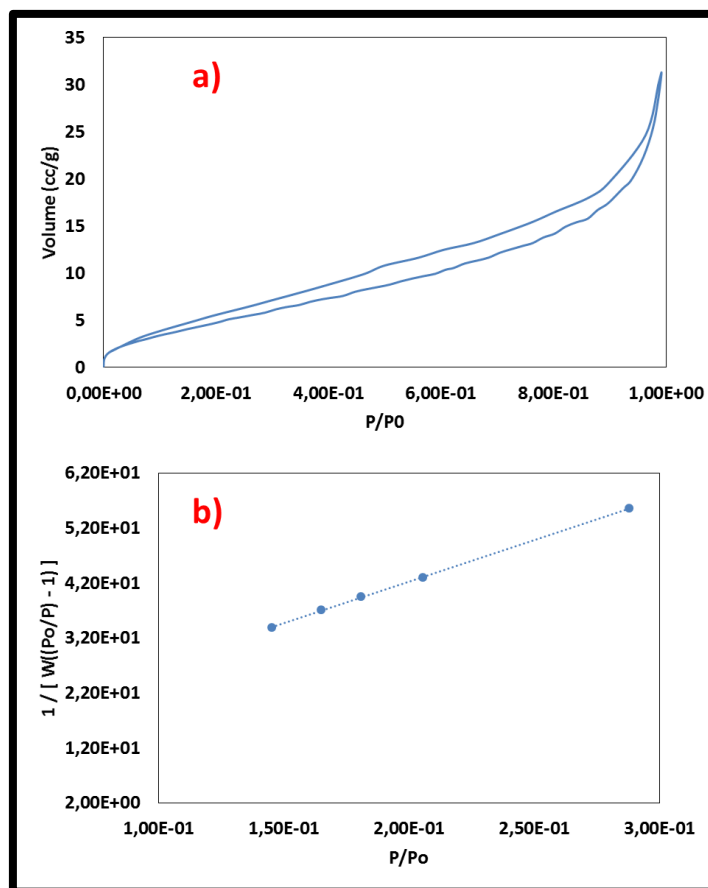


Figure 4.19 (a) is Nitrogen adsorption desorption isotherm of Fe₃O₄ powders and (b) is BET isotherm (FeSO₄/glucose mole ratio =1.25 (21.3 m²/g)).

4.1.3.3 Glucose Assisted Synthesis of Iron Oxide (FeSO₄/Glucose Mole Ratio =0.625)

Figure 4.20 shows SEM images of products. Increasing glucose content does not cause much change in particle size, the main effect is on particle irregularity as shown in Figure 4.20a, b, c and d, namely amount of particles possessing irregularity in terms of shape is pronounced in this product. But generally particles are in spherical shape (Figure 4.20a). Examples of irregular particles are indicated by red arrows in Figure 4.20 part c and part d. The mechanism behind particle irregularity is probably the consequence of having not enough time during synthesis for these irregular shape particles to bind and form spherical particles. High glucose content is believed to affect spherical particle formation kinetics. Average particle size is 900nm. This result is smaller than previous product. So it can be deduced that increasing glucose to FeSO₄ mole ratio slightly more than unity may lower particle size but induce irregularity for 12 h. synthesis at 200°C.

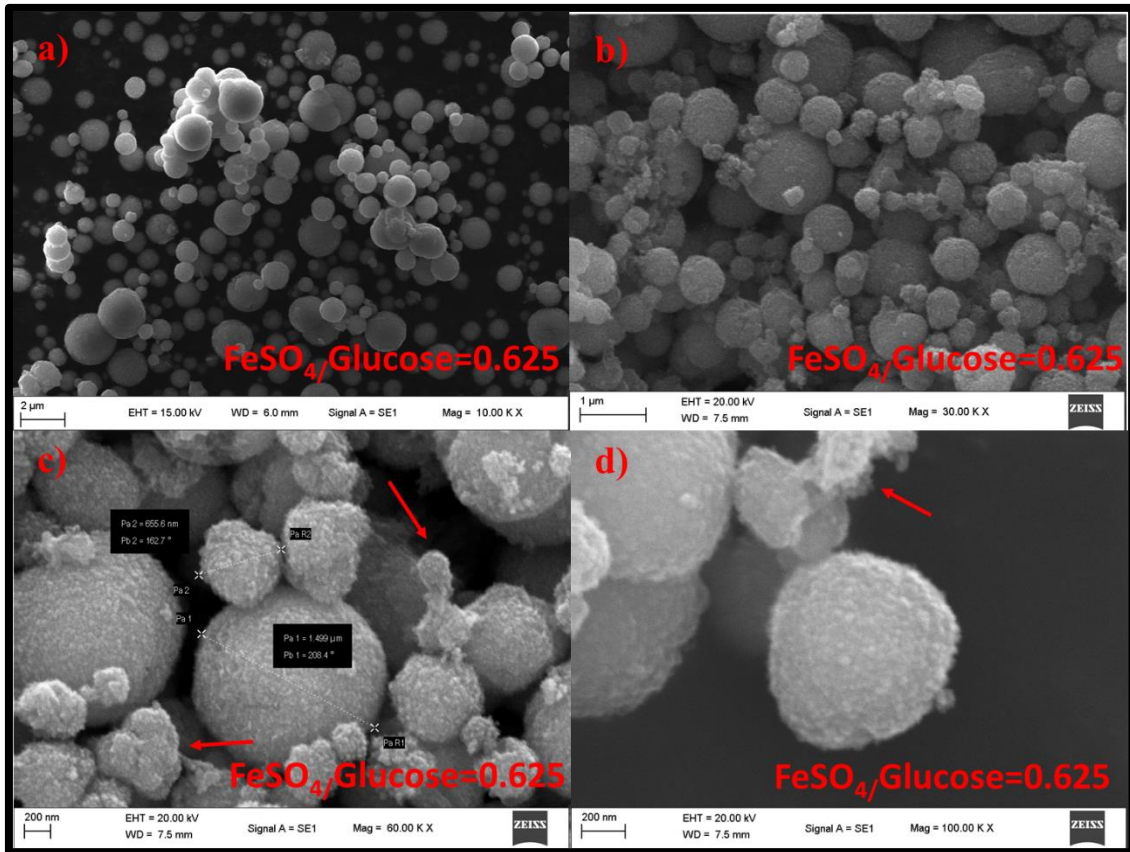


Figure 4.20 SEM images of glucose assisted synthesis products. (a) and (b) are relatively lower magnification images and (c) and (d) are higher magnification images. Red arrows indicate particles having irregular morphology ($\text{FeSO}_4/\text{glucose}$ mole ratio =0.625).

It is hard to interpret the XRD graph since signal to noise ratio is too low (Figure 4.21). There are peaks indicating presence of iron oxide. More investigations needs to be done to interpret the products' identity clearly.

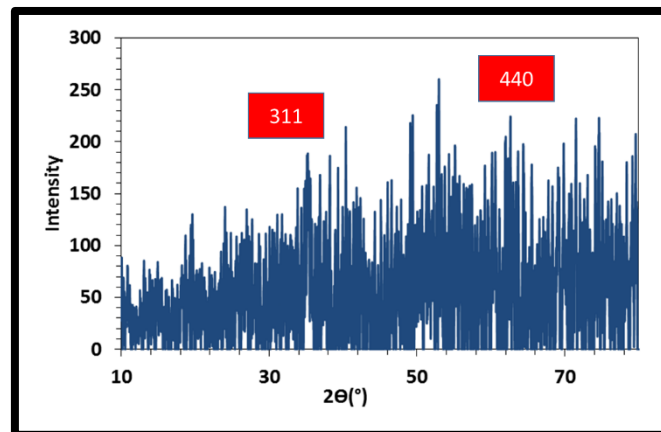


Figure 4.21 XRD graph of synthesized product ($\text{FeSO}_4/\text{glucose}$ mole ratio =0.625).

FTIR investigation results are identical found in previous product, revealing that synthesized material contain carbon in its structure resulting from the decomposition of glucose (Figure 4.22). FTIR spectra of glucose assisted synthesis products having $\text{FeSO}_4/\text{glucose}$ mole ratio =0.625 and 1.25 are almost identical. But the absorption peaks are slightly more intense in more glucose containing one.

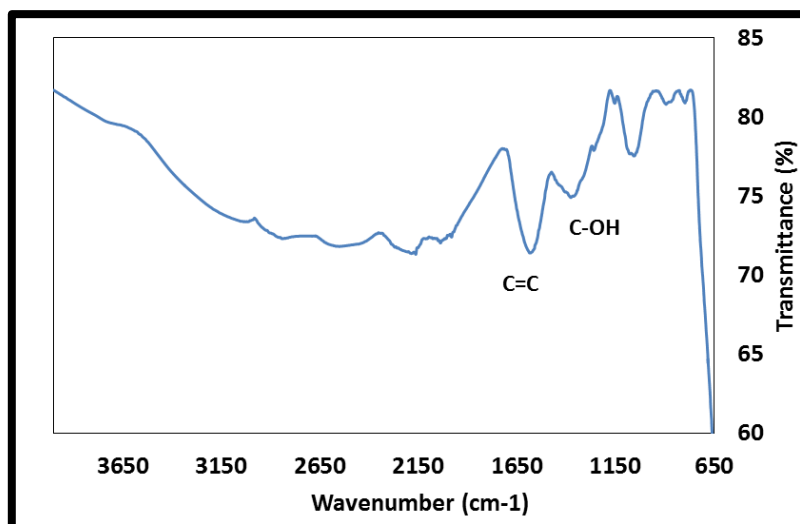


Figure 4.22 FTIR spectrum of iron oxide nanoparticles ($\text{FeSO}_4/\text{glucose}$ mole ratio =0.625).

It should be noted that before solvothermal synthesis ascorbic acid addition gives a red-brown hue to synthesis mixture of FeSO_4 and NaOH and after 20 min. of mixing glucose containing solution stays green.

4.2 Solvothermal Synthesis of Carbon Nanotube/Iron Oxide Hybrid Materials

In this part we will discuss the results of mixing homogeneously dispersed carbon nanotube suspensions and iron oxide precursors and composite or hybrid material production out of the mixture. In other study, as explained in Chapter 3 homogeneous dispersion of carbon nanotubes in IPA was obtained. Rather than mixing precursors in pure IPA we mixed them in carbon nanotubes containing IPA suspensions and the results were investigated.

There are several attempts to investigate the behavior of carbon nanotubes and synthesized nanoparticles. The main aim of this study was to make $\text{Fe}_3\text{O}_4@\text{C}$ nanoparticles and then investigating probable π - π stacking interaction between nanoparticles and nanotubes. Since we also want homogeneously dispersed particles showing no segregation during suspension preparation steps prior to applications.

4.2.1 SDBS Modified MWCNTs and Pure Fe₃O₄ Containing Nanocomposite Synthesis

We also evaluated the homogeneity of resultant nanoparticles after synthesis without ascorbic acid or glucose addition in nanocomposite production. SDBS modified MWCNTs suspensions were mixed with FeSO₄ and NaOH during ultrasonication and synthesis process was implemented identical to previous synthesis processes. Since we calculated the concentration of MWCNTs in suspensions we could say that there is 0.027 g of WMCNTs in 60 ml of reactant mixture. Quantity of Fe₃O₄ synthesized is 0.077 g in 60 ml. Therefore, MWCNTs weight percentage is ~25 in the composite.

After synthesis different solvents were tried during washing and decantation when magnetic separation was being applied. Mostly water is used for washing, but also IPA and acetone were also used, respectively. After precipitation of synthesis water added to the suspension and suspension was shaken or ultrasonicated then put at the top of a neodymium magnet. We found out that if suspension is only shaken there will be no separation between MWCNTs and Fe₃O₄ anoparticles during magnetic separation no matter how many magnetic separations are applied, but if suspension is ultrasonicated in an ultrasonic bath, the result is separation of nanotubes during magnetic separation. Figure 4.23 show sequence of events happened during magnetic separation after synthesis. The synthesis product was ultrasonicated in the third step after addition of disstiled water. The result is separation of MWCNTs from precipitated mass. The blackness of the solution is the result of SDBS modified carbon nanotubes.

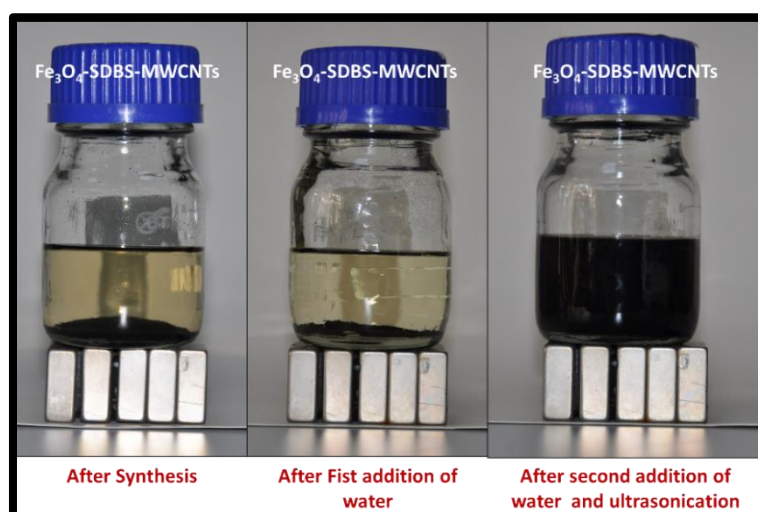


Figure 4.23 Consecutive washing with water during magnetic separation after synthesis of Fe₃O₄ SDBS MWCNTs. Ultrasonication prior to magnetic separation causes phase separation (Magnets are below the bottles).

Figure 4.24 shows SEM images of synthesis products washed using water. Prior to decantation of supernatant during magnetic separation, we haven't applied ultrasonication. The result is total sedimentation of products. Figure 4.24 part (a) is relatively low magnification SEM image of products. Particle size distribution is broad. Mean particle size is 310 nm (extracted from Figure 4.24a). Particle morphology is considerably different from pure Fe_3O_4 nanoparticles. There are still particles octahedral particle morphology, but rectangular shape or near spherical particle morphologies can also be seen. Figure 4.24b shows examples of such spherical particles. In Figure 4.20c and d blue arrows show rectangular prism shape particles. Figure 4.24d is a good example showing nanoparticles and nanotubes glued together by the presence of SDBS. It is known that if carboxyl groups containing carbon nanotubes are present in the structure, the functional groups may act as sites for nanoparticles to crystallize, therefore probably if functionalized carbon nanotubes were used structure would be different, namely, particle size may considerably would become lower. Besides, we believe that pristine carbon nanotubes does not influence particle morphology. The main factor in particle shape change is believed to be consequence of presence of SDBS.

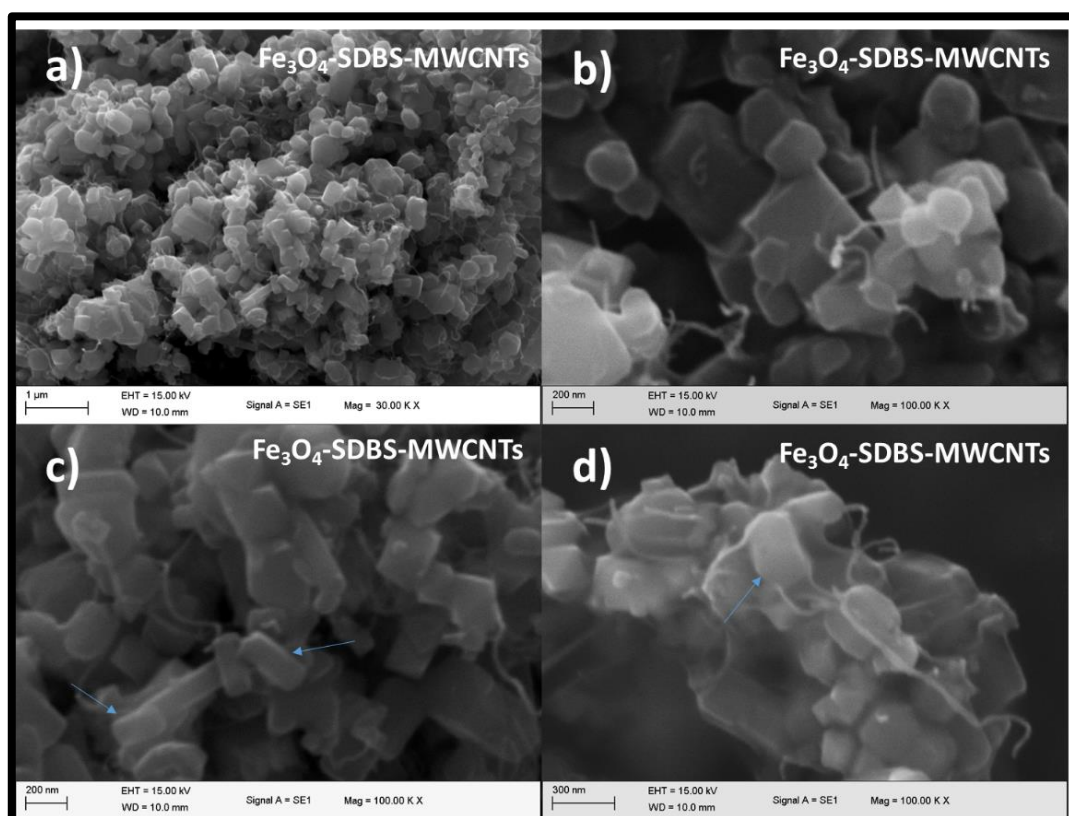


Figure 4.24 (a) and (b) are low magnification SEM images of Fe_3O_4 SDBS MWCNTs, (c) and (d) are high magnification images, clearly showing particles are glued by the presence of excess SDBS. Arrows indicate rectangular prism shape particles.

4.2.2 PVP Modified Carbon Nanotube and Pure Fe₃O₄ Containing Nanoparticle Synthesis

As explained above, rather than using SDBS, PVP was also used and the results are evaluated. Figure 4.25 is SEM images of Fe₃O₄ PVP MWCNTs. Compared to synthesis products obtained by using SDBS, particle morphology seem to be not affected by the presence of PVP (Figure 4.25a, b and c). Pure Fe₃O₄ tend to crystallize into octahedrons under equilibrium conditions and PVP containing synthesis products also show octahedral geometry. Interestingly particle size increased compared to pure Fe₃O₄. Avarage particle size for pure Fe₃O₄ is 175 nm, on the other hand mean particle size is 310nm for Fe₃O₄ PVP MWCNTs. This result is identical to Fe₃O₄ SDBS MWCNTs, but it is almost twice the size of pure Fe₃O₄. There are also few particles showing spherical geometry (Figure 4.25d). Inhomogeneity can be clearly seen in Figure 4.25a. Because there are regions where nanotubes are clustered and there are also regions were mostly iron oxide nanoparticles are present.

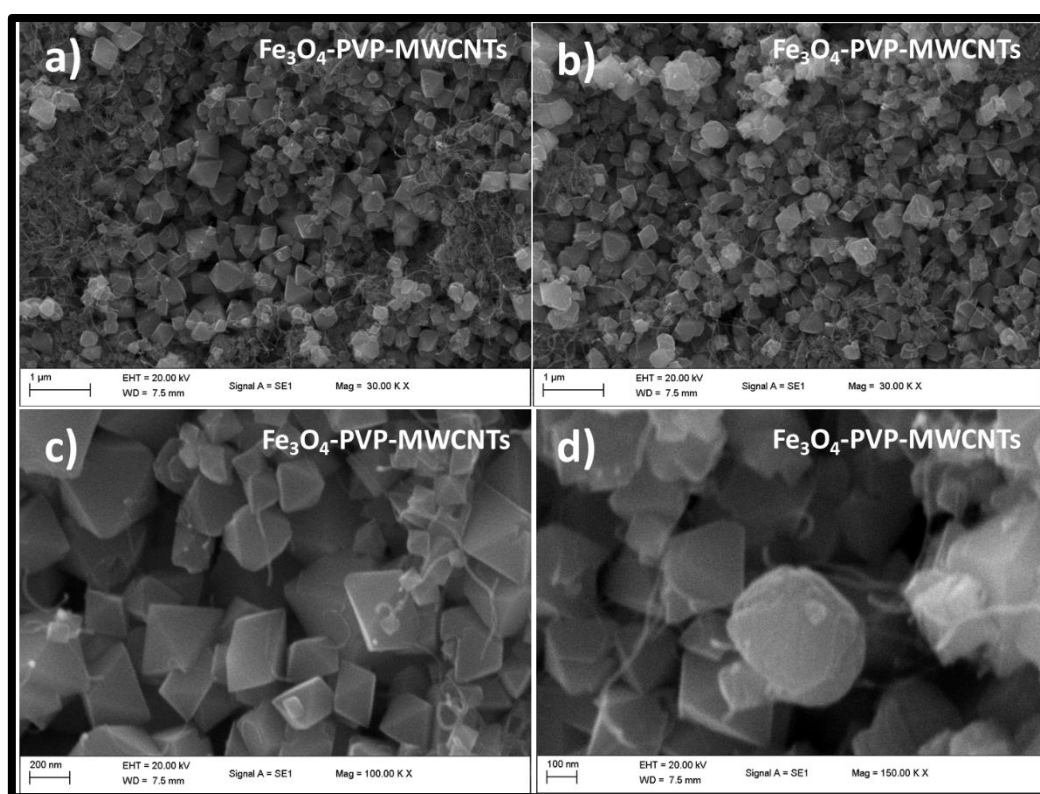


Figure 4.25 SEM images of Fe₃O₄ PVP MWCNTs. (a) and (b) are relatively low magnification images. (c) and (d) are higher magnification images revealing most of the particles have octahedral geometry, but there are few particles possess irregular geometry.

4.2.3 Ascorbic Acid and Glucose Aided Synthesis of PVP or SDBS Modified MWCNTs and Pure Fe₃O₄ Containing Nanomaterials

Glucose and ascorbic acid not only changes particle morphology from octahedron to spheroids, but also creates carbon layers on the surface. We investigated the resultant effect on composite material production.

Ascorbic acid added synthesis MWCNTs containing products are shown in Figure 4.26a, c and d. Figure 4.26b is a SEM image at the same magnification with samples in Figure 4.26a. The difference between two images is: former one was synthesized by adding PVP and MWCNTs. There is a considerable amount of particle size decrease, but unfortunately, most of the nanotubes seem washed away. It seems that, there is no molecular level interaction between MWCNTs and Fe₃O₄@C nanoparticles. Figure 4.26d is photo of synthesis products after mixing with acetone. In acetone both nanotubes and iron oxide nanoparticles sediment.

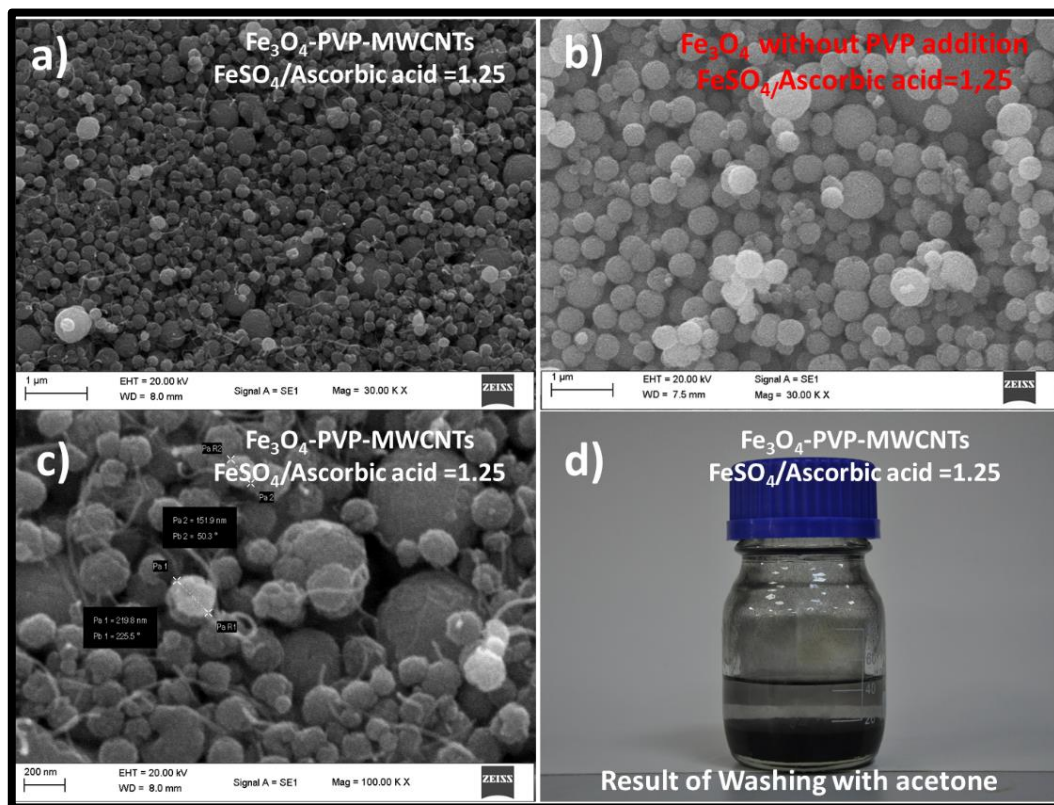


Figure 4.26 (a) is SEM image of water washed ascorbic acid aided synthesis product. Most of MWCNTs are washed away during separation. (b) is synthesis product without PVP and MWCNTs addition, (c) is higher magnification image of Fe₃O₄-PVP-MWCNTs (FeSO₄/Ascorbic acid = 1.25), (d) is resultant sediment after washing with acetone.

Using glucose instead of ascorbic acid lead to same result as expected. Neither Glucose nor ascorbic acid addition provide an interaction between nanotubes and $\text{Fe}_3\text{O}_4\text{@C}$ nanoparticles. Figure 4.27 shows sedimentation behavior of products with aid of magnetic forces during washing with IPA. After several washing steps nanotubes tend to separate.

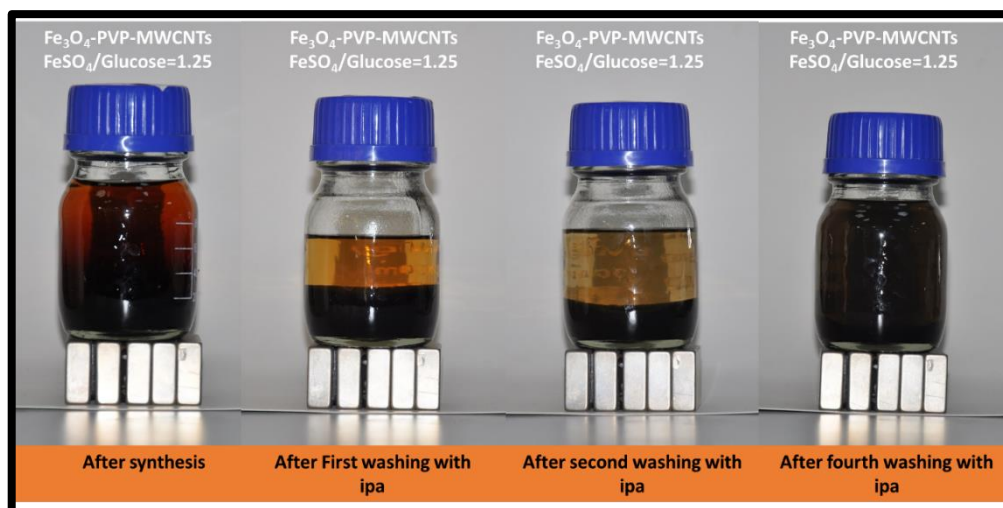


Figure 4.27 Glucose aided synthesis result of $\text{Fe}_3\text{O}_4\text{@C}$ -MWCNTs nanomaterials. PVP was used for dispersion of MWCNTs.

Instead of using PVP, products obtained by using SDBS is also investigated. Figure 4.28a and b are secondary electron and backscattered electron images of $\text{Fe}_3\text{O}_4\text{@C}$ -SDBS-MWCNTs ($\text{FeSO}_4/\text{Glucose}=1.25$), respectively. Washing step considerably influences the product sedimenting during magnetic separation. Presented nanomaterial in Figure 4.28a and b are washed with acetone instead of IPA or water. The result is total sedimentation of nanotubes, SDBS and iron oxide. SEM images contains heterogeneously distributed mass of these three components. Magnetic separation of this powder dispersed in acetone results in total migration of sediment to the magnet (Figure 4.28c) and if the powder is dispersed in water, result of magnetic separation is shown in Figure 4.28d. Phase separation occurs in aqueous suspensions.

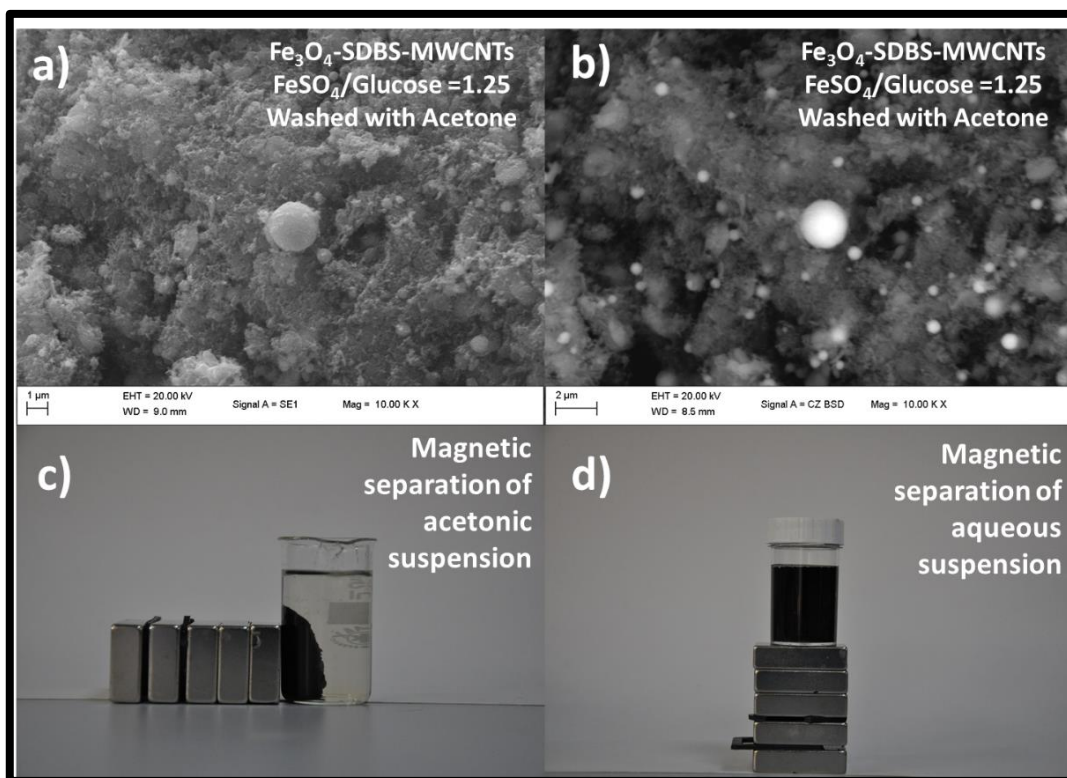


Figure 4.28 Secondary electron (a) and backscattered electron (b) SEM images of products ($\text{Fe}_3\text{O}_4\text{@C}$ MWCNTs) prepared by mixing with acetone each time prior to magnetic separation, (c) and (d) are samples subjected to magnetic separation dispersed in acetone and water, respectively. Along with $\text{Fe}_3\text{O}_4\text{@C}$ nanoparticles, SDBS and MWCNTs migrate towards magnets in acetone.

4.3 Results

1. Synthesize in ethylene glycol and IPA mixture at $200\text{ }^\circ\text{C}$ for 12 h. results in pure iron oxide (Fe_3O_4) nanoparticles having 175 nm average and octahedral geometry.
2. Ascorbic acid and glucose addition to synthesis mixtures cause formation of superparticles consisting of smaller sub 100nm size spherical particles.
3. As Ascorbic acid content increases particle size also increases. Particle size for system having $\text{FeSO}_4/\text{Ascorbic acid}$ mole ratio of 5 is 310 nm. Particle size for system having $\text{FeSO}_4/\text{Ascorbic acid}$ mole ratio of 1.25 is 480 nm and finally for products initially having $\text{FeSO}_4/\text{Ascorbic acid}$ mole ratio of 0.625 have 590 nm in diameter.
4. FTIR analysis revealed that ascorbic acid and glucose addition cause carbon to form on probably the surface of iron oxide nanoparticles. Carbon tends to crystallized on iron oxide surface.

5. If $\text{FeSO}_4/\text{Glucose}$ mole ratio is 1.25, resultant particle size is 1060 nm. If $\text{FeSO}_4/\text{Glucose}$ mole ratio is 0.625 is after solvothermal synthesis mean particle size decreases to 900nm. But there is a trade of between particle size and regularity of particles. $\text{FeSO}_4/\text{Glucose}$ mole ratio of 0.625 causes formation of irregular particles compared to products obtained by using $\text{FeSO}_4/\text{Glucose}$ mole ratio of 1.25.
Probably increasing the amount of glucose increases the thickness of the carbon shell on iron oxide nanoparticles.
6. Both glucose assisted and ascorbic assisted synthesis products are not stable in aqueous, ethanolic, butanolic and isopropanolic suspensions.
7. When FeSO_4 mixed with NaOH instantaneously $\text{Fe}(\text{OH})_2$ is formed. $\text{Fe}(\text{OH})_2$ is not stable and easily transform into $\text{Fe}(\text{OH})_3$ in air. Therefore a controlled atmosphere needs to be used to prevent transformation during mixing. After mixing process, during synthesis a good reducing agent needs to be used. EG is a good reducing agent, but may not be enough. Glucose containing Fe_3O_4 solutions may end up with very low amount of synthesized material after synthesis. Namely, transformed material quantity can be low probably due to oxidation during mixing. On the other hand ascorbic acid act as a reducing agent and the resultant products seem to be always in the same quantity.
8. PVP addition drastically lowers particle size.
9. MWCNTs and $\text{Fe}_3\text{O}_4@\text{C}$ nanoparticles does not form interaction by π - π stacking. Therefore, segregation may occur especially at ultrasonicated suspensions during magnetic separation.

SYNTHESIS OF TITANATE NANOTUBES AND THEIR CHARACTERIZATION

In this chapter synthesis, doping, coating and electronic properties of titanate nanotubes is explained. In experiments, first TiO₂ nanoparticles were synthesized by using Sol-gel method. Synthesized nanoparticles were dissolved in highly alkali solutions and transformed into titanate nanotubes under hydrothermal conditions. Resultant samples were neutralized by acid washing and subsequent water washing. Some of them also washed with hydrogen peroxide to increase the crystallinity of the products. Titanate nanotubes were also heat treated to assess the best heat treatment conditions which is needed to increase crystallinity and providing integrity of tubular structure. Then, stable suspensions of inorganic nanotubes were found by trying different additives and solvents. Semi-stable suspensions were used to make functional coatings on substrates. Finally, electronic properties of titanate nanotubes were investigated.

5.1 Sequence of Synthesis and Characterization of Titanate Nanotubes

5.1.1 TiO₂ Nanoparticles and Their Characterization

TiO₂ nanoparticles were synthesized using Sol-gel method. Washed and dried powders were calcined at 450 °C to convert amorphous structure into anatase form of TiO₂. TEM images of heat treated TiO₂ nanoparticles is shown in Figure 5.1. Particle size is lower than 10 nm. There is a uniformity in terms of particle size.

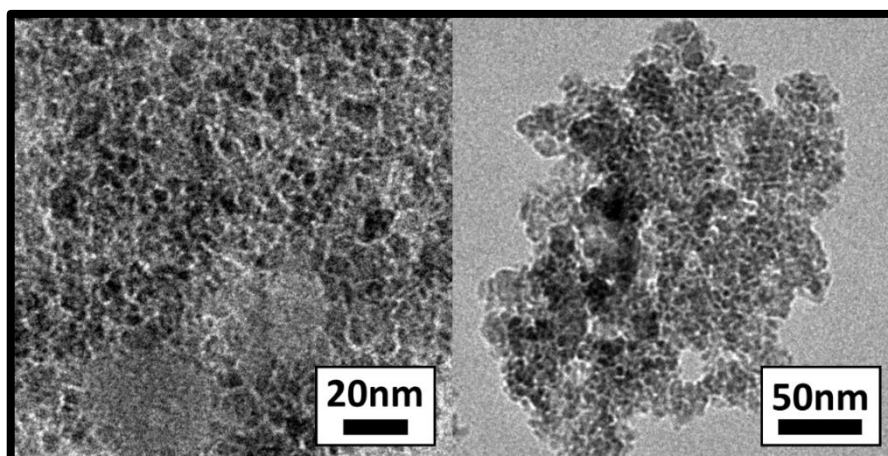


Figure 5.1 TEM images of TiO₂ nanoparticles synthesized via Sol-gel.

We also doped TiO₂ nanoparticles during Sol-gel process by adding Thiourea. Thiourea is source of Sulphur. The molar ratios of Titanium/thiourea are 1 and 4, respectively. Sulphur doped samples are denoted as 1S-TiO₂ and 4S-TiO₂. T. Ohno et al. used thiourea to prepare S-doped TiO₂ [108]. They mixed titanium isopropoxide with thiourea at a molar ratio of 1:4 in ethanol during Sol-gel. The procedure was also used by E.M. Rockafellow et al. [109]. A. Zaleska et al also implemented similar procedure [110]. They mixed thiourea, thioacetamide, monoethanolamine, acetonitrile and melamine with titanium isopropoxide and water allowed for hydrolysis and 24 h. mixing at 80 °C. All the groups calcined their samples at 450 °C to obtain anatase form of TiO₂. Our study is based on the above groups' procedures. Figure 5.2 shows XRD graphs of doped and undoped calcined TiO₂. All the synthesized and calcined products are corresponding to anatase crystal structure of TiO₂. There is an additional peak around 2 theta degree of 30°, which is not belonging to anatase. We believe that it is because of impurities in the structure.

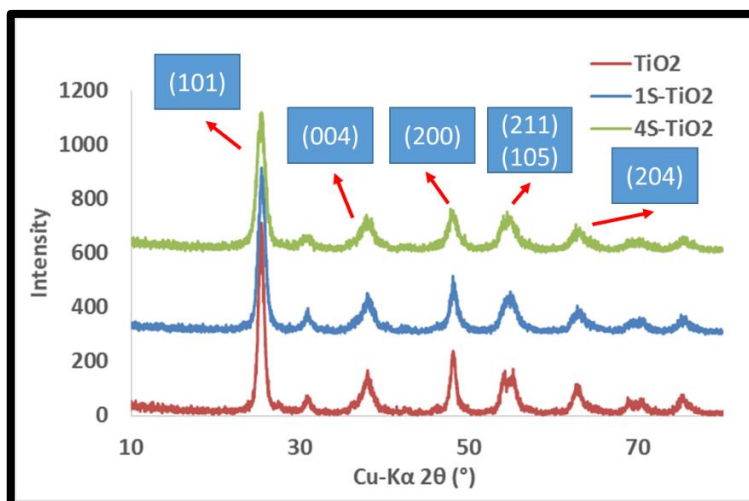


Figure 5.2 XRD graphs of synthesized and calcined pure (TiO_2) or S-doped TiO_2 (1S TiO_2 , 4S TiO_2) nanoparticles.

Figure 5.3 shows (101) peak region of same XRD patterns in Figure 5.3. The peak positions are shifted relative to each other, meaning that S-doping does not change d spacings. Crystallite sizes are calculated using Scherrer formula as shown in Equation 5.1 and (101) peaks.

$$d = 0.9\lambda/\beta 1\cos \Theta \quad (5.1)$$

Crystallites sizes of TiO_2 , 1S- TiO_2 and 4S- TiO_2 are 20 nm, 15 nm and 11 nm, respectively. It seems that thiourea addition lowered crystallite size.

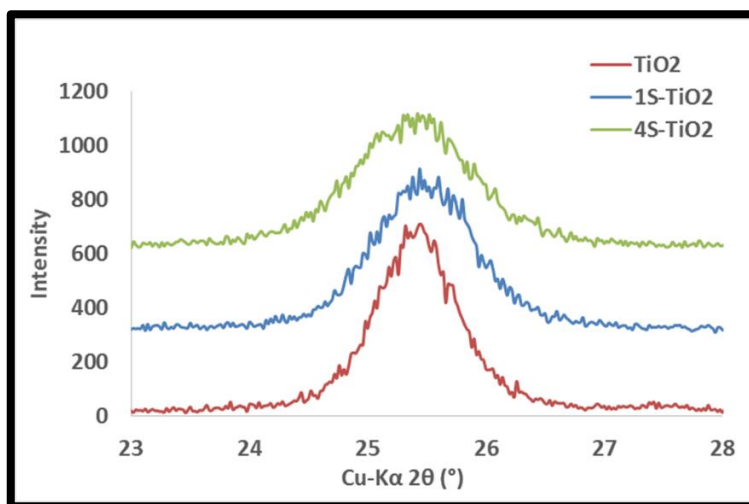


Figure 5.3 XRD patterns of TiO_2 and doped TiO_2 s between 2 theta degrees of 23° and 28° (Curves were shifted for clarity on y-axis).

5.1.2 Titanate Nanotubes and Their Characterization

Conversion of TiO_2 nanoparticles were carried out in highly alkali solutions. When mixed with alkali solutions Ti oxygen bonds becomes disrupted and partially dissolved structure emerge where nanomaterials can be considered in identity crisis. Under hydrothermal conditions nanotubes may began to emerge since the structure is far from equilibrium conditions. We have produced different nanotubes and in addition, implemented different heat treatment regimes onto nanotubes (Not all of them will be presented here). For example, we transformed pure TiO_2 nanoparticles into titanate nanotubes and 4S- TiO_2 nanoparticles were also used to produce nanotubes.

In heat treatment procedures, nanotubes were calcined at 300 °C, 350 °C and 400 °C, respectively. Heat treatment processes were implemented in inert atmospheres since under inert atmosphere tubular structures better preserve their integrity.

Synthesized nanotubes by using pure TiO_2 is denoted as TNT. TNTA abbreviation will be used for TNTs which are washed with acid solutions. Therefore they probably contain sodium ions only trace amounts. TNTaq indicates only water washed nanotube samples. Figure 5.4a and b shows SEM images of TNTA. Aggregates of nanotubes create a macroporous structure as shown in Figure 5.4a. Figure 5.4c and d are TEM images of TNTAs. Diameter of nanotubes is around 10nm. SEM images cannot resolve individual nanotubes. It should be noted that SEM images of this products is always different from TEM images. We think that this is because of agglomeration behavior of nanotubes; for this reason, nanotubes seen as rodlike bundles having very large diameters up to 60 nm. Unlike SEM, TEM can resolve individual nanotubes.

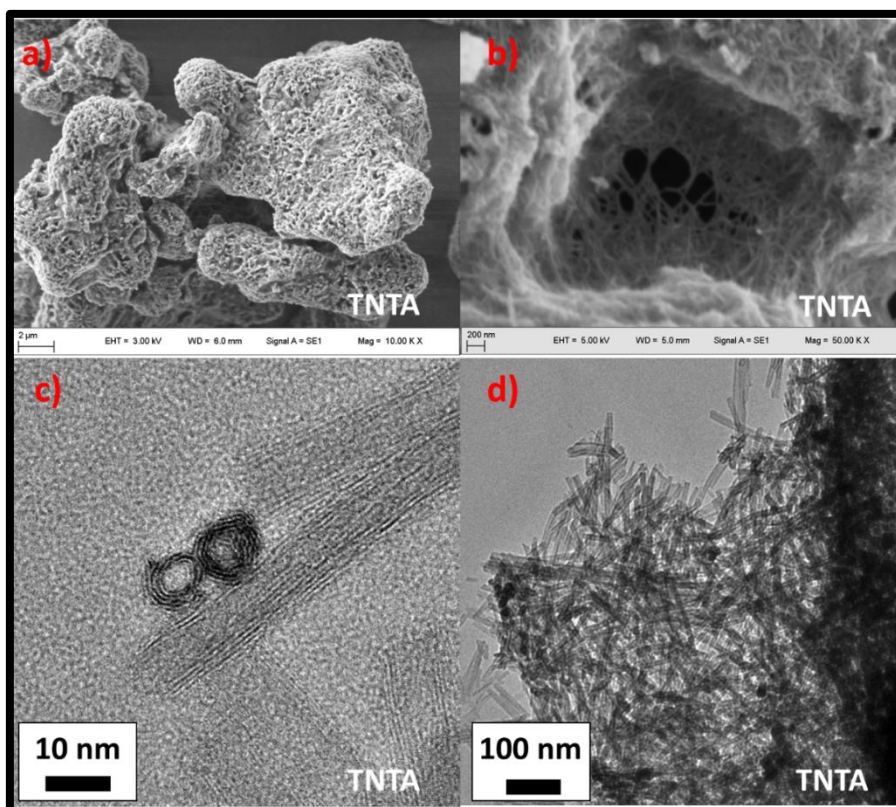


Figure 5.4 (a) and (b) are SEM images of acid washed titanate nanotubes (TNTA), (c) and (d) are TEM images of TNTA.

Calcination temperature is an important factor since calcination provide higher crystallinity. Different temperature regimes were investigated. We also found out that acid washing increase susceptibility to high temperatures. Since sodium ions is exchanged by hydrogen ions, the layered structure becomes weak. Presence of sodium on the other hand deteriorates photocatalytic activity because sodium ions act as recombination sites for electron-hole pairs. Figure 5.5a and b shows TEM images of acid washed TNTA samples calcined at 450 °C. All nanotubes transformed into spherical or rod like nanoparticles. Therefore, lower temperatures were chosen for calcination of nanotubes.

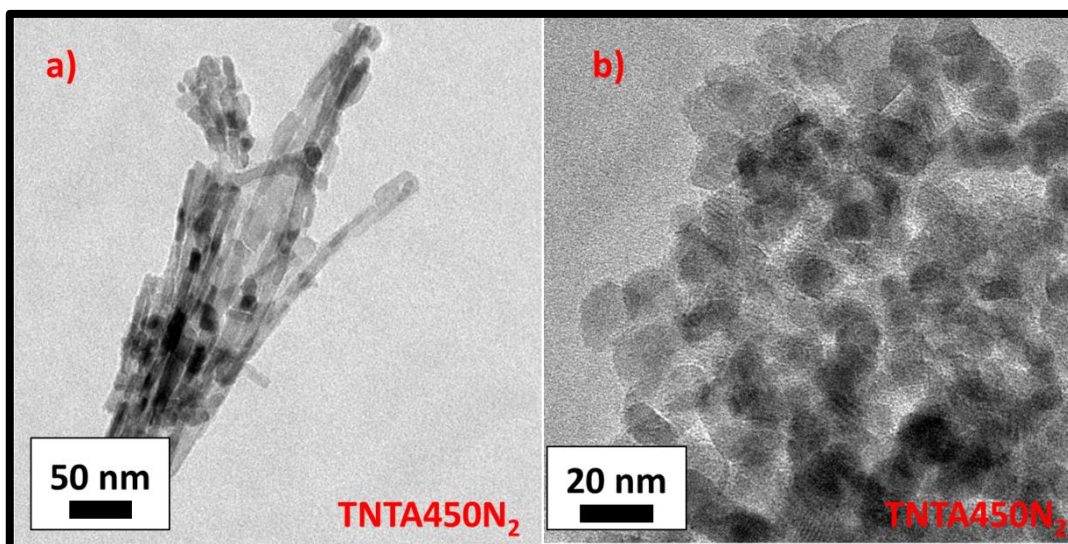


Figure 5.5 TEM images of acid washed nanotubes calcined at 450 °C. Tubular structure becomes disrupted at this temperature range. (a) contains rod like particles mostly and (b) contains spherical ones.

We have found out that nanoparticles can stay in the form of nanotubes at 350 °C. Figure 5.6a and b shows TEM images of calcined TNTA. It will be abbreviated as TNTA350N₂ since calcination took place at 350 °C under nitrogen atmosphere.

As synthesized nanotubes are inherently oxygen deficient. We have investigated the effect of oxygen deficiency of nanotubes on electronic properties. Therefore, Hydrogen peroxide washing was implemented to provide oxygen. The simplest manifestation of oxygen deficiency of as synthesized nanotubes is after calcination in inert atmosphere, the powder becomes grey in color. However hydrogen peroxide washed and calcined samples are white. Besides, if nanotubes are calcined in oxygen atmosphere, they become white too. Figure 5.6c and part d are TEM images of synthesized, hydrogen peroxide washed and then calcined products. They are abbreviated as TNTAH₂O₂350N₂. In terms of length and diameter there is no change between TNTA350N₂ and TNTAH₂O₂350N₂. It is found out that this temperature range is good to preserve nanotubes integrity since there is no visible change between calcined samples and TNTA. It is also understood that hydrogen peroxide does not give any harm to the tubular structure.

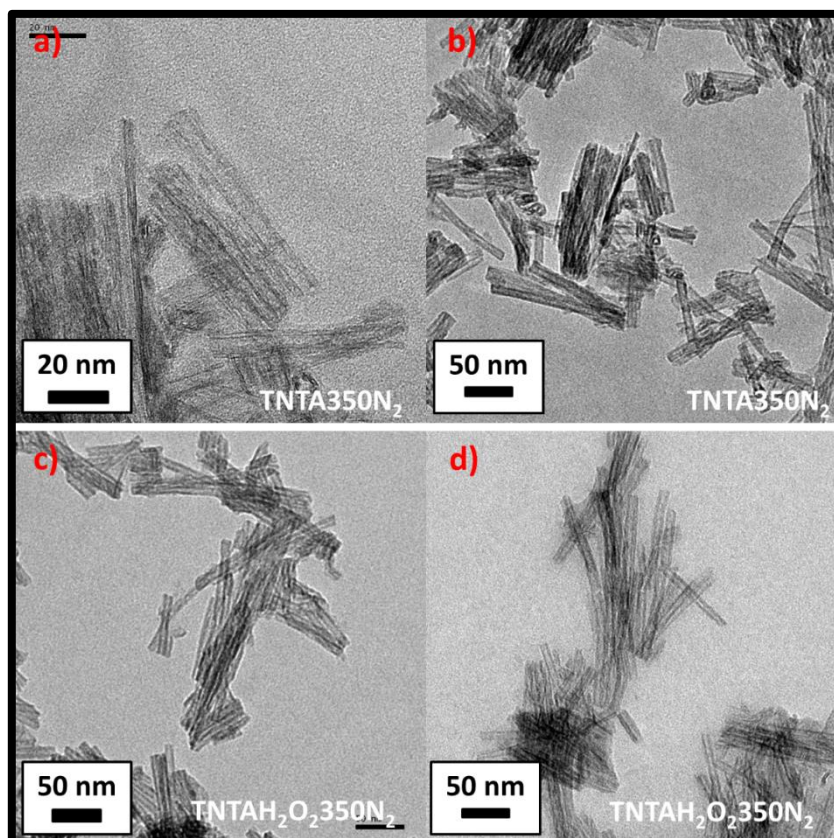


Figure 5.6 (a) and (b) are TEM images of TNTA350N₂ (Calcined and acid washed nanotubes), (c) and (d) are TEM images of H₂O₂ washed and calcined TNTAs.

Figure 5.7 shows TEM images of synthesized and calcined nanotubes obtained by using 4S-TiO₂ nanoparticles. Sulphur doped nanoparticles were subjected to same hydrothermal synthesis and calcination processes. From Figure 5.7a, b and c contains nanoparticles, somehow tubular structure became disrupted and fraction of nanotubes turned into nanoparticles. Figure 5.7d shows examples of nanotubes retained their integrity. This sample is labeled as 4STNTA350N₂. It should be noted that these micrographs were deliberately taken from places where mostly nanotube morphology has changed. Therefore, we should say that not all nanotubes transformed into nanoparticles.

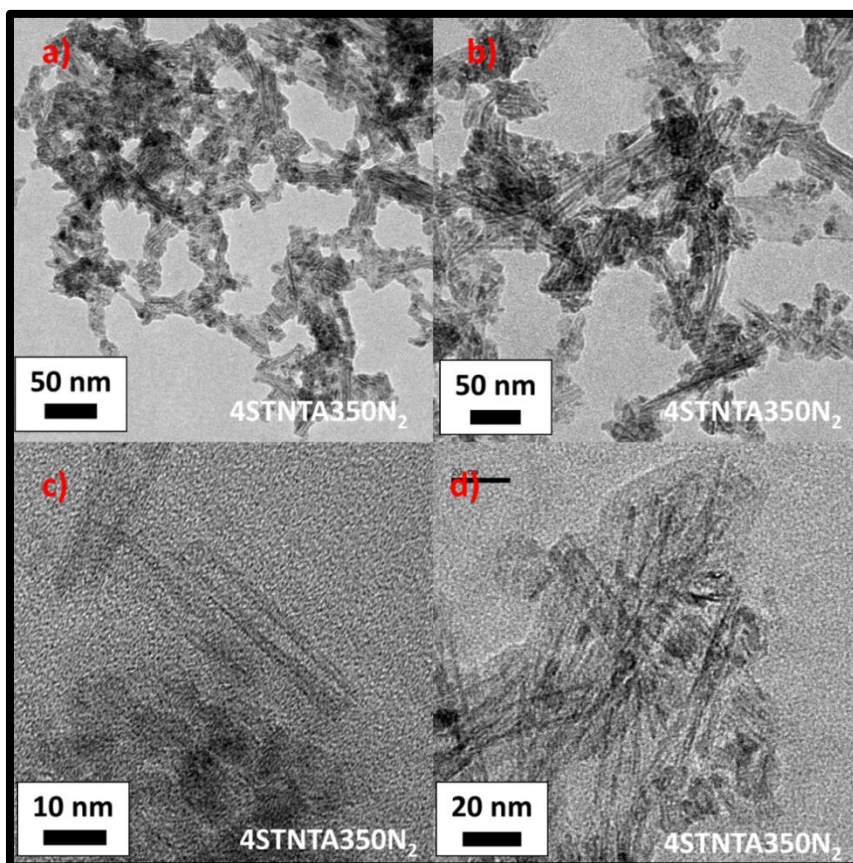


Figure 5.7 (a) and (b) are relatively low magnification TEM images of sulphur doped TNTAs, (c) and (d) are higher magnification TEM images. Tubularity couldn't be relatively successfully preserved as in the case of undoped samples.

FTIR spectra of as synthesized and washed and calcined nanotubes are shown in Figure 5.8a and b. Broad and intense band at 3300 cm^{-1} corresponds to O-H stretching vibration. OH groups also present in samples calcined at $350\text{ }^{\circ}\text{C}$. Peaks at 1637 cm^{-1} correspond to H-O-H deformation mode [111]. This confirms that -OH is present in nanotubes even in calcined ones ($350\text{ }^{\circ}\text{C}$). Band at wavenumber of 899 cm^{-1} is Ti-O stretching mode which is assigned to non-bridging oxygen atoms [112].

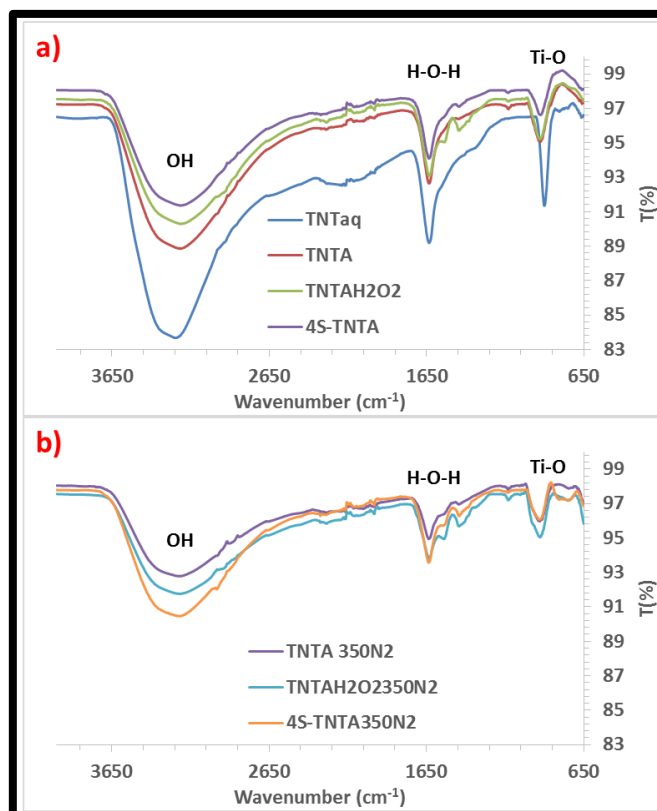
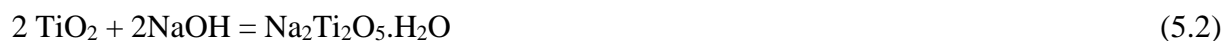


Figure 5.8 FTIR spectra of nanotubes: (a) contains spectra of synthesized and modified nanotubes not subjected to calcination and (b) contains FTIR spectra of calcined samples (350 °C).

XRD analysis results are shown in Figure 5.9. Graphs were shifted for ease of comparison. Products formed during hydrothermal treatment contains sodium ions before washing, which are almost certainly accommodated between the octahedral titania layers, generating sodium titanate structure [113]. Jin et al. reported that the product is $\text{Na}_2\text{Ti}_2\text{O}_5 \cdot \text{H}_2\text{O}$ and the reaction formula is [114]:



The diffraction peak at 2 theta degree of 28° for TNTaq corresponds to (600) plane and assigned to one of the peaks corresponding to sodium titanate.

The diffraction peaks of 10°, 24°, and 48° can be assigned to hydrogen titanates. N. Xiao et al. attribute this structure to $\text{H}_2\text{Ti}_4\text{O}_9 \cdot \text{H}_2\text{O}$ [115]. Du et al. assigned this to layered titanate $\text{H}_2\text{Ti}_3\text{O}_7$ [116]. The Peak at 10°-11° corresponds to the 200 diffraction which is an indication of the periodic layered structure. The intensity of 10°-11° of water washed samples is higher than acid

washed ones. The interlayer spacing diminishes (higher 2 theta values) with increasing calcination temperature as well. This peak is only pronounced in as synthesized nanotubes.

As synthesized nanotubes are low in crystallinity. Khan et al. used hydrogen peroxide to modify nanotubes [117]. They showed that low crystallinity of nanotubes can be enhanced with H₂O₂ treatment and after H₂O₂ treatment they calcined their sample in air at 350 °C. Hydrogen peroxide washing altered XRD patterns of products and hence crystallinity. Namely, Some anatase peaks, such as (004), (105), (211) which were absent in as synthesized TNTs are present in H₂O₂ washed samples. Unfortunately, we don't encounter pronounced change. However close inspection of the peaks reveals that some peaks are emerging and some are slightly intensified compared to TNTA350N₂. Khan et al. implemented H₂O₂ washing at 40 °C and calcined their samples in air [117]. We washed TNTAs with H₂O₂ at room temperature and calcined our samples in inert atmosphere. We thought that the difference in two studies is arising from these different procedures followed during washing. Khan et al. found more pronounced peaks after H₂O₂ washing compared to our finds.

XRD graphs of nanotubes obtained from sulphur doped TiO₂s (4STiO₂) is also different from the other samples. They are denoted as 4STNTA350N₂ since they were subjected to acid washing and calcination at 350 °C prior to analysis. 4STNTA350N₂ sample has clearly lower crystallinity compared to TNTA350N₂ and TNTAH₂O₂350N₂.

If TNTAs are calcined at 450 °C even in inert atmosphere they transform into anatase TiO₂. TEM images had revealed that the transformed materials are not nanotubes. High temperature provides high crystallinity, but tubular structure almost totally becomes disrupted. Small intensity peak at 2 theta degree of 10° indicates that there is a small amount of layered structure present in TNTA450N₂. However it is negligible.

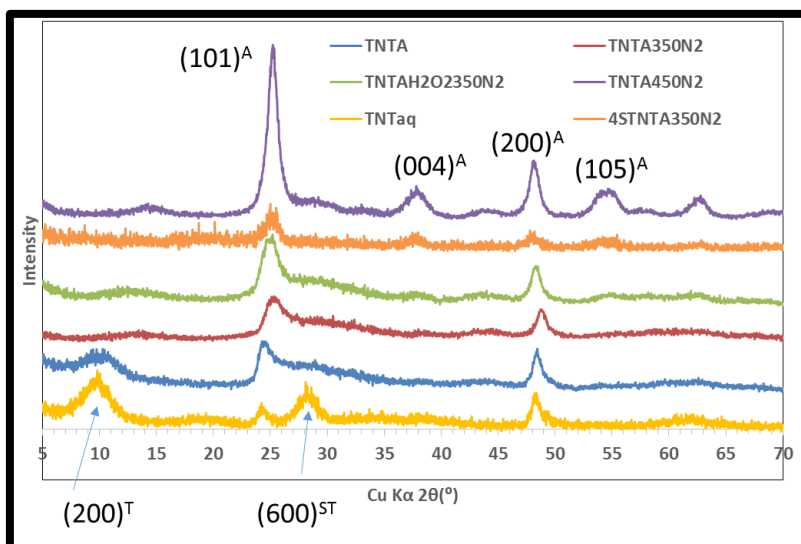


Figure 5.9 XRD patterns of synthesized, washed and calcined nanotube samples. “A” letter denotes anatase TiO₂, “T” denotes titanate and “ST” denotes sodium titanate.

We found out that there is an effect of hydrogen peroxide washing on titanate nanotubes. Color of as synthesized acid or water washed nanotubes are white, but after calcination, the color of titanate nanotubes become grey. It is well known that Ti³⁺ impurities and oxygen vacancy defects turn white TiO₂ yellow or blue [118], [119]. Further reduction with hydrogen gas will even lead formation of black TiO₂s. Hydrogen peroxide washed and calcined nanotubes appear white.

TiO₂'s most important aspect is its photocatalytic activity. Catalysis processes are surface related. Therefore, we have conducted surface area measurements on nanotubes. Specific surface area of TNTA sample is obtained by using BET theory as shown in Figure 5.10. Specific surface area of TNTA calculated as 549 m²/g.

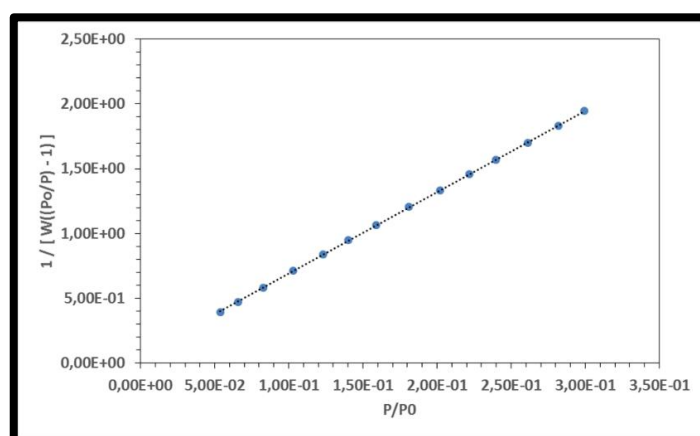


Figure 5.10 BET plot of TNTA sample degassed at 150 °C. Acid washed titanate nanotubes has 549 m²/g specific surface area.

Band gap values of semiconductors are important since it determines the wavelength threshold for generation of electron hole pairs on semiconductor surfaces. For determination of band gap values of titanate nanotubes, stable and optically clear suspensions were obtained. Firstly, suspensions were subjected to particle size analysis using dynamic light scattering technique. Prepared suspensions were subjected to same mixing and filtering processes. Figure 5.11 shows particle size distribution versus intensity. Average particle size values for samples is shown below the Figure 5.11. Average particle size is around 110 nm (± 3.1 nm) for all samples according to intensity based distribution. TEM images revealed that nanotube are 100nm in length and 10 n in diameter. Therefore, it is revealed that in inspected suspensions nanotubes form small bundles consisting of around 3 or 5 nanotubes. Average particle size values, particle size distributions and intensities are almost the same for all samples. The reason behind particle size measurement is to determine particle size after sample preparation for UV-Vis and the aggregation behavior of nanotubes. We have suspected that the environment around a nanoparticle or formation of bundles and and agglomerates may affect UV-Vis absorption of TNTs. It should be noted that volume based particle size distributions are close to the intensity based distributions.

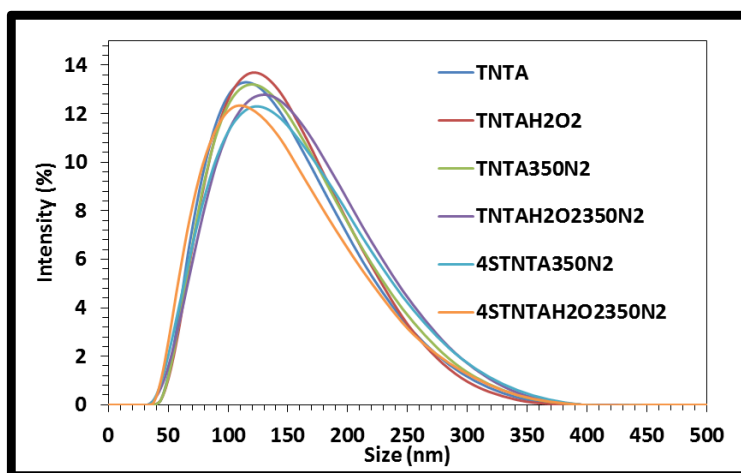


Figure 5.11 Particle size analysis results for stable optically clear dilute suspensions which were also subjected to UV-Vis absorption spectroscopy analysis for band gap calculation.

Triethanolamine was used as additive during preparation of nanotube suspensions. Figure 5.12a shows UV-Vis spectra of different titanate nanotubes after subtraction of contribution of TEA on absorbance. Tauc plot was drawn to determine band gap values for titanate nanotubes. By using UV-Vis curves, plots of $(\alpha h\nu)^{1/2}$ versus $h\nu$ were drawn. α values are obtained by multiplying absorbance values with 2,303 and dividing the resultant with 1, since the path

length in cuvette is 1 cm. Figure 5.12b shows tauc plots of selected titanate nanotubes. The extrapolated lines intersecting with x-axis showing band gap values of nanotubes. Band gap values of TNTs are as follows: TNTA=3,4 eV, TNTAH₂O₂=3,33 eV, 4STNTAH₂O₂350N₂=3,32 eV, 4STNTA350N₂=3,31 eV, TNTA350N₂=3,30 eV, TNTAH₂O₂350N₂=3,27 eV.

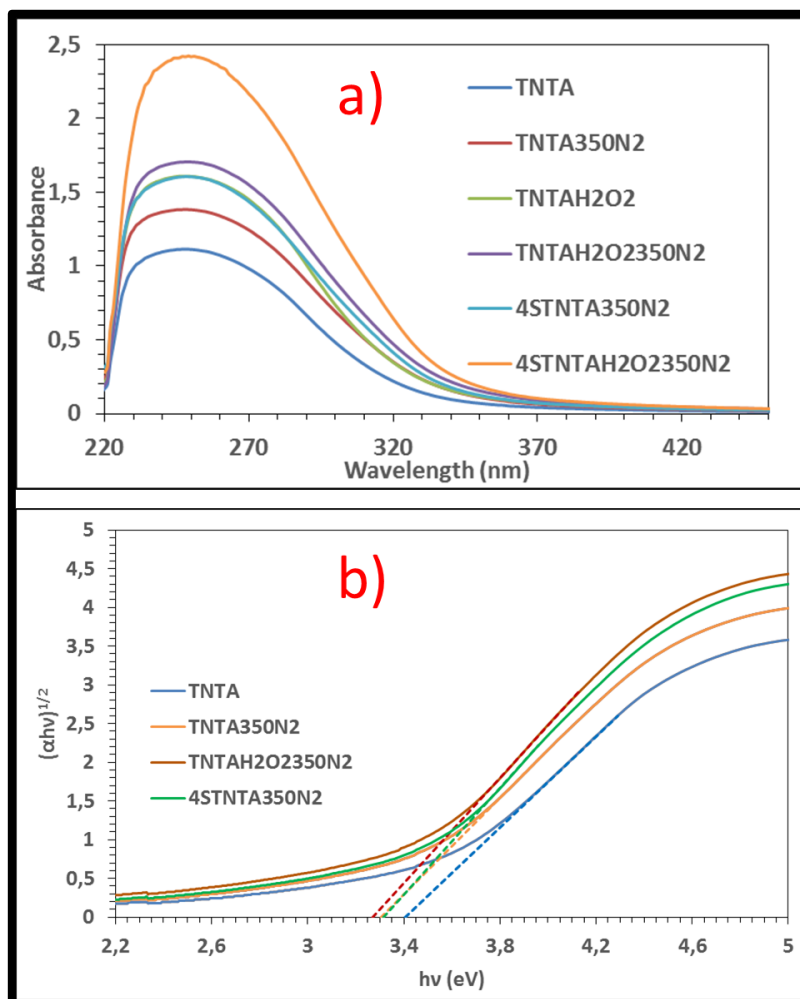


Figure 5.12 (a) UV-Vis absorption spectra of titanate nanotubes. (b) Tauc plots of selected nanotubes obtained from the above spectra.

Defect sites influences the catalytic activity of TiO₂s. For example, Ti³⁺ is one of the most important surface defects in TiO₂ [120]. It is known that TiO₂ is not practical in photocatalysis applications but presence of Ti³⁺ may provide visible light activity [121]. Besides, it provides reactive agents for many absorbates and this results in reduction of electron-hole pair recombination rate [122]. Presence of Ti³⁺ is result of missing bridging oxygens. One bridging oxygen atom leaves two T³⁺ sites. One of the other oxygen vacancy related defect is SETOV. It is reportet that SETOVs are unfortunately act as recombination centers for generated electron

hole pairs and photocatalytic behavior becomes bad [123]. In addition, It should be noted that surface defects can be induced by annealing under vacuum [121].

After calcination of our samples, resultant materials exhibit coloration (grey) whether they are calcined under vacuum or inert atmosphere, which infers that the stoichiometry of TiO_2 has changed. However hydrogen peroxide washed TNTs remain white after calcination under inert atmosphere. Deeper understanding and confirmation of defects in the structure is investigated via ESR.

There is numerous amount of studies about TiO_2 and titanate nanotubes using ESR since different defects may act differently and they may all effect photocatalytic activity. A symmetric ESR signal for SETOV ($g= 2.003$) and asymmetric ESR for Ti^{3+} ($g= 1.98$) was observed in titanate nanotubes [124], we searched for this defects in ESR spectra. Figure 5.13 shows ESR spectra of calcined acid washed TNTs (TNTA350N₂), acid washed and calcined TNTs at 450 °C (TNTA450N₂) and acid-hydrogen peroxide (H_2O_2) washed calcined (350 °C) TNTs (TNTAH₂O₂350N₂). It can be clearly seen that the higher the annealing temperature is, the higher the intensity of ESR peaks among TNTAs. This indicates that increasing annealing temperature increases the amount of unpaired electrons and, hence corresponding defects. g factor of 2.008 in TNTA350N₂ and 2.005 for TNTA450N₂ and 2.006 for TNTAH₂O₂350N₂ are all attributed to the single electron trapped oxygen vacancy defects. They are attributed to SETOVs because g values are close to reported values for SETOVs and the signals are symmetrical as encountered for SETOVs in literature.

It is inferred from the Figure 5.13 that hydrogen peroxide washing provide compensation for the oxygen vacancies on the surface of TNTs. Thereby, ESR intensity of sample washed with hydrogen peroxide is considerably low compared to untreated ones. The intensity alteration is also the reflection of structure of nanotubes. Considerable amount of oxygen atoms are present on the surface not in the bulk. This results in a profound affect of hydrogen peroxide washing on ESR intensity. It should be noted that crystallinity of hydrogen peroxide washed samples is higher due to the compensation for the oxygen vacancies on the surface as confirmed from XRD analysis.

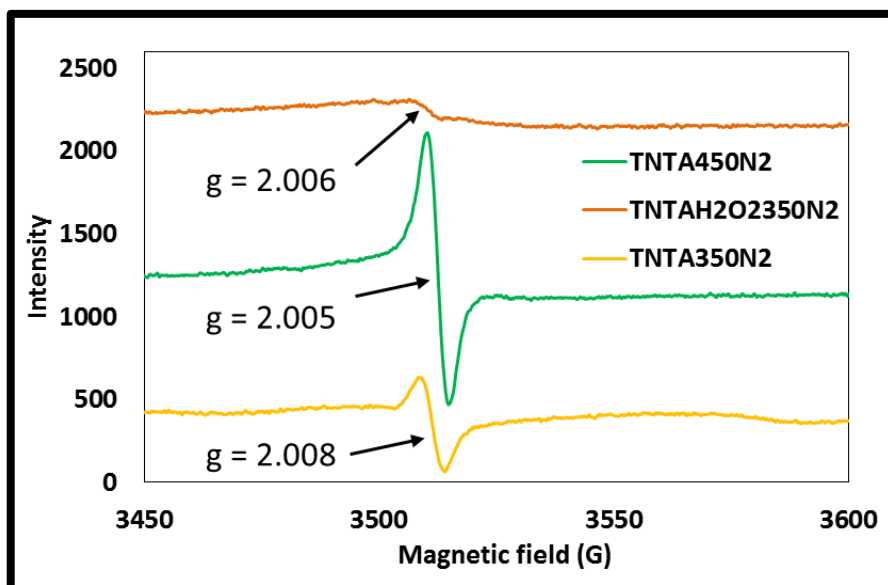


Figure 5.13 ESR spectra of TNTA350N₂, TNTA450N₂ and TNTAH₂O₂350N₂.

ESR spectra of TNTA350N₂ (g factor: 2.008) and sulphur doped 4STNTA350N₂ (g factor: 2.018) are shown in Figure 5.14a. The only difference in samples is the presence of sulphur in 4STNTA350N₂.

As confirmed from XRD analysis of titanium dioxides, we haven't experienced a shift in diffraction peaks when comparing pure TiO₂ nanoparticles and sulphur doped TiO₂ nanoparticles. Shifts in the diffraction peaks are the indication of alteration in d spacings by substitution of atoms. The ionic radius of S is larger than O, thus difficult to fit in into the TiO₂ crystal [125]. Asiri et al. stated that according to their investigations nitrogen or sulfur doping can substitute the titanium sites in small amounts without damaging the original tetragonal structure of titanium dioxide [126]. Therefore sulphur atoms in our titanate nanotubes probably resides in titanium sites and presence of sulphur atoms influence the local environment around oxygen vacancy defects and shifts the g value of unpaired electrons. Figure 5.14b shows both sulphur doped titanate nanotubes: 4STNTA350N₂ and 4STNTAH₂O₂350N₂. The only difference in samples is the hydrogen peroxide treatment (Figure 5.14b). The intensity of the ESR peak significantly low in hydrogen peroxide washed sample as expected. Values of g for both sulphur doped TNTs is 2.018.

Different g values for doped and undoped samples confirms the presence of sulphur in doped titanates.

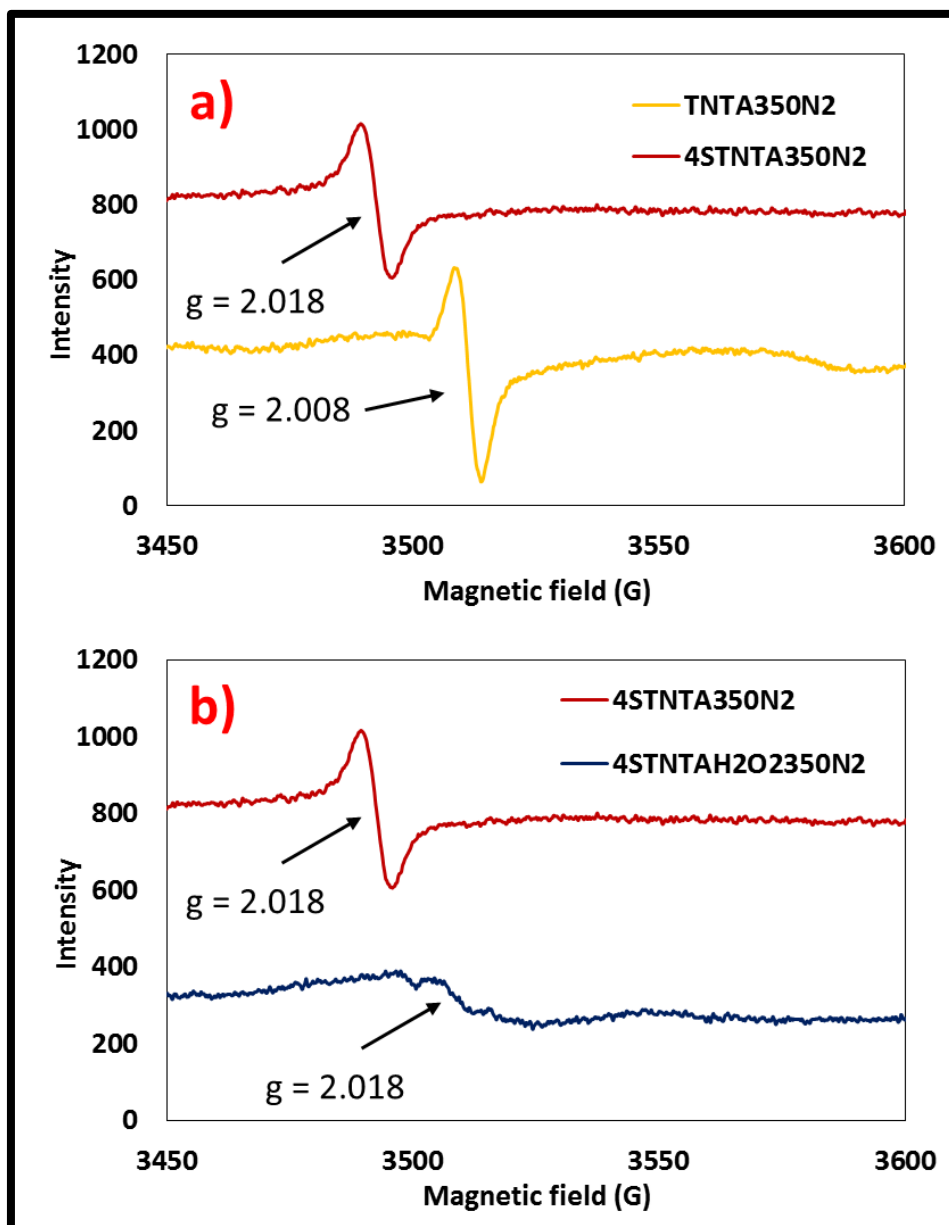


Figure 5.14 (a) Electron Spin resonance spectra of TNTA350N₂ and 4STNTA350N₂. (b) ESR spectra of 4STNTA350N₂ and 4STNTAH₂O₂350N₂.

5.1.3 Colloidal Coatings of Titanate Nanotubes

EPD was used to deposit TNT coatings on conductive substrates. Acid washed titanate nanotubes were used in deposition processes, they were not calcined. EPD from settling suspensions leads to gradient in deposition during EPD, thinner at the top thicker at the bottom. Therefore choosing right solvent and additive is important. Butanol was chosen as a solvent and Triethanolamine was chosen as additive in TNT suspensions. Butanol is simple alcohol having a backbone containing 4 carbon atoms. Butanols polarity is low which manifests itself as possessing a low dielectric constant (generally dielectric constant is needed to be high for a

successful EPD), but the benefit is its evaporation rate thereby, after deposition it slowly removes from the coating, which may lower the probability of cracking. We also tried IPA but IPA does not give stable suspensions.

TEA is a tertiary amine and used by some researchers to make stable suspensions of TiO_2 and to conduct EPD [127], [128]. We also used TEA in our previous study to aid dispersability of TNTs [19]. TEA has a nitrogen atom in the middle, bonded to 3 ethanol groups and it has a lone pair. TEA acts as a lewis base. Unbonded electrons dislodge protons from OH or OH^{2+} (OH^{2+} is formed after self protolysis of alcohol molecules) groups of alcohols on the surface of particles in proton rich environment, rendering the particle positively charged (Fig. 5.15). Therefore it provides electrostatic stabilization.

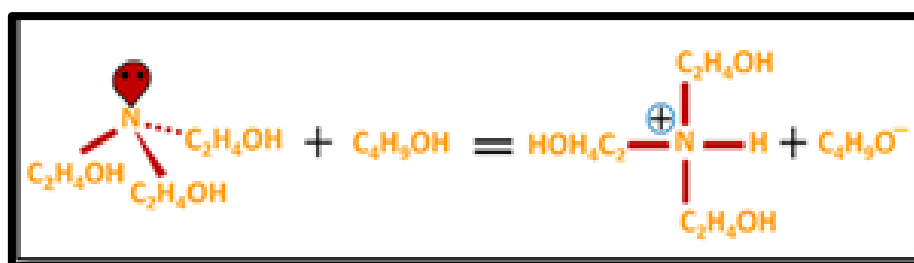


Figure 5.15 Schematic illustration of proton capture of TEA from butanol molecule.

Figure 5.16 shows the suspensions waited for 2 months. Immediately after resting, 0 g/L TEA containing suspension settles in hours but, even after two weeks all other suspensions show similar stability: white suspension at the top and a thin sediment at the bottom. At this stage the sedimentation behavior seem to be contradictory with surface quality of coatings obtained with respective suspensions explained below. But after waiting for around two months, 0.15 and 0.5 g/L TEA containing suspensions turn into a clear butanol at the top, a white slurry in the middle and a sediment at the bottom revealing that they are not as stable as the other TEA containing ones. For all the suspensions the pH is around 5. It is on isoelectric point of butanolic suspensions of TiO_2 and nanotubes (Suspensions and pure butanol have the same pH). Actually, with the addition of TEA the isoelectric point shifted towards higher pH values. Even though the 2 g/L or more TEA containing suspensions show high stability, immediately after resting all exhibit thin sediments. This may be because of the presence of hard big agglomerates of nanotubes which couldn't be broken during mixing. The most stable suspension was found to be 2g/L TEA containing suspensions.

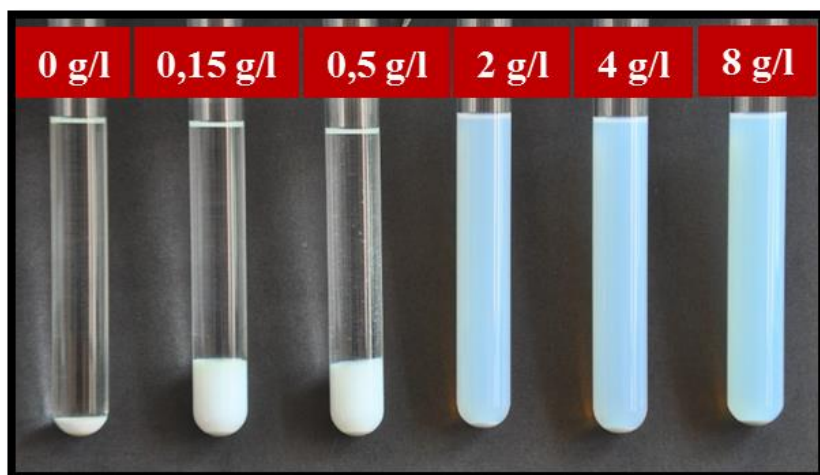


Figure 5.16 Image of 2 months waited TEA containing butanolic suspensions (4 g/L solid content is fixed for all samples.).

EPD processes were done under 65 V direct currents. 65 V was chosen because actually suspensions are prone to sedimentations. High voltages provide high rate of deposition. Dwelling time for coatings are fixed to 10 min. Ultrasonicated suspensions were waited for 5 min. to allow for the sedimentation of some amount of agglomerates. Figure 5.15a is the illustration of the set up for EPD process. Figure 5.17b shows coatings obtained from different suspensions. For all suspensions solid content is the same (4 g/L), but TEA content is varying from 0.15 to 4 g/l. Visual inspection of surface of coatings revealed that 0.15 g/L and 0.5 g/L TEA containing suspensions lead to rough surfaces. On the other hand coatings obtained from 2 g/L and 4g/L TEA containing suspensions resulted in smoother surfaces. It should be considered that optimum content of TEA is preferable for EPD because TEA may lead to porosity or cracking during removal from coating during calcination.

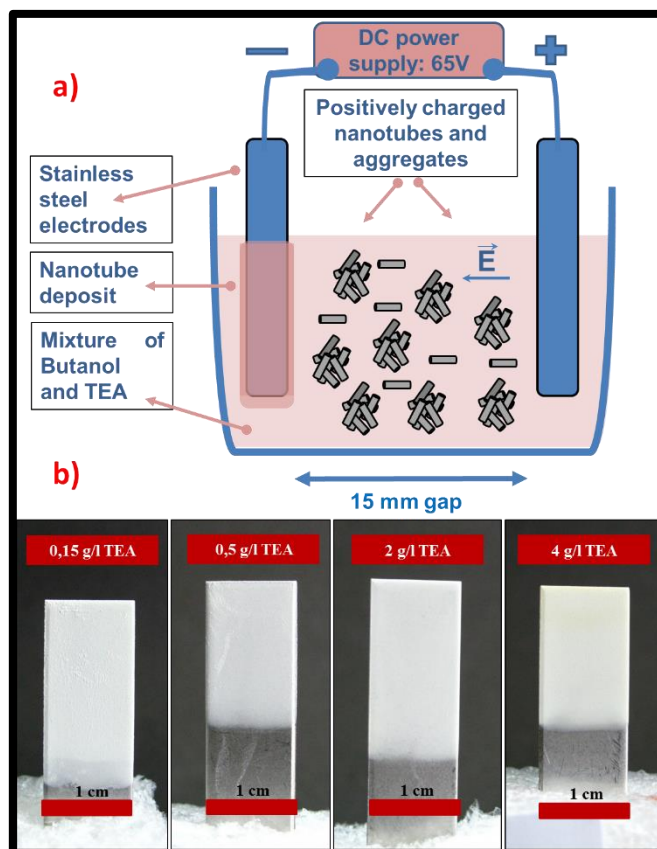


Figure 5.17 (a) Illustration of EPD cell, (b) images of as synthesized and acid washed nanotube (TNTA) coatings obtained from different suspensions with varying TEA content.

Titanate nanotube coating on metallic foams were also implemented. Figure 5.16a shows an uncoated metallic nickel foam. Figure 5.18b shows TNTA coating on nickel foam. SEM images of TNTA coatings are shown in Figure 5.18c and part d.

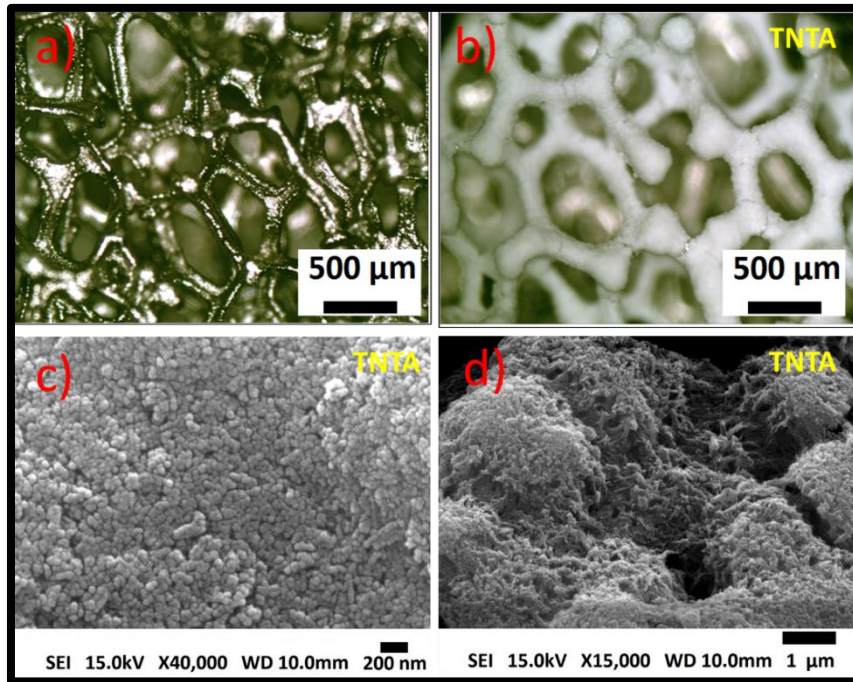


Figure 5.18 Optical microscopy images of uncoated metallic foam (a), TNTA coated metallic foam (b); (c) and (d) are SEM images of coatings on metallic foams.

5.2 Results

1. Sulphur doping lowers the crystallite size of TiO_2 .
2. Titanate nanotubes have around 10 nm in diameter and 100nm in length.
3. Doped or hydrogen peroxide washed or calcined nanotubes (up to 350 °C) have same diameter and length as acid washed as synthesized titanate nanotubes.
4. As synthesized titanate nanotubes contain oxygen vacancies and it is revealed after calcination under inert atmospheres. The resultant powders become grey.
5. Acid washed nanotubes exhibit high surface area (549 g/cm^2).
6. Hydrogen peroxide washing slightly increases crystallinity of titanate nanotubes by providing oxygen. Besides, H_2O_2 washed and calcined nanotube powders are white instead of being grey.
7. Band gap values for titanate nanotubes reveal that hydrogen peroxide washing redshifts the band gap (TNTA=3,4 eV, TNTAH₂O₂=3,33 eV).
8. Calcination under inert atmosphere also redshifts the band gap of acid washed titanate nanotubes (TNTA350N₂=3,30 eV).
9. Hydrogen peroxide washed and calcined samples exhibit highest redshift (TNTAH₂O₂350N₂=3,27 eV).

10. Sulphur doped titanate nanotubes do not exhibit a pronounced redshift. Calcined Sulphur doped titanate nanotubes show same band gap value as calcined undoped titanate nanotubes. Probability of synergistic effect is investigated as well. Sulphur doped hydrogen peroxide washed nanotubes does not show increased redshift (4STNTAH₂O₂350N₂=3,32 eV, 4STNTA350N₂=3,31 eV).
11. ESR studies revealed that titanate nanotubes contain single electron trapped oxygen vacancies on surface which can be eliminated by hydrogen peroxide washing.
12. Presence of sulphur is partially confirmed by comparing ESR signals of doped and undoped titanate nanotubes. Sulphur doped titanate nanotubes exhibit different value of g compared to undoped ones.
13. Triethanolamine was successfully used to make stable or semi stable suspensions of titanate nanotubes. It is also revealed that suspensions prepared with aged powders (1 year waited) exhibit lower stability.

GENERAL RESULTS AND DISCUSSION

6.1 Carbon Nanotube Dispersion in Organic Solvents and Quantitative Analysis

In this sections analysis results were briefly explained and reviewed.

6.1.1 SDBS Containing Suspensions

1. SDBS and PVP were successfully used to disperse MWCNTs in IPA. Additive (SDBS, PVP) concentration were kept 2 g/L and MWCNTs' concentration was (0.1 g/L). Subsequently ultrasonication (1 h. ultrasonic probe) and high power centrifugation (12000 RCF for 30min.) give rise to highly stable supernatants as evident by sedimentation tests and zeta potential measurements.
2. SDBS modified MWCNTs suspensions were prepared in ethanol, IPA, butanol, amyl alcohol, acetyl acetone and EG. Suspensions containing EG and ethanol does provide stability while using SDBS as additive. Other alcoholic suspensions exhibit high stability by which suspensions remain stable for months.
3. Stabilization mechanism of suspensions needs to be explained to clearly define the mechanism of stability in MWCNTs' suspensions. Stabilization of solid nanoparticles can be done in 3 different ways. One mechanism is electrostatic stabilization in which ions surrounding surface of particles prevent particles from clumping together, they repel each other because of the same charges they carry on the surface. Second is steric stabilization; steric forces can be thought of spaghetti like entities surrounding particle surfaces and this creates a barrier to agglomeration. There is also a possibility for combination of the stabilization mechanism listed above, called electro-steric stabilization in which long chains covering particles also carry electrical charges causing electrostatic stabilization. Third mechanism is depletion stabilization. In depletion stabilization hindrance of particle

attraction is done by entities between particles which do not adhere to the surface of particles.

Dispersion power of surfactants is the result of their molecular structure. For example, Rastogi et al. investigated 4 different surfactants [14]. They found that MWCNTs dispersing ability of follows this trend: SDS<Tween 20<Tween 80<Triton X-100. Triton X-100 is better because it has a benzene ring in its structure. Benzene molecules interact with π conjugated system of nanotubes by π - π stacking interaction [129]. SDBS is a well-known surfactant readily used in dispersion processes of MWCNTs and SWCNTs [130], [131], [5], [132]. Because it contains a pyrene/benzene ring in its structure as well. Under the presence of SDBS nanotube surface become adsorbed by surfactant molecules. SDBS form hemi-micelles on nanotube surfaces. SDBS molecules probably tend to form cylindrical micelles in bulk liquids. This is evident in zeta potential analysis results performed by us. Only SDBS containing IPA suspensions exhibit zeta potential distribution curves having broad FWHMs. Broad zeta potential distribution curves can be a result of presence of rod-like particles or cylindrical micelles in our case. Therefore, SDBS molecules probably form hemicylindrical micelles on nanotube surfaces. This find can be reinforced by using static light scattering measurements, because scattered light intensity is related to the shape of the particle.

Presence of SDBS provides electrostatic stabilization on nanotube surface. SDBS as being a surfactant composed of hydrophilic head group and hydrophobic tail. In hydrophilic side Na^+ dissociates and leave a negatively charged head group behind in polar solvents. Therefore, zeta potential of MWCNTs-SDBS aqueous suspension in natural pH values should exhibit negative sign of charge. On the other hand surfactants behave differently in non-polar media, namely zeta potential values of SDBS suspensions is positive in IPA. Because sodium ions in head groups stay undissociated in IPA at relatively high concentrations. Very dilute suspensions of SDBS-IPA may have a negative sign of charge.

4. UV-Visible absorption spectroscopy and TGA analysis were used to estimate the quantity of SDBS in suspensions. Initially 2 g/L SDBS and 0,1 g/L MWCNTs containing uncentrifuged suspensions turns out to contain around 1,6 g/L SDBS and approximately 0,06 g/L MWCNTs in suspensions (obtained result by UV-Vis measurement).
5. Though it is out of scope to better understand the dispersion behavior of SDBS, we also prepared suspensions having different initial concentrations: 2 g/L SDBS and 0.2 g/L MWCNTs. After centrifugation (12000 RCF 30 min.), this suspensions contain SDBS around 1.4 g/L and MWCNTs around 0,1 g/L (They are denoted as SDBS 0.2MWCNTs

IPA). In SDBS MWCNTs IPA, SDBS/MWCNTs weight ratio is ~ 32 and SDBS/MWCNTs weight ratio of SDBS 0.2MWCNTs IPA is ~14. It should be noted that suspensions were rested after centrifugation and measurements were conducted on suspensions which were decanted on the top of this rested suspensions.

Zeta potential measurements conducted on these different supernatants revealed that SDBS 0.2MWCNTs IPA has a zeta potential value of 53.3 mV and that of SDBS MWCNTs IPA has a value of 44.6 mV. Though SDBS 0.2MWCNTs IPA contains less SDBS and higher amount of MWCNTs, its stability is higher. The reason behind this phenomenon can be explained as follows:

At low concentrations SDBS molecules accumulate on nanotube surface because of their affinity. After saturation of nanotube surfaces excess SDBS molecules starts to form micelles in the bulk solution. Increasing concentration of SDBS above a certain concentration increases the size of micelles only. Big micelles exhibit lower electrophoretic mobility compared to small ones. Therefore, Zeta potential values of SDBS MWCNTs IPA is 44.6 mV and that of SDBS 0.2MWCNTs IPA is 53.3 mV.

It should be noted that pristine (unfunctionalized) MWCNTs (0.1 g/l) IPA suspensions are not stable. Non-functionalized pristine nanotubes does not totally sediment, but networks of agglomerates of nanotubes can easily be seen with naked eye. This may be arising from loose agglomeration of nanotubes having low density so they stay without sinking.

6.1.2 PVP Containing Suspensions

1. PVP was successfully used to disperse MWCNTs in IPA, butanol and in EG. Ipanolic suspensions were selected for further investigation. 2 g/L PVP and 0.1 g/L MWCNTs were mixed ultrasonically and centrifuged. After centrifugation the supernatant contains around 1.95 g/L PVP and 0,092 g/L MWCNTs. It is revealed most of PVP and MWCNTs remain in supernatant.
2. PVP-MWCNTs IPA suspensions have -35.9 mV zeta potential, this value is better than uncentrifuged suspension (-34.9 mV) revealing that agglomerates sediment out in suspensions. Sign of charge is negative. Stability of this suspension is believed to be obtained by steric stabilization. PVP molecules adsorb on nanotube surfaces due to the presence of heterocyclic ring structure present in branches of polymer backbone. Wang et al. [21] stated that in polar solvents electron density in heterocyclic ring localized on nitrogen atom creating negatively charged oxygen containing carbonyls. This negatively charged carbonyls is account for negative sign of charge of suspensions. Positively charged

nitrogen should be shielded by polymer backbone and does not contribute to charge generation.

6.1.3 UV-Vis Spectroscopy and Thermogravimetric Analysis

1. UV-Vis spectroscopy is coupled with thermogravimetric analysis to determine the material content in SDBS/PVP MWCNTs suspensions.
2. Dilution was found a critical factor to make accurate quantitative analysis by UV-Vis spectroscopy. It is also found that quantitative analysis can be possible around UV cut off wavelength of solvent, since generally devices accurately measure below absorbance value of 2 and above 0.2.
3. PVP-MWCNTs IPA and SDBS MWCNTs IPA suspensions binary systems in terms of solid material content, and unfortunately UV-Vis spectra of these suspensions contain overlapping peaks. These peaks may be used for quantitative analysis if they only represent quantity of one material. Attal et al. [24] dealt with that problem and subtracted the contribution of SWCNTs by using CTAB-SWCNTs suspension spectrum from SDBS-SWCNTs spectrum while the two spectra are overlapping in visible range. The resultant spectrum belongs only to SDBS and by using a calibration curve they obtained the SDBS concentration in suspensions. We followed similar route to determine surfactant and polymer concentrations. They used CTAB for dispersion of SWCNTs in suspensions used for subtraction because CTAB does not absorb photons in UV-Vis spectra. Because of it all the information is due to SWCNTs in CTAB-SWCNTs' spectra.
4. In our study we followed slightly different path. UV-Vis spectroscopy is suitable for stable suspensions or solutions, therefore subtraction suspensions couldn't be prepared by simple ultrasonication of MWCNTs in IPA. Although aqueous suspensions of CTAB-SWCNTs is stable, CTAB-MWCNTs IPA suspensions are not stable. The reason behind this was explained Clark et al. [132]. They stated that dispersion of MWNTs in an aqueous media is strongly diameter dependent suggesting that information gathered by examining SWNT dispersions may not be applied on MWNT dispersions.
To get over this problem we prepared carboxyl functionalized carbon nanotubes (COOH), then we dispersed COOH MWCNTs in IPA. It should be noted that UV-Vis spectra of COOH MWCNTs IPA suspensions or pristine MWCNTs containing suspensions does not exhibit any difference. We haven't detected peaks related to COOH functional groups.
5. A technique which can be called overlapping method was used to determine quantity of MWCNTs in suspensions. Before centrifugation quantity of MWCNTs is known in

suspensions if they are properly diluted, the obtained spectrum reflects a certain amount of MWCNTs. We also diluted supernatants till they overlap with uncentrifuged suspensions and determined MWCNTs' concentration. This method is simple but gives underestimated results. Extinction coefficients of agglomerated suspensions are low compared to exfoliated suspensions as Giordani stated [88]. This means that if spectra of two suspensions containing same amount of MWCNTs are compared in terms of their absorbance behavior, spectra obtained from agglomerated suspensions would have low absorbance. In PVP suspensions the underestimation turns out around 10% if they are compared with TGA analysis results.

6. Thermogravimetric analysis was implemented on dried sediments and supernatants. Characteristic mass losses of SDBS and PVP at particular temperatures enabled calculation of additive content in supernatants. Unfortunately, it is not easy since dried supernatants, precipitates and pure additives show different mass losses at low temperatures. This problem could be gotten over by shifting 2 of the curves on y axis at a particular temperature suitable for that system to overlap all the curves at that temperatures. Then, calculation of mass ratio was successfully done. Particular temperature to shift the curves is obtained by using derivatives of mass loss curves. It is found that using precipitate can give better results for determination of MWCNTs' quantity since in precipitate MWCNTs ratio is high. This was also encountered and explained in the work of Shtein et al. [25].

6.1.4 EPD and Estimation of Coating Thickness

1. EPD experiments were conducted using $MgCl_2$ added PVP-MWCNTs IPA suspensions. It is known that charger salts provide adhesion to substrates [93]. Three suspensions were evaluated to determine the optimum amount of Mg^{2+} ions for deposition. The better the zeta potential of suspensions, the better quality of electrophoretic coatings [93]. By considering this information 9 mM Mg^{2+} ion containing suspensions were chosen for EPD experiments. Under 50 V DC potentials 10 min coatings could end up smooth coating surface. UV-Vis spectroscopy was successfully used to assess the quantity of PVP and MWCNTs in coatings. Thickness of the coating was calculated using density values of each component and UV-Vis concentration results.
2. SEM images of cross-section view of MWCNTs coatings reveals that coating thickness is around 20 μm . On the other hand UV-Vis spectroscopy results yield $\sim 9 \mu m$. The difference probably arising from porosity in the coating. Estimation neglects porosity.

6.2 Carbon Nanotube/Iron Oxide Hybrid Nanoparticles

1. Many studies in making core-shell $\text{Fe}_3\text{O}_4@\text{C}$ nanoparticles contain various starting materials during production. In composite making additives influence the dispersibility of at least one of the components. For example Fe_3O_4 nanoparticles can be synthesized by using Fe^{3+} ion containing metal salts such as iron chloride (FeCl_3). 1/3 of iron needs to form Fe^{2+} ions to produce Fe_3O_4 during synthesis. This can be achieved by addition of other materials such as ammonium acetate. Complex reaction forms Fe_3O_4 in solvothermal or hydrothermal condition. The benefit of this technique is during the mixing process, there is no need for inert atmosphere, but in composite making with carbon nanotubes presence of additives may have a big influence on final properties.

In first trial and error approaches on producing carbon nanotube/ Fe_3O_4 hybrids. Highly dispersed carbon nanotubes were mixed with iron chloride solutions and then hydrazine was added to the system. Immediately after hydrazine addition nanotubes phase separate which can easily be seen even with naked eye. In latter experiments, we found that by using FeSO_4 homogenous dispersion of carbon nanotube/ $\text{Fe}(\text{OH})_2$ intermediate hybrid suspensions could be formed before solvothermal synthesis. FeSO_4 interacts with NaOH or carbamide (urea) and form $\text{Fe}(\text{OH})_2$. The choice of FeSO_4 is appealing because before synthesis suspension contains $\text{Fe}(\text{OH})_2$, excess NaOH and small amount of NaSO_4 in the structure. The evolution of small amount of materials is reflected in homogeneity in carbon nanotube and $\text{Fe}(\text{OH})_2$ containing suspensions when viewed with naked eye. There are two aspects needs to be considered when using FeSO_4 . FeSO_4 cannot be dissolved in semi polar or non-polar solvents. However carbon nanotubes are mixed with raw materials of iron oxide while dispersed in semi polar solvents. To overcome this problem FeSO_4 is dissolved in EG. (We also found that PVP can homogeneously disperse MWCNTs in EG but SDBS does not work well in EG.). Second problem is Fe^{2+} ions tend to oxidize in air. Therefore when using FeSO_4 , mixing and if possible synthesis should take place in inert atmosphere. We provide semi-inert atmosphere by bubbling nitrogen during ultrasonic mixing of raw materials.

In addition EG is a well-known reducing agent. It prevents oxidation of iron hydroxide to a certain degree. We also investigated the amount of EG needed to successfully produce iron oxide nanoparticles out of FeSO_4 . Namely, 20 ml of EG is sufficient for 0,001 mole iron sulfate to form iron oxide nanoparticles in 60 ml EG/IPA mixture. Immediately after mixing, mixture of raw materials should be placed in Teflon lined autoclave and sealed, otherwise Fe^{2+} ions oxidizes.

2. Crystal shape is governed by internal factors such as inherent crystal structure and external factors such as temperature, time and surfactants [133], [134], [135], [136]. Fe_3O_4 has an inverse spinel crystal structure. Under equilibrium conditions Fe_3O_4 crystals form octahedral nanoparticles to minimize the surface energy ((111) planes enclose all space). In this study, solvothermal synthesis of Fe_3O_4 nanoparticles is achieved by treatment at 200 °C for 12 hours (without additive). The resultant nanoparticles are octahedral in shape and around 175 nm in diameter.
3. Fe_3O_4 @C nanoparticles were prepared by using glucose and ascorbic acid as carbon sources. Under hydrothermal conditions in only glucose containing environments, glucose polymerized into polysaccharides by intermolecular dehydration and then carbonizes to form nanospheres [63], [137]. First attempts on encapsulation of materials with carbon was done using noble metal particles in literature. Noble metals exhibit catalytic behavior and carbon evolution proceeds around them, Wang et al. expand this to iron oxide containing core-shell nanoparticles [138].
In our studies, ascorbic acid and glucose were used to coat iron oxide particles' surfaces during solvothermal synthesis. We used same temperature regime as Zheng et al's [65]. In their study, they processed raw materials at 200 °C for 12 h in one step.
4. Ascorbic acid is known to coat iron oxide surface at mild temperature conditions during synthesis [102]. Ascorbic acid can also be used as an additive to provide carbon to the structure. At high temperatures ascorbic acid carbonizes. In our study, FTIR analysis of ascorbic acid aided synthesis of iron oxides nanoparticles revealed that ascorbic acid decompose partially during synthesis and evolve aromatic compounds and amorphous carbon on iron oxide surface. C=C vibrations at 1620 cm^{-1} is an indication of carbonization of ascorbic acid similar to results of glucose assisted synthesis [65]. FTIR analysis of products obtained using ascorbic acid or glucose are almost identical in terms of present peaks.
5. Mole ratios of FeSO_4 /Glucose and FeSO_4 /Ascorbic acid are 5, 1.25 and 0.625 were evaluated. Presence of this organic compounds change crystal morphology and particle size. Namely, under the presence of this compounds spherical superparticles consisting of smaller spherical particles emerge. We also found that mole ratios of FeSO_4 /Glucose and

FeSO₄/Ascorbic acid 1.25 is around the threshold for total conversion of octahedrons into spherical superparticles.

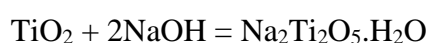
6. In ascorbic acid assisted synthesis, as the quantity of ascorbic acid increases the average particle size increases (from 310 nm to 480 nm and 590 nm). Comparison of FTIR analysis on two products having FeSO₄/Ascorbic acid mole ratios 1.25 and 0.625 reveals that higher amount of ascorbic acid intensifies C=C vibration peaks and hence it can be deduced that carbon shell around particles thickens as ascorbic acid concentration increases.
7. FeSO₄/Glucose and FeSO₄/Ascorbic acid mole ratio of 5 is not enough to totally hinder emergence of octahedrons to form Fe₃O₄@C superparticles or microspheres having spherical shapes. In glucose assisted synthesis spherical particles have average diameter of 850 nm. On the other hand, octahedron have around 300 nm in diameter. This is also encountered in ascorbic acid assisted synthesis results.
8. Glucose assisted synthesis results are different from ascorbic acid assisted synthesis results. If FeSO₄/Glucose mole ratio is 1.25 average particle size is 1060 nm, on the other hand FeSO₄/Glucose mole ratio of 0.625 results in 900 nm of average particle diameter.
9. Specific surface area of samples revealed that they are non-porous materials, having around 10-20 m²/g specific surface areas.
10. It is also found that PVP addition drastically lowers particle size in ascorbic acid assisted synthesis results. Negatively charged carbonyl groups present in PVP molecules probably act as nucleation sites for iron oxide nanoparticles and thereby particle size decreases dramatically. This effect is also seen in carboxyl group functionalized carbon nanotubes containing synthesis products in which presence of carboxyl groups drastically lowers particle size.
11. Evaluation of productability of carbon nanotube/ Fe₃O₄@C hybrid nanoparticles revealed that carbon nanotubes does not form entangled networks inside and outside of nanoparticles to form a wool yarn like hybrid nanoparticles as expected. During washing steps under the presence of magnetic fields iron oxide nanoparticles move towards to magnets, on the other hand MWCNTs remain in suspensions. In our first trial an error approaches, we obtained particles resembling wool yarns containing iron oxide nanoparticles covered by carbon nanotubes, but extensive investigations revealed that nanotubes cover surface of iron oxide nanoparticles with the aid of SDBS and PVP present in structure not by interaction with Fe₃O₄@C surface and carbon nanotube surface. Unfortunately, during extensive magnetic separation/filtration steps after synthesis. Containers containing synthesized products generally placed on a neodymium magnet and after each sedimentation water or IPA at the

top of the bottle taken away and pure IPA and water poured down to bottle. After several washing steps, phases start to separate probably because of change in ionic concentration of the suspensions. Namely, high amount of NaOH in synthesized suspension initially causes sedimentation of both carbon nanotubes and iron oxide nanoparticles. As the washing steps continues, carbon nanotubes stabilizes in suspensions while iron oxides are attracted to magnets.

12. Carbon shell around iron oxide nanoparticles is probably rich in functional groups such as hydroxyls. This hydroxyl groups may form hydrogen bonds between functional groups of PVP and SDBS, but does not interact with pristine MWCNTs.
13. We also know that production of Fe₃O₄@C/MWCNTs hybrid nanoparticles possessing interaction between components could be produced by using functionalized carbon nanotubes. In our study we didn't implement such method because our aim is to make hybrid materials using intact nanotubes.
14. Pure Fe₃O₄ nanoparticles exhibit 175 nm average diameter if there is no additive present during synthesis. However provided that PVP is added as a dispersant to the system particle size increases. Interestingly, Ascorbic acid and PVP aided synthesis of MWCNTs-Fe₃O₄ nanostructures reveals that particle size substantially decreases. Probably aromatic group on PVP interacts with ascorbic acid or other derivatives during crystallization process and Carbon/Fe₃O₄ particle size decreases. Initially we aimed to have this effect. However we expected that PVP molecules attached on MWCNTs surface may provide crystallization sites for carbonized Fe₃O₄ nanoparticles and hence MWCNTs surfaces will be covered with nanoparticles. Unfortunately, it seems that crystallization is not limited to nanotube surface during synthesis.

6.3 Synhtesis and Characterization of Titanate Nanotubes

1. Synthesis of titanate nanotubes aroused interest in scientific community because if they possess catalytic behavior they can be utilized in many pollutant removal applications since they exhibit high surface area. Under alkali hydrothermal conditions between around 110 °C and 150 °C titanium dioxide decompose and rearrange to form layered titanates, probably to minimize surface energy this layered titanates wrap on themselves forming scroll-like or onion-like cylinders called titanium nanotubes or more realistically titanate nanotubes. Jin et al. reported that the product is Na₂Ti₂O₅.H₂O and the reaction formula is [114]:



Limitation of use of titanate nanotubes is the presence of sodium ions between layers. During photocatalysis electron hole pairs generate. The rate of combination of electron hole pairs effect photocatalytic activity. Presence of sodium increases the rate of combination therefore, it is not wanted.

1. Samples were synthesized at 130 °C for 24 h. After synthesis titanate nanotubes contains high amount of sodium between titanate layers. In this state, material is sodium titanate. After extensive washing with water and subsequently with 0.1 M HCl most or all of the sodium is removed from the system by intercalation with protons. In this state, material is called hydrogen titanate.
2. Several nanotubes are characterized. Effect of water washing, acid washing or acid and subsequent hydrogen peroxide washing on nanotube properties was evaluated. Influence of calcination temperature on integrity and electronic properties was also investigated. Finally, some nanotubes were produced from sulphur doped TiO₂ powders, we also assessed the properties of this doped titanate nanotubes.
3. XRD analysis of only water washed titanate nanotubes have a distinctive peak at 2 theta degree of 28° (600) can be assigned to sodium titanates revealing that water washing does not totally remove Na⁺ from nanotubes. Peak at 10° (2theta) is caused by diffraction of X-rays between the layers of nanotubes. The interlayer distance between nanotubes is 0.78 nm. This peak is clear when encountered in as synthesized nanotubes. Since calcination disrupts the integrity of tubular structure of nanotubes, presence of this peak is also affected from calcination.

The diffraction peaks of 10°, 24°, and 48° can be assigned to hydrogen titanates. N. Xiao et al. attribute this structure to H₂Ti₄O₉·H₂O [115]. Du et al. assigned this to layered titanate H₂Ti₃O₇ [116]. As synthesized nanotubes are low in crystallinity as confirmed by XRD analysis. Khan et al. used hydrogen peroxide to modify nanotubes [117]. They showed that low crystallinity of nanotubes can be enhanced with H₂O₂ treatment and after H₂O₂ treatment they calcined their sample in air at 350 °C. The resultant material exhibit XRD peaks absent in untreated ones. We implemented hydrogen peroxide washing at room temperature. XRD patterns of Hydrogen peroxide washed and calcined samples revealed that some peaks are beginning to emerge unlike “only acid washed” samples, but our results does not contain intense peaks of TiO₂. We found that the difference between our studies and Khan et al.’s studies is the hydrogen peroxide washing/treatment temperature. They implemented that treatment at 40 °C.

4. XRD graphs of nanotubes obtained from sulphur doped nanotubes (4STiO₂) is also different from the other samples. Sulphur doped sample has clearly lower crystallinity compared to “acid washed and calcined” (350 °C), and “hydrogen peroxide washed and subsequently calcined (350 °C)” samples.
5. If calcination temperature is raised to 450 °C, nanotubes transform into anatase form of TiO₂. 2 theta degree of 10 almost disappears at this temperature range.
6. TEM analysis revealed that calcination temperature of 450 °C is high. At this temperature range nanotubes collapse and form small rods and particles of anatase TiO₂. Calcination temperature of 350 °C is suitable to preserve tubular structure. When we compare TEM images of as synthesized nanotubes (uncalcined) and calcined nanotubes at 350 °C, we see there is almost no difference in terms of morphology and length.
7. Synthesized nanotubes are 100 nm in length and around 10 nm in diameter (according to TEM observations). They exhibit scroll-like or onion-like structure.
8. H₂O₂ washing on nanotubes does not seem to negatively affect nanotube morphology.
9. Surface area of acid washed hydrogen titanate nanotubes revealed that nanotubes exhibit a high specific surface area reaching 549 g/m².
10. UV-Vis absorption spectroscopy was used to assess the band gap values of titanate nanotubes.

Tauc relation [139] is used for determination of optical band gap of products:

$$\alpha h\nu = A(h\nu - E_g)^n$$

A is a constant, $h\nu$ is photon energy, E_g is the band gap energy, $n = 1/2$ for allowed direct transition and $n = 2$ for allowed indirect transition.

$\alpha = 2.303A/d$, where d is the path length of the cuvette and A is the absorbance determined from the UV-visible spectrum [140] [141]. Average band gap is calculated from the intercepting linear portion of $(\alpha h\nu)$ vs. $h\nu$ plot on $h\nu$ axis where $\alpha h\nu$ is zero.

Titanate nanotubes are indirect semiconductors [142], [143]. Therefore, their band gaps were obtained from this equation below:

$$(\alpha h\nu)^{1/2} = A(h\nu - E_g)$$

11. UV-Visible absorption spectroscopy is only applicable to stable and transparent or semitransparent materials. To achieve this goal triethanolamine (TEA) was used as dispersant. 0.5 g/L TEA and 1 g/L TNT is mixed in butanol by ultrasonication. Filtration with 0.45 μm filter allow production of stable, transparent suspensions. UV-Vis spectra only belonging to TNTs were extracted by subtracting contributions (absorbance) of butanol and TEA.

12. Particle size analysis (Dynamic light scattering) were also conducted on nanotube suspensions. Because band gap of semiconductors is also influenced by particle size. We didn't only rely on TEM measurements since ultrasonication can cause shortening of TNTs.
13. It is found that different TNTs exhibit same intensity profile and almost same average particle size values (around 110 nm). This finding reveals that aggregation behavior of TNTs are almost same even they are as synthesized, calcined (350 °C) or H₂O₂ washed. It should be noted again that the TEM images of TNTs revealed that nanotubes are around 100 nm in length and 10 nm in diameter.

DLS is designed to accurately measure spherical particles. If rod-like particles are being measured by DLS, particle size result is a spherical particle having same diffusion coefficient as those rod-like particles. In addition, DLS results differ from TEM or SEM results for another reason: DLS measures hydrodynamic radius. Particles or aggregates have electrical double layers around them which influence DLS measurements. If individual nanotubes were present in suspension DLS result would be probably between 30 nm to 40 nm. 110 nm of average particle size means: titanate nanotubes are present as small bundles in these filtered suspensions. These small bundles probably consist of 3 to 5 nanotubes. We suspected that nanotubes may exhibit different photon absorption and scattering behavior due to difference in interaction with additive or solvent molecules and due to particle shape when they stay individual or in bundled form. They are in bundled form and in each bundle almost same amount of TNTs are present. Therefore we believe that comparison of obtained values by means of UV-Vis absorption spectroscopy is believed to be relevant.

14. Calculated band gap values of TNTs are as follows:

$$\text{TNTA}=3.4 \text{ eV},$$

$$\text{TNTAH}_2\text{O}_2=3.33 \text{ eV},$$

$$4\text{STNTAH}_2\text{O}_2/350\text{N}_2=3.32 \text{ eV},$$

$$4\text{STNTA}/350\text{N}_2=3.31 \text{ eV},$$

$$\text{TNTA}/350\text{N}_2=3.30 \text{ eV},$$

$$\text{TNTAH}_2\text{O}_2/350\text{N}_2=3.27 \text{ eV}.$$

15. When as synthesized acid washed TNTs are compared with their calcined (350 °C under N₂ atmosphere) ones. We encounter that calcination causes redshifting (TNTA=3.4 eV, TNTA/350N₂=3.30 eV). Hydrogen peroxide washing provide almost the same band gap value on as synthesized (without implementation of calcination) TNTs, but if hydrogen

peroxide washed TNTs are subjected to calcination band gap value reaches the lowest level observed: $\text{TNTAH}_2\text{O}_2\text{350N}_2=3.27$ eV. We had also used 4S-TiO₂ powders to produce doped TNTs called 4STNTs. We found out that calcined 4STNTs is not different from calcined undoped TNTs in terms of band gap values. To make a comprehensive statement over this issue we also washed 4STNTs with hydrogen peroxide to look for whether there is a synergistic effect present or not (between crystallinity and presence of sulphur). Unfortunately, band gap value is even higher than “as synthesized and calcined nanotubes”. We can conclude that synthesized and processed nanotubes in this study have band gap values around 3.3 eV and the lowest band gap value could be obtained by samples which are calcined at 350 °C and at the same time H₂O₂ washed.

It should be noted that UV-Visible absorption spectroscopy is rarely used to determine band gap values of semiconductors. Instead UV-Vis diffuse reflectance spectroscopy is utilized since it measures the samples in powder form. Our measurements were conducted using colloids. Solvents and additives may influence the absorption spectra and can yield misleading results.

16. ESR spectroscopy is conducted to acquire a deeper understanding of electronic structure of nanotubes. ESR spectra of acid washed and calcined (350 °C under nitrogen atmosphere) undoped nanotubes (TNTA350N₂) exhibit only one symmetrical ESR signal which can be attributed to SETOV. A symmetric ESR signal for SETOV ($g= 2.003$) and an asymmetric ESR for Ti³⁺ ($g= 1.98$) can be observed in titanate nanotubes [124]. All investigated nanotubes exhibit same SETOV signal. We also found that signal intensity increases as the calcination temperature increases (under inert atmosphere). This implies that amount of oxygen vacancies increases during annealing under inert atmosphere conditions. Hydrogen peroxide washed TNTAs has significantly low ESR signals compared to TNTA350N₂ and TNTA450N₂. It can be deduced that H₂O₂ treatment compensate for the oxygen vacancy defects on nanotube surfaces, since the ESR intensity of peroxide treated nanotubes is very low, we deduce that most of the oxygen vacancies resides on nanotube surfaces.
17. Sulphur doped samples exhibit different g values compared to undoped ones. Both 4STNTA350N₂ and 4STNTAH₂O₂350N₂ have g values of 2.018. On the contrary, for example TNTA350N₂ and TNTA450N₂ have a g values of 2.008 and 2.005, respectively. The shift in g values of sulphur doped samples is attributed to change in the environment around paramagnetic centers. Namely, sulphur atoms substitute titanium atoms and this effects paramagnetic behavior of the whole structure.

18. It is reported that SETOVs act as recombination centers for generated electron hole pairs and photocatalytic behavior becomes bad [123]. UV-Vis measurement results and ESR measurement results are in correlation with each other. Although there is slight changes in found band gap values, the most redshifted band gap is obtained in hydrogen peroxide washed TNTAs. The lowest ESR signal for SETOV is also obtained at H₂O₂ washed TNTAs.

6.3.1 Suspension Preparation and EPD of TNTs

19. It is important to prepare stable suspensions to enhance photocatalytic efficiency of titania nanoparticles. Besides, suspensions stability also effects coating properties [128]. The same is true for titanate/titania nanotubes and any other materials. Stability of suspensions is the reflection of repulsion of particles in suspensions via the ions or molecules surrounding particles. Ions dissociate and tightly or loosely bind to the surface of particles to construct electrical double layers. Solvents ability to dissociate ions directly influences the suspensions stability. Therefore, aqueous suspensions is a good choice at first glance since water has a dielectric constant of 80. However we have also implemented EPD on suspensions. EPD processes are generally conducted in alcoholic suspensions. Because aqueous suspensions generate bubbles of oxygen and hydrogen on the electrode surfaces during EPD above 4V. In our experiments we used butanol to prevent gas evolution during coating processes. Unfortunately, butanol does not provide stability on its own. Therefore, TEA was used as a dispersant in suspensions. TEA is a suitable choice for use in stable alcoholic suspensions. Therefore, it was used successfully in some studies [128], [144].

20. Butanol was chosen for the preparation of TNT (Acid washed as synthesized TNTs: TNTA) suspensions. Using only butanol does not provide stable TNT suspensions. TEA addition to butanol provide stability. IPA was also investigated. Unfortunately, IPA does not provide stability even if TEA is used in suspensions. It is found that for 4g/L TNT containing butanolic suspensions, 2 g/L TEA is suitable to conduct relatively successful EPD. Success of EPD processes is evaluated by visual inspection of surface roughness of coatings. 4 g/L TNTs is too much to provide the whole material to sustain in dispersed state. Therefore, after ultrasonication processes suspensions were rested around for 5 min. Some of the particles were sediment and EPD processes conducted on supernatants. Considerable amount of the solid sediment after 1 day of sedimentation, but 2 g/L, 4 g/L and 8 g/L TEA containing suspensions still exhibit milky appearance. Excess amount of TEA in suspensions reflects itself a gradually increasing yellowish color in coatings. Since presence

of higher amount of foreign material other than TNTs may cause porosity during the removal, 4 g/L or 8 g/L TEA containing suspensions were discarded. Removal of TEA by heat treatment is possible while preserving nanotube integrity since TEA leaves the system at around 300 °C.

21. Unfortunately, we found that character of TNTs changes over time in terms of suspensions stability. Around 1 year after synthesis, same acid washed TNT powders does not provide same stability even if they are mixed with TEA in butanol.
22. SEM images of coatings revealed that TNTs are in agglomerated form.

6.4 Future Work

1. Aromatic adsorbents effects the electronic structure of carbon nanotubes and it leads to change in absorbance [145]. When comparing different surfactant/MWCNTs suspensions having different ratio of components this absorbance may limit the precise identification of quantities. Therefore its effect should be investigated to make a correlation.
2. Stages of surfactant adsorption on nanotube surface involves adsorption of surfactant monomers (i), then monolayers (ii), hemimicelles (iii) and formation of micelles in bulk solution (iv) [146]. This stages could be investigated in order to find lowest amount of surfactant should be added to the suspensions while rendering highest amount of MWCNTs become individually suspended in suspension. Because presence of surfactants or additives may adversely effect the properties of functional coatings or composites.
3. It is found that pristine carbon nanotubes does not at least sufficiently interact with carbonized surfaces during hydrothermal conditions. This insufficiency may be hindered by elimination of functional groups on carbonized surfaces of Fe₃O₄ nanoparticles. Therefore, suitable reducing agents like hydrazine may serve for this purpose.
4. Unlike making one step synthesis two step synthesis can be employed. Synthesized and calcined Fe₃O₄@C nanoparticles may be mixed with pristine carbon nanotube suspensions to make functional nanocomposites.
5. Sulphur doping on nanotubes may be differently implemented. Proses may be implemented as follows: synthesized undoped nanotubes may be treated with sulphur containing compounds.

REFERENCES

- [1] Iijima, S., (1991). "Helical microtubules of graphitic carbon" *Nature*, (354):56–58.
- [2] Dresselhaus, M.S., Dresselhaus, G., and Saito, R., (1995). "Physics of carbon nanotubes" *Carbon*, 33(7):883–891.
- [3] Iijima, S., (2002). "Carbon nanotubes: Past, present, and future" *Physica B: Condensed Matter*, 323(1-4):1–5.
- [4] Berber, S., Kwon, Y. and Tomanek, D., (2000). "Unusually high thermal conductivity of carbon nanotubes" *Physical review letters*, 84(20):4613–6.
- [5] Vaisman, L., Wagner, H. D. and Marom, G., (2006). "The role of surfactants in dispersion of carbon nanotubes." *Advances in Colloid and Interface Science*, 128-130(2006):37–46.
- [6] Clark, M. D. and Krishnamoorti, R., (2009). "Dispersion of functionalized multiwalled carbon nanotubes" *Journal of Physical Chemistry C*, 113(49):20861–20868.
- [7] O'Connell, M. J., Boul, P., Ericson, L. M., Huffman, C., Wang, Y., Haroz, E., Smalley, R. E., (2001). "Reversible water-solubilization of single-walled carbon nanotubes by polymer wrapping" *Chemical Physics Letters*, 342(3-4):265–271.
- [8] Bergin, S., Sun, Z., Rickard, D. and Streich, P., (2009). "Multicomponent solubility parameters for single-walled carbon nanotube– solvent mixtures Cited by me" *Acs Nano*, 3(8):2340-2350.
- [9] Monthieux, M., Smith, B. W., Burteaux, B., Claye, A., Fischer, J. E. and Luzzi, D. E. (2001). "Sensitivity of single-wall carbon nanotubes to chemical processing: an electron microscopy investigation" *Carbon*, 39(8):1251–1272.
- [10] Shieh, Y. T., Liu, G. L., Wu, H. H. and Lee, C. C., (2007). "Effects of polarity and pH on the solubility of acid-treated carbon nanotubes in different media." *Carbon*, 45(9):1880–1890.
- [11] Sa, V. and Kornev, K. G., (2011). "Analysis of stability of nanotube dispersions using surface tension isotherms." *Langmuir*, 27(22):13451–13460.
- [12] Fleming, B. and Wanless, E., (2000). "Soft-contact Atomic Force Microscopy Imaging of Adsorbed Surfactant and Polymer Layers." *Microscopy and microanalysis: the official journal of Microscopy Society of America*, 6(2):104–112.
- [13] Yurekli, K., Mitchell, C. A. and Krishnamoorti, R., (2004). "Small-angle neutron

- scattering from surfactant-assisted aqueous dispersions of carbon nanotubes.” *Journal of the American Chemical Society*, 126(32):9902–9903.
- [14] Rastogi, R., Kaushal, R., Tripathi, S. K., Sharma, A. L., Kaur, I. and Bharadwaj, L. M., (2008). “Comparative study of carbon nanotube dispersion using surfactants.” *Journal of Colloid and Interface Science*, 328(2):421–428.
- [15] Yu, T., (2014). “Surfactant Assisted Dispersion of Single-Walled Carbon Nanotubes in Polyvinylpyrrolidone Solutions,” The University of Western Ontario, The School of Graduate and Postdoctoral Studies, Ontario, Canada.
- [16] Hasan, T., Scardaci, V., Tan, P., Rozhin, A. G., Milne, W. I. and Ferrari, A. C., (2007). “Stabilization and ‘debundling’ of single-wall carbon nanotube dispersions in N-methyl-2-pyrrolidone (NMP) by polyvinylpyrrolidone (PVP)” *Journal of Physical Chemistry C*, 111(34):12594–12602.
- [17] Manivannan, S., Jeong, I. O., Ryu, J. H., Lee, C. S., Kim, K. S., Jang, J. and Park, K. C., (2009). “Dispersion of single-walled carbon nanotubes in aqueous and organic solvents through a polymer wrapping functionalization.” *Journal of Materials Science: Materials in Electronics*, 20(3):223–229.
- [18] Rouse, J. H., (2005). “Polymer-assisted dispersion of single-walled carbon nanotubes in alcohols and applicability toward carbon nanotube/sol-gel composite formation” *Langmuir*, 21(3):1055–1061.
- [19] Moore, V. C., Strano, M. S., Haroz, E. H., Hauge, R. H., Smalley, R. E., Schmidt, J., and Talmon, Y., (2003). “Individually Suspended Single-Walled Carbon Nanotubes in Various Surfactants” *Nano Letters*, 3(10):1379–1382.
- [20] Sun, Z., Nicolosi, V., Rickard, D., Bergin, S. D., Aherne, D. and Coleman, J. N., (2008). “Quantitative Evaluation of Surfactant-stabilized Single-walled Carbon Nanotubes: Dispersion Quality and Its Correlation with Zeta Potential” *Journal Of the physical Cehmistry C*, 112(29):10692–10699.
- [21] Salzmann, C. G., Chu, B. T. T., Tobias, G., Llewellyn, S. A. and Green, M. L. H., (2007). “Quantitative assessment of carbon nanotube dispersions by Raman spectroscopy” *Carbon*, 45(5):907–912.
- [22] Li, Z. F., Luo, G. H., Zhou, W. P., Wei, F., Xiang, R. and Liu, Y. P., (2006). “The quantitative characterization of the concentration and dispersion of multi-walled carbon nanotubes in suspension by spectrophotometry” *Nanotechnology*, 17(15):3692–3698.
- [23] Bahr, J. L., Mickelson, E. T., Bronikowski, M. J., Smalley, R. E. and Tour, J. M., (2001). “Dissolution of small diameter single-wall carbon nanotubes in organic solvents?” *Chemical Communications*, (2):193–194.
- [24] Attal, S., Thiruvengadathan, R. and Regev, O., (2006). “Determination of the Concentration of Single-Walled Carbon Nanotubes in Aqueous Dispersions Using UV-Visible Absorption Spectroscopy” *Analytical Chemistry*, 78(23):8098–8104.
- [25] Shtein, M., Pri-bar, I. and Regev, O., (2013). “A simple solution for the determination of pristine carbon nanotube concentration” *The Analyst*, 138(5):1490–6.
- [26] Barbusinski, K., (2009). “Fenton Reaction - Controversy Concerning The Chemistry” *Ecological Chemistry and Engineering S*, 16(3):347–358.
- [27] Heinz-Jiirgen and Warneck, P. B., (1995). “Photodecomposition of Iron(III) Hydroxo and Sulfato Complexes in Aqueous Solution: Wavelength Dependence of OH and sod-

- Quantum Yields" *J. Phys. Chem.*, 99:5214–5221.
- [28] Rahim Pouran, S., Abdul Raman, A. A. and Wan Daud, W. M. A., (2014). "Review on the application of modified iron oxides as heterogeneous catalysts in Fenton reactions" *Journal of Cleaner Production*, 64:24–35.
- [29] Ramankutty, C. G. and Sugunan, S., (2001). "Surface properties and catalytic activity of ferrosinels of nickel, cobalt and copper, prepared by soft chemical methods" *Applied Catalysis A: General*, 218(1-2):39–51.
- [30] Mohapatra, M. and Anand, S., (2011). "Synthesis and applications of nano-structured iron oxides/hydroxides – a review." *International Journal of Engineering, Science and Technology*, 2(8):127–146.
- [31] J. William D. Callister., (2006). "Magnetic Properties of Materials." In *Materials Science and Engineering: An Introduction*, 7th Edition (pp. 57–102). John Wiley & Sons.
- [32] Flinn, R. A. and Trojan, P. K., (1990). "Engineering Materials and Their Applications". John Wiley & Sons.
- [33] Yue, J., Jiang, X., Kaneti, Y.V. and Yu, A., (2012). "Experimental and Theoretical Study of Low-Dimensional Iron Oxide Nanostructures." 6:119–146, *Smart Nanoparticles Technology, Nanotechnology and Nanomaterials* » "Smart Nanoparticles Technology" Editor: Abbas Hasim.
- [34] Vatta, L. L., Sanderson, R. D. and Koch, K. R., (2007). "An investigation into the potential large-scale continuous magnetite nanoparticle synthesis by high-pressure impinging stream reactors" *Journal of Magnetism and Magnetic Materials*, 311:114–119.
- [35] Sun, S., Zeng, H., Robinson, D. B., Raoux, S., Rice, P. M., Wang, S. X. and Li, G., (2004). "Monodisperse MFe_2O_4 (M = Fe, Co, Mn) Nanoparticles." *J. Am. Chem. Soc.*, 126(4):273–279.
- [36] Zhao, L., Zhang, H., Xing, Y., Song, S., Yu, S., Shi, W. and Cao, F., (2008). "Morphology-controlled synthesis of magnetites with nanoporous structures and excellent magnetic properties." *Chemistry of Materials*, 20(1):198–204.
- [37] Peng, Z.A. and Peng, X., (2002). "Nearly monodisperse and shape controlled CdSe nanocrystals via alternative routes: nucleation and growth." *J. Am. Chem. Soc.*, 124(8):3343.
- [38] Cornell, R. M. and Schwertmann, U., (2004). "The Iron Oxides." John Wiley & Sons.
- [39] Zou, G., Xiong, K., Jiang, C., Li, H., Li, T., Du, J. and Qian, Y., (2005). " Fe_3O_4 Nanocrystals with Novel Fractal" *The Journal of Physical Chemistry. B*, 109(39):18356–18360.
- [40] Wang, X., Zhao, Z., Qu, J., Wang, Z. and Qiu, J., (2010). "Shape-control and characterization of magnetite prepared via a one-step solvothermal route" *Crystal Growth and Design*, 10(7):2863–2869.
- [41] Kim, I. T., Nunnery, G. A., Jacob, K., Schwartz, J., Liu, X. and Tannenbaum, R., (2010). "Synthesis, characterization, and alignment of magnetic carbon nanotubes tethered with maghemite nanoparticles." *Journal of Physical Chemistry C*, 114(15):6944–6951.
- [42] Qu, X.F., Zhou, G.T., Yao, Q.Z. and Fu, S.Q., (2010). "Aspartic-Acid-Assisted Hydrothermal Growth and Properties of Magnetite Octahedrons." *The Journal of Physical Chemistry C*, 114(1):284–289.

- [43] Ge, S., Shi, X., Sun, K., Li, C., Baker, J. R., Banaszak Holl, M. M. and Orr, B. G., (2009). “A Facile Hydrothermal Synthesis of Iron Oxide Nanoparticles with Tunable Magnetic Properties.” *The Journal of Physical Chemistry C*, 113(31):13593–13599.
- [44] Daou, T. J., Pourroy, G., Begin-Colin, S., Greneche, J. M., Ulhaq-Bouillet, C., Legare, P. and Rogez, G., (2006). “Hydrothermal synthesis of monodisperse magnetite nanoparticles” *Chem. Mater.*, 18(18):4399–4404.
- [45] Hu, M., Jiang, J. S. and Li, X. D., (2009). “Surfactant-Assisted Hydrothermal Synthesis of Dendritic Magnetite Microcrystals” *Crystal Growth & Design*, 9(2):820–824.
- [46] Grabs, I.M., Bradtmöller, C., Menzel, D. and Garnweitner, G., (2012). “Formation Mechanisms of Iron Oxide Nanoparticles in Different Nonaqueous Media” *Crystal Growth & Design*, 12(3):1469–1475.
- [47] Wu, X., Tang, J., Zhang, Y. and Wang, H., (2009). “Low temperature synthesis of Fe₃O₄ nanocrystals by hydrothermal decomposition of a metallorganic molecular precursor.” *Materials Science and Engineering B: Solid-State Materials for Advanced Technology*, 157(1-3):81–86.
- [48] Zhang, J., Kong, Q., Du, J., Ma, D., Xi, G. and Qian, Y., (2007). “Formation, characterization, and magnetic properties of Fe₃O₄ microoctahedrons” *Journal of Crystal Growth*, 308(1):159–165.
- [49] Hu, M., Ji, R. P. and Jiang, J. Sen., (2010). “Hydrothermal synthesis of magnetite crystals: From sheet to pseudo-octahedron” *Materials Research Bulletin*, 45(12):1811–1815.
- [50] Li, Z., Chen, H., Bao, H. and Gao, M. (2004). “One-Pot Reaction to Synthesize Water-Soluble Magnetite Nanocrystals” *Chemistry of Materials*, 16(8):1391–1393.
- [51] Goya, G. F., Berquó, T. S., Fonseca, F. C. and Morales, M. P. (2003). “Static and dynamic magnetic properties of spherical magnetite nanoparticles” *Journal of Applied Physics*, 94(5):3520–3528.
- [52] Paramês, M. L., Mariano, J., Rogalski, M. S., Popovici, N. and Conde, O. (2005). “UV pulsed laser deposition of magnetite thin films” *Materials Science and Engineering B: Solid-State Materials for Advanced Technology*, 118(1):246–249.
- [53] Puentes, V. F., Krishnan, K. M. and Alivisatos, A., (2001). “Colloidal nanocrystal shape and size control: the case of cobalt.” *Science*, 291(5511):2115–2117.
- [54] Gleiter, H., (1990). “Nanocrystalline Materials” 33:223–315.
- [55] Zheng, Y., Cheng, Y., Bao, F. and Wang, Y., (2006). “Synthesis and magnetic properties of Fe₃O₄ nanoparticles” *Materials Research Bulletin*, 41(3):525–529.
- [56] Chen, C., Jiang, X., Kaneti, Y. V. and Yu, A., (2013). “Design and construction of polymerized-glucose coated Fe₃O₄ magnetic nanoparticles for delivery of aspirin.” *Powder Technology*, 236:157–163.
- [57] Szabó, D. Y., & Vollath, D., (1999). “Nanocomposites from coated nanoparticles.” *Advanced Materials*, 11(15):1313–1316.
- [58] Dumitrache, F., Morjan, I., Alexandrescu, R., Morjan, R. E., Voicu, I., Sandu, I. and Woodward, A., (2004). “Nearly monodispersed carbon coated iron nanoparticles for the catalytic growth of nanotubes/nanofibres.” *Diamond and Related Materials*, 13(2):362–370.

- [59] Poizot, P., Laruelle, S., Grugeon, S., Dupont, L. and Tarascon, J. M., (2000). "Nano-sized transition-metal oxides as negative-electrode materials for lithium-ion batteries" *Nature*, 407(6803):496–499.
- [60] Cabana, J., Monconduit, L., Larcher, D. and Palacín, M. R., (2010). "Beyond intercalation-based Li-ion batteries: The state of the art and challenges of electrode materials reacting through conversion reactions" *Advanced Materials*, 22(35):170–192.
- [61] Demir-Cakan, R., Hu, Y. S., Antonietti, M., Maier, J. and Titirici, M. M., (2008). "Facile one-pot synthesis of mesoporous SnO₂ microspheres via nanoparticles assembly and lithium storage properties." *Chemistry of Materials*, 20(4):1227–1229.
- [62] Chen, Y., Huang, Q. Z., Wang, J., Wang, Q. and Xue, J. M., (2011). "Synthesis of monodispersed SnO₂@C composite hollow spheres for lithium ion battery anode applications" *Journal of Materials Chemistry*, 21(43):17448.
- [63] Sun, X. and Li, Y., (2004). "Colloidal Carbon Spheres and Their Core/Shell Structures with Noble-Metal Nanoparticles" *Angewandte Chemie - International Edition*, 43(5):597–601.
- [64] Chen, Y., Xia, H., Lu, L. and Xue, J., (2012). "Synthesis of porous hollow Fe₃O₄ beads and their applications in lithium ion batteries." *Journal of Materials Chemistry*, 22(11):5006.
- [65] Zheng, J., Liu, Z. Q., Zhao, X. S., Liu, M., Liu, X. and Chu, W., (2012). "One-step solvothermal synthesis of Fe₃O₄@C core-shell nanoparticles with tunable sizes" *Nanotechnology*, 23(16):165601.
- [66] Kim, D., Kim, K. and Park, S., (2012) "Synthesis and Electrochemical Performance of Polypyrrole- Coated Iron Oxide / Carbon Nanotube Composites" 13(3):157–160.
- [67] Khiew, P., Ho, M., Chiu, W., Shamsudin, R. and Azmi, M., (2013) "Synthesis and Electrochemical Characterization of Iron Oxide / Activated Carbon Composite Electrode for Symmetrical Supercapacitor" 7(8):86–90.
- [68] Tenne, R. and Rao, C. N. R., (2004) "Inorganic nanotubes." *Philosophical Transactions A*, 362:2099–2125.
- [69] Rao, C. N. R. and Govindaraj, A., (2009) "Synthesis of inorganic nanotubes" *Advanced Materials*, 21(42):4208–4233.
- [70] Mayers, B. and Xia, Y., (2002) "Formation of tellurium nanotubes through concentration depletion at the surfaces of seeds" *Advanced Materials*, 14(4):279–282.
- [71] Wang, Z., Wang, L. and Wang, H., (2008). "PEG-mediated hydrothermal growth of single-crystal tellurium nanotubes" *Crystal Growth and Design*, 8(12):4415–4419.
- [72] Fan, H. J., Gösele, U. and Zacharias, M., (2007). "Formation of nanotubes and hollow nanoparticles based on kirkendall and diffusion processes: A review" *Small*, 3(10):1660–1671.
- [73] Yoshimura, M. and Byrappa, K., (2008). "Hydrothermal processing of materials: Past, present and future" *Journal of Materials Science*, 43(7):2085–2103.
- [74] Mullin, J. W., (1997) "Crystallization" 3rd Ed. John Wiley & Sons, Butterworth-Heinemann, Oxford.
- [75] Randolph, A. D., (1989) "Theory of Particulate Processes" New York: Academic Press.

- [76] Jolivet, J.P., (2000) "Metal oxide chemistry and synthesis: from solution to solid state" John Wiley & Sons, Chichester.
- [77] Wu, J., Lu, X., Zhang, L., Huang, F. and Xu, F., (2009) "Dielectric Constant Controlled Solvothermal Synthesis of a TiO₂ Photocatalyst with Tunable Crystallinity: A Strategy for Solvent Selection." *European Journal of Inorganic Chemistry*, (19):2789–2795.
- [78] Qin, A., Fang, Y., Tao, P., Zhang, J. and Su, C., (2007) "Silver telluride nanotubes prepared by the hydrothermal method" *Inorganic Chemistry*, 46(18):7403–7409.
- [79] Kumbhar, A. and Chumanov, G., (2005) "Synthesis of iron(III)-doped titania nanoparticles and its application for photodegradation of sulforhodamine-B pollutant." *Journal of Nanoparticle Research*, 7(4-5):489–498.
- [80] Zhou, W., Tang, S., Wan, L., Wei, K. and Li, D., (2004) "Preparation of nano-TiO₂ photocatalyst by hydrolyzation-precipitation method with metatitanic acid as the precursor" *Journal of Materials Science*, 39(3):1139–1141.
- [81] Hwang, S. J., Petucci, C. and Raftery, D., (1998) "In situ solid-state NMR studies of trichloroethylene photocatalysis: Formation and characterization of surface-bound intermediates." *Journal of the American Chemical Society*, 120(18):4388–4397.
- [82] Asiltürk, M., Sayilkan, F. and Arpac, E., (2009) "Effect of Fe³⁺ ion doping to TiO₂ on the photocatalytic degradation of Malachite Green dye under UV and vis irradiation" *Journal of Photochemistry and Photobiology A: Chemistry*, 203(1):64–71.
- [83] UV-Vis Spectroscopy (Electronic transitions of σ , π , and n electrons): <http://teaching.shu.ac.uk/hwb/chemistry/tutorials/molspec/uvvisab1.htm>, Access date:05.01.2015.
- [84] Delgado, A.V., González-Caballero, F., Hunter, R. J., Koopal, L. K. and Lyklema, J., (2007) "Measurement and interpretation of electrokinetic phenomena" *Journal of Colloid and Interface Science*, 309(2):194–224.
- [85] Koutsoukos, P. K., Klepetsanis, P. G. and Spanos, N., (2006). "Calculation of Zeta-Potentials from ElectroKinetic Data." In P. Somasundaran (Ed.), *Encyclopedia of Surface and Colloid Science* (Second Edi., p. Volume 2 1097–1114). CRC Press Taylor and Francis Group.
- [86] ASTM. (2013) "Standard Guide for Measurement of Electrophoretic Mobility and Zeta Potential of Nanosized Biological Materials," 1–7.
- [87] Ye, Y., Cai, S., Yan, M., Chen, T. and Guo, T., (2013) "Concentration detection of carbon nanotubes in electrophoretic suspension with UV-vis spectrophotometry for application in field emission devices" *Applied Surface Science*, 284:107–112.
- [88] Giordani, S., Bergin, S. D., Nicolosi, V., Lebedkin, S., Kappes, M. M., Blau, W. J. and Coleman, J. N., (2006) "Debundling of single-walled nanotubes by dilution: Observation of large populations of individual nanotubes in amide solvent dispersions" *Journal of Physical Chemistry B*, 110(32):15708–15718.
- [89] Tadros, T. F., (2010) "Colloid Stabilization of Paint Dispersions" In *Colloids in paints* (pp. Volume 6, 71–108). Weinheim: Wiley-VCH Verlag GmbH & Co. KGaA.
- [90] Hiemenz, P. C. and Rajagopalan R., (1997). "Principles of Colloid and Surface Chemistry" (3rd ed.). CRC Press, New York: Marcel Dekker.
- [91] White, B., Banerjee, S., Brien, S. O., Turro, N. J. and Herman, I. P., (2007). "Zeta-Potential Measurements of Surfactant-Wrapped Individual Single-Walled Carbon

Nanotubes,” 2(1):13684–13690.

- [92] Boccaccini, A. R., Cho, J., Roether, J. a., Thomas, B. J. C., Jane Minay, E., & Shaffer, M. S. P. (2006). “Electrophoretic deposition of carbon nanotubes.” *Carbon*, 44(15):3149–3160.
- [93] Sarkar, P., De, D., Uchikochi, T. and Besra, L., (2012). “Electrophoretic Deposition (EPD): Fundamentals and Novel Applications in Fabrication of Advanced Ceramic Microstructures.” In J. H. Dickerson and A. R. Boccaccini, *Electrophoretic deposition of Nanomaterials* (p. 190), Springer, New York.
- [94] Wang, P., Shi, Q., Liang, H., Steurman, D. W., Stucky, G. D. and Keller, A., (2008). “Enhanced environmental mobility of carbon nanotubes in the presence of humic acid and their removal from aqueous solution.” *Small*, 4(12):2166–2170.
- [95] Richards, E. G., (1980). "An Introduction to Physical Properties of Large Molecules in Solution". An introduction to physical properties of large molecules in solution (1st ed.). New York: Cambridge University Press.
- [96] Wang, J., Tsuzuki, T., Tang, B., Cizek, P., Sun, L. and Wang, X., (2010) “Synthesis of silica-coated ZnO nanocomposite: The resonance structure of polyvinyl pyrrolidone (PVP) as a coupling agent” *Colloid and Polymer Science*, 288(18):1705–1711.
- [97] Oh, S. J., Zhang, J., Cheng, Y., Shimoda, H. and Zhou, O., (2004) “Liquid-phase fabrication of patterned carbon nanotube field emission cathodes.” *Applied Physics Letters*, 84(19):3738–3740.
- [98] Van der Biest, O. O. and Vandeperre, L. J., (1999). “Electrophoretic Deposition of Materials.” *Annual Review of Materials Science*, 29:327-352.
- [99] Geng, J., Johnson, B. F. G., Wheatley, A. E. H. and Luo, J. K., (2013) “Spectroscopic route to monitoring individual surfactant ions and micelles in aqueous solution: A case study.” *Central European Journal of Chemistry*, 12(3):307–311.
- [100] Ma, M., Zhang, Y., Guo, Z. and Gu, N., (2013) “Facile synthesis of ultrathin magnetic iron oxide nanoplates by Schikorr reaction” *Nanoscale research letters*, 8(1):16.
- [101] Du, J., Cullen, J. J. and Buettner, G. R., (2012) “Ascorbic acid: Chemistry, biology and the treatment of cancer.” *Biochimica et Biophysica Acta - Reviews on Cancer*, 1826(2):443–457.
- [102] Sreeja, V., Jayaprabha, K. N. and Joy, P. A., (2015) “Water-dispersible ascorbic-acid-coated magnetite nanoparticles for contrast enhancement in MRI.” *Applied Nanoscience*, 5(4):435–441.
- [103] Pot, O. N. E., Synthesis, S., Organic, O. F., Coated, A. and Iron, M., (2013) “One Pot Solvothermal Synthesis Of Organic Acid Coated Magnetic Iron Oxide Nanoparticles” 4:2011–2015.
- [104] Mohapatra, S., Pramanik, N., Mukherjee, S., Ghosh, S. K. and Pramanik, P., (2007) “A simple synthesis of amine-derivatised superparamagnetic iron oxide nanoparticles for bioapplications” *Journal of Materials Science*, 42(17):7566–7574.
- [105] Bae, H., Ahmad, T., Rhee, I., Chang, Y., Jin, S.-U. and Hong, S., (2012) “Carbon-coated iron oxide nanoparticles as contrast agents in magnetic resonance imaging.” *Nanoscale Research Letters*, 7(1):44.

- [106] Seo, M., Yoon, D., Hwang, K. S., Kang, J. W. and Kim, J., (2013) "Supercritical alcohols as solvents and reducing agents for the synthesis of reduced graphene oxide." *Carbon*, 64(0):207–218.
- [107] Qi, D., Lu, J., Deng, C. Zhang, X., (2009) "Magnetically Responsive Fe₃O₄ @C@SnO₂ Core–Shell Microspheres: Synthesis, Characterization and Application in Phosphoproteomics." *The Journal of Physical Chemistry C*, 113(36):15854–15861.
- [108] Ohno, T., Akiyoshi, M., Umebayashi, T., Asai, K., Mitsui, T. and Matsumura, M., (2004) "Preparation of S-doped TiO₂ photocatalysts and their photocatalytic activities under visible light." *Applied Catalysis A: General*, 265(1):115–121.
- [109] Rockafellow, E. M., Stewart, L. K. and Jenks, W. S., (2009) "Is sulfur-doped TiO₂ an effective visible light photocatalyst for remediation?" *Applied Catalysis B: Environmental*, 91(1-2):554–562.
- [110] Zaleska, A., Górska, P., Sobczak, J. W. and Hupka, J., (2007) "Thioacetamide and thiourea impact on visible light activity of TiO₂." *Applied Catalysis B: Environmental*, 76(1-2):1–8.
- [111] Bavykin, D. V., & Walsh, F. C., (2009) "Titanate and Titania Nanotubes" *The Royal Society of Chemistry, Cambridge*.
- [112] Ferreira, O. P., Souza Filho, A. G., Mendes Filho, J. and Alves, O. L. (2006). "Unveiling the structure and composition of titanium oxide nanotubes through ion exchange chemical reactions and thermal decomposition processes." *Journal of the Brazilian Chemical Society*, 17(2):393–402.
- [113] Menzel, R., Peiro, A. M., Durrant, J. R. and Shaffer, M. S. P., (2006) "Impact of Hydrothermal Processing Conditions on High Aspect Ratio Titanate Nanostructures" (5):6059–6068.
- [114] Yang, J., Jin, Z., Wang, X., Li, W., Zhang, J., Zhang, S. and Zhang, Z., (2003) "Study on composition, structure and formation process of nanotube Na₂Ti₂O₄(OH)₂" *Dalton Transactions*, 4(20):3898.
- [115] Xiao, N., Li, Z., Liu, J. and Gao, Y., (2010) "Effects of calcination temperature on the morphology, structure and photocatalytic activity of titanate nanotube thin films." *Thin Solid Films*, 519(1):541–548.
- [116] Du, G. H., Chen, Q., Che, R. C., Yuan, Z. Y. and Peng, L. M., (2001) "Preparation and structure analysis of titanium oxide nanotubes" *Applied Physics Letters*, 79(22):3702–3704.
- [117] Khan, M. A., Jung, H. and Yang, O., (2006) "Synthesis and Characterization of Ultrahigh Crystalline TiO₂ Nanotubes." *J. Phys. Chem. B*, 110:6626–6630.
- [118] Chen, X., Chen, X., Burda, C. and Burda, C., (2008) "The Electronic Origin of the Visible-Light Absorption Properties of C-, N- and S-Doped TiO₂ Nanomaterials" *Journal of the American Chemical Society*, 5018–5019.
- [119] Chen, X. and Mao, S. S., (2007) "Titanium Dioxide Nanomaterials :Synthesis, Properties, Modifications, and Applications", 107:2891–2959.
- [120] Xiong, L. Bin, Li, J. L., Yang, B. and Yu, Y. (2012) "Ti³⁺ in the surface of titanium dioxide: Generation, properties and photocatalytic application", *Journal of Nanomaterials*, 2012.
- [121] Cho, J. M., Yun, W. J., Lee, J.-K., Lee, H. S., So, W. W., Moon, S. J. and Wu, Y., (2007)

- “Electron spin resonance from annealed titania nanotubes.” *Applied Physics A*, 88(4):751–755.
- [122] Jun, J., Dhayal, M., Shin, J. H., Kim, J. C. and Getoff, N., (2006) “Surface properties and photoactivity of TiO₂ treated with electron beam” *Radiation Physics and Chemistry*, 75(5):583–589.
- [123] Zhang, M., Jin, Z., Zhang, J., Guo, X., Yang, J., Li, W. and Zhang, Z., (2004) “Effect of annealing temperature on morphology, structure and photocatalytic behavior of nanotubed H₂Ti₂O₄(OH)₂” *Journal of Molecular Catalysis A: Chemical*, 217(1-2):203–210.
- [124] Cho, J. M., Seo, J. M., Lee, J.-K., Zhang, H. and Lamb, R., (2009) “Electronic properties of oxygen vacancies in titania nanotubes.” *Physica B: Condensed Matter*, 404(1):127–130.
- [125] Asahi, R., Morikawa, T., Ohwaki, T., Aoki, K. and Taga, Y., (2001) “Visible-light photocatalysis in nitrogen-doped titanium oxides.” *Science*, 293(5528):269–271.
- [126] Asiri, A. M., Al-Amoudi, M. S., Bazaid, S.A., Adam, A.A., Alamry, K. A. and Anandan, S., (2014) “Enhanced visible light photodegradation of water pollutants over N-, S-doped titanium dioxide and n-titanium dioxide in the presence of inorganic anions.” *Journal of Saudi Chemical Society*, 18(2):155–163.
- [127] Farrokhi-Rad, M. and Ghorbani, M., (2011) “Electrophoretic deposition of titania nanoparticles in different alcohols: Kinetics of deposition” *Journal of the American Ceramic Society*, 94(8):2354–2361.
- [128] Farrokhi-Rad, M. and Ghorbani, M., (2012) “Stability of titania nano-particles in different alcohols.” *Ceramics International*, 38(5):3893–3900.
- [129] Islam, M. F., Rojas, E., Bergey, D. M., Johnson, A.T. and Yodh, A.G., (2003) “High weight fraction surfactant solubilization of single-wall carbon nanotubes in water.” *Nano Letters*, 3(2):269–273.
- [130] Simmons, T. J., Hashim, D., Vajtai, R. and Ajayan, P. M., (2007) “Large area-aligned arrays from direct deposition of single-wall carbon nanotube inks” *Journal of the American Chemical Society*, 129(33):10088–10089.
- [131] Blanch, A. J., Lenehan, C. E. and Quinton, J. S., (2010) “Optimizing surfactant concentrations for dispersion of single-walled carbon nanotubes in aqueous solution” *Journal of Physical Chemistry B*, 114(30):9805–9811.
- [132] Clark, M. D., Subramanian, S. and Krishnamoorti, R., (2011) “Understanding surfactant aided aqueous dispersion of multi-walled carbon nanotubes” *Journal of Colloid and Interface Science*, 354(1):144–151.
- [133] Manna, L., Scher, E.C. and Alivisatos, A.P., (2000) “Synthesis of soluble and processable rod-, arrow-, teardrop-, and tetrapod-shaped CdSe nanocrystals” *Journal of the American Chemical Society*, 122(51):12700–12706.
- [134] Cho, K. S., Talapin, D. V., Gaschler, W. and Murray, C. B., (2005) “Designing PbSe nanowires and nanorings through oriented attachment of nanoparticles” *Journal of the American Chemical Society*, 127(19):7140–7147.
- [135] Ould-Ely, T., Prieto-Centurion, D., Kumar, a., Guo, W., Knowles, W. V., Asokan, S. and Whitmire, K. H., (2006) “Manganese(II) oxide nano-hexapods: Insight into controlling the form of nanocrystals.” *Chemistry of Materials*, 18(7):1821–1829.

- [136] Liu, J., Xia, H., Xue, D., and Lu, L., (2009) “Double-Shelled Nanocapsules of V₂O₅ - Based Composites as High-Performance Anode and Cathode Materials for Li Ion Batteries” *Journal of the American Chemical Society*, 12086–12087.
- [137] Yu, S. H., Cui, X., Li, L., Li, K., Yu, B., Antonietti, M. and Cölfen, H., (2004) “From starch to metal/carbon hybrid nanostructures: Hydrothermal metal-catalyzed carbonization” *Advanced Materials*, 16(18):1636–1640.
- [138] Wang, Z., Guo, H., Yu, Y. and He, N. (2006) “Synthesis and characterization of a novel magnetic carrier with its composition of Fe₃O₄/carbon using hydrothermal reaction.” *Journal of Magnetism and Magnetic Materials*, 302(2):397–404.
- [139] Tauc, J. and Mentel, A., (1972) “States in the gap.” *Journal of Non-Crystalline Solids*.
- [140] Soltani, N., Saion, E., Hussein, M. Z., Erfani, M., Abedini, A., Bahmanrokh, G. and Vaziri, P. (2012) “Visible light-induced degradation of methylene blue in the presence of photocatalytic ZnS and CdS nanoparticles” *International Journal of Molecular Sciences*, 13(10):12242–12258.
- [141] Seoudi, R., Shabaka, a., Eisa, W. H., Anies, B. and Farage, N. M., (2010) “Effect of the prepared temperature on the size of CdS and ZnS nanoparticle.” *Physica B: Condensed Matter*, 405(3):919–924.
- [142] Umek, P., Pregelj, M., Gloter, A., Cevc, P., Jaglic, Z., Miran, C. and Uni, V., (2008). “Coordination of Intercalated Cu²⁺ Sites in Copper Doped Sodium Titanate Nanotubes and Nanoribbons” 15311–15319.
- [143] An, Y., Li, Z. and Shen, J. (2013) “The visible light absorption property of Cu-doped hydrogen titanate nanotube thin films: An experimental and theoretical study” *Physica B: Condensed Matter*, 429:127–132.
- [144] Zaman, A. C., Üstündağ, C. B., Kaya, F. and Kaya, C., (2012). “Synthesis and electrophoretic deposition of hydrothermally synthesized multilayer TiO₂ nanotubes on conductive filters” *Materials Letters*, 66(1):179–181.
- [145] Fernandes, R. M. F., Abreu, B., Claro, B., Buzaglo, M., Regev, O., Furó, I. and Marques, E. F., (2015) “Dispersing Carbon Nanotubes with Ionic Surfactants under Controlled Conditions: Comparisons and Insight.” *Langmuir*.
- [146] Hsieh, A. G., Korkut, S., Punckt, C. and Aksay, I. A., (2013) “Dispersion stability of functionalized graphene in aqueous sodium dodecyl sulfate solutions” *Langmuir*, 29(48):14831–8.

CURRICULUM VITAE

PERSONAL INFORMATION

Name Surname : Ali Can ZAMAN
Date of birth and place : 13/06/1983-Zonguldak
Foreign Languages : English (YDS-2015: 92,5)
E-mail : alicanzaman@gmail.com

EDUCATION

Degree	Department	University	Date of Graduation
Master	MaterialsScience and Engineering	Yildiz Technical University	2010
Undergraduate	MaterialsScience and Engineering	Yildiz Technical University	2007
High School	Mehmet Celikel High School		2001
Elementary School	TED Zonguldak College		1998

WORK EXPERIENCE

Year	Corporation/Institute	Enrollment
2008-2012	Yildiz technical University/ The Scientific & Technological Research Council of Turkey	Researcher
2012-2014	Kocaeli University	Research Assistant
2014-	Yildiz Technical University/ Science and Technology Application and Research Center	Specialist

PUBLICATIONS

Papers

1. Zaman, A. C., & Kaya, C. (2015). Determination of Quantity of Materials in Suspensions and in Electrophoretic Coatings by UV-Visible Absorption Spectroscopy. *JOURNAL OF THE ELECTROCHEMICAL SOCIETY*, 162(11), D3109-D3111.
2. Zaman, A. C., Ustundag, C. B., Kaya, F., & Kaya, C. (2012). OH and COOH functionalized single walled carbon nanotubes-reinforced alumina ceramic nanocomposites. *CERAMICS INTERNATIONAL*, 38(2), 1287-1293.
3. Noberi, C., Zaman, A. C., Ustundag, C. B., Kaya, F., & Kaya, C. (2012). Electrophoretic deposition of hydrothermally synthesised Ag-TiO₂ hybrid nanoparticles onto 3-D Ni filters. *MATERIALS LETTERS*, 67(1), 113-116.
4. Zaman, A. C., Ustundag, C. B., Kaya, F., & Kaya, C. (2012). Synthesis and electrophoretic deposition of hydrothermally synthesized multilayer TiO₂ nanotubes on conductive filters. *MATERIALS LETTERS*, 66(1), 179-181.
5. Zaman, A. C., Ustundag, C. B., Celik, A., Kara, A., Kaya, F., & Kaya, C. (2010). Carbon nanotube/boehmite-derived alumina ceramics obtained by hydrothermal synthesis and spark plasma sintering (SPS). *JOURNAL OF THE EUROPEAN CERAMIC SOCIETY*, 30(16), 3351-3356.
6. Zaman, A. C., Ustundag, C. B., Kuskonmaz, N., Kaya, F., & Kaya, C. (2010). 3-D micro-ceramic components from hydrothermally processed carbon nanotube-boehmite powders by electrophoretic deposition. *CERAMICS INTERNATIONAL*, 36(5), 1703-1710.
7. Zaman, A. C., Ustundag, C. B., & Kaya, C. (2010). Boehmite derived surface functionalized carbon nanotube-reinforced macroporous alumina ceramics. *JOURNAL OF THE EUROPEAN CERAMIC SOCIETY*, 30(12), 2525-2531.

Conference Papers

1. Ali Can Zaman, C. Kaya, C. B. Ustundag, "Structure and Properties of Carbon Nanotube-Reinforced Alumina Based Ceramics" NanoTR5, 08-12 June 2009 Eskisehir, Turkey.
2. Ali Can Zaman, Cem B. Üstündağ, Ali Çelik, Alpagut Kara, Figen Kaya and Cengiz Kaya, "Carbon nanotube (CNT) Reinforced Alumina Based Ceramic Nanocomposites by means of Hydrothermal Synthesis and Spark Plasma Sintering" NanoTR6, 15-18 June 2010, Izmir, Turkey.
3. Ali Can Zaman, Cem B. Üstündağ, Cengiz Kaya "Production of Carbon Nanotube Reinforced Alumina Ceramic Gears by means of Electrophoretic Deposition and Their Characterization" 15th International Metallurgy and Materials Congress 11-13 November 2010, Istanbul, Turkey.
4. Ali Can Zaman, Cem B. Üstündağ, Ali Çelik, Alpagut Kara, Figen Kaya and Cengiz Kaya "Carbon Nanotube Reinforced Alumina Ceramics by Means of Hydrothermal Synthesis and Spark Plasma Sintering" 12th Conference of The European Ceramic Society 19-23 June 2011, Stockholm Sweden.
5. Ali Can Zaman, Cem B. Üstündağ, Ali Çelik, Alpagut Kara, Figen Kaya and Cengiz Kaya "Structure and Properties of OH And COOH Functional Group Attached Single Wall

Carbon Nanotube Reinforced Alumina Ceramics” NanoTR7, 27 June- 1 July 2011, Istanbul Turkey.

6. Cansu Noberi, Ali Can Zaman, Cem B. Ustundag, Figen Kaya, Cengiz Kaya, Emrah Sefik Abamor, Melahat Bagirova and Adil Allahverdiyev “Synthesis and Characterization of Ag-TiO₂ Nano-composite Particles for Antimicrobial Applications” BioMat (European Symposium on Biomaterials and Related Areas) 13-14 April 2011, Jena, Germany (Poster Presentation).
7. Cansu Noberi, Ali Can Zaman, Cem B. Ustundag, Figen Kaya, Cengiz Kaya, Emrah Sefik Abamor, Melahat Bagirova and Adil Allahverdiyev “Ag-TiO₂ Nano-Powders by Hydrothermal Synthesis and Their Antimicrobial Properties” NanoTR7, 27 June- 1 July 2011, Istanbul Turkey.
8. Ali Can Zaman, Cem B. Üstündağ, Figen Kaya and Cengiz Kaya “Characterization of functional coatings obtained by electrophoretic deposition from hydrothermally synthesized titanate nanotubes on conductive flat surfaces and foams”, NanoTR8, 25-29 June 2012, Ankara, Turkey.
9. Noberi, C., Zaman, A.C., Ustundag, C.B., Kaya, F. ve Kaya C., “Structure and Properties of Hydrothermally Synthesized Ag Dopped TiO₂ Nano Composite Particles and Their Coatings onto 3-D Filters”, NanoTR8, 25-29 June 2012, Ankara, Turkey.
10. Noberi, C., Zaman, A.C., Ustundag, C.B., Kaya, F., Kaya C., Abamor, E.S., Bagirova, M. ve Allahverdiyev, A., “Structure and Properties of Ag-Dopped TiO₂ Nano Composite Particles by Hydrothermal Synthesis”, 16th International Metallurgy and Materials Congress, 13-15 September 2012, Istanbul Turkey.
11. Ustundag, C.B., Zaman, A.C., Kaya, F., Kaya C., “Hydrothermally Prepared Ceramic-Carbon Nanotube Nanocomposite Structure”, 10th International Conference on Nanosciences & Nanotechnologies (NN13), 9-12 July 2013, Thessaloniki, Greece (Poster presentation).
12. Ustundag, C.B., Zaman, A.C., Kaya, F., Kaya C.,”Fabrication of Porous Hydroxyapatite by Electrophoretic Deposition”, International Porous and Powder Materials Symposium and Exhibition (PMM 2013), September 3-6, 2013, Izmir, Turkey.

Patents

National

1. Ahmet Özkan, Cengiz Kaya, Figen Kaya, Cansu Noberi, Burçin Özbay, Nergis Özkan, Serhat Çoban, Ezgi Aydın, Ahmet Altun, Ali Can Zaman “Uv destekli antimikrobiyal a-Fe₂O₃ kaplı çok katmanlı havalandırma filtresi tasarımı” Başvuru no:2013/05487, 2014/08/21, Türkiye.

PROJECTS

1. Project Assistant: The Support Programme for COST (European Cooperation in Science and Technology) and The Scientific and Technological Research Council of Turkey (TUBITAK) under the title of “The Production and Characterization of Antimicrobial Coatings on 3D Metallic Filters Using Electrophoretic Deposition”: contract number 109R007.

2. Project Assistant: The Support Programme for Scientific and Technological Research Council of Turkey (TUBITAK) under the title of “Processing and Characterisation of Aligned and Surface Modified Carbon Nanotube Reinforced Alumina and Hydroxyapatite Nano Functional ceramics”: contract number 108T651.
3. Researcher: Yildiz Technical University Research Project; Synthesis of Various nanotubes and Their Characterization, Project Number: 2012-07-02-DOP02).
4. Researcher: Yildiz Technical University Research Project; Production and characterization of aligned carbon and oxide based nanotubes containing anisotropic layers and micro parts, Project number: 2012-07-02-KAP05

CERTIFICATES and PARTICIPATIONS

Participations in COST (European cooperation in science and technology) Action MP0902 Composites of Inorganic Nanotubes and Polymers (COINAPO)

1. Participation in COINAPO Summer School "Characterization Work Group: From Functional Nanomaterials to Composites", 25-27 July 2011 Oxford University, Oxford, United Kingdom.
2. Participation in COINAPO Summer School, "Advances in Nanocomposite Materials: Preparation and Characterization" 3-7 September 2012, Institute of Physical Chemistry Romanian Academy, Bucharest, Romania.
3. Zaman, A.C., Noberi, C. Ipeksac, T., Kaya, F., Kaya, C., Synthesis of TiO₂ and ZnO Nanotubes by Hydrothermal Synthesis Followed by Electrophoretic Deposition to Obtain Functional Coatings on Conductive Fillers, 4th Topical meeting of the COST Action MP0902 COINAPO, Lyublyana, Slovenia, 8-9 December, 2011,
4. Ali Can Zaman, Tugba İpeksac, Figen Kaya and Cengiz Kaya, Synthesis of CuO and TiO₂ Nanotubes and Their Antibacterial Activity COINAPO Workshop Ercolano (Naples), Italy, 20-22 March 2013.

Other Certificates

1. Spectroscopy Graduate Summer School 16-21 June 2014, Faculty of Pharmaceutical Sciences, Erzincan University.

SKILLS

Characterization

1. Scanning electron microscopy (SEM): Zeiss EVO LS 10
2. Gas Sorption Surface Area and Pore Size Analyzer: Quantachrome QUADRASORB SI
3. UV-Visible Absorption spectrophotometer: PGeneral T80+
4. Fourier Transformation Infrared Spectrometer (FTIR): Perkin Elmer Spectrum 100
5. Zeta Potential and Particle Size Analyzer: Malvern Zetasizer NanoZS
6. Differential Thermal Analyzer (TG/DTA): Hitachi SII6000
7. Laser Particle Size Analyzer: Malvern Mastersizer (MS 2000)
8. Fatigue Test System (Instron 8870)